Glacial landforms and Gully Formation on Mars

Thesis submitted to

Indian Institute of Technology Gandhinagar, India

For the degree of

Doctor of Philosophy

in

Earth Sciences

by

Rishitosh Kumar Sinha

(Roll No. 17330001)

Under the guidance of

Dr. Dwijesh Ray

Associate Professor

Planetary Sciences Division

Physical Research Laboratory, Ahmedabad

July 2022

To,

My family

Declaration

I declare here that this thesis report represents my own ideas in my own words and I have included others ideas with appropriate citations from original sources. I also declare that I have followed all principles of academic honesty and integrity and have not fabricated or falsified any idea/fact/source/data in my submission. I understand that any violation of the above can cause disciplinary action by the Institute and can evoke penal action from the sources.

Rishitosh Kumar Sinha

Date: July 12th, 2022 (Roll no.: 17330001)

Department of Earth Sciences
Indian Institute of Technology, Gandhinagar
Gandhinagar, Gujarat-382355

CERTIFICATE

It is certified that the work contained in the thesis titled **"Glacial landforms and Gully Formation on Mars"** by **Mr. Rishitosh Kumar Sinha** (Roll no: 17330001), has been carried out under my supervision and that this work has not been submitted elsewhere for a degree.

Dr. Dwijesh Ray
(Thesis Supervisor)
Associate Professor,
Planetary Sciences Division,
Physical Research Laboratory,
Ahmedabad, India

Date: July 12th, 2022

ACKNOWLEDGMENTS

After serving in Physical Research Laboratory (PRL) for four years, I got the opportunity to pursue my PhD research work, which ended after another period of five years into this thesis as a result. During the last five years, I have worked as an employee of PRL and carried out my PhD research work as a PRL-IIT Gandhinagar student. It has been a mixture of emotions, responsibilities, expectations, challenges and assignments during the last five years. Emotions were added to this PhD when my wife (Mrs. Surabhi Sinha) gave birth to our first child Anay (at the start of my PhD) and then the second child Tia (just before the end of PhD). I cannot express the real feeling of being a father in words, but I want to mention them here because this PhD thesis is dedicated to my sweet and cute children's and especially to my wife who has sacrificed a lot in order for me to pursue this PhD. I hope one day I can repay you for all the beautiful life moments we have missed just because I was busy with my research work. Nevertheless, with so many helpful, kind and intelligent people around me, I have had a fantastic and amazing five years. Now I would like to express my gratitude here to all those people.

Dr. Dwijesh Ray, my PhD supervisor, I would say that he is the coolest person and an awesome scientist in PRL, who always has a very genuine and comfortable approach towards doing things. He has inspired and motivated me by providing endless support to me in my research, and the freedom and faith he has shown in me was the reason I admire him a lot. I would like to express my sincere gratitude to my DSC members (Dr. Neeraj Srivastava, Dr. Vijayan S., and Dr. Anil D. Shukla) for time-to-time encouragement and critical review remarks, which

helped to improve the quality of the work done in this research work.

One of the best things that happened to me is that I got a chance to attend a workshop on "Martian Gullies and their Earth Analogues" held in London, UK during 20-21 June 2016. Dr. Susan Conway at the University of Nantes was one of the conveners of the workshop. The science talks and discussions happened during that workshop gave my PhD research work an invaluable kick start. Then Susan Conway showed faith in me and continued to guide me as a mentor as well as collaborate on some of the chapters of this thesis - I learned a lot from her and I am still learning. Susan introduced me to Dr. Tjalling De Haas at the Utrecht University. He is an amazing scientist and a gentle person from whom one can learn endless things about debris-flows. Tjalling, thanks a lot for sharing your thorough knowledge, helping for doing updated research on Martian gullies, and for keeping me highly motivated by sending detailed responses and suggestions over emails. I am thankful to Dr. Colin Dundas at the United States Geological Survey for collaborating on one of the chapter in this thesis. The global survey of gullies done by Colin has always motivated me to embark on the global analysis of gullies presented in this thesis. I also thank Colin for sharing his thorough knowledge of present-day activity in gullies.

Thanks to Mr. Rajiv Bharti, who not only spent time with me as an office colleague, but also as an elder brother throughout these past five years. Whenever I had to relax, I used to go to his office. His advises have been always helpful and I admire him for all the support he has provided to me. Our trip to Allahabad was a very memorable one. Thanks again to Dr. Neeraj and Dr. Vijayan for always keeping a great atmosphere in the department by discussing the

amazing geological aspects of the Mars and Moon. Thanks to Dr. Anil Shukla for sharing his field experiences of glaciated landscapes, which motivated me to explore the fascinating Mars-like Ladakh Himalaya during my PhD.

I would like to express my sincere gratitude to Director PRL, Chairman, Planetary Science Division, PRL, Head, Planetary Remote Sensing Section, PRL, and Director IIT Gandhinagar, without their support, this PhD would have never got completed. I would also like to thank the academic committee of PRL for extending their kind support whenever required during the entire tenure of the PhD research work.

Then I would also like to thank my dear friends and family members for their interest in my research. My elder brother (Mr. Rimitosh Sinha) and sister-in-law (Mrs. Krishnakali Sinha), my elder sisters (Mrs. Surabhi Verma and Mrs. Shruti Bhalla) and my brothers-in-law (Mr. Vineet Verma and Mr. Vineet Bhalla), my niece Saanvi and nephew Siddhant- their never-ending care and happiness on learning about my successes would be always cherished in my life. I thank my father-in-law (Dr. Anil Sinha) and mother-in-law (Dr. Uma Sinha), who have always been the source of inspiration during my PhD research work. Their endless faith in me always reminded me to work hard. My brother-in-law (Mr. Saurabh Sinha), the *'hanuman'* of my family - has always been around me to help me in all aspects. To my parents (Father- Mr. Arun Kumar Sinha and Mother- Mrs. Rupak Sinha), I would like to thank them for making me worthy enough to reach this position in my life. I hope I can one day repay for the sacrifices they have made in life. Finally, I thank God for always being around me and making the entire tenure a very healthy, peaceful, and rewarding moment of my life.

ABSTRACT

Two of the most common landforms in the mid-latitudes of Mars are glaciers and gullies. Their ubiquitous presence has substantiated evidence of multiple ice-related episodes that played a key role in landscape evolution during the last one to hundreds of millions of years. The primary objectives of this thesis were to analyze the nature of glacial activities at locations away from the dichotomy boundary and then examine the potential of debris-flows in forming gullies that are similar in morphology and morphometry to terrestrial gullies. I have conducted a survey of the northern mid-latitudes of Mars and found Erebus Montes region with glacial landforms, which were examined in detail to infer the history of glaciation in this region. To address the role of debris-flows in Martian gully formation, I have first discovered 20 new locations (craters) where gullies have preserved morphological attributes of terrestrial debris-flow like deposits and then performed a comparative analysis of the morphometry of Martian and terrestrial gully systems to infer the potential involvement of debris-flow like processes. My work has provided new insights into the role of latitude dependent mantle (LDM) in the formation and evolution of glaciers and gullies found on Mars.

The study of glacial landforms in the Erebus Montes region revealed that this region has mainly formed lobate debris aprons (LDA) which were extensively mantled by LDM during the recent past, and lacks the evidence for superposed lobate deposits on the main LDA. This revealed two things in particular: (1) LDA deposits in this region may be once more extensive in the past and have undergone significant modification/degradation due to the emplacement and removal of LDM, and (2) there is a lack of alcove-fed multi-stage glaciation of a more limited

magnitude and shorter duration in the Erebus Montes region. The observational evidence of linear-curvilinear ridges on LDA deposits help substantiates the proposal of LDA degradation in this region. We find that the LDAs in this region are one of the youngest (~30 Ma) LDAs on Mars, although we attribute this as a manifestation of extensive mantling of the surface of the debris apron that resulted in burial and modification of the craters on LDA surface. The small size and the closely packed spacing between the mesa-LDA systems declined the detection of buried extant ice in this region. We find that the LDA deposits examined here are more consistent with the cold-based glacial behavior - morphological observations support the existence of the sublimation process in the region. Taken together, the findings presented in this thesis support the results of previous studies carried out elsewhere along the dichotomy boundary that find evidence for the past presence of extensive debris-covered glacial landsystems in the northern mid-latitudes of Mars.

Detailed investigation of gullies formed inside newly found 20 gullied craters widespread in the northern and southern mid-latitudes led to the finding of morphological attributes of debris-flow like deposits on the gully fan surfaces. The debris-flow like deposits typically includes leveed channels and overlapping lobate deposits with abundant embedded clasts. At first, the finding of levees and lobate deposits aided in proposing that debris-flow like processes were not rare on Mars in the past. This inference is contrary to what was proposed in the previous studies. Furthermore, we proposed that the preservation of lobate deposits is the key to their paucity in the gully population. Subsequently, upon adding some more gullied craters to my study, I embarked on a detailed investigation of the influence of substrates within which gullies

have formed on Mars and found that the morphology and morphometry of gullies formed in LDA/glacial deposits differ from gullies formed in bedrock. Then, I calculated several morphometric variables to characterize the catchment and fan of the gully systems in order to infer the flow types that led to Martian gully formation. The analysis of combinations of the relationships between alcove length and fan gradient with melton ratio of Martian gully systems were compared with the terrestrial gully systems, which aided in the interpretation that Martian gullies are from terrestrial debris-flow like processes in the past. As far as the present-day activity in gullies is concerned, I have discovered several new locations where currently active gullies are evident. A comparison of changes in both dust/sand-filled gully channels and dune gullies led to the proposal that the currently active processes have similar effects on the loose, unconsolidated substrate in both gully types. Identification of CO_2 frost inside the dust/sand-filled gully channels in the image acquired during winter and prior to the image in which recent changes have been observed suggests a connection with the sublimating frost inside the channels and indicates a seasonal control that subsequently produces extensive changes during defrosting seasons in approximately a Mars year.

TABLE OF CONTENTS

List of figures

List of tables

Abbreviations

LDA	Lobate debris apron
CCF	Concentric crater fill
LVF	Lineated valley fill
GLF	Glacier-like form
LDM	Latitude dependent mantle
HiRISE	High resolution imaging science experiment
CTX	Context camera
MRO	Mars Reconnaissance Orbiter
MOLA	Mars Orbiter Laser Altimeter
HRSC	High resolution stereo camera
MEX	Mars express
MGS	Mars global surveyor
SHARAD	Shallow radar
DEM	Digital elevation model
DTM	Digital terrain model
MUTED	Multi-temporal database of planetary image data
MarsSI	MARS système d'Information
QGIS	Quantum geographic information system
RDR	Reduced data record
CO-SHARP	Colorado SHARAD processing system
GIS	Geographic information system
CSFD	Crater size-frequency distribution
HNt	Hesperian Noachian terrain
TAR	Transverse aeolian ridges
MY	Mars year
L_s	Solar longitude

CHAPTER 1

Introduction

He who can listen to the music in the midst of noise can achieve great things.

- Dr. Vikram A. Sarabhai

1. Introduction

The mid-latitudes of Mars host a suite of landforms that experienced episodic ice-related activity during the Late Amazonian period and widespread presence of ice in the subsurface **(e.g., Plaut et al., 2009; Baker et al., 2010)**. Atmospheric models relating average obliquity parameters to climate change and the landforms observed on the surface have further suggested the episodic migration of ice from polar caps to the mid-latitudes during the Late Amazonian **(Costard et al., 2002; Laskar et al., 2004; Forget et al., 2006; Madeleine et al., 2009, 2014)**. This thesis focuses on improving our fundamental understanding of two of the most popular landforms: glaciers and gullies. The research carried out in this thesis is motivated by the importance of these two landforms in surface modification during the recent (~1 Ma) and past ten to hundreds of million years (~10 Ma - 1 Ga) **(e.g., Head et al., 2006a; Sinha and Murty, 2015)**. Glacial landforms formed within the Erebus Montes region in the northern mid-latitudes have been investigated in detail, previously not attempted **(Sinha and Ray, 2021)**. Additionally, a detailed investigation of gullies has been undertaken to aid in the interpretation of gully formation mechanisms in present conditions and in the geologically recent past **(Sinha et al., 2020)**. Both glaciers and gullies are strongly linked to the recently (~0.1-5 Ma) emplaced latitude dependent mantle (LDM) - an airfall deposit of ice-dust mixture in the mid-latitudes **(e.g., Mustard et al., 2001; Dickson et al., 2015; De Haas et al., 2019a)**. Therefore, a detailed examination of the interplay between glaciers, gullies, and LDM is pertinent for a holistic understanding of the evolutionary history of Mars during the Late Amazonian.

In the upcoming subsections, a summary of published reports related to formation and distribution of glaciers and gullies, and their interaction with LDM is provided. Then, a summary of current understanding and gap areas concerning glaciers and gullies is discussed. This is followed by aims and objectives of the thesis, and an overall architecture of the thesis.

1.1. Glacier Formation and Distribution on Mars

Glaciers on Mars are significant ice reservoirs and are broadly identified in the form of lobate debris apron (LDA) **(e.g. Squyres and Carr, 1986; Baker et al., 2010)**, concentric crater fill (CCF) **(e.g., Levy et al., 2010a)**, lineated valley fill (LVF) **(e.g., Levy et al., 2007)**, and glacier-like form (GLF) **(Hubbard et al., 2011)**. Collectively, these landforms are represented as viscous flow features (VFF) in the mid-latitudes **(e.g., Conway et al., 2018)**. The VFFs are estimated to have ages in the range of ~10 Ma to ~1 Ga.

Based on the differences in the inferred amounts of water ice involved in LDA formation, LDAs have been proposed to have formed by frost creep **(Carr and Schaber, 1977)**, rock-glacier flow **(e.g., Squyres, 1978; Mangold, 2003)**, and debris-covered glacier flow **(Head et al., 2006a)**. In a debris-covered glacier flow model, the sequence of the LDA formation mechanism begins at a period of net ice accumulation, which caused complete burial of adjoining terrains as a result of ice sheet advance **(e.g., Head et al., 2010)**. The retreat of the ice sheets during an ablating environment lead to the exposure of steep flanks of mesas that eventually eroded and mixed debris with the ice sheet surface **(Fastook et al., 2014)**. The debris cover then advanced and reduced the loss of ice from beneath by protecting it from sublimation during an ablating environment **(Fastook et al., 2014)**. Subsequently, the downslope topography further assisted in the advance of debris cover away from the mesa flanks, protecting the ice sheet, and finally forming a stagnant debris-covered glacier represented as LDA on Mars **(Figure 1.1a) (Fastook et al., 2014)**. The SHAllow RADar (SHARAD) instrument onboard the Mars Reconnaissance Orbiter (MRO) has detected pure ice under a thin layer of debris in a majority of LDAs **(e.g., Plaut et al., 2009)**. Regional mapping of LDA distribution between ~±30 and 50° latitude revealed that they cover an area of 3.9 x 10^5 km^2 (largest among the other VFFs) primarily distributed in Deuteronilus and Protonilus Mensae

along the dichotomy boundary, plains region of Acidalia, region surrounding Hellas and Argyre basins, and Tempe Terra/Mareotis Fossae **(Levy et al., 2014)**. On a global scale, LDAs have been appraised as the most common glacial landforms formed along the dichotomy boundary **(e.g., Head et al., 2006a; Levy et al., 2007; Sinha and Murty, 2013)**. The sources of ice proposed for LDA formation involves (1) direct deposition from the atmosphere **(Squyres, 1978)**, (2) ground ice **(e.g. Lucchitta, 1984; Carr, 2001)**, and (3) precipitation in form of snow **(Head et al., 2006a)**. Analysis of the crater size-frequency distribution (CSFD) on LDA surfaces revealed that their ages range from ~100 Ma to 1 Ga **(e.g., Mangold, 2003; Levy et al., 2007; Morgan et al., 2009)**.

CCFs represent craters whose floors are infilled by deposits emplaced in a manner similar to the formation of debris-covered glaciers or LDAs on Mars **(Levy et al., 2010a)**. The surfaces of crater infilling deposits often exhibit lineations concentric to the crater walls from all sides or lineations originating only from one side of the walls **(Figure 1.1b) (e.g., Levy et al., 2010b; Dickson et al., 2012; Sinha et al., 2017)**. The orientation of these lineations is found to vary with latitude in both the hemispheres - lineations originate from the pole-facing walls of the craters lying within 30-45° and concentric lineations are found in craters located at >45° latitudes **(e.g., Sinha et al., 2017)**. Craters lacking concentric lineations have been termed low-definition CCFs **(Levy et al., 2010a)**, although **Sinha et al., 2017** argued that the craters having interior deposits consistent with surface lineations oriented in one direction are more representative of craters hosting small-scale LDAs in the mid-latitudes of Mars. Small-scale LDAs are always associated with arcuate ridges at the headwards boundary of LDAs on the floor **(e.g. Sinha et al., 2017)**. Arcuate ridges have been inferred as moraine deposits **(e.g. Arfstrom and Hartmann, 2005)**. The presence of arcuate ridges in front of the gully fans formed on the walls of the crater implies that the crater was formerly glaciated **(e.g., De Haas et al., 2019a)**. Count of craters on the surfaces of deposits consistent with concentric and

unidirectional lineations revealed that their formation ages range from ~10 Ma to 700 Ma **(e.g., Levy et al., 2009; Fassett et al., 2014; Sinha et al., 2017)**. In terms of surface area coverage, CCFs stands out as the second largest representative (after LDA) of VFFs found on Mars **(Levy et al., 2014)**.

The third-largest representative of VFFs is the LVFs found to be mainly concentrated near the dichotomy boundary of Mars **(e.g., Levy et al., 2007)**. LVFs originated as debris-covered glaciers during the same period as LDA and are particularly characterized by lateral flow lines formed as a part of LDAs flow and compression between valley walls **(Figure 1.1c) (e.g., Squyres, 1978; Carr, 2001)**.

GLFs are elongated, lobate, or tongue-shaped deposits that closely resemble terrestrial valley glaciers in terms of their morphology and visual appearance **(Hubbard et al., 2011; Souness and Hubbard, 2012)**. Between 25 and 65° latitudes in the northern and southern hemispheres, GLFs appear to have been sourced from alcoves in the walls of mesa, valleys and craters, which then extend downslope onto plains to emplace an elongated (<5 km long) tongue-shaped deposit **(Figure 1.1d) (Souness et al., 2012)**. Age estimates for GLFs range from ~10 - 100 Ma **(e.g., Hepburn et al., 2019)**, thereby suggesting that they are relatively younger than other VFFs found on Mars.

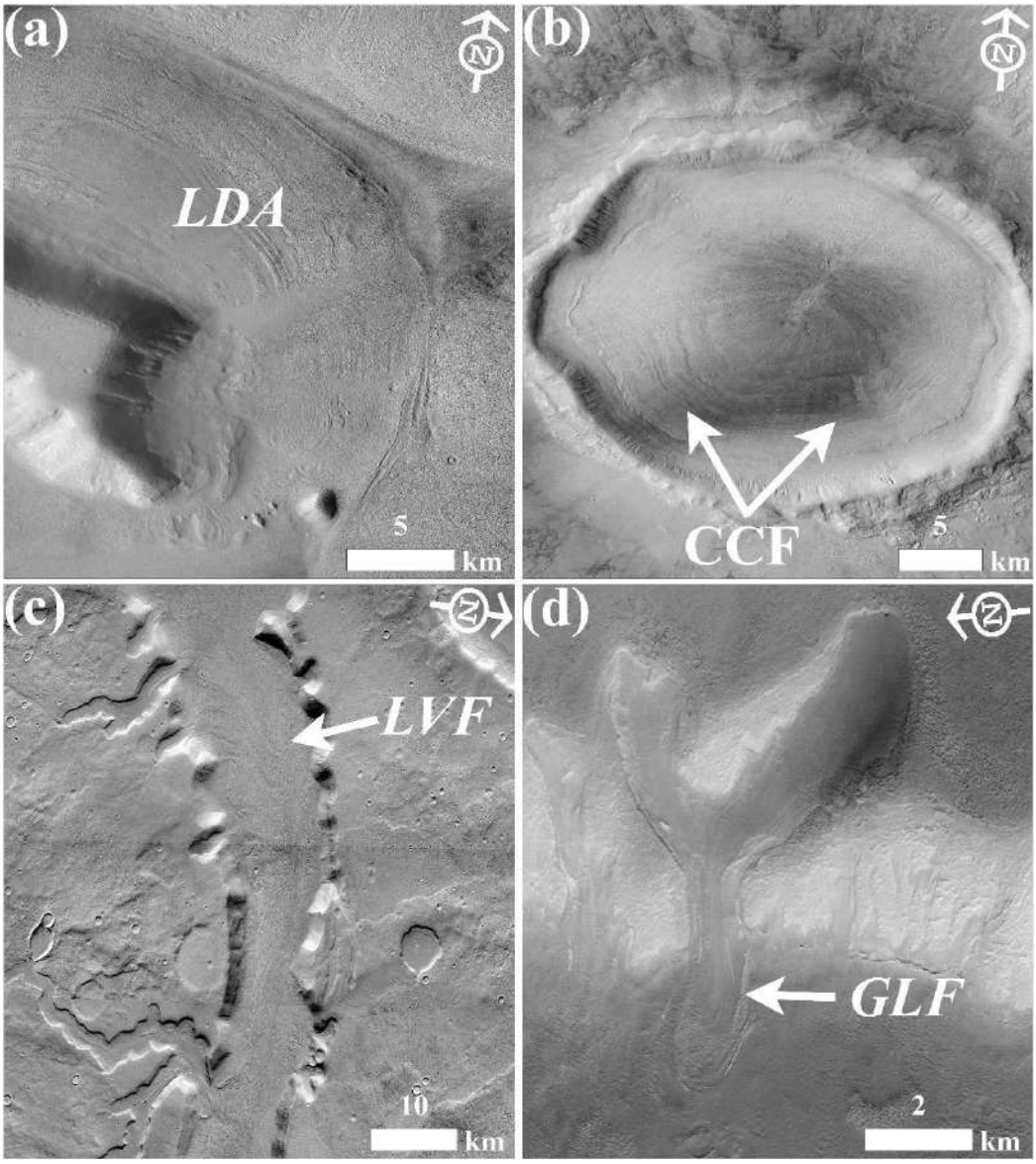

Figure 1.1. Examples of viscous flow features (VFFs) in the mid-latitudes of Mars. (a) Lobate debris apron (LDA) located at 43.6° N, 28.3° E in Deuteronilus Mensae region (CTX image B05_011513_2241). (b) Concentric crater fill (CCF) located at 42.1° N, 23.3° E in Deuteronilus Mensae region (CTX image P19_008441_2247). (c) Lineated valley fill (LVF) located at 36.7° N, 33° E in Deuteronilus Mensae region (CTX images D16_033468_2175, P03_002138_2194, and P22_009680_2175). (d) Glacier-like form (GLF) located at 43.7° N, 28.3° E in Deuteronilus Mensae region (CTX image B05_011513_2241). CTX image credit: NASA/JPL-Caltech/MSSS.

1.2. Gully Formation and their Relation to Water and Ice on Mars

Gullies are kilometer-scale, geologically young landforms comprising an alcove, transportation channel, and depositional fan **(e.g., Malin and Edgett, 2000; Dickson et al., 2007; Reiss et al., 2004; Schon et al., 2009)**. The general population of gullies found in both the hemispheres suggests that gullies are found between 30°-90° latitude band on surfaces having mean slopes in the range of 20 to 30° **(e.g., Conway et al., 2019)**. In this wide latitude band, gullies are found in a wide variety of geologic settings ranging from crater walls, flanks of valleys-mesa-central peaks of craters, and steep surfaces of hills, polar pits, and dunes **(Figure 1.2) (e.g. Balme et al., 2006; Dickson et al., 2007; Dickson and Head, 2009; Conway et al., 2011, 2015; Harrison et al., 2015)**.

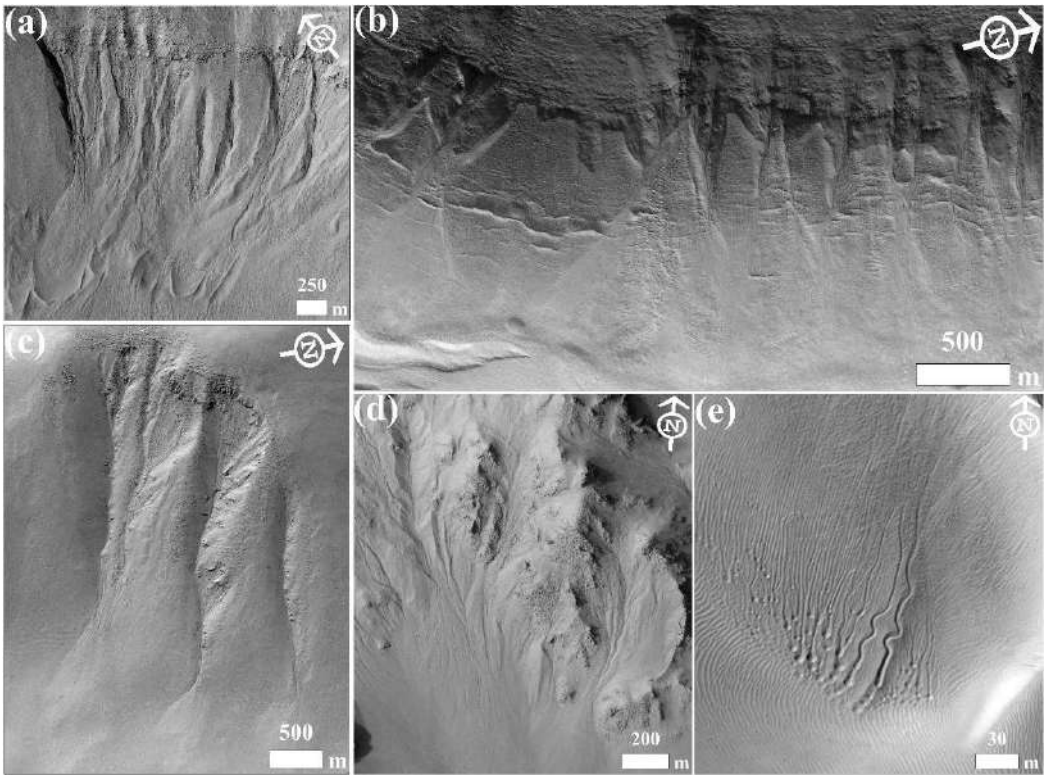

Figure 1.2. Examples of gullies formed over a variety of geologic settings on Mars. (a) Gullies on the walls of an unnamed crater (41.13° S, 163.4° W) in the west of Newton basin (HiRISE image ESP_051040_1385). (b) Gullies on the steep flanks of Harmakhis Vallis (39.3° S, 91.98°

E) located east of Hellas basin (HiRISE image ESP_024249_1405). (c) Gullies on the flanks of a mesa (51.76° N, 71.19° W) in the Tempe Terra region (HiRISE image ESP_034553_2320). (d) Gullies on the central peak of Hale crater (35.4° S, 36.6° W) (HiRISE image ESP_030425_1440). (e) Linear gullies with terminal pits in Matara crater dune field (49.2° S, 34.8° E) (HiRISE image ESP_013834_1300). HiRISE image credit: NASA/JPL-Caltech/University of Arizona.

The orientation of surfaces hosting gullies is generally poleward-facing between 30 to 40°, but the trend reverses to the conjugate equatorward-facing surfaces poleward of 40° **(e.g., Conway et al., 2019)**. Detailed investigation of probable gully formation mechanisms suggests them to have formed involving a variety of models, which includes fluvial flows **(e.g. Heldmann and Mellon, 2004; Heldmann et al., 2005; Dickson et al., 2007; Reiss et al., 2011)**, both wet and dry debris-flows **(e.g. Costard et al., 2002; Levy et al., 2010b; Conway et al., 2011; Johnsson et al., 2014; de Haas et al., 2019a; Sinha et al., 2020)**, and slope failure caused by dry flows **(e.g., Cedillo-Flores et al., 2011; Dundas et al., 2012, 2015; Pilorget and Forget, 2016)**. Liquid water in gullies is proposed to have been sourced from aquifers and melting of ice/snow deposits **(e.g., Malin and Edgett, 2000; Costard et al., 2002; Christensen, 2003)**, whereas dry flows are primarily triggered by sublimation of seasonal CO_2 frost **(e.g., Dundas et al., 2019)**.

Currently, the gully formation mechanism by water flow is under strong dispute, mainly because the Late Amazonian climate was unable to sustain surficial water flow **(e.g., Mellon and Phillips, 2001)**, yet gullies undergo modification during the present-day scenario **(Figure 1.3) (e.g., Diniega et al., 2010; Dundas et al., 2010, 2012, 2015, 2019, 2022)**. Long-term monitoring of the present-day activity in gullies has attributed the new formations in gullies to a mechanism seeking support only from the sublimated CO_2 frost **(e.g., Dundas et al., 2015a,**

2019, 2022). It has been proposed that the gas entrained from the sublimation of CO_2 frost can provide adequate fluidization to modify pre-existing gullies **(e.g., De Haas et al., 2019b; Dundas et al., 2019)**, as well as transport sediments to form entirely new gully **(Dundas et al., 2022)**.

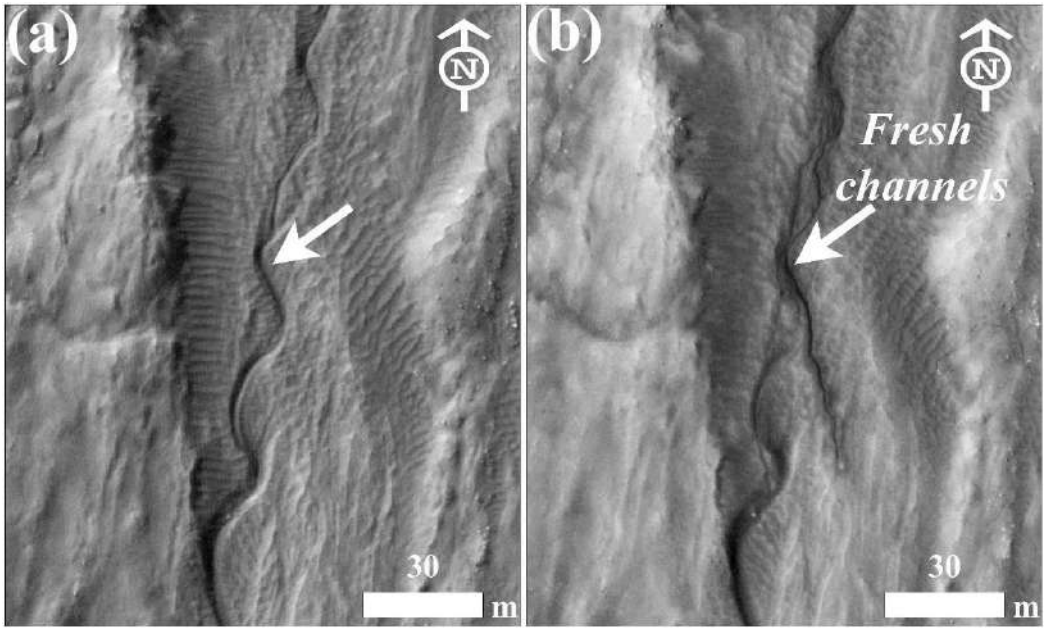

Figure 1.3. Present-day activity leading to fresh channel formation (arrow) in Gebog crater located at 37.26° S, 124.16° E (HiRISE image a- ESP_016046_1425 and b- ESP_066775_1425). HiRISE image credit: NASA/JPL-Caltech/University of Arizona.

1.3. Latitude Dependent Mantle on Mars

LDM is ubiquitous on the surface of Mars – nearly 23% of the surface is covered by LDM deposits **(Kreslavsky and Head, 2002)**. The average orbital obliquity of Mars during the past ~5 Ma varied between 15° and 30°, which increased to a range of 28 to 45° during the past ~5-10 Ma **(e.g., Laskar et al., 2004)**. These changes in obliquity lead to the mobilization and redistribution of ice from polar caps to the Mars' mid-latitudes **(Levrard et al., 2004, 2007; Madeleine et al., 2009)**. The ice mass redistributed during these recent epochs was emplaced

as a mixture of ice and dust and is referred to as LDM **(Figure 1.4) (e.g., Mustard et al., 2001)**. LDM can be identified on steep flanks of mesa/valley or crater walls and over VFFs based on their unique surface texture – brain-terrain and polygonal cracks **(Figure 1.5a-1.5b) (e.g., Levy et al., 2010a; Conway et al., 2018)**. The brain-terrain texture is common on the surfaces where LDM is deposited and is recognized as a combination of mounds and furrows **(Levy et al., 2010a)**. Detailed investigation of this texture has revealed evidence for the grouping of 'open and closed' cells relating to the sublimation of ice from the LDM deposits **(Levy et al., 2010a)**. Polygonally patterned surfaces have been also observed on the mantling deposits, which relates to thermal-contraction cracking, and differential sublimation of ice in LDM deposits **(Levy et al., 2009a)**. Both these textures have been regarded as diagnostic evidence for the presence of LDM deposits **(e.g., De Haas et al., 2019a)**. Furthermore, on VFFs, ring-mold craters consistent with varying morphologies inclusive of a plateau, etched plateau, mound, torus, filled torus, ring, and pit have been also identified **(Figure 1.5c) (e.g., Kress and Head, 2008; Baker and Carter, 2019)**. These different crater morphologies have been inferred as supporting evidence for the loss of ice from the recently emplaced LDM deposits **(e.g., Sinha and Ray, 2021)**. Taken together, the presence of brain-terrain, polygonal cracks, and ring-mold craters on VFFs have led to the inference that VFFs were subjected to extensive degradation by emplacement and removal of ice from/within the LDM deposits during the past ~10 Ma **(e.g., Berman et al., 2015)**.

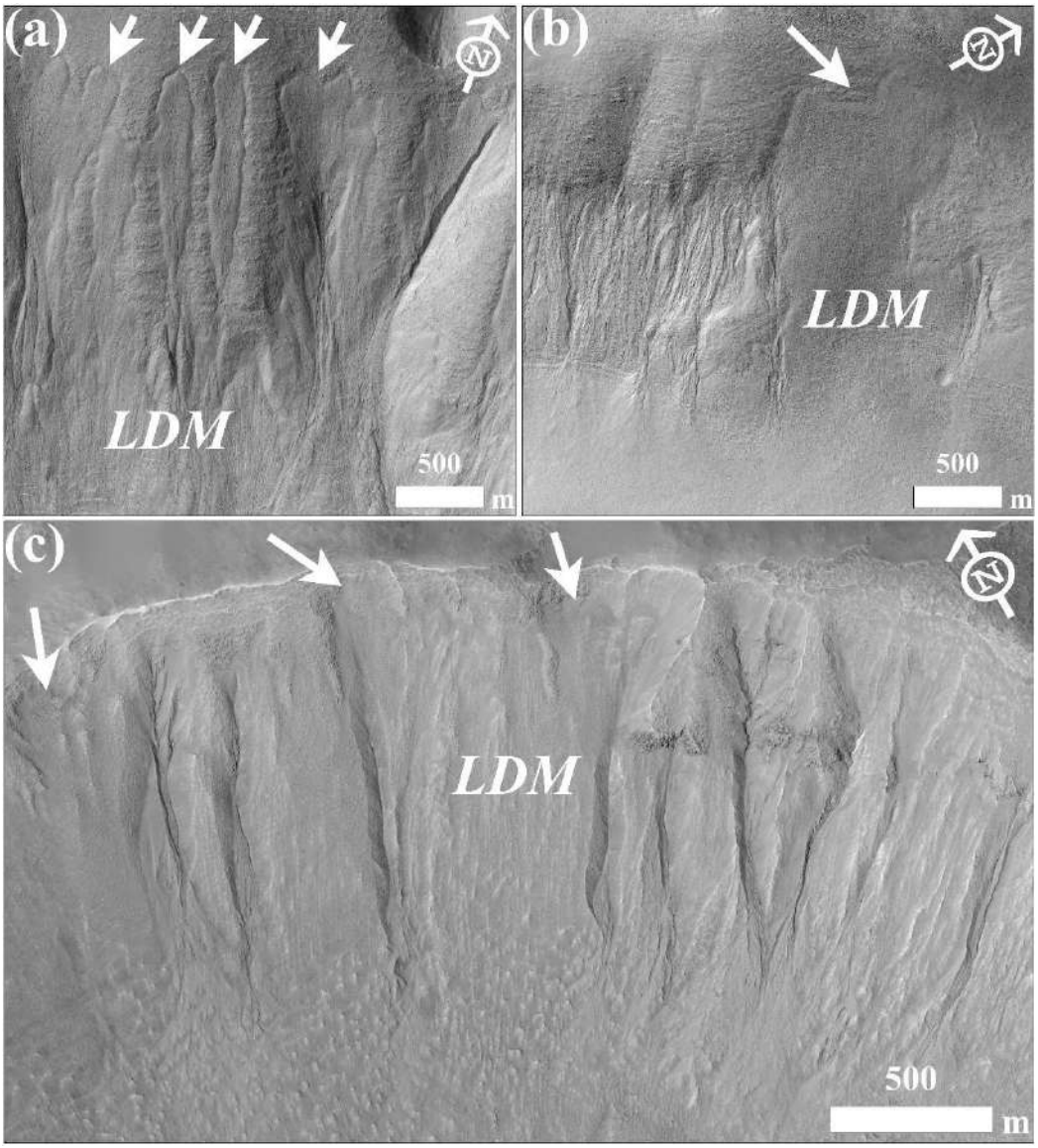

Figure 1.4. Examples of LDM covered surfaces in the mid-latitudes of Mars. (a) LDM deposits (arrow) in alcoves formed on the steep flanks of Niger Vallis (32.8° S, 93.3° E) (HiRISE image ESP_020926_1470). (b) LDM cover (arrow) on the steep flanks of a mesa in the Tempe Terra region (51.2° N, 70.8° W) (HiRISE image ESP_061032_2315). (c) LDM deposits in the alcoves (arrow) and on the pole-facing walls of Taltal crater located at 39.5° S, 125.8° W (HiRISE image ESP_031259_1400). HiRISE image credit: NASA/JPL-Caltech/University of Arizona.

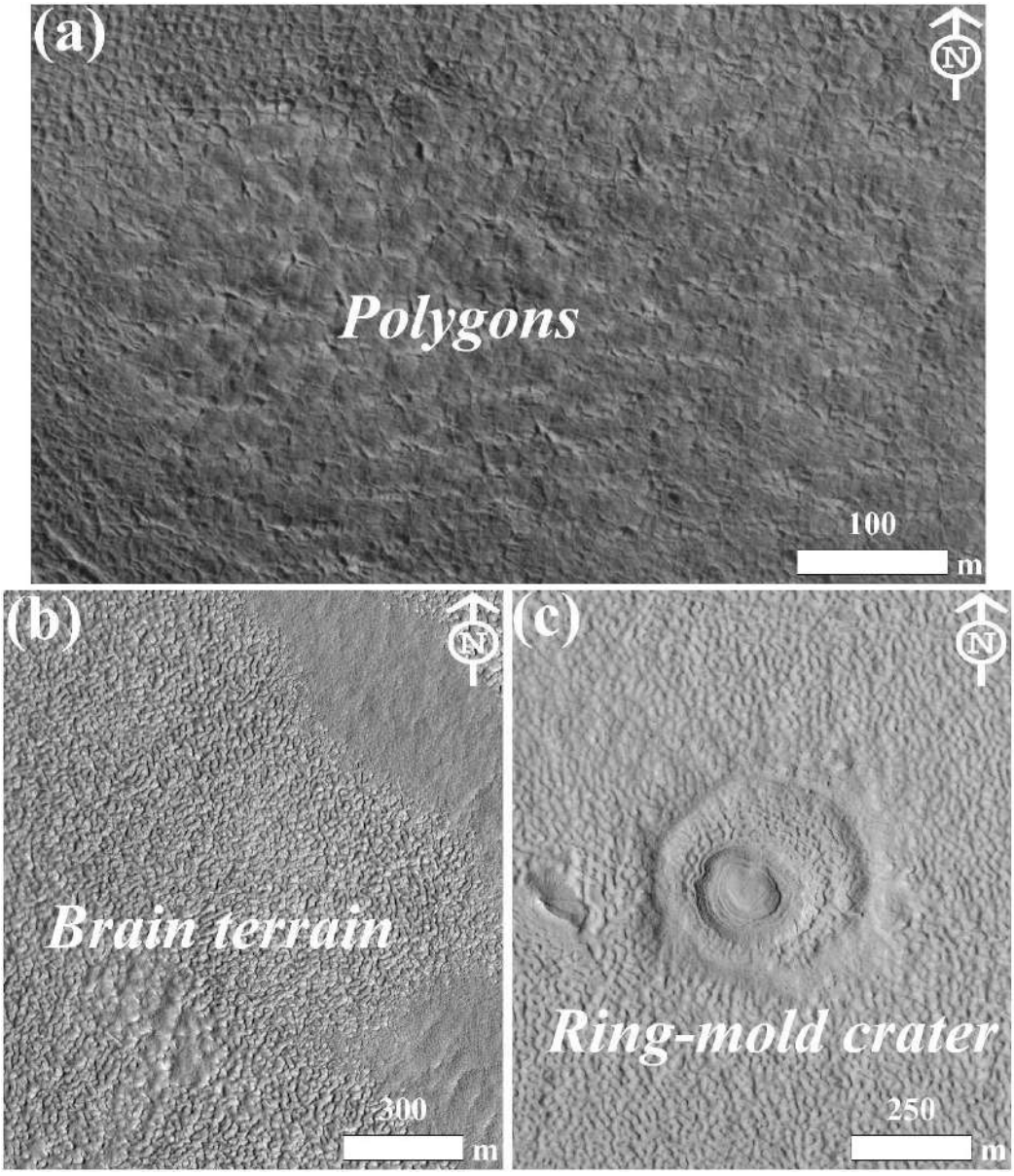

Figure 1.5. Examples of surface texture associated with LDM deposits in the Deuteronilus Mensae region. (a) Polygonal cracks (43.2° N, 28.4° E) (HiRISE image ESP_047011_2240). (b) Brain terrain texture (43.6° N, 28.6° E) (HiRISE image ESP_016959_2240). (c) Ring-mold crater (40.3° N, 23.8° E) (HiRISE image PSP_009799_2205). HiRISE image credit: NASA/JPL-Caltech/University of Arizona.

The LDM covered steep mesa flanks or crater walls that led to the emplacement of VFFs in the mid-latitudes are also consistent with gullies **(e.g., Dickson et al., 2015)**. The

morphology of gullies formed on the formerly glaciated, LDM covered surfaces are strongly influenced by the LDM deposits. Gullies that formed into LDM deposits tend to have originated from elongated alcoves and have a unique V-shaped incision in the mid-section **(e.g., Conway et al., 2018; De Haas et al., 2019a)**. These gullies do not begin from the top of the crater rim, which is contrary to gullies formed in bedrock **(e.g., Johnsson et al., 2014)**. Therefore, the surfaces that formed VFFs were subsequently subjected to LDM emplacement in which gullies incised during the recent epochs **(Figure 1.6)**.

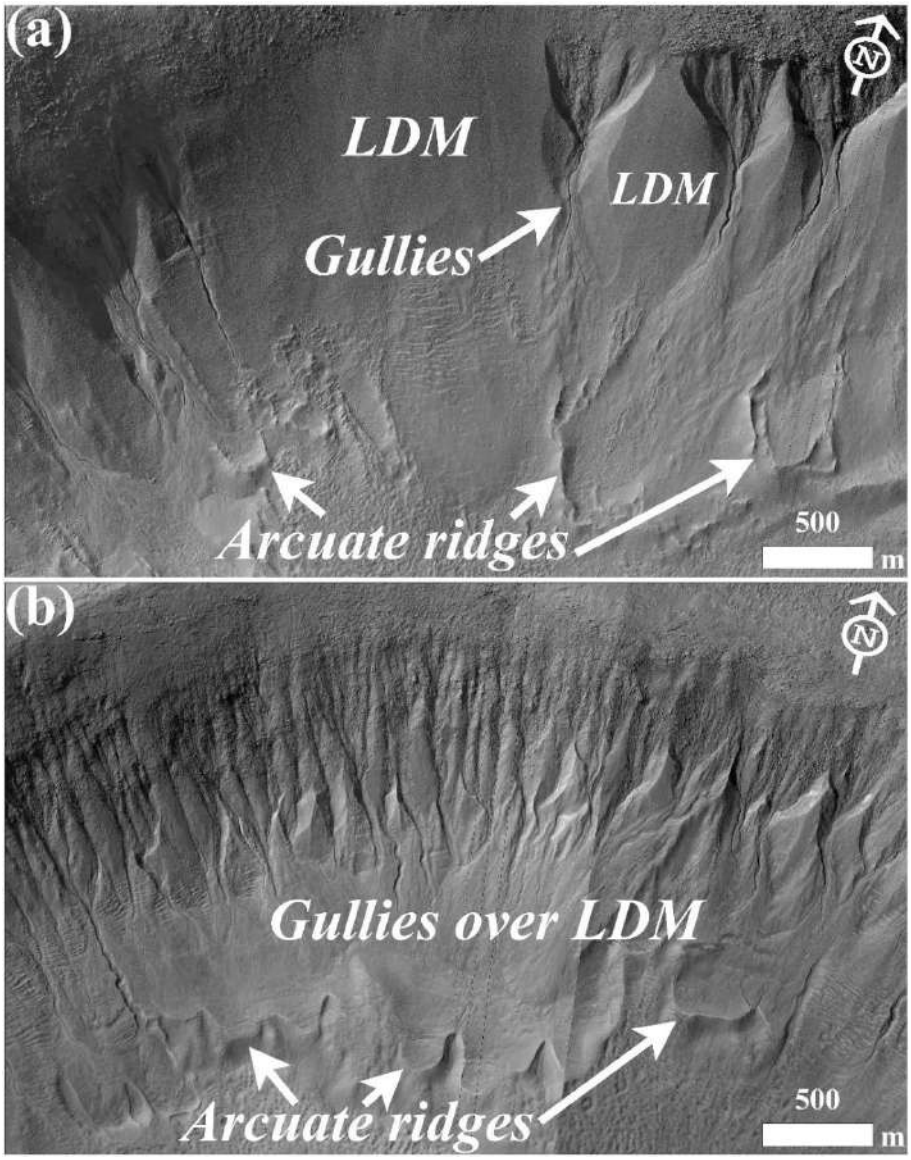

Figure 1.6. a-b. Examples showing gully formation on the walls of craters that were formerly glaciated and subsequently covered by LDM deposits. Evidence of glaciation comes in the form of arcuate ridges (arrows), LDM is emplaced as a smooth mantling deposits over the crater walls, and gullies have incises into the LDM deposits. Crater in (a) is located at 42.2° S, 164.4° W (HiRISE image ESP_064517_1375) and Crater in (b) is located at 38.8° S, 158.6° W (HiRISE images ESP_046926_1405 and ESP_011995_1410). HiRISE image credit: NASA/JPL-Caltech/University of Arizona.

1.4. Summary of Current Understanding of Glaciers and Gullies

Based on observations presented in Section 1.1, the current state of understanding for glaciers is as follows:

- LDA and LVF are two of the most common modification feature formed in the fretted terrain along the dichotomy boundary, implying that glaciation was dominant along the dichotomy boundary **(e.g., Levy et al., 2007)**.
- While LDA and LVF represent landforms common during the extensive glacial epoch **(e.g., Sinha and Murty, 2013)**, smaller lobes sourced from alcoves in the mesa/plateau/valley wall and superposed on the main LDA represent the minor phases of glaciation **(e.g., Baker et al., 2010)**. The majority of previously investigated glaciated regions have preserved evidence of a superposed lobe on the main LDA, implying that multi-stage glaciation was facilitated by alcove microclimatic conditions in the glaciated regions.
- Mantling deposits (i.e. LDM) are ubiquitous on the surfaces of VFFs **(e.g., Berman et al., 2015)**. This evidence comes in the form of brain-terrain texture, polygonal cracks, and ring-mold craters on the surface of VFFs **(Levy et al., 2010a; Kress and Head, 2008)**.

- Episodic emplacement of LDM over mid-latitude VFFs and subsequent removal of the ice component from LDM by sublimation resulted in degradation of VFF surfaces' over the last ~5-10 Ma **(e.g., Berman et al., 2015)**.
- Late-stage episodes of glaciation resulted in localized flow on interior and exterior crater walls, which eventually advanced in a manner similar to the formation of kilometer-thick glacial deposits along the dichotomy boundary **(Dickson et al., 2010)**.
- Subsurface of LDA and LVF deposits have preserved extant pure ice as revealed by SHARAD-based investigations - 15 m thick surface till layer protects the ice from sublimation during the present-day **(Holt et al., 2008; Plaut et al., 2009)**.
- In general, VFFs are more consistent with cold-based glacial behavior, however, the recent identification of eskers in Tempe Terra, Phlegra Montes, and Chukhung crater suggest probable basal melting of VFF **(Gallagher and Balme, 2015; Butcher et al., 2017, 2020, 2021)**, thereby indicating wet-based glaciation in these regions during the Late Amazonian.

Based on recently published reports on long-term monitoring of gullies and the observations presented in section 1.2, the current state of knowledge is outlined as follows:

- Gullies formed on the walls of craters are found to have incised into the LDM covered surfaces, surfaces modified by former episodes of glaciation, and bedrock **(e.g., De Haas et al., 2019a)**.
- Gully formation on Mars is primarily due to the sublimation of seasonal CO_2 ice **(e.g. Dundas et al., 2012, 2015, 2019)**. As a result, liquid water is proposed to be not required or a prerequisite for gullies, and it may never have been involved in gully formation in the past **(e.g., Dundas et al., 2019)**.
- CO_2 sublimation may lead to flow fluidization on Mars in a manner similar to

fluidization by water in terrestrial debris flows **(De Haas et al., 2019b)**; a concept supported by the recent finding of lobate deposits and boulder-rich levees formation during the present-day in Istok crater **(Dundas et al., 2019)**.

- The probable occurrence of debris-flow like processes in the formation of Martian gullies is found to be rare - morphological evidence of lobate deposits and levees in gullies is limited to only 5-6 sites on a global scale on Mars **(Lanza et al., 2010; Levy et al., 2010b; Reiss et al., 2011; Johnsson et al., 2014; De Haas et al., 2015a; Sinha et al., 2019)**.

1.5. Research Motivation

Despite this recent and updated understanding of glaciers and gullies, a number of fundamental aspects relating to the extent of VFFs, multi-stage glaciation, style of downslope flow, VFF and LDM interaction, the evolution of VFFs, and subsurface ice deposits in VFFs are still in its infancy. Additionally, our understanding of the role of debris-flow like processes in gully formation and the influence of the substrate within which gullies have formed is still not complete to provide new insights into the process by which gullies have formed on Mars. The key scientific gap areas can be briefly summarized as follows:

- The state of glaciation beyond the dichotomy boundary remains to be explored, i.e. whether glaciation was prevalent in locations away from the dichotomy boundary. Furthermore, how do the glacial landforms formed away from the dichotomy boundary compare with those formed along the dichotomy boundary. LDM emplacement has taken over the mesa-LDA systems during the recent epochs, but what role they have played in LDA modification (i.e. evolutionary history) is not clear.
- Gullies have formed over surfaces with and without LDM/glacial deposits, but the

morphology and morphometry of gully systems formed in distinct substrates differ or not is not clear. Additionally, how do the morphometric characteristics of gullies formed on Mars compare to those formed by a range of processes on Earth, and what does that tell us about the formative processes of Martian gullies is not clear. Furthermore, it is important to understand what keeps the gullies active in the present day.

1.6. Aims and Objectives

This thesis aims to refine the fundamental understanding of glaciers by detailed analysis of glacial landforms formed at a location far away from the dichotomy boundary. Additionally, to find new gullied craters in the mid-latitudes that have preserved morphological attributes of debris-flow deposits, and then build on new insights to substantiate the role of debris-flow like processes in Martian gullies.

These aims have been accomplished by addressing the following objectives:

1. Investigate how LDM has interacted with glacial landforms on Mars and provide a conceptual model for the evolution of the glaciated landscape.
2. Decipher the morphological attributes of deposits in gullies that can indicate the role of potential debris-flow like process in gully formation in the past.
3. Determine the control of substrate on gully morphometry and on the mechanism of gully formation.
4. Investigate 'how and why' gullies are currently active.

The four main objectives of the thesis have been further elaborated in form of scientific questions in Chapters 3-6.

1.6. Thesis Structure

In total, there are seven chapters in this thesis. In Chapter 1, an introduction to understanding of glacier and gully formation and their distribution on Mars is presented and an explanation of how does LDM have interacted with glaciers and gullies during the Late Amazonian is included. Additionally, the current state of our knowledge regarding glaciers and gullies and the key scientific gap areas have been included and based on that the aims and objectives of the thesis are presented. In Chapter 2, an overview of the variety of datasets and software used in addressing the objectives of the thesis is included. Additionally, a brief methodology depicting the ways by which the objectives of the thesis would be eventually accomplished and the types of research outcomes are presented. In Chapter 3, outcomes of the detailed investigation of the morphology, topography, chronological history, and subsurface details of the Erebus Montes region are presented. In Chapter 4, a global investigation of Martian gullies using high-resolution imagery and topography datasets is presented. In Chapter 5, a detailed investigation of the morphology and morphometry of gully systems formed in discriminated substrates is presented, and based on the comparative study of the morphometry of terrestrial and Martian gullies; an attempt has been made to decipher the formation mechanism of Martian gullies. In Chapter 6, gully systems in the southern mid-latitudes of Mars have been investigated to decipher new insights into the extent and nature of present-day activity in gullies. Finally, in Chapter 7, a summary of the main findings and key conclusions from the thesis is given and synthesis of improved fundamental aspects relating to glaciers and gullies is presented. Chapter 7 is finished by providing possible avenues for future research.

CHAPTER 2

Data, Methods and Software

Choosing to lead one kind of life means putting aside the desire to pursue other options.

- Dr. Vikram A. Sarabhai

2. Data, Methods and Software

2.1. Data

The work done in this thesis uses a morphological and morphometric approach to study glaciers and gullies. Therefore, the primary datasets are mainly of two types: imaging and elevation data **(Table 2.1)**.

2.1.1. Imaging data

The regional geological context of the study regions is investigated using the Mars Reconnaissance Orbiter (MRO) Context (CTX) camera images **(Malin et al., 2007)**. CTX images are publically available datasets having around 100% coverage of the Martian surface. Images are downloaded from the Mars Orbital Data Explorer (ODE) website (https://ode.rsl.wustl.edu/mars/indexProductSearch.aspx), which is a part of the NASA Planetary Data System (PDS) geosciences node. CTX images are acquired in grayscale (500 to 800 nm) at a spatial resolution of ~6 m/pixel over a 30 km wide swath. The images used in the thesis work were orthorectified and pre-processed by the Arizona State University (http://global-data.mars.asu.edu/). The CTX images were useful in the search for glaciated landscapes located away from the dichotomy boundary region of Mars. The mapping of glacial landforms presented in this thesis has been performed using the CTX images.

For a detailed investigation of glaciers and gullies, we have used the High Resolution Imaging Science Experiment (HiRISE) images **(McEwen et al., 2007a)**. HiRISE is an imaging instrument onboard MRO. Similar to CTX images, HiRISE images are publically available and downloaded from the Mars ODE. HiRISE images can be also downloaded from the HiRISE Planetary Data Systems (PDS) data node (https://www.uahirise.org/). Unlike CTX, HiRISE

operates in targeted mode, which means that HiRISE images are acquired only for those locations where a previous dataset (e.g., CTX images) has identified a feature of interest. The HiRISE imaging operations are managed by the University of Arizona and Lunar & Planetary Laboratory, Arizona. HiRISE performs imaging in three different wavelength ranges, which include blue-green (400–600 nm), red (550–850 nm), and near-infrared (800–1,000 nm) wavelengths. The images are acquired at a spatial resolution of ~25–60 cm over a swath of width ~ 5–6 km and length up to ~60 km. The HiRISE images used in the thesis were orthorectified and pre-processed by the University of Arizona. Global investigation of Martian gullies to identify new gullied craters hosting morphological attributes of debris-flow like deposits on the gully fan surfaces was done using HiRISE images. Additionally, HiRISE images were found to be extremely useful in the identification of mantling deposits on the surface of glacial landforms.

To refine the fundamental understanding of the morphology of Martian gully systems analyzed in this thesis, field observations of gullies and debris-flow deposits in Ladakh were undertaken. Using NIKON digital camera, photographs of interesting sites were acquired for comparison with Martian gullies.

2.1.2. Elevation data

For regional elevation and topography measurements of glacial landforms, Mars Orbiter Laser Altimeter (MOLA) - High-Resolution Stereo Camera (HRSC) blended global digital elevation model (DEM) v2 (retrieved from http://bit.ly/HRSC_MOLA_Blend_v0) is used **(Fergason et al., 2018)**. This MOLA-HRSC DEM is generated by utilizing the ~463 m/pixel MOLA DEM and blending it with the HRSC DEMs (~50 m/pixel) into it **(Fergason et al., 2018)**. The final blended MOLA-HRSC DEM has a spatial resolution of ~200 m/pixel.

Both CTX and HiRISE instruments have the capability to acquire stereo-pairs. Stereo-pair is an image pair, in which the same spot on the surface has been observed at different angles. Using the stereo-restitution pipeline of the Mars System of Information (Mars SI-emars.univ-lyon1.fr) **(Lozac'h et al., 2015; Quantin-Nataf et al., 2018; Tao et al., 2018)**, CTX stereo-pair image-based digital terrain model (DTM) aligned on the Mars Orbiter Laser Altimeter (MOLA) topography were generated at a resolution of ~18 m/pixel. The CTX images were overlaid on the DTM to extract the elevation data and perform morphometric measurements. Mars SI was also used to generate HiRISE stereo-pair image-based DTM having a spatial resolution of 1-2 m and vertical precision in the tens of centimeters. Detailed morphometric measurements of the different morphological attributes of debris-flow like deposits were carried out using HiRISE DTM.

Apart from the imaging and elevation data, SHARAD radargrams have been used to investigate the subsurface of glacial landforms for the presence of extant ice. SHARAD is a shallow radar sounder instrument onboard MRO, which is designed to emit a 10-watt chirped pulse at a central frequency of 20 MHz, providing a 15-meter range resolution in free space. The instrument is capable of detecting the presence of underground frozen ice up to 1-kilometer depth. The SHARAD radargrams used in the thesis were processed by the Italian SHARAD team **(Seu et al., 2007)**.

Table 2.1. Summary of instruments and datasets used in this thesis for the analysis of glaciers and gullies.

Spacecraft	Instrument	Resolution	Wavelength	Data types	Type of analysis
Mars Reconnaissance Orbiter	Context camera (CTX)	~6 m/pixel	500 to 800 nm	Imagery	Regional investigation of study area
Mars Reconnaissance Orbiter	High Resolution Imaging Science Experiment (HiRISE)	~25–60 cm/pixel	400–600 nm, 550–850 nm and 800–1,000 nm	Imagery	Morphological investigation
Mars Reconnaissance Orbiter	CTX stereo-pair DTM	~18 m/pixel, vertical precision in metres	-	Elevation	Morphometric investigation
Mars Reconnaissance Orbiter	HiRISE stereo-pair DTM	~1-2 m/pixel, vertical precision in the tens of centimeters	-	Elevation	Morphometric investigation
Mars Reconnaissance Orbiter	Shallow Radar (SHARAD)	15-meter range resolution in free space	15 meters	Radargram	Subsurface investigation
Mars Global Surveyor/Mars Express	Mars Orbiter Laser Altimeter (MOLA) – High Resolution Stereo Camera (HRSC) blended DTM	~200 m/pixel, vertical precision up to 10 m	-	Elevation	Topographic investigation

2.2. Methods and Software

For the study of glaciation beyond the dichotomy boundary, we have performed morphological survey of Mars' mid-latitudes (between 30-60° N) to search and identify glacial regions warranting investigation at a detail previously not attempted. The studies on gullies also involved global investigation for the identification of (1) gullied craters having morphological attributes of debris-flow deposits, (2) craters having discriminated gully systems and (3) identification of gully systems that have sand/dust trapped inside the channels. The surveys were mainly carried out using the online tool Multi-Temporal Database of Planetary Image Data (MUTED). MUTED (http://muted.wwu.de/) allows quick identification of the spatial and multi-temporal coverage of planetary image data from Mars. All the mapping and image analysis work was carried out using ESRI's ArcMap10.5 Geographic Information System (GIS) software. Using ArcMap, we re-projected all the DEMs from equirectangular to local sinusoidal projection and created a hillshade image for each DEM. Typically, a hillshade is defined as a grayscale 3-dimensional illustration of the surface, with the sun's relative position taken into consideration for the shading of the image. For topographic measurements of gullies, the hillshade images of gullies were exported into Quantum GIS and overlaid on their respective DTMs for manually capturing line elevation data from the DEM by digitizing along the line of the profile of the alcove – channel – fan. The flowchart for the basic methodology adopted in addressing the objectives of the thesis is shown in **Figure 2.1**. In Chapters 3-6, details of other specific methodologies related to the analysis of glaciers and gullies have been elaborated for clarity.

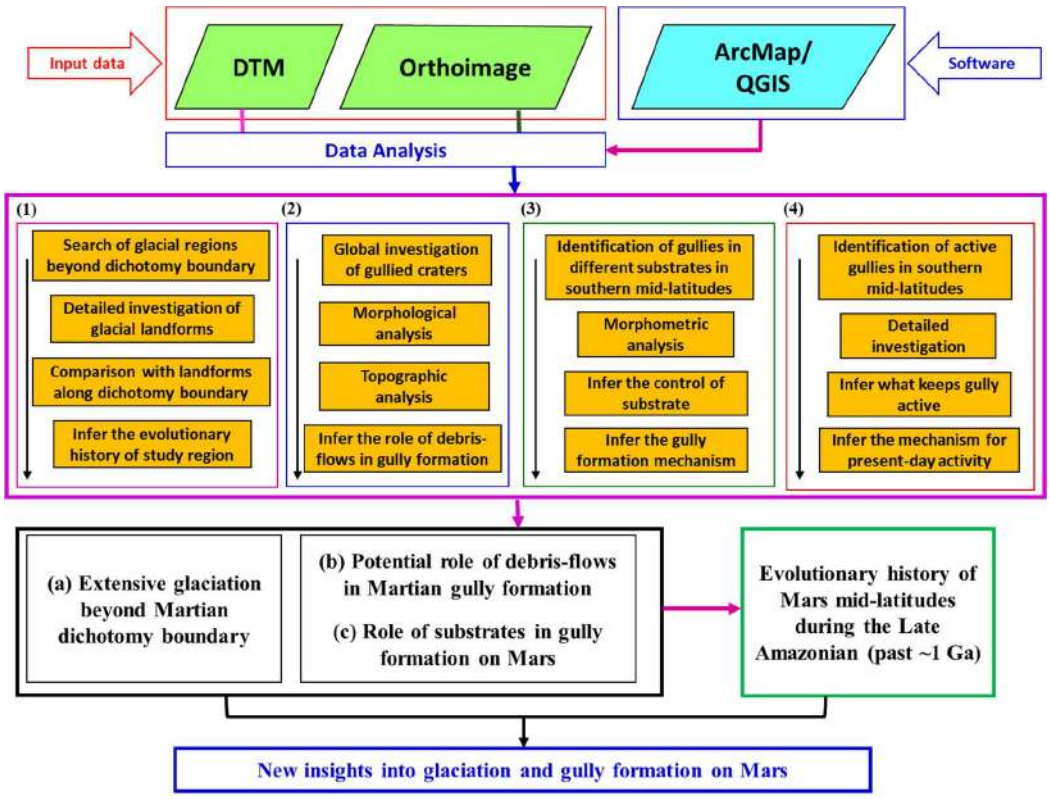

Figure 2.1. Flowchart depicting the basic methodology adopted to address the objectives of the thesis. The steps given in the boxes numbered 1-4 have been elaborated in Chapter 3-6 for clarity of presentation. The main outcomes from the work presented in this thesis have been synthesized to decipher the evolutionary history of Mars mid-latitudes during the Late Amazonian (past ~1 Ga). Together, the work done in the thesis provides new insights into glaciation and gully formation on Mars.

CHAPTER 3

Extensive glaciation in the Erebus Montes region of Mars

If you want to shine like a sun. First burn like a sun.

- Dr. APJ Abdul Kalam

3. Extensive glaciation in the Erebus Montes region of Mars

3.1. Introduction

Lobate debris apron (LDA) and lineated valley fill (LVF) are landforms representing the Mars' Late Amazonian geological history **(e.g., Squyres, 1978, 1979; Luchitta, 1981; Head et al., 2006a, 2009; Carr and Head, 2009; Dickson et al., 2008, 2010; Baker et al., 2010; Sinha and Murty, 2013a; Sinha et al., 2017)**. LDA originate from the walls of isolated and clustered massifs and undergo down-gradient flow into the plains surrounding the massifs **(Squyres, 1979; Head et al., 2010; Baker et al., 2010)**. LVF is found confined within valleys and the surface lineations on LVF indicate them to be sourced from alcoves in the mesa walls **(Squyres, 1979; Levy et al., 2007)**. LDAs formed in the northern mid-latitudes (between 30-50˚ N) are apparent along (1) the dichotomy boundary **(e.g., Chuang and Crown, 2005; Head et al., 2006b, 2010; Levy et al., 2007, 2014; Dickson et al., 2008; Morgan et al., 2009; Baker et al., 2010; Sinha and Murty, 2013b, 2015)**, (2) the Acidalia Planitia **(Orgel et al., 2019)**, (3) the northeast of the Elysium Mons **(Dickson et al., 2010; Safaeinelli et al., 2009)**, and (4) the highland region of Alba Mons **(Sinha et al., 2017)**. LVFs are mainly observed along the dichotomy boundary **(Levy et al., 2007; Morgan et al., 2009; Baker et al., 2010)**. LDAs in the southern mid-latitudes are scattered throughout the highland regions but they are dominant in the east-southeast of Hellas and Argyre basins **(Squyres and Carr, 1986; Pierce and Crown, 2003; Chuang et al., 2014)**, respectively. LVFs are mostly limited to the east of the Hellas basin **(Pierce and Crown, 2003)**.

Previous investigations of LDA and LVF along the dichotomy boundary have provided evidence of (1) ridge and furrow patterns **(Head et al., 2010, Baker et al., 2010)**, (2) compressing and bending of flowlines around topographic obstacles **(Head et al., 2010)**, (3) superposed small-scale flow lobes over the main LDA **(Levy et al., 2007; Dickson et al., 2008; Head et al., 2010; Souness et al., 2012; Hepburn et al., 2020)**, and (4) debris-covered glacial origin of LDA/LVF from the investigation of radar return signals from SHAllow RADar (SHARAD) instrument **(Li et al., 2005; Head et al., 2006a, 2006b, 2010; Seu et al., 2007; Baker et al., 2010; Fastook et al., 2014; Levy et al., 2014)**. Additional morphologies such as brain-terrain texture **(Levy et al., 2010a; Sinha et al., 2017)** and ring-mold craters **(Kress and Head, 2008; Sinha et al., 2017; Baker and Carter, 2019a)** have been recognized on top of LDA/LVF at scale of High Resolution Imaging Science Experiment (HiRISE) images (~0.25-0.5 m/pixel) **(McEwen et al., 2007a)**. Furthermore, the ages calculated from the count of superposed craters on the surfaces of LDA/LVF and superposed flow lobes on the main LDA have led to the idea of episodic glacial activity during the past ~10 Ma to 1 Ga **(e.g., Mangold, 2003; Kress and Head, 2009; Levy et al., 2007; Morgan et al., 2009; Berman et al., 2015; Sinha et al., 2017; Hepburn et al., 2020)**. While these studies provide new insight into the LDA/LVF formation and provide inferences for the Late Amazonian climate during which they formed, a key question remains as to whether the glaciated regions away from the dichotomy boundary show LDA/LVF consistent with alike flow characteristics as a result of multi-stage glaciation. Erebus Montes (centered at 35˚ N, 175˚ W) region in the central Arcadia Planitia is one such example of a glaciated region **(Figure 3.1a)**. Previously, Erebus Montes has been never investigated in detail. In some of the previous studies, flow units from the Erebus Montes

region hosting geomorphic evidence for the presence of LDA/LVF deposits have been mainly presented **(e.g., Head et al., 2010)**. Global mapping of the distribution of debris-covered glaciers in the mid-latitudes have simply mapped the presence of LDA deposits in Erebus Montes **(Levy et al., 2014)**, but not investigated any of the LDA deposits in this region. Recently, regional mapping of the Arcadia Planitia using the Context Camera (CTX) (~6 m/pixel) on the Mars Reconnaissance Orbiter (MRO), together with other complementary datasets, have also shown presence of LDA deposits in the Erebus Montes region **(Ramsdale et al., 2019; Hibbard et al., 2021)**. In this study, we embarked on the mapping of LDA deposits in Erebus Montes and examined them in a detail not previously attempted. Detailed geologic investigation comprising of morphological, topographic, subsurface and chronological studies of the LDA deposits have been undertaken to address the following scientific aspects:

(1) Infer the extent of glaciation in the Erebus Montes and decipher the probable geologic periods of the glacial activity.

(2) What is the evidence for multi-stage glaciation (i.e. superposed flow over the main LDA) in the region?

(3) Examine the influence of emplacement and removal of mantling deposits from LDA identified in the region.

(4) Identify landforms to support localized flow and glaciation in the region.

(5) Detect presence of subsurface ice in the region.

(6) Examine the climatic conditions that led to the formation of landforms identified in this region.

Together, we deliberate upon the inferences made from the observations in the context of other glaciated regions along the dichotomy boundary of Mars and finally propose a conceptual model to illustrate the evolutionary history of the Erebus Montes region.

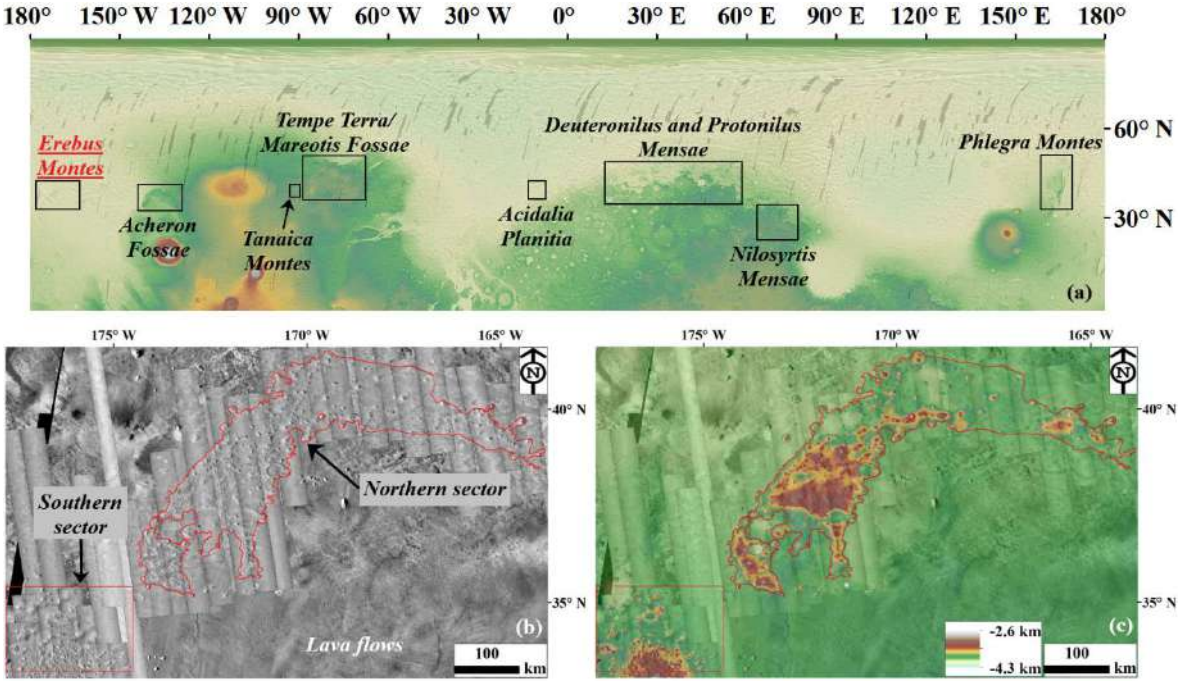

Figure 3.1.a. Context map of the glaciated regions in the northern mid-latitudes over the Mars Orbiter Laser Altimeter (MOLA; white is high elevation and light green is low elevation) topographic data superposed on the Mars Odyssey THEMIS daytime thermal infrared global mosaic (100 m/pixel). The Erebus Montes region studied in this paper is the westernmost glaciated region on Mars. The study regions of previous studies of LDA/LVF landforms that presented evidence of extensive glaciation on Mars are shown on the map: Phlegra Montes **(Dickson et al., 2010; Gallagher et al., 2020)**, Nilosyrtis Mensae **(Levy et al., 2007)**, Deuteronilus and Protonilus Mensae **(Head et al., 2006a; Morgan et al., 2009; Baker et al., 2010; van Gasselt et al., 2010; Sinha and Murty, 2013b, Baker and Head, 2015, Sinha and**

Murty, 2015), Acidalia Planitia **(Orgel et al., 2018)**, Tempe Terra/Mareotis Fossae **(Chuang and Crown, 2005)**, Tanaica Montes **(Sinha et al., 2017)**, and Acheron Fossae **(Head et al., 2009)**. Basemap image credit: MOLA/GSFC/USGS and THEMIS/ASU. **Figure 3.1.b:** Northern and Southern sectors of the study region - red solid lines. All images are from the CTX camera (Malin et al., 2007) and they are superposed on the Mars Odyssey THEMIS daytime thermal infrared global mosaic (100 m/pixel). CTX image credit: NASA/JPL-Caltech/MSSS. THEMIS image credit: THEMIS/ASU. MOLA image credit: MOLA/GSFC/USGS. **Figure 3.1.c:** Topography of the study region shown using the Mars MGS MOLA – Mars Express (MEX) High-Resolution Stereo Camera (HRSC) blended global DEM (200m/pixel). The background is THEMIS daytime thermal infrared global mosaic (100 m/pixel). DEM credit: USGS Astrogeology Science Center.

3.2. Data and Methods

3.2.1. LDA Distribution and Morphological Investigation

In this study, CTX images have been used for mapping the distribution of LDA deposits within the study region. We have downloaded images from the Mars Orbital Data Explorer (ODE) website (https://ode.rsl.wustl.edu/mars/indexProductSearch.aspx), which is a part of the NASA Planetary Data System (PDS) geosciences node. Images were analysed at a map scale of 1:1000 using ESRI's (Environmental Systems Research Institute, Inc. Redlands, CA, USA) ArcMap10.0. The flowlines of LDA deposits were identified based on the criteria established for recognizing LDAs in the northern mid-latitudes of Mars **(Head et al. (2010)**. We examine the down-gradient flow characteristic of LDA deposits on the basis of evidence of folding,

wrapping, bending, compressing, and tightening of flowlines around topographic obstacles **(e.g., Baker et al., 2010)**. The terminus of the LDA deposit is denoted as the flow extent of LDA from the base of the flanks of mesa. HiRISE and CTX images have been used for investigating the surface morphology of LDA deposits. The "latitude-dependent mantle (LDM)" (emplaced during the cold and arid climatic conditions within the past tens of thousands to a few million years) **(Mustard et al., 2001; Head et al., 2003; Laskar et al., 2004)** offer new insights into the modification of the LDA deposits in the region **(Berman et al., 2015)**. LDM is typically described as a layer or multiple layers of ice-cemented dust that is subsequently dissected through sublimation of ice and liberation of dust **(Baker and Head, 2015)**. Textural representatives of LDM emplaced on the LDA deposit include brain-terrain texture and polygonal cracks **(Figure 3.2a) (e.g. Levy et al., 2009, 2010a)**. The brain-terrain texture is identified as 'mounded and furrowed' texture on the LDA deposits **(Levy et al., 2010a)**. Polygonal cracks are recognized as a network of fractures that intersect to form polygonal areas bounded by depressed surface troughs **(Levy et al., 2009a)**. The trough intersections are usually near orthogonal. Ring-mold craters have been also identified on the top of LDA deposits that helps to further substantiate the emplacement of LDM **(Figure 3.2b) (e.g. Kress and Head, 2008; Baker and Carter, 2019b)**. These craters have seven different morphological characteristics, which includes plateau, etched plateau, torus, mound, ring, filled torus, and pit **(e.g. Baker and Carter, 2019b)**. Morphological characteristics of these different ring-mold craters are described in detail in **Baker and Carter, 2019b**. We searched for these crater morphologies on the top of LDA deposits. Furthermore, networks of raised linear-curvilinear

ridges have been also recognized on the surface of LDA deposits as a supporting line of

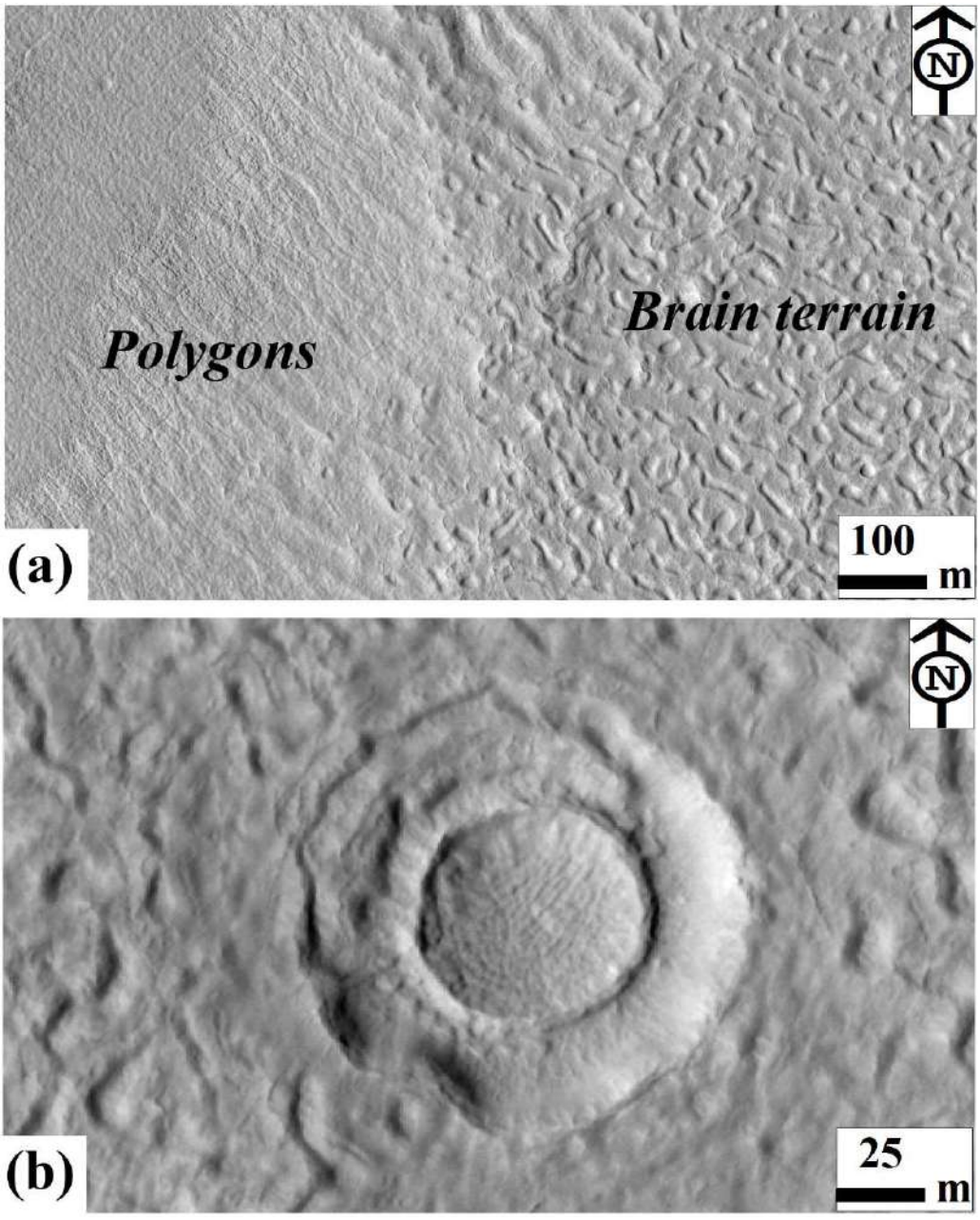

evidence for the loss of buried ice from beneath the LDA deposits.

Figure 3.2. Typical examples of (a) brain-terrain texture and polygons, and (b) ring-mold craters within the study region.

3.2.2. Topographic Investigation

Down-gradient flow characteristics of LDA deposits have been examined using Mars Orbiter Laser Altimeter (MOLA) - High-Resolution Stereo Camera (HRSC) blended global digital elevation model (DEM) v2 (retrieved from http://bit.ly/HRSC_MOLA_Blend_v0) **(Fergason et al., 2018)**. This DEM is based on the full-resolution (463 m/pixel) MOLA DEM and blending the high-resolution HRSC DEMs (~50 m/pixel) into it. Using a bilinear interpolation method, a cell-size of 200 m/pixel was selected for up-sampling the MOLA and down-sampling the HRSC DEMs **(Fergason et al., 2018)**. Spatial resolution of the blended DEM is about 200 m/pixel and is projected into the simple cylindrical projection. The effective DEM pixel resolution for a region is similar to the resolution of MOLA DEM if there is no HRSC DEM coverage. We have used the function 'r.param.scale' for 9 pixels in QGIS to convert the elevations of MOLA+HRSC DEM into slopes. Typically, this function uses a 9-pixel- moving window to fit a plane to the elevations and calculate a slope, hence minimizing noise in the resulting slope map. The uncertainty in projection can lead to additional distortion in the local slope and this can be corrected by first determining the fractional slope in a conformal Mercator projection **(Conway et al., 2019)**. After that, the data is projected into the initial simple cylindrical projection and corrected for the distortion by dividing the fractional slope by the cosine of the latitude **(Conway et al., 2019)**. In this study, we have not directly accounted for the rectification of distortion in the regional slope due to projection uncertainty, as it is beyond the scope of the study. Therefore, we acknowledge that it is likely that the

distortion in slope have affected our regional slope analysis of the LDA deposits to some extent.

3.2.3. Subsurface Ice Investigation

The presence of buried ice in the mapped LDA deposits is examined using the SHARAD Reduced Data Record (RDR) datasets (generated by the Italian SHARAD team) **(Seu et al., 2007)**. SHARAD datasets are processed using the Colorado SHARAD Processing System (CO-SHARPS) Processing Boutique **(Putzig et al., 2016)**. Clutter simulation and production of time-domain and depth-domain radargrams (at a dielectric constant value of 3.15 for water ice) is done using the CO-SHARPS processing boutique. In general, the clutters are across-track surface reflections that appear in larger delay and thus look like they are from beneath the subsurface. However, these clutter can be recognized easily by comparing the position of subsurface reflections in the radargram with their positions in the simulated radargram. If the reflections appear to occur at the same position in both the radargram and the simulated radargram, then it indicates that the subsurface reflections are cluttered and then they are not included in the interpretation. However, when the clutter is not apparent in the simulated radargram, but a reflection appears in the radargram, we interpret that as a subsurface interface and determine its position and time delay. Generally, the radar signal in the subsurface splits into two interfaces on proceeding from the surrounding plains region to the LDA deposit **(Plaut et al., 2009)**. This splitting of radar signal is inferred as initial identification of the subsurface interfaces. On plugging in the dielectric constant value of 3.15 for water ice into the CO-SHARPS processing boutique, if the time-depth conversion results in coplanar alignment of the subsurface reflection with the reflection from the surrounding plains region, then it

indicates that there is presence of subsurface ice. The extent of subsurface ice is estimated as the distance of coplanar signal from the bottom of mesa flanks in the depth-domain radargram.

3.2.4. Crater Size-frequency Distribution Measurement

CTX images have been used for the count of craters on the mapped LDA deposits within the study region. *CraterTools* **(Kneissl et al., 2011)**, an *ArcGIS* extension, was used for estimating the diameter of superposed craters on the mapped LDA deposits. The crater count data was compiled into the crater size-frequency distribution (CSFD). Age estimation was performed on the cumulative CSFD plot by combining all the mapped LDA deposits within the study region as one single unit. The crater diameter axis in the CSFD plot was binned logarithmically **(Hartmann, 2005; Michael and Neukum, 2010)**. We used the "Mars, **Hartmann (2005)**" production function, along with the "Mars **Hartmann (2004)** iteration" chronology system and "Mars, **Michael (2013)**" chronology function. CSFD plot fitting was done using the *CraterStats 2.0* software **(Michael and Neukum, 2010)**, which yielded the best-fit age and corresponding estimates of error. The age is inferred by comparing the distribution of craters larger than 250 m (i.e. the fit segment) with the slope of the isochrons (i.e. isochrons separated by ages of 10 Ma, 100 Ma, and 1 Ga; **Michael, 2013**) in the CSFD plot. This minimum crater diameter range is chosen to compare the ages of LDA in the study region and those present along the dichotomy boundary **(**e.g. ages of LDA reported in **Baker et al., 2010 and Morgan et al., 2009)**. The slope of the fit segment (for crater diameter larger than 250 m) tends to match with the slope of isochrons, which determines the best-fit age **(Berman et al., 2015)**. If the fit-segment in the CSFD plot for selected crater diameter do not match and deviates from the slope of an isochron, then maximum ages are provided using the largest bin

with more than 1 crater (at 250 m) **(Berman et al., 2015)**. The error bars in the CSFD plot is given by $\pm[N_{cum}(D)]^{1/2}/A$, where N_{cum} is the cumulative number of craters having diameter D, and the count are is represented by A **(Michael and Neukum, 2010)**. The aggregation of individual LDA deposits in the study region as one single, large unit could likely minimize the large error bars from small counting units **(Hepburn et al., 2020)**. Furthermore, we have included a variety of crater morphologies such as bowl-shaped craters (both fresh and degraded), ring-mold craters, and degraded craters (with intact crater rim for diameter measurement) in the crater count and estimated their best-fit ages. In our study, the best-fit ages for the different crater morphologies is useful in revealing the crater retention ages for distinct geologic events **(Berman et al., 2015; Hepburn et al., 2020)**. Only those degraded craters whose outermost edge can be recognized for the diameter measurements have been included in crater counts. For deriving the crater retention age of the surfaces, we will initially consider all the superposed craters on the LDA deposits **(Michael and Neukum, 2010; Hepburn et al., 2020)**. Then, we will discuss the overall variation in the derived ages (from the count of all the superposed craters) by including or excluding craters with different morphologies on the LDA deposits. Previously, expanded craters have been also observed in the Erebus Montes region **(Viola et al., 2019)**. These craters are represented as a form of sublimation thermokarst on Mars **(Viola et al., 2019)**. They are believed to have formed in places, where subsequent to an impact, the shallow subsurface ice has destabilized and sublimated leading to collapse of the overlying dry regolith to finally produce an expanded appearance of the crater diameter **(Dundas et al., 2019; Viola et al., 2019)**. We have excluded expanded craters from the best-fit age estimation because: (1) they are believed to be secondary craters, so cannot be included

with the ages estimated using the primary craters, (2) there is no scaling factor to which the diameter of these craters have expanded, so there is no idea of the true crater diameter of these craters, and (3) these craters have subdued morphology that often merges with the surrounding surface, so often it is difficult to recognize the edge of the crater for diameter measurements **(Dundas et al., 2015b; Viola et al., 2015)**. Additionally, care was exercised to not include clusters of secondary craters, flat-topped knobs, features consistent with crater-like rims but do not form a closed depression, and sublimation and/or collapsed pits, in the estimation of age. Although we acknowledge that some of these features might appear as impact craters at the resolution of CTX imagery, so some of them may have been falsely counted as craters.

3.3. Observations

3.3.1. Geological Setting

The Erebus Montes region in the Arcadia Planitia (geographically located as the westernmost region in the northern mid-latitudes) is positioned between the Phlegra Montes and Olympus Mons aureole deposits **(Figure 3.1b)**. We analyze those LDA deposits distributed in the Erebus Montes region within 41.5° N, 164° W – 33.5° N, 177.7° W **(Figure 3.1b)**. The study region is classified in the Mars' geologic map as dissected areas of the highland region characterized by geologic unit representative of the Hesperian and Noachian geological epochs **(Tanaka et al., 2014)**. The elevation of the highland region (over which the mesa-LDA deposits are distributed) ranges from -2600 to -4300 m **(Figure 3.1c)**. The northern sector of the study region extends from 35.2° N to 41.5° N and the southern sector is located between 33.5° N to 35.2° N **(Figure 3.1b)**. The longitudinal extent of the northern and southern sectors is not same,

probably because the study region is an erosional remnant of the Mars geologic past **(Tanaka et al., 2014)**. The northern sector is between 174.5° - 164° W and the southern sector is between 177.7° - 174.5° W. The portions surrounding the highland region is flat (elevation <-4000 m) and mostly filled with lava flow units **(Figure 3.1b)**. Some of the portions between the northern and southern sector of the study region is also filled with lava deposits **(Tanaka et al., 2014)**.

3.3.2. Distribution of LDA Deposits

We observed well-developed LDA deposits surrounding individual mesa, group of mesas, and in the interior of craters. There are 236 individual mesas with LDA, 84 groups of mesas (comprising of minimum 2-3 mesas in each of the groups) with LDA, and 7 craters infilled with ice-related flow units that collectively presents the evidence for integrated LDA deposits within the study region. LDAs originate from the walls (slope 5-30°) of individual mesa having height and spatial length in the range of 0.1-1 km and 1-10 km, respectively **(Figure 3.3)**. LDAs extend in the range of few kilometers (~2 – 20 km) at slopes of 1-5° from the mesa wall and terminate over the surrounding plains region at slopes of 1-2° **(Figure 3.3)**. The topographic profiles over the LDA deposits (individual and grouped) exhibits a convex-up, steep terminus profiles typical of LDA mapped elsewhere along the dichotomy boundary **(Figure 3.4a-b) (Baker et al., 2010)**. The overall relief from base of the mesa wall to the LDA surface and the surrounding plains are in the range of 0.1-0.5 km. The surface of individual LDAs and LDAs in the grouped mesa-LDA systems are generally at gentle slopes of <5° and the flow directions inferred from the surface lineations are perpendicular to the DEM derived contours suggesting for the down-gradient component in the flow **(Figure 3.4c-d)**. Although

there are some of the LDA deposits (in both individual and grouped mesa-LDA systems) that are at steeper slopes of 5-10°, and they terminate at slopes less than 2°. The surface of LDAs around the eastern and western margin of the northern sector of the study region are at maximum slope of 4° and terminate abruptly at slopes of 1-2°.

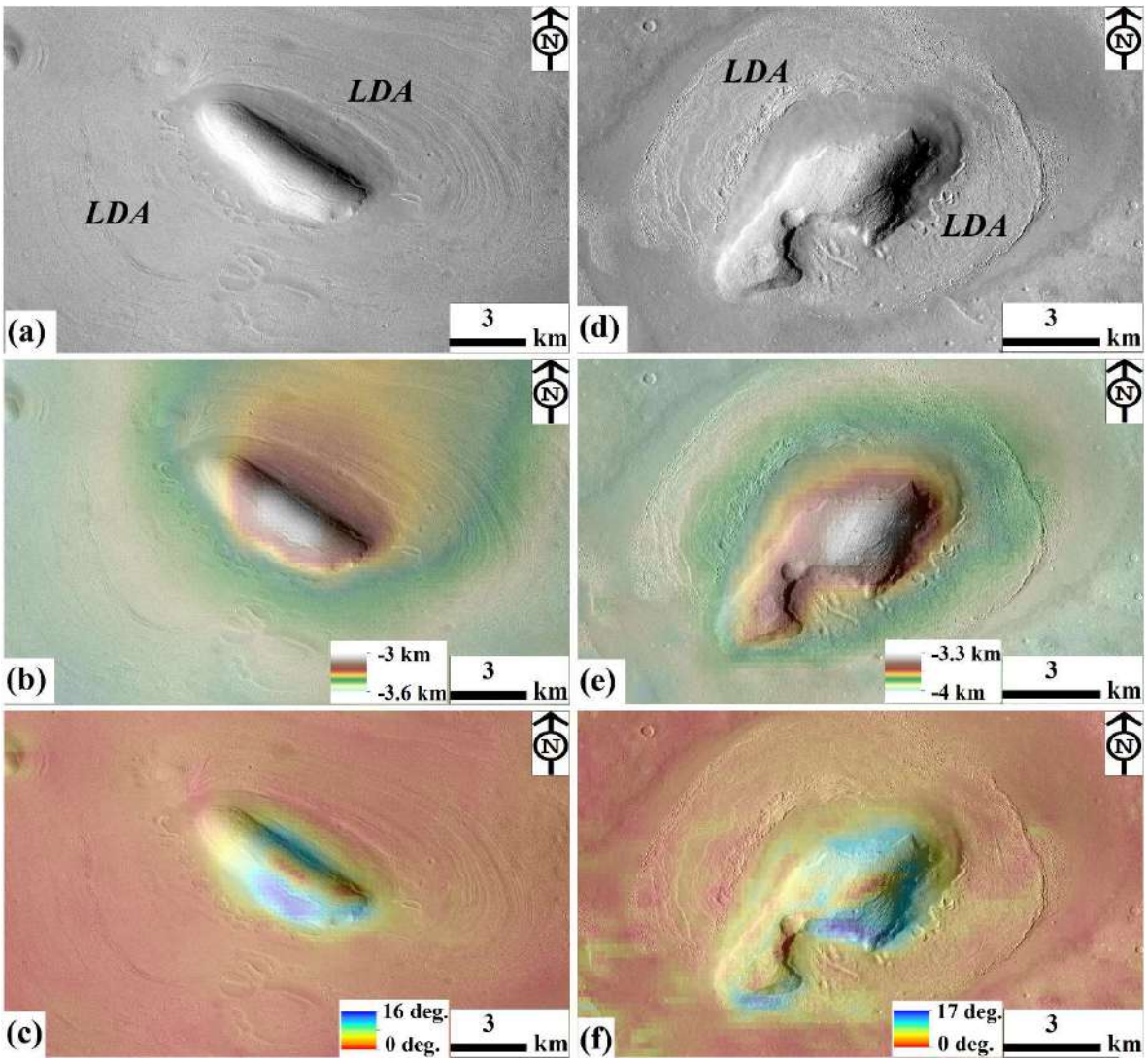

Figure 3.3. (a-f) CTX image based examples of well-developed debris apron surrounding the individual mesas within the study region. The outlines of the main apron body surrounding the mesa are defined by the surface flow lineations. MOLA-HRSC DEM shows the topography and slope variation along steep escarpments and apron surface. (a) Subset of image

P15_006932_2181; approximate location of image center: 38.72˚ N, 171.49˚ W. (d) Subset of image B01_009859_2171; approximate location of image center: 36.5˚ N, 173.15˚ W. CTX image credit: NASA/JPL-Caltech/MSSS.DEM credit: USGS Astrogeology Science Center.

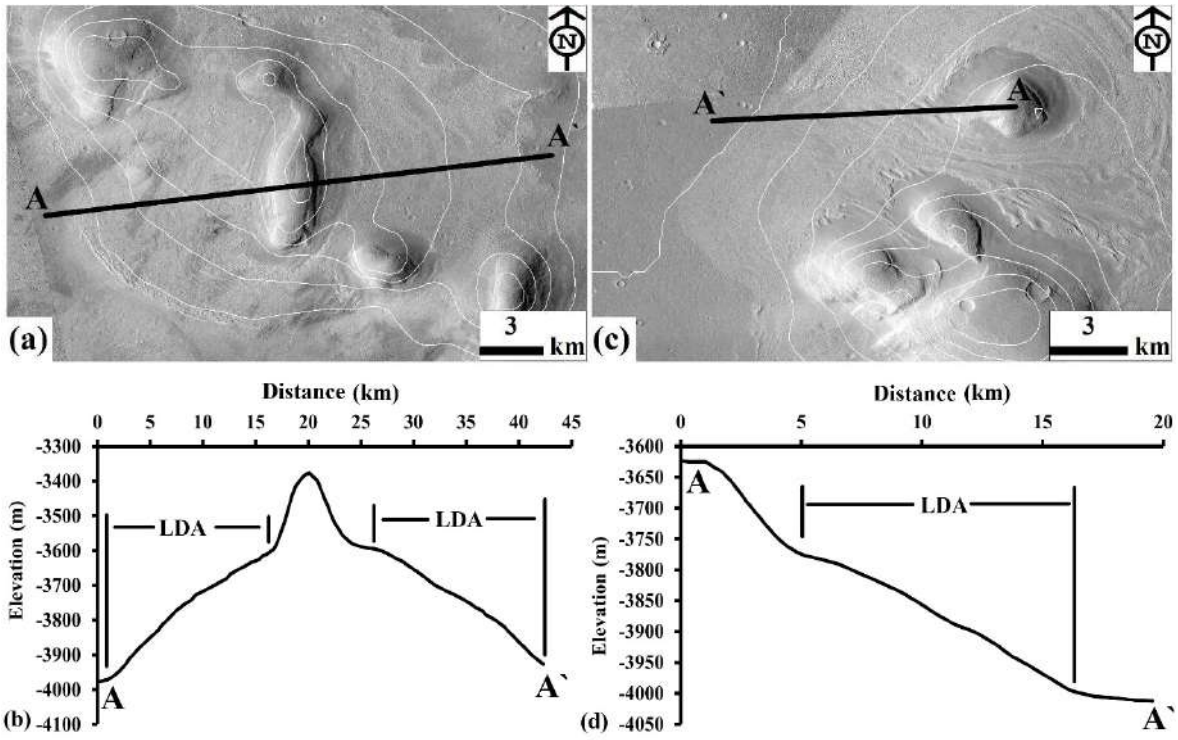

Figure 3.4. (a-d) MOLA-HRSC DEM based topographic profiles (A-A`) showing the convex-up, steep terminus profiles, and down-gradient flow characteristic typical of debris aprons within the study region. (a) Subset of image D22_035796_2198; approximate location of image center: 39.21˚ N, 164.84˚ W. (c) Subset of image B01_009859_2171; approximate location of image center: 36.85˚ N, 173.12˚ W. CTX image credit: NASA/JPL-Caltech/MSSS.DEM credit: USGS Astrogeology Science Center.

We have observed six infilled craters (diameter range 6-24 km) in the northern sector and one infilled crater (diameter: ~13 km) in the southern sector of the study region **(Figure 3.5a-b)**. The interior of these craters are consistent with LDA deposits originating from the steep crater walls that resulted in crater infilling **(Figure 3.5a)**, flattening of crater floor, subsequent crater wall breach, and flow out of the crater. Four craters out of six in the northern sector of the study region show the evidence of crater wall breach and flow. The crater (diameter: ~13 km) in the southern sector is a layered ejecta crater **(Barlow, 2006)** and is characterized by concentric flow lineations on the crater floor, which suggests that the flows originated from the crater wall. This type of flow within a crater interior is termed as concentric crater flows (CCF) **(Figure 3.5b) (Levy et al., 2010a)**. There are many more infilled craters within the study region, but due to their small diameter (<6 km) they have not been chosen for detailed mapping and investigation in this study.

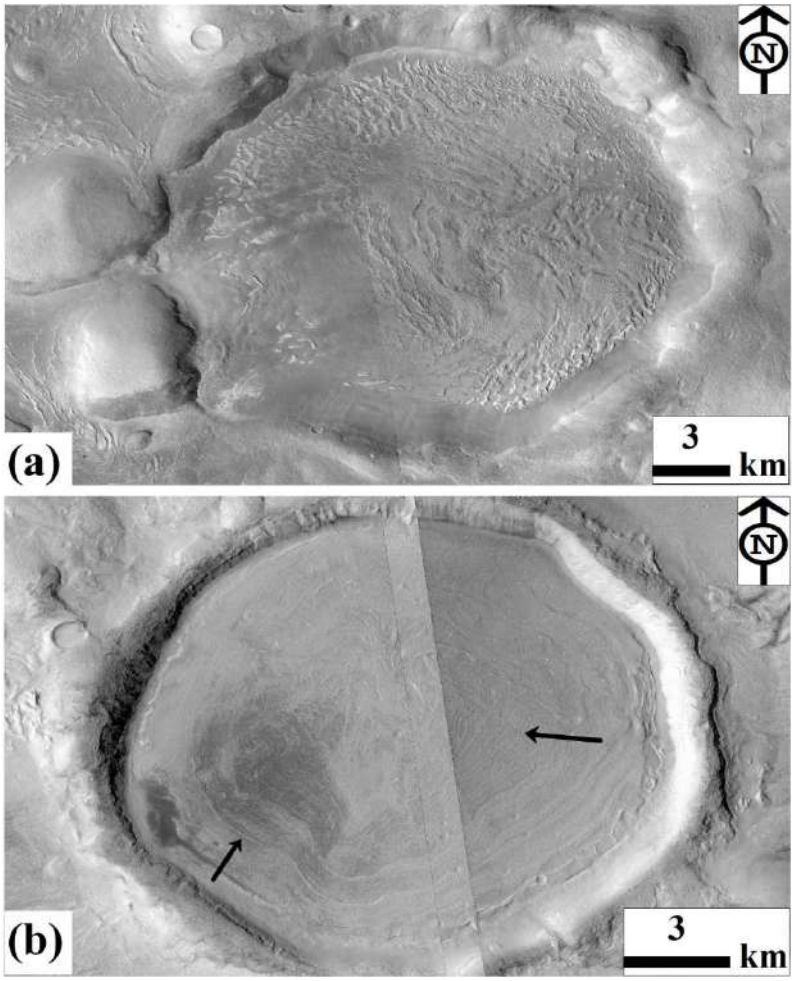

Figure 3.5. (a) Example of an infilled crater in the northern sector of the study region. Subset of CTX image P16_007354_2161; approximate location of image center: 36.35˚ N, 173.65˚ W. (b) CCF in the southern sector of the study region. Subset of CTX image B21_017850_2172; approximate location of image center: 34.50˚ N, 176.34˚ W. CTX image credit: NASA/JPL-Caltech/MSSS.

3.3.3. Morphological Mapping

The exterior boundary of the northern sector of the study region is outlined based on the identification of the margin of LDA deposits within 35.2° - 41.5° N and 174.4° - 163.2° W.

The southern sector is outlined as a simple rectangle as there is no defining boundary of the study region but the individual mesa-LDA deposits are outlined between 33.5° – 35.2° N and 174.9° – 178.2° W. The geologic units within the study region are outlined in the morphological map at the 1:50,000 scale as mesas, individual LDA deposits, grouped LDA deposits, infilled craters, concentric crater fill, and plains regions **(Figure 3.6)**. The study region lacks the morphological evidence for lobate flow units emanating from alcoves in the mesa flanks and superposed on the main LDA deposit. Morphological units (such as brain terrain texture, ring-mold craters, and polygonal cracks) observed using the HiRISE images are presented separately in the subsequent sections and their extents are not outlined on the map. Additional morphologic units such as pits and sharp, arcuate ridges on the LDA deposits are also presented separately and excluded from the map. Wrinkle ridges and lava flow features were morphologically distinguished from each other but excluded from the mapping process and detailed investigation, as they are beyond the scope of this paper.

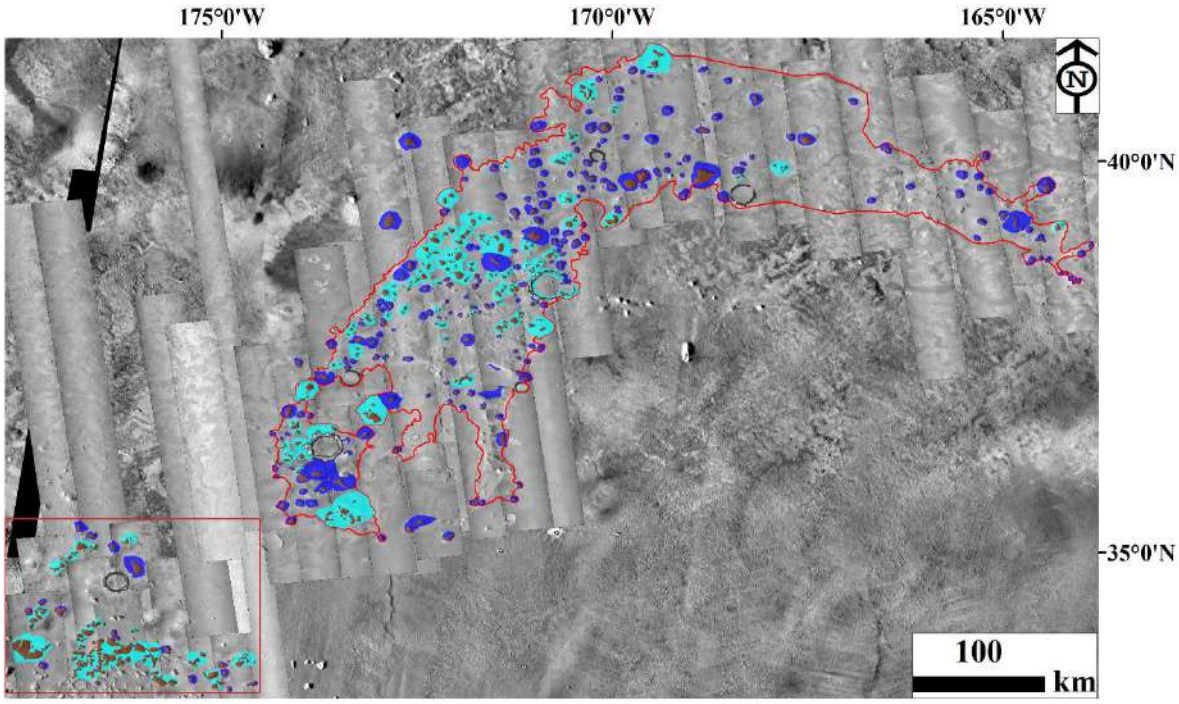

Figure 3.6. CTX image based morphologic map of the study region. The background is THEMIS daytime thermal infrared global mosaic (100 m/pixel). The map illustrates the key features within the study region, including the mesa (brown), individual LDA deposits (blue), grouped LDA deposits (cyan), and boundary of infilled craters (black). CTX image credit: NASA/JPL-Caltech/MSSS. THEMIS image credit: THEMIS/ASU.

3.3.4. Ridges on LDA Deposits

The surface of LDA deposit is characterized by ridges that display positive relief and a curvilinear pattern **(Figure 3.7)**. The ridges appear to be either aligned to the terminus of LDA deposits or are at the interface between the smooth unit adjacent to the mesa wall and the LDA deposit **(Figure 3.7a-b)**. LDA deposits emplaced along the western side of the northern sector of the study region are consistent with extensive ridges (entire or majority of the LDA deposits have ridges on them) **(Figure 3.7c-d)**. Here the ridges extend outward from mesa wall and are

progressively folded and flattened as the ridges deform and merge with the plains region. The extensive ridges may be branched and connect to each other to form ridge networks for long distances (~1-10 km), and the depressions formed on the LDA deposits by these long ridge networks are 100-200 m wide. Progressive broadening of ridges is evident where there are no topographic obstacles **(Figure 3.8a)**. The orientation of these ridges (curvilinear pattern) is such that it mimics the flow pattern of the LDA deposits **(Figure 3.8b)**. However, there are numerous patches of isolated ridges on LDA deposits in the other parts of the study region that often forms closed loop-like or elliptical structures. Isolated ridges are also evident on the LDA deposits formed in the southern sector of the study region. The depressions adjacent to or in between the ridges are marked by smooth texture and sometimes by a typical mound-and-tail terrain **(**similar to Figure 12 in **Hubbard et al., 2011) (Figure 3.8c-d)**.

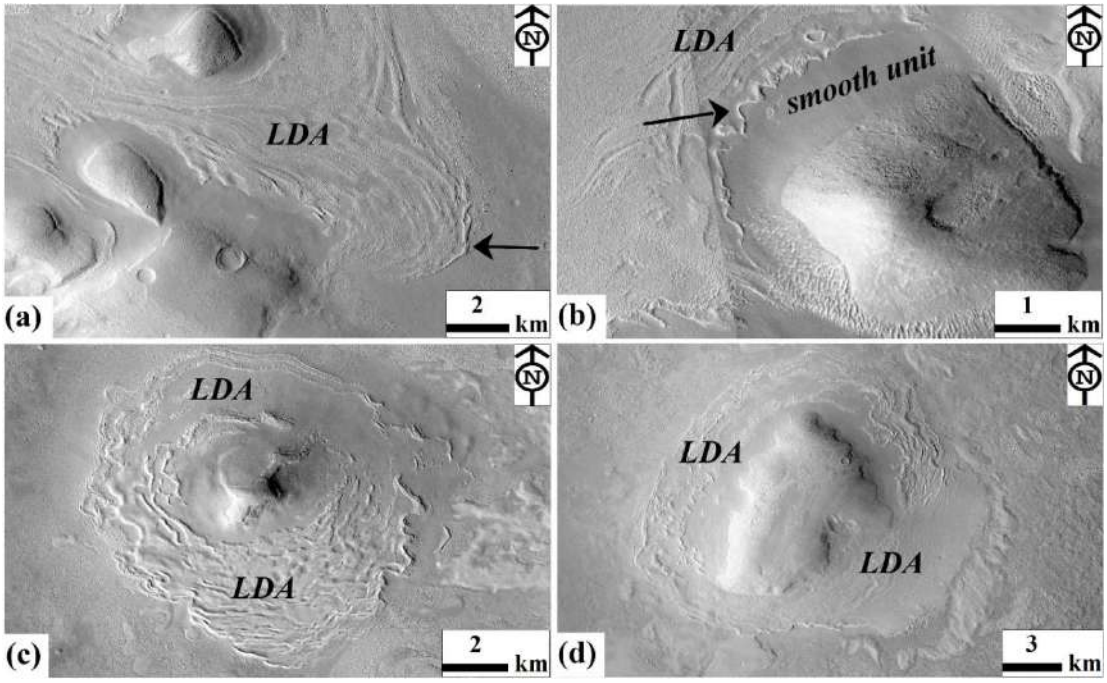

Figure 3.7. Close-up CTX views of linear-curvilinear ridges on the surface of LDA deposits mapped in the study region. (a) Ridges that are aligned to the terminus of LDA deposits. (b) Ridges at the interface between the smooth unit adjacent to the mesa wall and the LDA surface. (c-d) Examples of LDA deposits consistent with the evidence of extensive ridges. (a) (CTX image B01_009859_2171; approximate location of image center: 36.82˚ N, 172.99˚ W). (b) (CTX image B01_010004_2181; approximate location of image center: 39.05˚ N, 171.96˚ W). (c) (CTX image P15_006932_2181; approximate location of image center: 39.98˚ N, 171.93˚ W). (d) (CTX image P17_007644_2187; approximate location of image center: 39.23˚ N, 172.85˚ W). CTX image credit: NASA/JPL-Caltech/MSSS.

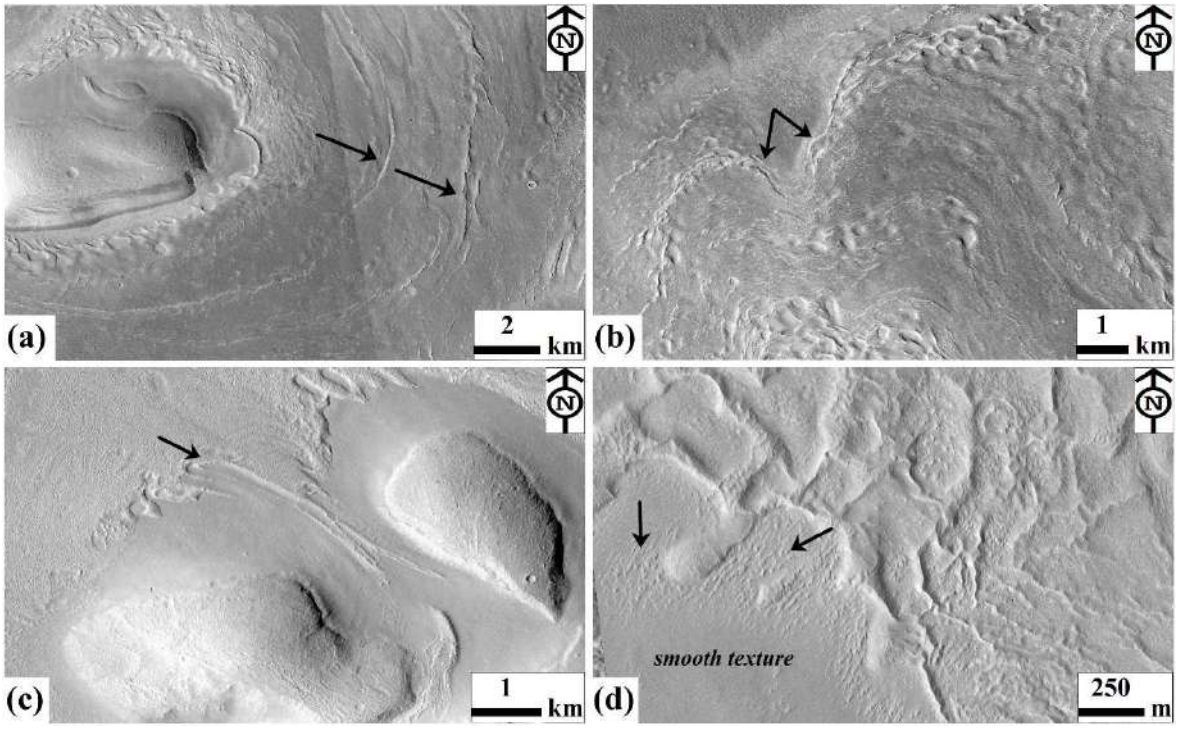

Figure 3.8. Close-up CTX/HiRISE views of the patterns exhibited by the ridges on the LDA deposits. (a) Ridges mimic the flow pattern of the LDA deposits. Note the folds in the ridges in (b). (c) Isolated ridge (arrow) with a closed loop-like formation. (d) Typical mound-and-tail

terrain texture (arrow) in the depression enclosed by the ridges. (a) (CTX image P16_007354_2161; approximate location of image center: 36.01˚ N, 173.69˚ W). (b) (HiRISE image PSP_008501_2160; approximate location of image center: 35.66˚ N, 173.49˚ W). (c) (CTX image B01_009859_2171; approximate location of image center: 36.81˚ N, 173.15˚ W). (d) (HiRISE image ESP_036548_2160; approximate location of image center: 35.52˚ N, 173.21˚ W). CTX image credit: NASA/JPL-Caltech/MSSS. HiRISE image credit: NASA/JPL-Caltech/University of Arizona.

3.3.5. Flow patterns

Progressive broadening of LDA deposit is evident in cases where there are no topographic obstacles (unobstructed flow of LDA). LDA deposits in this case form a continuous apron extending from the base of the mesa wall. Here flow patterns (as suggested by the flowlines) are generally perpendicular to the DTM-derived contour lines, indicating that the flow is down-gradient. Lineations around the groups of mesas show flow patterns of LDA deposits that extend from the walls of mesa, flow down-gradient into the surrounding plains, and are emplaced as a single, large entity emerged from the coalescing of multiple flows **(Figure 3.9)**. Several examples from LDA deposits are evident where the flow encountered a topographic obstacle (blocks/mounds, adjacent mesas, and adjacent flows) in its way. In these examples, the primary flow was obstructed in the following manners: (1) compression and looping of flow around an obstacle, subsequent broadening **(Figure 3.9a)**, (2) compression of LDA deposit between flows from adjacent mesa and a topographic obstacle, subsequent narrowing **(Figure 3.9b)**, (3) initial coalescing of flows, then compressing between flows from

adjacent mesas on both sides, and extending as an elongated lobe **(Figure 3.9c)**, (4) compressing, bending, looping and coalescing of flows around adjacent mesas and small mounds, to form a single, large entity **(Figure 3.9d)**, and (5) flow overtopping the small mounds. In addition to these observations, we have noted several LDA deposits lacking surficial evidence of prominent flow lines and patterns. This is more evident in the case of LDA deposits from the grouped mesas.

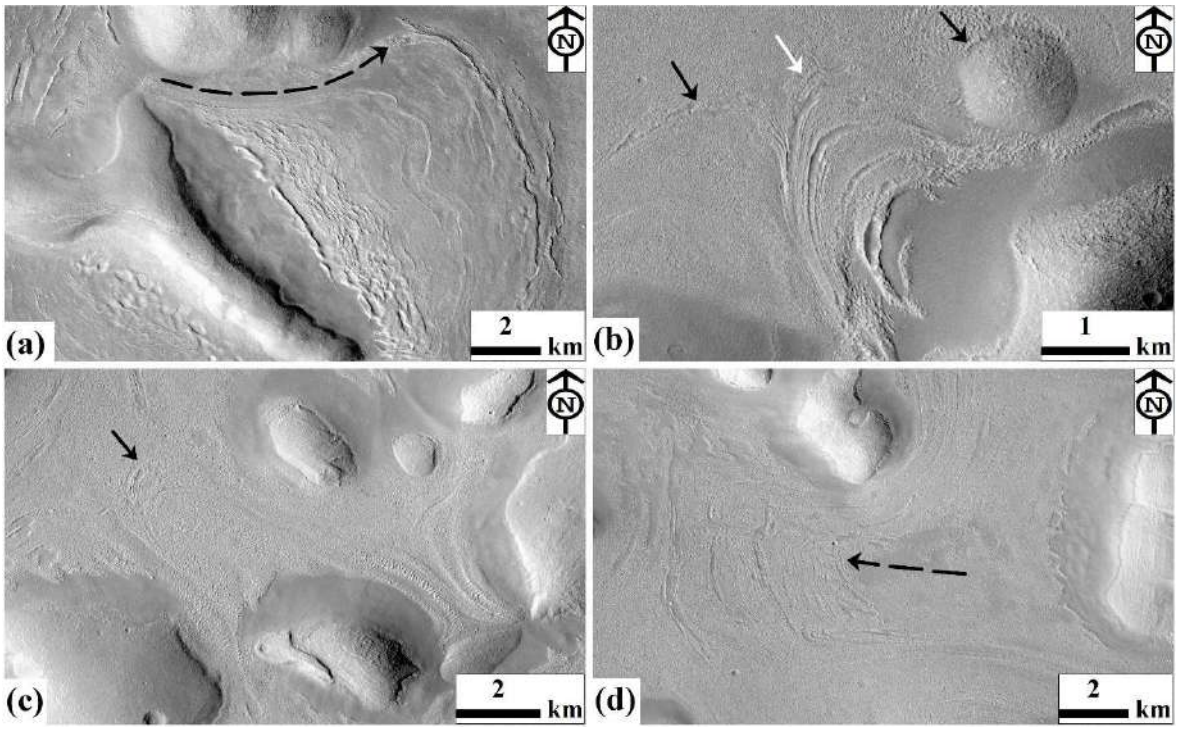

Figure 3.9. Close-up CTX views of flow patterns within LDA deposits mapped in the study region. (a) LDA compression, initially looping around obstacle (arrows), and then broadening (CTX image P16_007354_2161; approximate location of image center: 35.89˚ N, 173.41˚ W). (b) LDA compressing on interacting with the obstacles and debris apron from the adjacent mesa

(black arrow), flow becoming narrow and extending as a lobate flow (white arrow). (CTX image P17_007644_2187; approximate location of image center: 38.51˚ N, 172.54˚ W). (c) LDA merging/coalescing and extending as long lobe (arrow).(CTX image B01_010004_2181; approximate location of image center: 38.76˚ N, 172.13˚ W). (d) LDA compressing, bending, looping, and coalescing to emerge as a large flow unit (arrow) (CTX image P15_006932_2181; approximate location of image center: 38.88˚ N, 171.57˚ W). CTX image credit: NASA/JPL-Caltech/MSSS.

An additional flow pattern is evident from the LDA deposits in the southern sector of the study region **(Figure 3.10a-b, d)**. Here the broad piedmont-like lobe is sourced from a ~1 km high massif with wall slopes of >10°. The source alcove for the piedmont-like lobe is at an elevation of ~-3100 m and the lobe elongates for nearly ~15 km with the relief in the range of -3100 to -3900 m. The slope at which the lobe extends from the source alcove is in the range of 10-20°, exits at a slope around of 4-8° into the surrounding plains through a low point (between ~-3400 to -3500 m), elongates further at slopes of 1-6°, and terminates abruptly at slopes of 1-3°. Another broad flow in the southern sector of the study region exits into the surrounding plains at slopes of 1-4° after being compressed between the adjacent mesa walls **(Figure 3.10c)**. The topographic profile of the compressed portion of the LDA deposit shows that it bulged by ~200 m in comparison to the two ends of LDA deposits on either side **(Figure 3.10e)**.

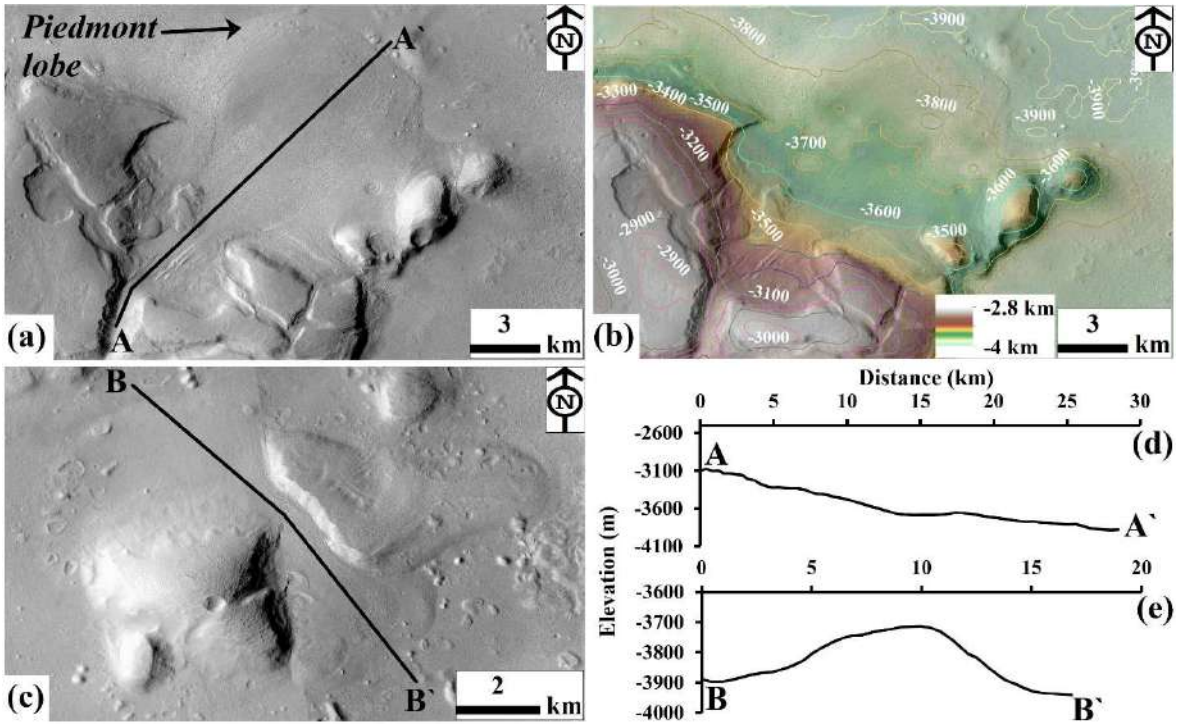

Figure 3.10. (a) Close-up CTX view of the broad piedmont-like lobe (arrow) in the study region. CTX image G22_026975_2137; approximate location of image center: 33.84˚ N, 177.34˚ W. (b) MOLA-HRSC DEM draped over the CTX image of the broad piedmont-like lobe. Note the elevation change in the topography of the lobe extending from the top (broad alcove) and flow down gradient to the surrounding plains region. Colored lines are the contours at 100-m intervals. Elevation values are shown as labels to the contour lines. (c) Another example of LDA flow pattern, wherein, the LDA is emplaced between the adjacent mesa walls and extends over the surrounding plains as a broad deposit. CTX image G21_026421_2123; approximate location of image center: 33.30˚ N, 175.05˚ W. (d) Surface elevation profile A-A` (as delineated by solid line in (a)) extending downwards from the broad alcove. (e) Surface elevation profile B-B` (as delineated by solid line in (c)) highlighting the bulge in the LDA

caused as a result of emplacement between the adjacent mesa walls. CTX image credit: NASA/JPL-Caltech/MSSS. DEM credit: USGS Astrogeology Science Center.

Similar flow patterns are also observed along the walls of impact craters. There is morphologic evidence in terms of down-gradient flow lineations for the flow (at a slope of 1-2°) from a smaller crater into the larger crater **(Figure 3.11)**. We acknowledge that this combination of smaller and larger craters can be also due to an oblique impact **(Herrik, 2014)**. The smaller crater-like feature superposed on the rim of a ~20 km impact crater has evidence of flow lineations on its floor that suggests outward flow and deposition on the floor of the larger crater **(Figure 3.11a)**, which is also evident as a terminus-like feature in the topographic profile **(Figure 3.11b-d)**, similar to terrestrial glacial land systems. There is a sharp increase of ~1° in slope at the terminus of the flow. In the topographic profile, the terminus of the flow is at ~-3880 m, which is ~200 m below the initiation point of the flow unit. The crater wall breach and outward flow into the surrounding plains spotted in some of the craters in the northern sector of the study region have a peak slope of ~2-4° around the crater wall region from where the wall breached. The crater floor with CCF in the southern sector of the study region is apparently flat as revealed in the topographic profile and the majority of the crater floor is at slopes of <1°.

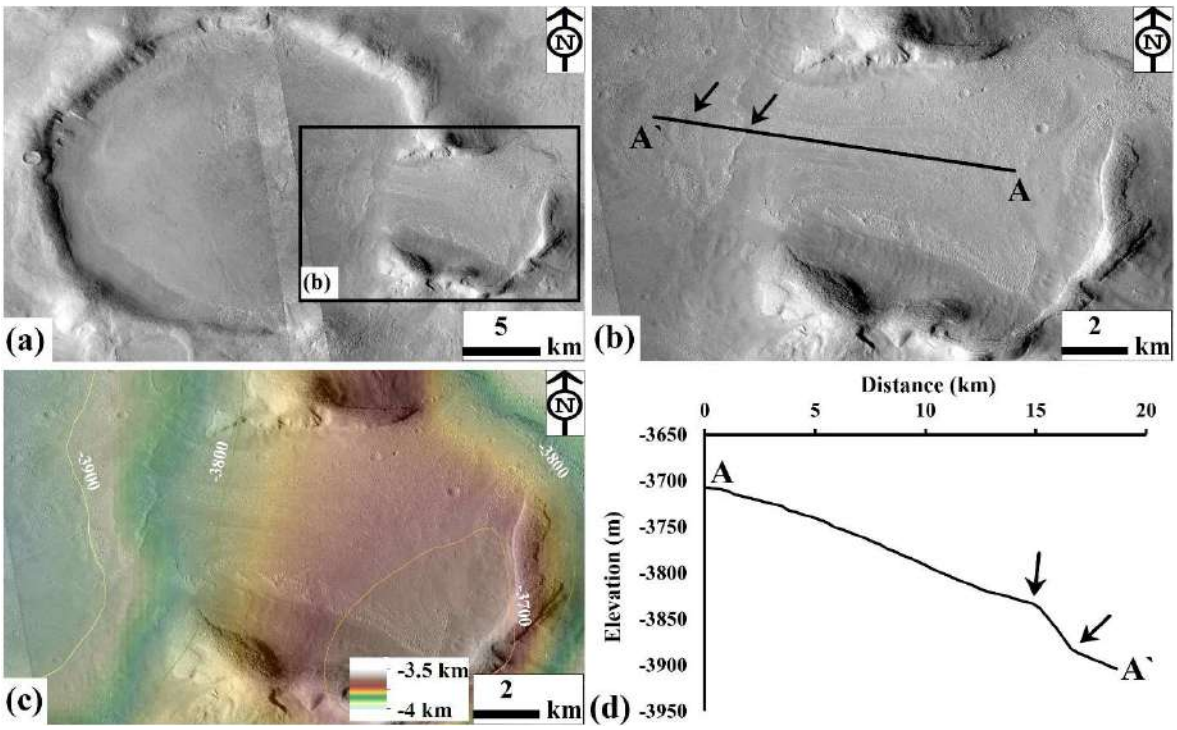

Figure 3.11. (a) Flow pattern of LDA emplaced from the crater walls. This crater system could be a possible oblique impact. (b) Close-up CTX view of the flow lineations extending from the smaller crater and extends outward on the floor of larger crater. Note the flow lineations along the solid line A-A`. (c) MOLA-HRSC DEM draped on the CTX image to show the downward flow of materials (from higher elevation to the lower elevation) from the smaller crater to the floor of the larger crater. (d) Surface elevation profile A-A` (as delineated in (b)) depicts the typical down gradient flow characteristic. The arrows placed in (b) and over the topographic profile show the possible position of the flow terminus. CTX image G20_026223_2192 and B18_016663_2198; approximate location of image center: 38.41˚ N, 170.80˚ W. CTX image credit: NASA/JPL-Caltech/MSSS. DEM credit: USGS Astrogeology Science Center.

3.3.6. Integrated flow extents

LDA deposits in the northern sector of the study region are most extensive and exhibit morphologic evidence for merging of individual flows with the adjacent flows to form a continuous apron for ~5000 km^2 in the region between massifs **(Figure 3.12a)**. The whole system of this continuous apron integrates over a distance of over 50 km before it terminates to form the western margin of the northern sector of the study region. Similar examples of apron integration are evident from the other areas of the northern sector that terminated to form the eastern margin of the study region **(Figure 3.12b-d)**. Several other examples of convergence, divergence and integration of individual flow from one mesa to the other is well illustrated by the expressions on the surface of LDA deposits within the groups of mesas in both the northern and southern sectors of the study region.

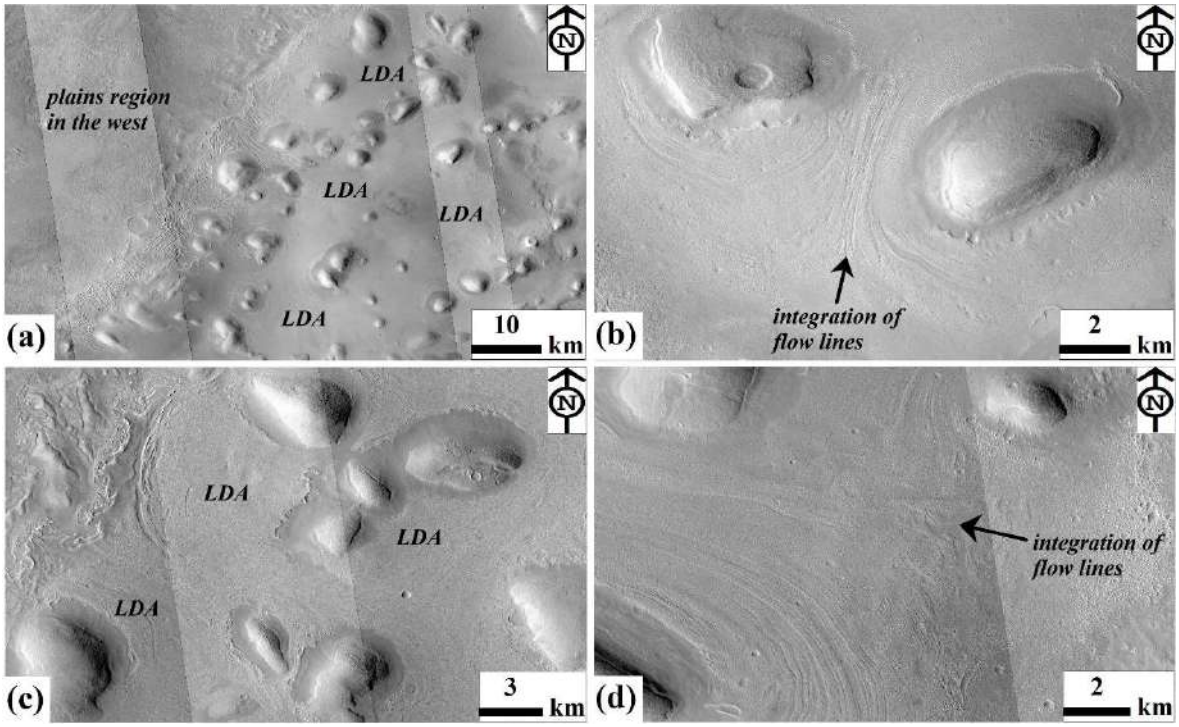

Figure 3.12. (a) CTX view of the integrated LDA over a distance of ~50 km before it terminates to form the western margin of the northern sector of the study region. CTX image P17_007644_2187, B01_010004_2181, P15_006932_2181, B01_009859_2171 and P20_008936_2182; approximate location of image center: 38.02˚ N, 172.76˚ W. (b-d) Close-up CTX views of other example of convergence, divergence and integration of LDA deposits within the study region. (b) CTX image P16_007433_2181; approximate location of image center: 37.86˚ N, 170.96˚ W. (c) CTX image B01_010215_2182 and B01_010004_2181; approximate location of image center: 38.68˚ N, 172.42˚ W.(d) CTX image P15_006932_2181; approximate location of image center: 38.80˚ N, 171.36˚ W. CTX image credit: NASA/JPL-Caltech/MSSS.

3.3.7. Surface texture of LDA deposits

The surface texture related to individual LDA deposits, LDA deposits in grouped mesa-LDA systems, continuous LDA deposits, broad piedmont-like lobe, CCF, and infilled craters comprises complex terrain consisting of irregular pits and buttes, which is described as a texture termed as "brain-terrain" **(Figure 3.13a) (Mangold, 2003; Dobrea et al., 2007; Levy et al., 2010a)**. Both open-cell and closed-cell brain-terrain textures (textures that are commonly associated with CCF, **Levy et al., 2010a**) are evident on the surface of LDA deposits **(Figure 3.13a)**. These textures are arcuate-shaped, wide (at the 10s of meters scale) features, and are more characterized by their pit (open-cell) or mound-like (closed-cell) appearances. We have also noted evidence for relatively low-albedo mantling material overprinting the brain-terrain textures. Interestingly, this mantling material shows little to no evidence of deformation

associated with LDA flow. Morphologic evidence of polygonal thermal contraction cracks is apparent on this low-albedo mantling material **(Figure 3.13b)**.

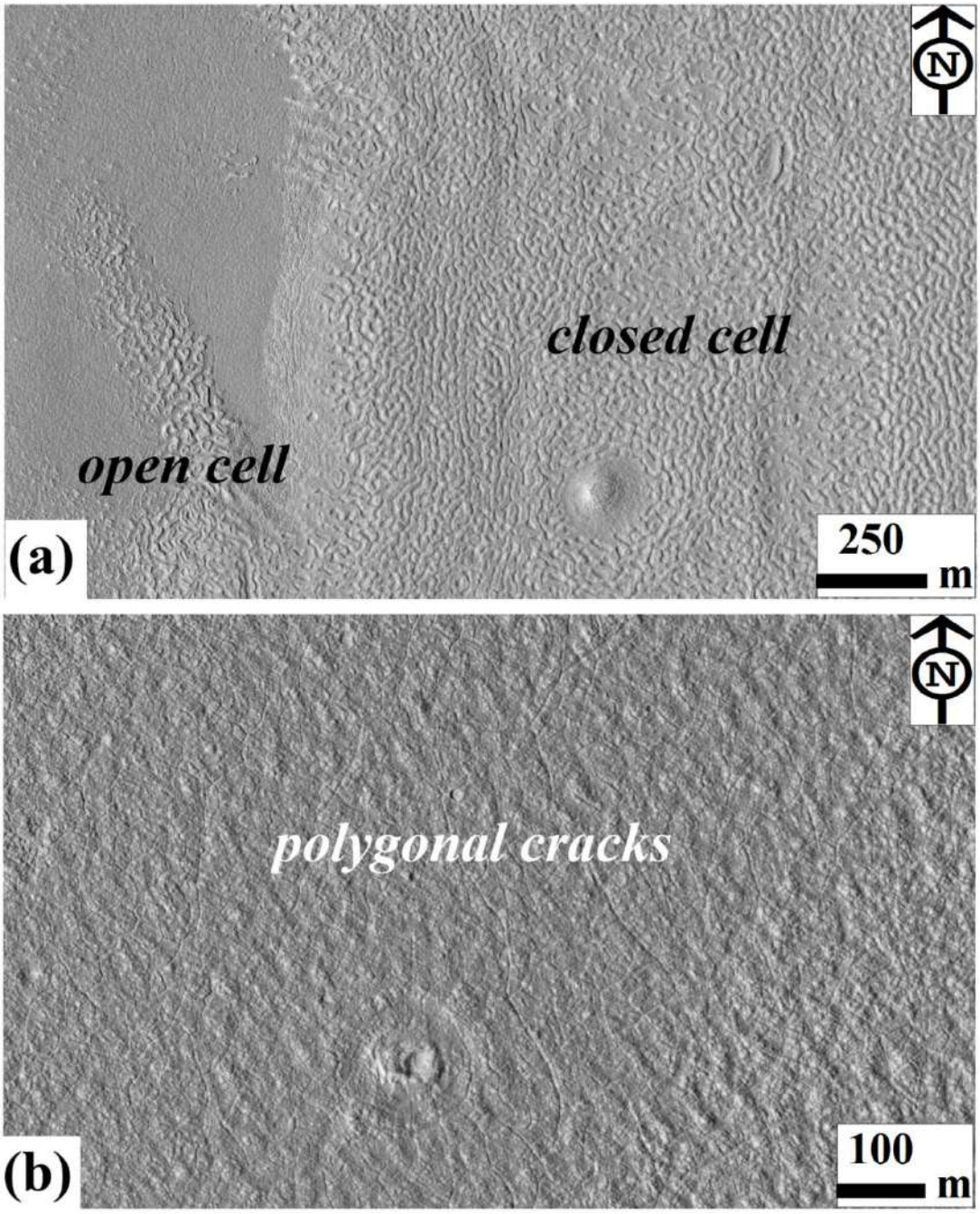

Figure 3.13. (a) Close-up HiRISE view of the brain-terrain texture on the upper surface of LDA deposit. (a) HiRISE image ESP_019063_2185. (b) Close-up HiRISE view of the polygonal patterned LDM surface. HiRISE image ESP_054798_2180. HiRISE image credit: NASA/JPL-Caltech/University of Arizona.

3.3.8. Radar observations

10 radargrams give a good coverage of LDA deposits in both the northern and southern sectors of the study region. We analyzed these radargrams for the identification of potential subsurface interfaces and examined whether the reflections are predicted at the same location in the simulated radargram. Out of these 10 radargrams, we could detect a subsurface signals in only one of the radargrams that covers a LDA deposit in the study region **(Figure 3.14)**. The subsurface reflection cross over or near to a well-preserved LDA, and we have not observed reflections predicted at the same location in the simulated radargram. In general, reflections that are not evident in the simulations are considered probable interfaces (these criteria is used in several studies such as **Plaut et al., 2009; Choudhary et al., 2016** to detect likely interfaces). However, note that this reflector does not split into two interfaces on proceeding from the surrounding plains region to the LDA deposit **(Seu et al., 2007; Plaut et al., 2009).** Moreover, on applying the dielectric constant of 3.15 we could not see the coplanar alignment of the subsurface signal with the surrounding terrain, which further suggests that the distinct subsurface signal may not be consistent with positive detection of water ice and is likely to be a clutter. If the reflection appears flat and aligns with the plains beyond the LDA, then the subsurface material properties are consistent with water ice. We propose that within the study

region: (1) the small size of mesa-LDA systems, the closely spaced mesas/mounds and surrounding LDA deposits, and the extensive network of linear-curvilinear ridges on the LDA deposits may scatter the radar signal, (2) the top and bottom of the subsurface ice are close enough to the surface that the radar does not detect them unambiguously in the swath, and (3) the low-albedo mantling deposits on the LDA deposits may not allow radar signals to penetrate deep enough to detect interfaces. These factors may collectively determine the detection of subsurface water ice in this region. Further, even in the other regions (e.g. Nereidum Montes), if the lobate flows are small in areal extent and in proximity to sloped surfaces that cause radar clutter, the subsurface reflectors may not be detected positively **(Berman et al., 2021)**. Among the previously published works, **Ramsdale et al., 2019** have analyzed 96 observations from SHARAD to report that the northern Arcadia Planitia region is inconsistent with the evidence of extensive radar-based subsurface reflections, with only a few areas showing radar reflectors for subsurface ice in the southern Arcadia Planitia (35-55° N). Furthermore, our observations of the dearth of subsurface signals from the studied LDA deposits are also consistent with the findings of the Subsurface Water Ice Mapping (SWIM) Team that they report real dielectric constants in the range of 4-5 within our study region (e.g. in the northern sector), which is inconsistent with the dielectric value of water-ice **(**see Figure 4 in **Bramson et al., 2019)**. Nevertheless, on a regional basis, widespread excess subsurface ice is present in the Arcadia Planitia region as reported previously from the analysis of subsurface reflections in the radar-sounding data of the terraced impact craters **(Bramson et al., 2015)**. Although, we have not observed terraced craters on the LDA deposits within the study region to further examine their potential in the investigation of buried ice using the radar observations. More recently,

Hibbard et al., 2021 also substantiate the evidence for regional presence of subsurface ice in the Arcadia Planitia **(**see Figure 9 in **Hibbard et al., 2021)**.

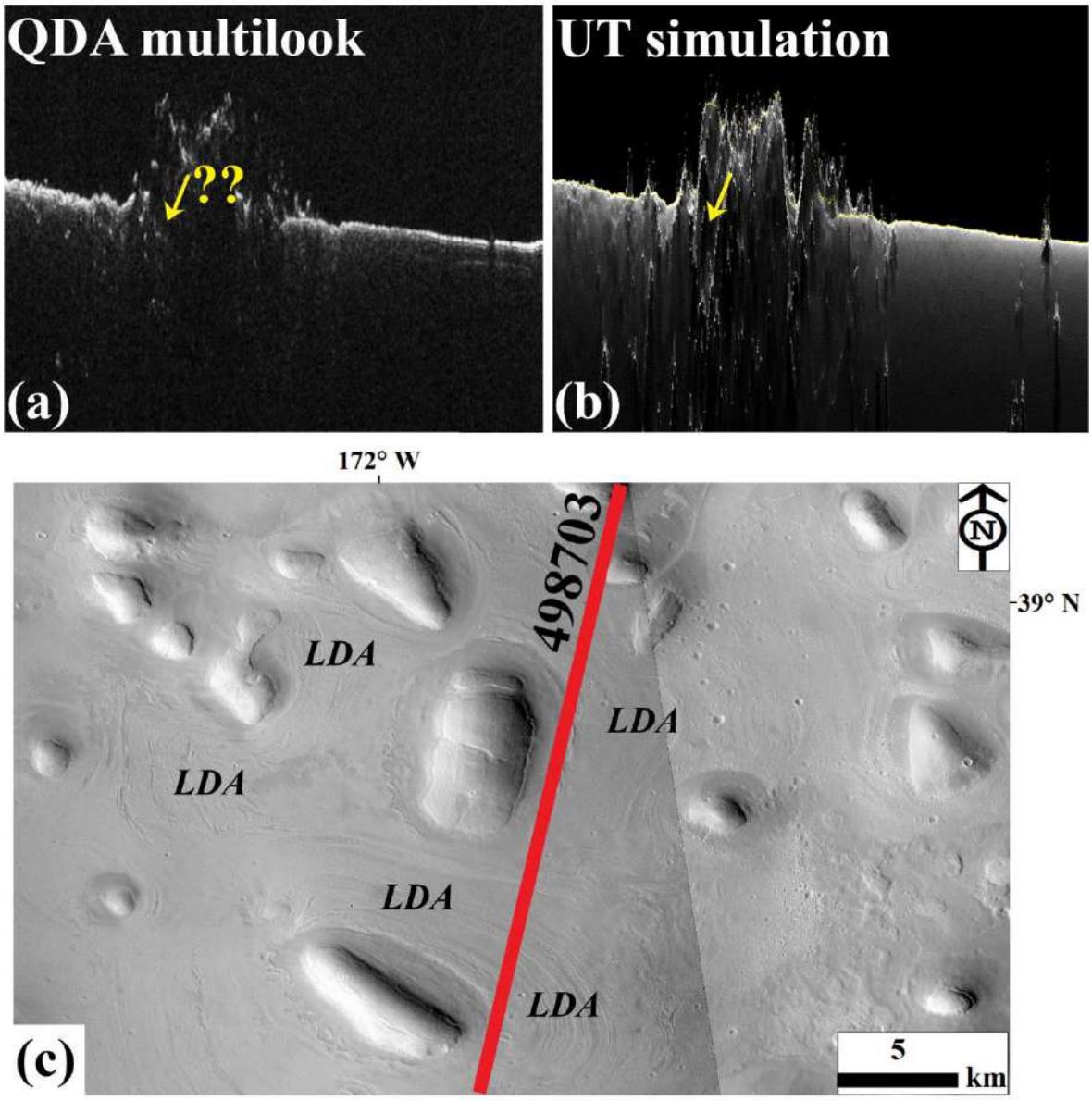

Figure 3.14. (a) Section of SHARAD profile 498703 crossing over the study region. The QDA products are based on the SHARAD processor from the JPL (Jet Propulsion Laboratory, Caltech). For the QDA products, the multi-look bandwidth is fixed to 15 Hz. The position of

the questionable reflector identified in this multi-look is shown by an arrow (yellow). White arrow (shown in (a and c)) indicates the direction of the swath covered by the SHARAD profile. (b) The QDA products used in this study are simulated using MOLA DEM for the purpose of clutter identification. The University of Texas (UT) developed an incoherent facet-based clutter simulator that enables one to distinguish the subsurface reflections from clutter (off-nadir surface returns). We used the CO-SHARPS processing boutique for the purpose of clutter simulation. This questionable reflector (yellow arrow) in (a) is not observed at the same position (yellow arrow) in the clutter simulation. (c) The SHARAD profile is shown in red on the CTX image that shows the location of the LDA at which the questionable reflector appeared in the QDA multilook product.

3.3.9. Age of LDA deposits

In total, we have counted 1746 craters superposed on the mapped LDA deposits in our study region. The crater types recognized over the entire LDA deposits are distributed as: (1) bowl-shaped fresh craters: craters with sharp rims and smooth interiors **(Figure 3.15a)**, (2) bowl-shaped degraded craters: craters with irregular rims but retain smooth interiors **(Figure 3.15b)**, (3) ring-mold craters: craters with complex interior typically surrounded by a rimless, circular moat **(Figure 3.15c)**, and (4) degraded craters: typically bowl-shaped with irregular rims, but which do not maintain smooth interiors **(Figure 3.15d)**. Both the fresh and degraded bowl-shaped craters comprise about 55% of the total crater population. Among this population of all bowl-shaped craters, craters with fresh morphologies constitute around 54% and 46% are consistent with degraded morphologies. The maximum, minimum, and average diameters of

the bowl-shaped craters are 656 m, 12 m, and 70 m, respectively. Ring-mold craters contribute about 30% of all crater populations, with a maximum diameter of 477 m, a minimum of 29 m, and an average diameter of 103 m. The degraded craters account for about 15% of the total crater population, with a maximum diameter of 555 m, a minimum of 26 m, and an average diameter of 109 m.

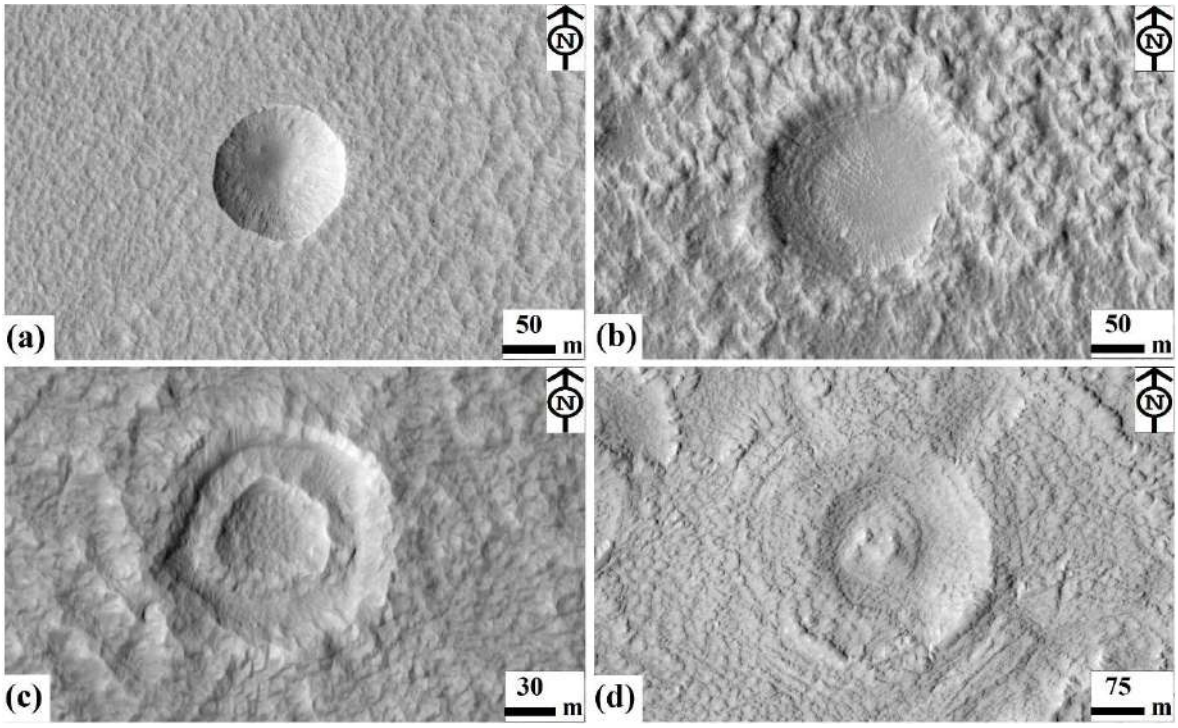

Figure 3.15. Close-up HiRISE view of craters included in the crater count. (a) Bowl-shaped fresh crater. (b) Bowl-shaped degraded crater. (c) Ring-mold crater. (d) Degraded crater. (a) HiRISE image ESP_026223_2185. (b) HiRISE image ESP_052530_2190. (c) HiRISE image ESP_036548_2160 (d) HiRISE image ESP_035203_2155. HiRISE image credit: NASA/JPL-Caltech/University of Arizona.

The total area (16841.3 km^2) over which the crater count is performed is inclusive of the areas covered by the individual LDAs, grouped LDAs, and infilled craters. The area of mesas is excluded from the total area considerations. The maximum and minimum diameter observed for all the craters is 656 m and 12 m, respectively. The average crater diameter is 86 m. The best-fit age determined from the crater counts of all four crater types yields a best-fit age of 30±5 Ma for crater diameter >250 m, and 35 craters in the fitting bin **(Figure 3.16; Table 3.1)**. In the crater size-frequency distribution plot we have noted that there is a downturn in the number of craters per diameter bin per unit area for crater diameter <150 m. This downturn has been attributed as an outcome of the resurfacing of the smallest population of craters (diameter <150 m) typically due to sublimation of ice from beneath the target layers, aeolian erosion or mantling by dust **(Mangold, 2003; Baker et al., 2010)**. **Hepburn et al., 2020** suggest that the downturn at small crater diameters is universally observed in all the CSFDs, which could be also due to the undercounting of craters near the image-resolution limits.

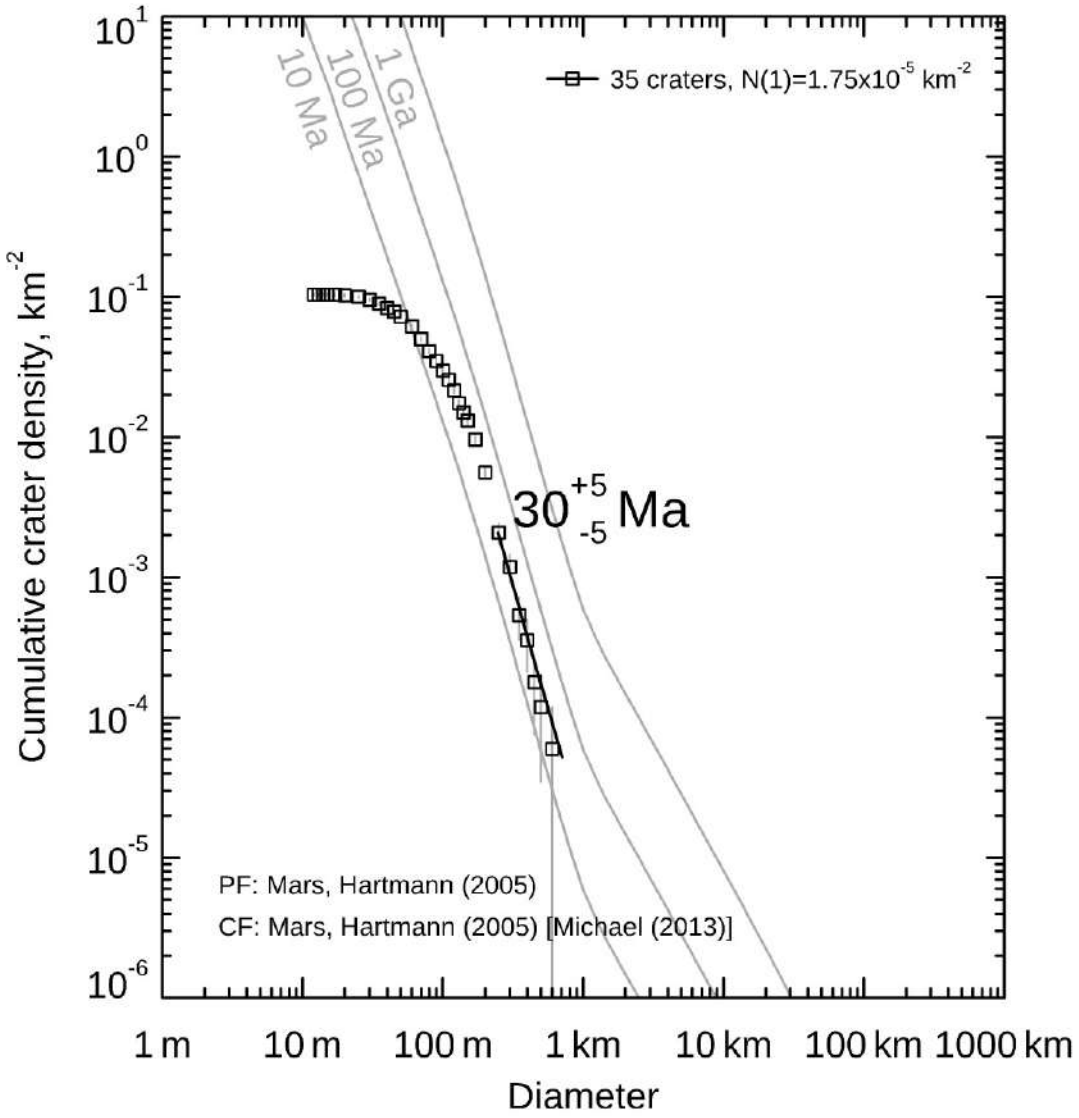

Figure 3.16. Impact crater size-frequency distribution (CSFD) using the entire craters counted on the surface of individual LDAs, grouped LDAs, and infilled craters. The best-fit age is 30±5 Ma for crater diameter >250 m, and 35 craters in the fitting bin. Production function: Mars, Hartmann (2005). Chronology function: Mars, Michael (2013). Note that there is a downturn in the number of craters per diameter bin per unit area for crater diameter <150 m.

Further, with respect to the individual crater morphologies, the best-fit age for crater diameter >150 m vary as: (1) fresh bowl-shaped craters yield a best-fit age of 5.4±1 Ma (28

craters) **(Figure 3.17a)**, (2) fresh and degraded bowl-shaped craters together yield a best-fit age of 14±2 Ma (81 craters) **(Figure 3.17b)**, (3) ring-mold craters yield a best-fit age of 13±1 Ma (82 craters) **(Figure 3.17c)**, and (4) degraded craters yield a best-fit age of 9.7±1 Ma (57 craters) **(Figure 3.17d) (Table 3.1)**. The relatively older age of fresh and degraded bowl-shaped craters in comparison to the fresh bowl-shaped craters is due to the larger number (53 craters) of degraded bowl-shaped craters in the CSFD best-fit plot for crater diameter >150 m. The fresh bowl-shaped craters are nearly two times younger than the ring-mold and degraded craters, which is in agreement with the inferences reported in the previously published papers that the formation of bowl-shaped craters postdates ring-mold craters **(e.g. Baker et al., 2010)**. We also estimated the combined age of the ring-mold craters and the degraded craters and found that together, they are the oldest crater morphologies (23±2 Ma, crater diameter> 150 m, and 139 craters in fit bins) on the LDA deposits.

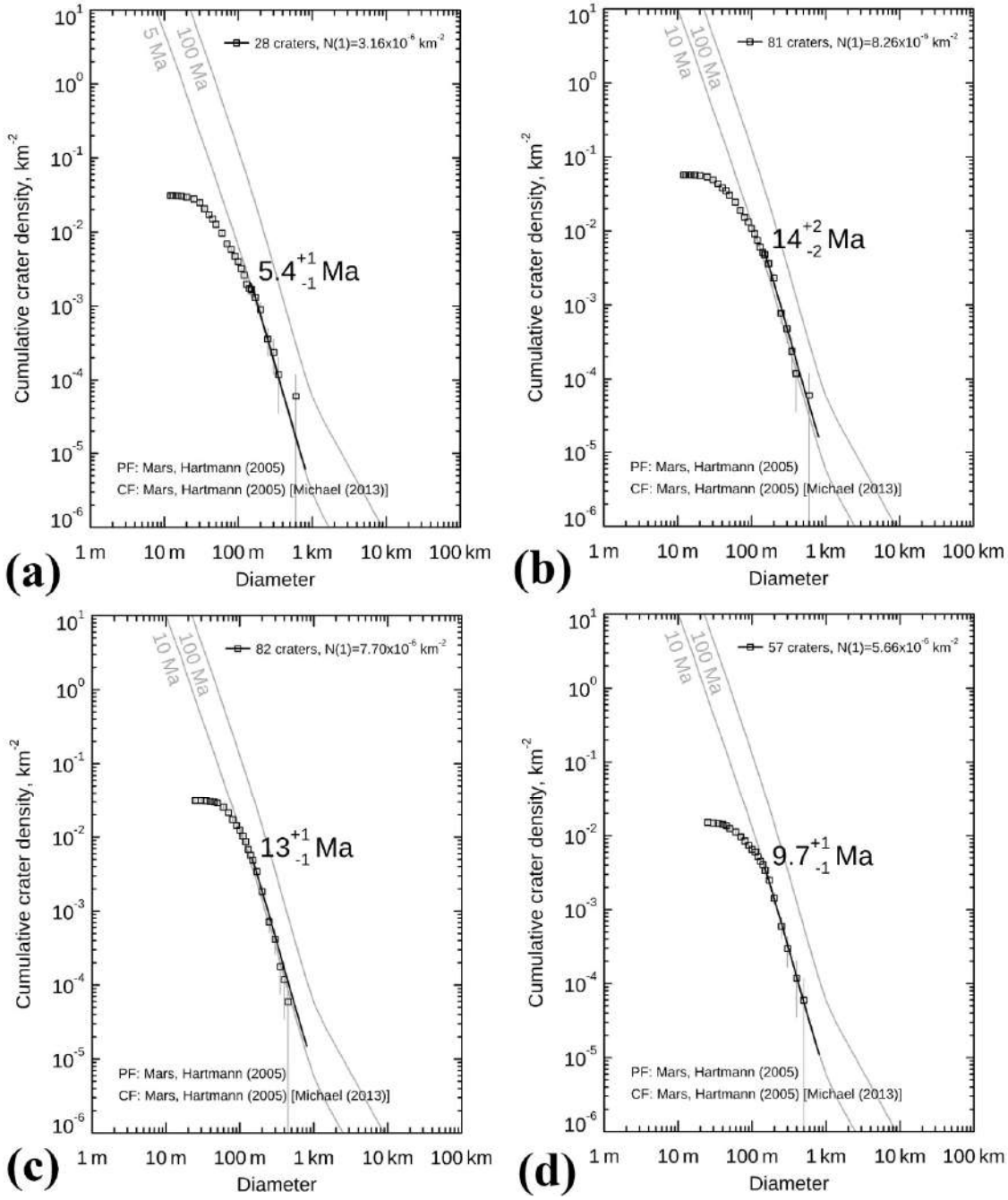

Figure 3.17. Best-fit ages of LDA deposits with respect to the individual crater morphologies and crater diameter >150 m. (a) 5.4±1 Ma for bowl-shaped fresh craters, (b) 14±2 Ma for both fresh and degraded bowl-shaped craters, (c) 13±1 Ma for ring-mold craters, and (d) 9.7±1 Ma for degraded craters.

Table 3.1. Crater count data. The total area of all LDA groups in our study is 16841.3 km^2.

	Best-fit age (Ma)	Age error (Ma)	Min. bin fit (m)	Max. bin fit (m)	No. of craters in fit
All LDA groups	~30	±5	250	656	35
Fresh bowl-shaped craters	~5.4	±1	150	656	28
Fresh and degraded bowl-shaped craters	~14	±2	150	656	81
Ring-mold craters	~13	±1	150	477	82
Degraded craters	~9.7	±1	150	555	57

3.4. Summary of Observations

We have found morphologic evidence of hundreds of LDA deposits surrounding individual mesa, groups of mesas and in the interior of the craters **(Figure 3.3, 3.5, 3.6)**. The LDA deposits are extensive and exhibit integrated flow patterns, convex-upward profiles, and have down-gradient flow directions. These are some of the typical characteristics of LDA deposits along the dichotomy boundary of Mars **(e.g. Chuang and Crown, 2005; Head et al., 2006a, 2006b; Morgan et al., 2009; Baker et al., 2010) (Figure 3.4, 3.9, 3.10, 3.11)**. We found some occurrences of LDA deposits as relatively less extensive because their flow lineations or patterns are less prominent. The LDA deposits show evidence of extensive ridge

networks on their surfaces **(Figure 3.7, 3.8)**. Furthermore, the textures on the surface of LDA deposits are consistent with the evidence of brain-terrain texture and polygonal cracks. Additionally, we found evidence of ring-mold craters superposed on the LDA deposits. These surface textural characteristics and superposed craters on the LDA deposits are common to debris aprons along the dichotomy boundary in the northern mid-latitudes **(e.g. Levy et al., 2009b; Baker et al., 2010; Baker and Carter, 2019a; Berman et al., 2021)**. Our radar observations do not substantiate the presence of extant water-ice preserved in the subsurface of LDA deposits **(Figure 3.14)**. Concentric flows inside a crater (which has been proposed to be genetically related to LDA; **Levy et al., 2010a**) are found in the region **(e.g. Figure 3.5b)**. Additionally, several craters consistent with infilling by lobate/concentric flows up to the rim and subsequent outflow from the breached crater wall portions have been found **(e.g. Figure 3.5a)**. Debris apron extending in the form of a broad piedmont-like flow unit has been found **(Figure 3.10a-b)**. Best-fit ages suggest a relatively younger crater retention age of 30 Ma for the mapped LDA deposits **(Figure 3.16)**. Furthermore, the categorized crater counts based on the morphologies of superposed craters on the LDA deposits revealed that the crater retention age of the fresh bowl-shaped craters is nearly two times younger than the ring-mold and degraded craters.

3.5. Interpretations and Discussions

3.5.1. Extent of Glaciation in the Erebus Montes

The observed flow patterns of integrated systems of LDA deposits within the study region suggest extensive accumulation of ice/snow that resulted in the formation of continuous

flow units for several kilometers **(Figure 3.9, 3.12)**. The (1) flow extent of LDA deposits from the base of the mesa wall **(Figure 3.3)**, (2) formation of a broad piedmont-like lobe and bulged LDA **(Figure 3.10)**, (3) crater infilling and subsequent outflow from the breached crater wall portions **(Figure 3.5)**, and (4) flow from the smaller crater-like feature into a larger crater **(Figure 3.11)**, all indicate an earlier period of significant ice accumulation and glaciation. We have observed extensive networks of linear-curvilinear ridges on the LDA deposits **(Figure 3.7, 3.8)**, which suggests that LDA deposits in the study region may be once more extensive in the past and have undergone significant modification/degradation since their formation. *Hitherto*, our radar investigation did not detect signals corresponding to subsurface ice beneath the LDA deposits in the study region **(Figure 3.14)**. Together, our findings support the results from previous studies carried out elsewhere along the dichotomy boundary that suggest LDA deposits as evidence for the past presence of extensive debris-covered glacial land systems. The lack of evidence for the small-sized lobes superposed on the main LDA deposits indicates that the most recent glacial phases within the study region were likely not characterized by alcove microclimatic conditions of a more limited magnitude and shorter duration.

3.5.2. Evidence for Multiple Glacial Phases

Along the dichotomy boundary, the majority of the glaciated regions have preserved the morphologic evidence for multiple glacial phases of LDA emplacement, typically in the form of a lobate flow unit sourced from alcoves that superposes on the main LDA deposit **(e.g. Levy et al., 2007; Dickson et al., 2008; Morgan et al., 2009; Baker et al., 2010; Hepburn et al., 2020)**. The snout of the superposed lobate flow unit can be differentiated from the main

LDA deposit in the topographic profile as well as in the image with no evidence of merging and/or integration with the main LDA deposit. The material forming this lobate flow unit appears (as inferred from the surface lineations) to have been sourced from the valley headwall alcoves and/or small alcoves in the mesa flanks. The superposed lobate flows have been reported as chronologically younger than the underlying LDA deposits **(Hepburn et al., 2020)**. This has suggested that the superposed lobate flows are from a period of glacial activity that involved a relatively small-scale of ice accumulation and flow than the earlier periods of main LDA formation, thus leading to an idea of multiple phases of glaciation or polyphase glaciation **(e.g. Levy et al., 2007; Morgan et al., 2009; Baker et al., 2010; Hepburn et al., 2020)**. In our study region, we have not observed an evidence for lobate flow unit sourced from the alcoves (in the mesa flanks/walls) and superposed on the main LDA deposit **(Figure 3.6)**. We have observed flow units from adjacent mesas that show evidence of merging, convergence, and integration, but the evidence that the flow units I sourced from alcove in the mesa flank/wall and superpose the main LDA is not evident. The flows that comprise the main LDA have originated directly from the mesa flanks (as inferred from the lineations on the surface of the main LDA) **(Figure 3.3, 3.9)**. We find this observation to be consistent with another study that showed no reliable identifications of superposed lobate flow units within the entire Arcadia Planitia region **(Ramsdale et al., 2019)**. **Hepburn et al., 2020** have reported only one superposed glacial-like flow (SGLF) in our study region; however, this SGLF does not appear to have been sourced from alcoves in the mesa walls. This observation is interesting as it implies that the study region lacks evidence for a less extensive glacial phase – a phase defined by the observational evidence for formation of minor LDA and lobes confined to alcoves and

superposed on the main LDA deposits along the dichotomy boundary. If this is indeed the case, it could also mean that glacial modification in the study region has not occurred in multiple stages, i.e. glacial stages were not facilitated by the alcove microclimatic conditions. Although, we acknowledge the possibility that LDM is expected to cover the flow lineations on the LDA deposits and therefore may diminish or subdue the evidence of superposition or contact of a raised lobe or moraine like ridge. This can contribute in indistinguishing the lobate flow units sourced from alcoves and superposed on the main LDA deposits.

3.5.3. Mantling and Modification of LDA Deposits

Investigation of the surface texture of LDA deposits have revealed that a large number of surface units are consistent with complex terrains consisting of pits and buttes, which is more commonly referred to as a texture termed 'brain-terrain' **(e.e. Mangold, 2003a; Levy et al., 2009b; Morgan et al., 2009; Baker and Carter, 2019a, 2019b; Berman et al., 2021)**. The formation of this texture has been attributed to the significant loss of ice through differential sublimation **(Mangold, 2003a; Levy et al., 2009b; Baker and Carter, 2019a)**. A low-albedo polygonized mantling material is found to be usually associated with or in contact with the brain-terrain texture. **Levy et al., 2009b** found that the mantling material usually postdates the brain-terrain texture by ~10 to 100 Ma. They further explain the age difference by proposing that the brain-terrain textures are from ice deposited during the periods of peak glaciation that ended at ~10-100 Ma and the polygonal cracks are from a recent ice age period of ~1-2 Ma **(Levy et al., 2009b)**. Such a contact between brain-terrain and polygonized mantle in the Deuteronilus Mensae region has been analyzed more recently by **Baker and Head, 2015.**

They also noted that the polygonized patches of the upper plains are being dissected into brain-terrain textures. These observations make clear that the textures formed on the LDA deposits are within the upper plains emplaced more recently on the LDA deposits, and that the textures are a combined product of dissection and modification of the upper plains. This particular observational evidence of combined occurrence of brain-terrain texture and polygonized mantle material has been utilized as the primary evidence to show that the surfaces of lobate deposits have been extensively modified by superposed LDM (i.e. upper plains) undergoing differential sublimation and subsequent aeolian erosion **(Mangold, 2003a; Baker and Head, 2015; Berman et al., 2015)**. In our study, we have found extensive modification of the upper surface of LDA deposits in form of textures akin to brain-terrain and polygonal cracks **(Figure 3.2, 3.13)**. Brain-terrain texture and polygonal cracks have been observed in a manner that the polygonized material overprints the brain-terrain texture. We interpret this material on the upper surface of LDA deposit as the LDM material reported to have been deposited repeatedly throughout the Middle to Late Amazonian to as recently as ~0.1 Ma **(Mustard et al., 2001; Head et al., 2003; Schon et al., 2009; Madeleine et al., 2014)**. We have noted that the LDM drape almost all the LDA deposits within our study region. Our observations and interpretations are consistent with the consensual hypotheses for brain-terrain and polygonal crack formation, which include an initial process of thermal contraction that formed polygons and later undergoes subsequent modification by the differential sublimation mechanism to form brain-terrain texture **(Levy et al., 2009b; Baker and Head, 2015)**.

Further adding to the evidence of LDM in the region, we have observed ring-mold crater morphologies on the surface of LDA deposits **(Figure 3.15c)**. Previously, **Kress and**

Head, 2008 interpreted that the ring-mold craters are relatively larger impacts than the circular bowl-shaped craters, and they proposed that the larger impacts were large enough to impact into and excavate the glacial ice-rich material below from the subsurface of LDA deposits. The impacts on the ice-rich targets and their subsequent modification led to a wide range in the morphology of ring-mold craters **(Kress and Head, 2008)**. However, this hypotheses proposed by **Kress and Head, 2008** has been recently tested and it was found that (1) the magnitude of difference in the size of ring-mold and bowl-shaped craters are too small to account for the morphological difference among them, (2) the original diameter of the ring-mold craters were likely smaller than their present state due to the fact that there is abundant observational evidence of erosion and expansion of the rim of ring-mold craters, and (3) the excavation depths of ring-mold and bowl-shaped craters are quite small to cause a dramatic difference in the crater morphologies **(Baker and Carter, 2019a)**. Furthermore, it was noted that crater morphologies resembling ring-mold craters also form over the non-LDA deposits **(Baker and Carter, 2019a)**. As a result, the formation of ring-mold craters is hypothesized to be more related to the cyclic deposition of LDM and their subsequent degradation, a formation mechanism more similar to the previous interpretations that suggested ring-mold craters is the modification of bowl-shaped craters by post-impact deposition and sublimation of ice-rich mantle **(Mangold, 2003a; McConnell et al., 2007; Berman et al., 2007)**.

In our study, from the measurement of superposed craters on the LDA deposits, we have found that the maximum diameter of the fresh bowl-shaped craters (656 m) is relatively higher than that of the ring-mold craters (477 m). Actually, we found that the bowl-shaped craters and ring-mold craters follow similar diameter distribution trends. Additionally, we found that the

spatial distribution of bowl-shaped craters (total: 521 craters) and ring-mold craters (total: 526 craters) are nearly alike. Taken together, based on these observations it is difficult to envisage a scenario that indicates a likely link between the ring-mold craters and the glacial ice-rich material underneath LDA deposits. Therefore, we agree with the findings from recent studies that proposed that the formation of ring-mold craters is more likely by the deposition and erosion of the ice-rich mantle units that superpose the LDA deposits in our study region **(Baker and Carter, 2019a)**. All in all, brain-terrain, polygons, and ring-mold craters, add to the evidence of LDM that underwent differential sublimation and erosion resulting in the modification of LDA deposits in our study region.

Additionally, we have found that the LDA surfaces within the study region are extensively dominated by raised linear-curvilinear ridges **(Figure 3.7 and 3.8)**. Similar to the brain-terrain texture and polygonal cracks, these ridges are also formed in the upper surface draped on the LDA deposits. Although, we found that the ridges are not simply on the surface of LDA deposits but they are (1) aligned to the LDA terminus, (2) evident throughout on the LDA surface and (3) commonly found at the interface between the smooth (dark albedo) unit adjacent to the mesa wall and the LDA surface. Isolated ridges as well as networks of ridges are found to be common within the study region. Similar ridges have been observed on the upper surface of dichotomy boundary LDAs and have been interpreted as ribbed upper plains unit **(Baker and Head, 2015)**. **Baker and Head, 2015** interpreted that the ribbed upper plains unit comprised of ridge and furrow patterns as a representation of the various forms of preservation and modification of the debris apron surface. They proposed sublimation of pore ice at fracture planes as the cause of the widened depressions or troughs within the ribbed upper

plains. In our study, we have observed that the ridges are very well aligned in the direction of the lineations observed on the LDA surface. In some cases, ridges can be also traced as the LDA margin **(e.g. Figure 3.7a)**. Additionally, the individual ridges are consistently above the elevation of the valley surface, and the two adjacent ridges often border collapsed depressions. These morphological characteristics clearly demonstrate that the ridges are three-dimensional structure because a surface-only structure could not withstand in this manner **(e.g. Glasser et al., 2015)**. Based on our observations, we interpreted the ridges as the remnant of the internal flow lineations, and that they are most likely preserved by the sublimation of debris-rich ice. We propose that sublimation has removed ice from the subsurface, leading to surface collapse and formation of depressions. These depressions are typically enclosed by ridges on the surface of LDA **(Figure 3.7, 3.8)**. The size and depth of the depressions as well as the width of ridges may vary based on the presence of ice in the LDM layers. Given the fact that there is a ubiquitous presence of ridges in the study region **(Figure 3.7, 3.8)**, we suggest that the surfaces of LDA deposits in the study region are extensively modified. Therefore, if our interpretation that the ridges enclosing the collapsed depressions on the surface of LDA are from sublimation of debris-rich ice is correct, then it implies that the study region has lost a large amount of buried ice from the subsurface. Previous studies have also interpreted ridges/furrows and depressions on the LVF at the dichotomy boundary as an evidence for loss of subsurface ice as a result of ice sublimation because of thinning of debris cover or changes in the climatic environment **(van Gasselt et al., 2010)**.

3.5.4. Localized Flow and Glaciation

Accumulation of ice/snow on the interior crater walls has led to localized flow and deposition of glacial landforms on the floor of the crater. The landform evidence have been most prominently presented from craters with concentric flows (viz. CCF – **Levy et al., 2010a**), craters with lobate deposits on the floor (**Sinha and Vijayan, 2017; Conway et al., 2018**), infilled craters, and flow from one crater to the other proximal crater **(Dickson et al., 2010)**. In the Erebus Montes region we have found evidence for (1) concentric flows inside a crater, as inferred from the concentric ridges on the crater floor **(Figure 3.5b)**, (2) flows from a smaller crater-like feature to a larger crater **(Figure 3.11)**, and (3) infilling and outflow from craters **(Figure 3.5a)**. We have found topographic evidence for downslope flow lineations presented by downslope trending ridges within these craters to interpret evidence of localized ice accumulation and flow. In the case of flow from a smaller crater-like feature to a larger crater **(Figure 3.11)**, the downslope flow lineations terminated as a snout-like feature on the floor of the larger crater, similar to terrestrial glaciers. This led us to consider that the smaller crater-like feature possibly acted as a localized trap of accumulated ice deposits where the downslope topography guided the flow of ice-rich material into the larger crater. In the case of CCF and infilled craters, we interpret that ice accumulated locally on the interior walls of the crater to result in flow and deposition on the crater floor. Infilled craters are the ones that were more dominated by relatively extensive flows resulting in infilling of the crater up to the rim and overtopping to flow outside the crater as indicated by the breached rim of some of the craters. Although infilling of the crater up to the rim could be also dependent upon the diameter of the crater as well. We infer the CCF ridges on the crater floor to be representative of glacial activity in the region that facilitated ice accumulation and flow from all directions of the interior crater

wall. This crater has not undergone complete infilling up to the rim and possibly hosts LDM on the surface of crater filling units as suggested by the presence of ring-mold craters. Another example of localized flow and glaciation is observed in the walls of a large massif that deposited a piedmont-like lobe in the downslope **(Figure 3.10a-b)**. The formation of piedmont-like flow lobe is an example of a glacial activity that facilitated extensive ice accumulation and flow in one place (within a broad alcove in the mesa wall) than the regional LDA formation along the mesa walls.

3.5.5. Comparison between Flow Patterns of LDAs in Erebus Montes and along Dichotomy Boundary

The mapped LDA deposits have showed evidence of flow lineations compressing, narrowing, broadening, bending, looping and coalescing down-slope to form a single, large entity **(Figure 3.9)**. These flow patterns are similar to dichotomy boundary LDA deposits formed by the flow of debris-covered glaciers **(e.g. Baker et al., 2010)**. However, the flow lines and patterns are not as prominent as they are on some of the isolated massif LDA along the dichotomy boundary **(e.g. Morgan et al., 2009; Baker et al., 2010)**. The small height of mesas and large extent of LDAs mapped within the study region substantiates extensive (1) shedding of debris from mesa steep walls and (2) accumulation of ice/snow to create debris-covered glaciers that flowed down-gradient to form integrated glacial systems. Crater interior LDA within the study region occupy entire crater interior in most of the cases, however, the flow lines are not as prominent as the main LDA deposits mapped within the study region. The evidence of down-gradient flow pattern is not always present in the infilled craters **(Figure**

3.5). These infilled crater related flow patterns are in line to the dichotomy boundary infilled craters with LDA. One occurrence of CCF identified in the southern sector of the study region groups into the broad category of crater confined glaciation recognized over a large portion of Mars within the mid-latitudes **(Figure 3.5b)**. We have not observed an evidence of flowlines emerging from small alcoves in the mesa flanks/walls. As a result, the study region lacks evidence of small lobes sourced from alcoves to superpose the main LDA in the down-slope. The down-slope flow of LDA from one small crater to a large crater does not fall in any of the defined LDA flow pattern classifications, whereas it mainly represents the influence of localized glaciation within a region of Mars than any process that can be related to the dichotomy boundary LDA. This sequence of flow among proximal craters is more similar to that interpreted from the study of **Dickson et al., 2008** along the dichotomy boundary and **Dickson et al., 2010** at the Phlegra Montes. We have also found topographically controlled integrated flow patterns showing formation of a broad piedmont-like flow lobe within the study region **(Figure 3.10a)**. In this case, the parallel walls of the mesa acts as an obstacle to the down-slope flow, where they converge laterally instead of expanding, and flow through a low-point to create a piedmont-like lobe. This type of deposit is observed at a few locations along the dichotomy boundary **(e.g. Head et al., 2010)**.

3.5.6. Probable Period of Glacial Activity in the Region

We infer the age of glacial activity in the region by first discussing the robustness of the dating results in our study. We discuss this concerning the parameters in the CSFD fitting, i.e. the fitting range in diameter of the craters and the number of craters used in determining

the age of the LDA deposits. Previously, **Baker et al., 2010** and **Morgan et al., 2009** estimated the ages of the LDA and LVF deposits along the dichotomy boundary. They found (1) 90 Ma (total area: 12, 929 km^2, crater diameter > 250 m, number of craters in fit bins: 75) for LDA and LVF in the north of Ismeniae Fossae **(Baker et al., 2010)** and (2) >100-500 Ma (total area: LDA extending for ~190 km, crater diameter >250 m) for LDA and LVF in the Deuteronilus Mensae region **(Morgan et al., 2009)**. In both these studies, craters smaller than 150 – 250 m in diameter were observed to have undergone resurfacing, therefore ages were estimated using craters larger than 250 m. In our study, we have also noted that the craters smaller than 150 m show evidence of resurfacing, as inferred from the downturn in the crater distribution plot. This justifies why we have used craters larger than 250 m for deriving the ages of the mapped LDA deposits in our study. Subsequent to these two studies, **Berman et al., 2015** estimated the ages of the LDA deposits in the Deuteronilus Mensae region. **Berman et al., 2015** have not used craters larger than 250 m to derive the age; instead, they extracted the diameter range of craters from a 'fit segment' that paralleled the isochrons **(Hartmann, 2005)**. **Berman et al., 2015** derived best-fit ages of (1) 1100 Ma (total area: 3513 km^2, crater diameter range 500 – 1000 m, number of craters in fit bins: 19) and (2) 300 Ma (total area: 1600 km^2, crater diameter range: 250 – 500 m, number of craters in fit bins: 25), for two apron complexes in the Deuteronilus Mensae region. More recently, **Hepburn et al., 2020** derived the ages of the LDA/LVF deposits in the Deuteronilus Mensae region. They have reported best-fit age of ~70 Ma (total area: ~806 km^2, crater diameter range: 95 – 250 m, number of craters in fit bins: 66) for the LVF in the region. In our study, we have derived the ages of the mapped LDA deposits (total area: 16841.3 km^2, total craters: 1746) to be around 30 Ma (between 10-100 Ma) using a crater diameter

range of 250 – 656 m, and 35 craters in the fitting bin **(Figure 3.16)**. Based on these statistics we have some confidence that the derived ages reported in this study are comparable to the previously published age estimates. In terms of the counting area in our study; the counting area is large enough in comparison to the counting area of the previous studies. Additionally, the number of craters in the fit bins is comparable to the number of craters in the fit bins used to estimate the ages of the LDA deposits in the previous studies. The fitted diameter range was chosen to cover the data points that form the lower part of the plot to ensure that we are not estimating the age of the resurfaced craters over the LDA deposits. Also, note that the best-fit ages reported here are the minimum ages because it is suggested that debris layers form late in the formation of stagnant ice masses with supraglacial debris, which allows the preservation of craters **(Fastook et al., 2014; Hepburn et al., 2020)**. Therefore, it is reasonably fair to suggest that the ~30 Ma age estimated for the mapped LDA deposits in our study may represent the minimum age and not the true formation age of the LDA deposits. Furthermore, we should keep in mind that these ages are largely dependent on the preservation extent of the craters after the resurfacing period. Therefore, all ages reported herein are the crater retention ages of different crater morphologies over the mapped LDA deposits. Therefore, we suggest that the age of the mapped LDA deposits in our study should be better represented by a broad age range of ~10-100 Ma than one age of 30 Ma.

3.5.7. Influence of LDM on Glacial Activity in Erebus Montes

From our observations, we have noted that the study region hosts LDA deposit of a younger age but lacks an evidence for glacial flows (emanating from alcoves) and superposed on the main LDA deposit. This is not consistent with the previous studies reporting small

superposed lobes originating from alcoves in the mesa walls along the dichotomy boundary **(e.g. Levy et al., 2007; Morgan et al., 2009; Baker et al., 2010; Hepburn et al., 2020)**. Smaller lobes superposed on the main LDA deposits have been used to represent evidence for a younger, less extensive glacial period that was constrained by the accumulation of ice/snow. In addition, younger ages have been estimated for the superposed lobes on the regional LDA deposits, providing further suggestions for a later, less extensive glacial episode. So, if the less extensive glacial episodes during the younger periods (10-100 Ma) have not formed superposed lobes, what do the younger ages of the mapped LDA deposits represent in our study? Our comprehensive analysis of crater morphologies and crater size-frequency distributions on LDA deposits suggests that LDM was repeatedly emplaced and modified during the past several to tens of Ma during the Late Amazonian. This interpretation is based on the difference in the crater retention age of the bowl-shaped craters (~5 Ma) and the ring-mold craters (~13 Ma) **(Figure 3.17a, c)**, wherein, the bowl-shaped craters are those that are not modified by the mantle layers and the ring-mold craters are the ones largely modified by the mantle layers **(Baker and Carter, 2019a)**. These crater retention ages record the periods of LDM emplacement much prior to the most recent period of LDM emplacement (i.e. <2 Ma) **(Mustard et al., 2001; Head et al., 2003)**. This may also mean that the surface modification by thermal contraction, differential sublimation and erosion of LDM draped on the LDA deposits were undergoing since the past several to tens of Ma, as revealed by the extensive brain-terrain texture and polygonal cracks observed on the surface of LDA deposits in our study region **(Baker and Carter, 2019a; Berman et al., 2021)**. Note that the emplacement of LDM on the apron surface and their subsequent degradation will also result in filling, burial and

removal of both fresh and degraded craters as a function of the thickness of the emplaced mantle **(e.g. Berman et al., 2015; Baker and Carter, 2019a, 2019b)**. Therefore, we suggest that the derived best-fit age of the ~30 Ma for the LDA deposits indicates age of the debris apron that has been mantled. Bowl-shaped craters reveal the youngest ages of ~5 Ma, which is likely the ages of recent LDM deposits.

3.5.8. Nature of Climate in Erebus Montes

The thermal state of the Martian glaciers that formed and evolved along the dichotomy boundary has been most prominently cold-based. A large number of published papers report that the LDA deposits are consistent with cold-based glacial behavior as their surfaces do not show evidence of landforms from glacial melt water for the interpretation of wet-based glacial activity (for example, an esker as shown in **Gallagher and Balme, 2015; Gallagher et al., 2020; Butcher et al., 2020**). Within the study region, there is no evidence for glacial meltwater-related distributary features or deposits to relate to any wet-based glacial activity. Therefore, we interpret the observed LDA deposits to be consistent with cold-based glacial behavior, similar in nature to that proposed for glacial features along the dichotomy boundary **(e.g. Li et al., 2005; Head et al., 2005, 2006a, 2006b, 2010; Fastook et al., 2014)**. In the cold-based glacial environment, the temperature of the LDA deposit is below the pressure melting point and the deformations within these features occur internally. With the change in climatic conditions (i.e. the change in ice/snow accumulation extent – waning stages of glaciation) within a cold-based glacial system, the development of sublimation till would take place as a product of the shedding of debris from the mesa flanks **(Fastook et al., 2014; Baker and Head,**

2015). The evidence of extensive ridges **(Figure 3.7, 3.8)**, brain-terrain texture and polygonal cracks on the surface of LDA deposits **(Figure 3.13)**, and the lack of ice melting-related features, support the existence of the sublimation process within the study region.

3.6. Evolutionary History of Erebus Montes

The study region is a part of the Hesperian and Noachian transition unit (HNt) primarily composed of Noachian-aged volcanic deposits and Hesperian-aged mass-wasted materials **(Tanaka et al., 2014)**. Given the likelihood that Mars' Late Amazonian glaciation may have been more extensive in the past, it is possible that a regional ice sheet might have previously formed in the study region if the region was in net accumulation **(e.g. Madeleine et al., 2009; Morgan and Head, 2009; Dickson et al., 2008, 2010; Fastook et al., 2011, 2014; Baker and Head, 2015; Ramsdale et al., 2019; Hibbard et al., 2021)**. This ice sheet would have completely buried the underlying terrain **(Figure 3.18a – Stage 1; e.g. Madeleine et al., 2009; Head et al., 2010; Fastook et al., 2010, 2014; Baker and Head, 2015)**. In stage 2 **(Figure 3.18b)**, as the environment changed from an accumulating environment to an ablating environment **(e.g. Fastook et al., 2014; Baker and Head, 2015)**, the regional ice sheet would have collapsed primarily through sublimation **(Stage 2; Figure 3.18b)**. The collapse would have resulted in the exposure of bedrock scarps/mesa flanks from where dust-rich sublimation till layer and the LDA deposits have formed **(Stage 2; Figure 3.18b)**. The subsequent retreat of the ice sheet would have continued during an ablating environment, down-gradient glacial flow and debris apron formed from extensive erosion and down wasting of the bedrock scarps/mesa flanks **(Stage 3; Figure 3.18c)**. Additionally, in stage 3, the dust-rich sublimation

till layer integrated with the debris aprons would have also thickened. By stage 3, glacial ice accumulation likely ceased, and the debris apron observed in the study region was largely formed. Our observations suggest that the linear-curvilinear ridges possibly began to form at this stage 3 **(Figure 3.7, 3.8)**. In stage 4, a thick LDM unit was emplaced all over the study region **(Figure 3.18d; e.g. Bramson et al., 2015; Ramsdale et al., 2019; Hibbard et al., 2021)**, which we interpreted as the upper surface of the LDA deposits. This LDM unit would have likely covered the extensive flow lineations within the main LDA deposits in the region. Observational evidence for LDM over and within the spacing between ridges is also evident **(Figure 3.8)**. The LDM was subjected to compressional stresses and thermal contraction that led to the development of the polygonal fractures in the upper surface of the debris apron in the study region **(Stage 5; Figure 3.18e, 3.13b)**. Subsequent to this, in stage 6 **(Figure 3.18f)**, the fracturing facilitated further erosion and differential sublimation of the upper surface leading to brain-terrain surface texture formation, as observed in the study region **(Figure 3.13a)**. Note that craters of varying diameters formed during stage 5 and 6 have undergone degradation due to impact into these LDM layers. These craters show morphological characteristics akin to ring-mold and degraded craters reported elsewhere in the northern mid-latitudes along the dichotomy boundary **(Figure 3.15c, d)**. The crater retention age of the bowl-shaped craters reveal that the emplacement of the LDM layers likely ceased around ~5 Ma **(Figure 3.17a)**, although the most recent deposition in the northern mid-latitudes is proposed to have occurred as recently as past ~0.1 Ma **(e.g. Mustard et al., 2001; Head et al., 2003; Schon et al., 2009)**.

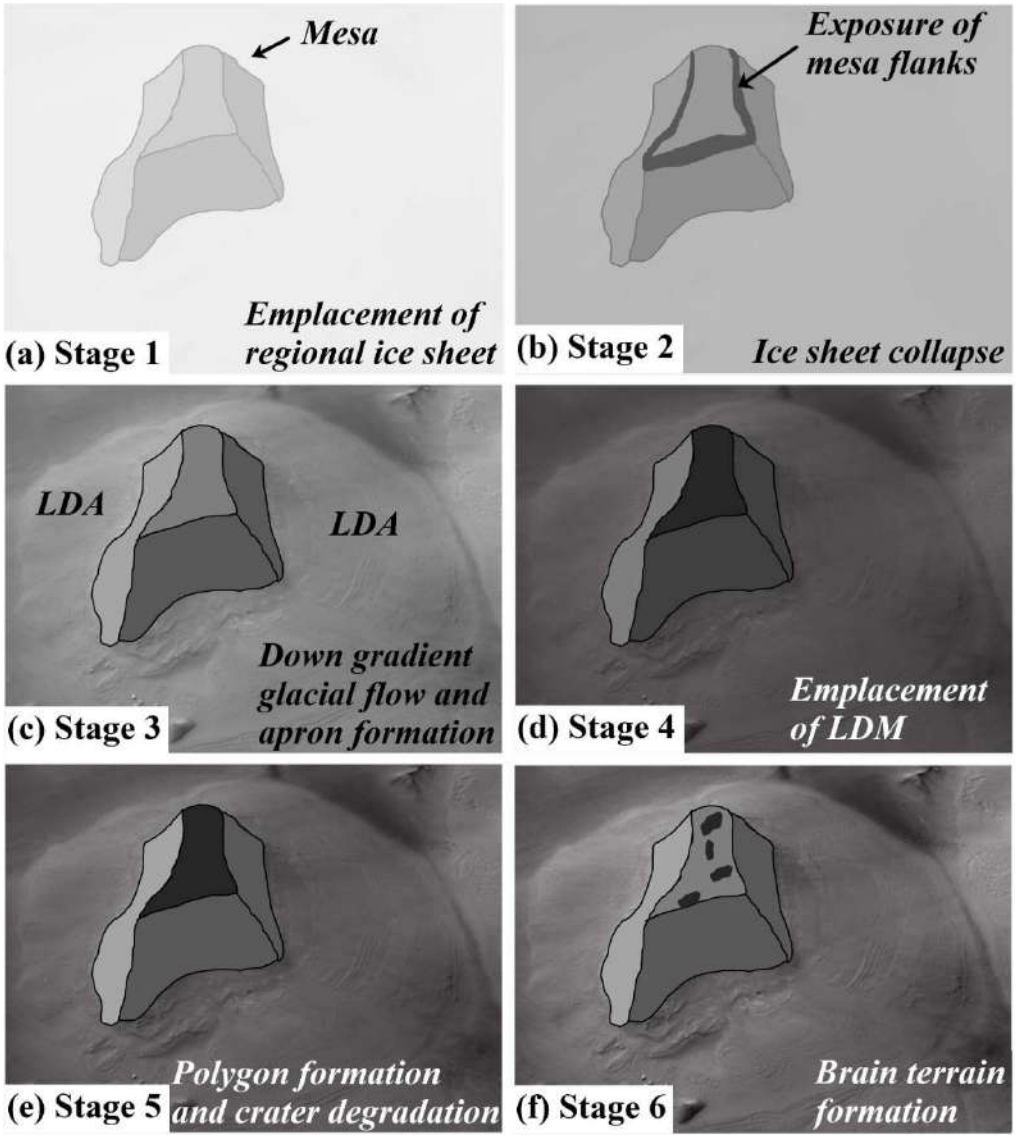

Figure 3.18. Schematic evolutionary history for the Erebus Montes region. (a) Stage 1: Emplacement of regional ice sheet over a period of net accumulation. (b) Stage 2: Collapse of ice sheet primarily by sublimation during an ablating environment. Eventual exposure of bedrock scarps/mesa flanks. (c) Stage 3: Subsequent ice sheet retreat, down gradient glacial flow, and apron formation. Glacial ice accumulation ceased. Linear-curvilinear ridges began to form on apron surface. (d) Stage 4: Emplacement of LDM. (e) Stage 5: Onset of compressional

stresses and thermal contraction leading to polygonal crack formation in the LDM. Degradation of the superposed craters on apron surface. (f) Stage 6: Subsequent differential sublimation of the thermally contracted upper surface of apron leading to brain terrain formation. Retention of bowl-shaped craters on the apron surface.

3.7. Key Findings

We have mapped and examined 236 individual mesa-LDA systems, 84 groups of mesa-LDA systems, and 7 craters infilled with ice-related flow units within the Erebus Montes region in the northern mid-latitudes of Mars. The observations reported in this study present evidence for extensive glaciation in the westernmost glaciated region of Mars, which is also located far away from the typically glaciated regions along the dichotomy boundary in the northern mid-latitudes. The study region hosts LDA deposits that show convex-up, steep terminus topographic profiles consistent with down-gradient flow characteristics, and are consistent with surficial evidence of flow lineations and patterns akin to the glacial landforms that have been previously noted along the northern dichotomy boundary. The observational evidence for broad piedmont-like lobe, down-gradient flow from one crater to the other (possible oblique impact crater), craters consistent with concentric flows lines, and evidence of infilling and subsequent outflow from the breached portions of the crater wall, are all indicative of more focused localized flow and glaciation. The study region lacks the morphological evidence for lobate flow units emanating from small alcoves in the mesa flanks/walls and superposed on the main LDA deposits - which might also suggest that glaciation in the study region, was not facilitated by the alcove microclimatic conditions. However, visual evidence of extensive LDM is

ubiquitous, which might cover the flow lineations on the LDA deposits and therefore may diminish or subdue the evidence of superposition or contact of a raised lobe or moraine-like ridge. The observational evidence of extensive linear-curvilinear ridges provides some clues to the loss of buried ice as a result of sublimation from beneath the LDA deposits. Brain-terrain texture, polygonal cracks, and ring-mold craters collectively substantiate the morphological evidence for the deposition of LDM within the study region during the past several to tens of Ma in the Late Amazonian. The subsequent removal of LDM led to the extensive modification of the LDA deposits in the study region. *Hitherto*, radar observations do not provide substantial evidence for the presence of extant ice in the LDA deposits in this region. The surface texture and morphologies associated with the mapped LDA deposits examined here are found to be more consistent with the cold-based glacial behavior, similar in nature to that proposed for glacial features along the dichotomy boundary. Using crater dating, we estimate a best-fit age of ~30 Ma (for crater diameter >250 m) for the mapped LDA deposits in the study region. We interpret this young age as the crater retention age and suggest that this age better represents the age of the upper surface of the apron surface. As a result, we propose that the glaciation in the study region should be better represented by a broad age range of ~10-100 Ma (Late Amazonian). Together, our findings support the results of previous studies carried out elsewhere along the dichotomy boundary that find evidence for the past presence of extensive debris-covered glacial landsystems in the northern mid-latitudes of Mars.

CHAPTER 4

Global documentation of overlapping lobate deposits in Martian gullies

Failure will never overtake me if my determination to succeed is strong enough.

- Dr. APJ Abdul Kalam

4. Global documentation of overlapping lobate deposits in Martian gullies

4.1. Introduction

Martian gullies are steep slope drainage systems typically consisting of an alcove, a channel, and a depositional apron **(Malin and Edgett, 2000; Hartmann et al., 2003; Dickson and Head, 2009; Morgan et al., 2010; Reiss et al., 2011; Johnsson et al., 2014)**. Lateral levees and lobate deposits have been identified in some gullies, and many workers **(e.g. Costard et al., 2002; Christensen, 2003; Reiss and Jaumann, 2003; Lanza et al., 2010; Levy et al., 2010b; Johnsson et al., 2014; De Haas et al., 2015a; Conway et al., 2015; Sinha et al., 2019)** have studied such levees and lobate deposits and suggested that they may have been formed by aqueous debris flows. The hypothesis that these flows were water-bearing has emerged from (1) morphological comparison with lobate deposits found on Earth **(Costard et al., 2002; Mangold et al., 2003b; Conway, 2010; Lanza et al., 2010; Johnsson et al., 2014; Sinha et al., 2019)**, (2) detailed morphological analysis of lobate structures **(Levy et al., 2010b)**, (3) correlation of Martian debris flow frequency with obliquity variations **(De Haas et al., 2015b)**, and (4) sedimentological analysis of outcrop exposures in Martian gully-fans **(De Haas et al., 2015a)**. However, the hypothesis of water-bearing debris flows in gully formation does not comply with the fact that: (1) the Martian climate could not have supported substantial amounts of liquid water to flow on the surface during the last few million years of the Late Amazonian period **(Ingersoll 1970; Haberle et al. 2001; Hecht 2002; Richardson & Mischna 2005; Sears & Moore 2005)**, (2) gully-fans bearing debris flow like deposits have

only been reported at a few sites **(Levy et al., 2010b; Lanza et al., 2010; Johnsson et al., 2014; De Haas et al., 2015a)** and (3) morphological features akin to wet debris flows have been reported to also form from CO_2 frost sublimation (dry flows) **(Dundas et al., 2010, 2012, 2015, 2019; De Haas et al., 2019b)**. Apart from wet debris flow formation, there are thus a number of alternative models for gully formation, which include: (1) fluvial **(e.g., McEwen et al., 2007b; Head et al., 2008; Morgan et al., 2010; Reiss et al., 2011)**, (2) dry granular flows **(e.g., Treiman, 2003; Bart, 2007; Pelletier et al., 2008)**, and (3) flows driven by CO_2 frost sublimation **(e.g., Hoffman, 2002; Ishii & Sasaki, 2004; Cedillo-Flores et al., 2011; Hansen et al., 2011)**.

Previous studies comparing several hundred Martian gullies with their terrestrial counterparts have shown that most Martian gullies do not possess typical evidence of levees and lobate deposits **(Reiss et al., 2009, 2011)**. Nevertheless, some of the Martian gullies lacking levees and lobate deposits exhibit slope-area relationships similar to that of terrestrial debris flow channels **(Lanza et al., 2010; Conway et al., 2011)**. **De Haas et al. (2015a)** pointed out that surficial observations may not be always useful in explaining the processes involved in gully formation, because the surface of gully-fans can be severely influenced by post-depositional processes, which would hide surface expressions of lobate deposits.

Over the last decade, multiple studies using repeat High Resolution Imaging Science Experiment (HiRISE) imagery have revealed widespread contemporary activity in some gullies, interpreted to result from gas released during CO_2 frost sublimation **(Diniega et al., 2010; Dundas et al., 2010, 2012, 2015, 2019; Pasquon et al., 2019a, 2019b)**. These studies have

documented morphological evidence for new channel incision, apron deposition, terraces, levees and lobate deposits, as a result of this ongoing gully activity. The previous assertion that well-developed leveed channels formed in wet flows should not be evident in dry flows **(Reiss et al., 2009; De Haas et al., 2015a)**, is thus challenged by these reports of morphologic evidence of boulder-rich leveed flows formed at the present day **(Dundas et al., 2019)**. Accordingly, theoretical models involving flows triggered by CO_2 gas sublimation in current Martian conditions have been proposed to explain ongoing gully activities **(Cedillo-Flores et al., 2011; Pilorget and Forget, 2016)**. Together, these recent observations raise the question of whether liquid water was needed for the formation of Martian gullies, and whether the lobate deposits found in gullies stem from aqueous flows, dry flows, or both? A major step towards solving this question is unravelling the global distribution of lobate deposits in Martian gullies. Previous studies have estimated that gullies have been forming for the last several million years **(e.g. Reiss et al., 2004; Schon et al., 2009; De Haas et al., 2015b, 2019b)**, and they are found on slopes where both H_2O and CO_2 have likely undergone phase changes, under very different orbital configurations **(e.g., Costard et al., 2002; Forget et al., 2008; Dundas et al., 2015a; Pilorget and Forget, 2016)**. Hence, it is possible that multiple processes could have formed gullies and could contribute to the formation of the lobate deposits in Martian gullies.

Here we present an extensive morphological survey utilizing the available HiRISE images of the craters emplaced between 30˚-75˚ in both the northern and southern hemispheres to document evidence of overlapping lobate deposits. Our primary objectives are to quantify the global distribution of overlapping lobate deposits in Martian gullies, and infer whether their distribution reflects a global climate signal. We further aim to quantify the (1) orientation

preferences of crater walls with overlapping lobate deposits, (2) the morphometry and geomorphic setting of crater walls with overlapping lobate deposits, and (3) the (relative) timing of their formation. This will enable us to test the following hypotheses:

A. the formation of lobate deposits is integral to gully-formation
B. the formation of lobate deposits is one of the processes that occur within gullies and is not a dominant mechanism in forming gullies in general

For hypothesis 'A' we would expect to find that lobate deposits occur throughout the gully population, with their frequency modulated by their preservation. According to this hypothesis if lobate deposits are easily preserved they would be found in all gullies independent of when the last activity occurred. However, given our current knowledge we know already that this is not the case, as reports of lobate deposits are rare. Hence, we posit that if hypothesis 'A' is true then by deduction lobate deposits have poor preservation potential and we might expect to find evidence for degraded lobate deposits and/or a correlation between "youthfulness" of the deposit and the occurrence of lobate deposits. For hypothesis 'B' we would expect to find a systematic relation between lobate deposits and one of the other measured parameters, for example latitude, slope gradient or orientation, and/or presence/absence of latitude dependent mantle deposits.

4.2. Datasets and Methods

At a pixel scale ranging from ~25-60 cm, HiRISE images cover a swath of width ~5-6 km and length up to ~60 km **(McEwen et al., 2018)**. In our survey, we investigate the HiRISE images located between 30˚-75˚ in both hemispheres. We have chosen this latitudinal extent

because previous studies have revealed that gullies are typically found in these regions **(Heldmann and Mellon, 2004; Balme et al., 2006; Heldmann et al., 2007; Kneissl et al., 2010; Dickson et al., 2015; Harrison et al., 2015)**. Within the survey region, we have analysed 1004 HiRISE images for the evidence of lobate deposits in gullies. As noted in previous studies **(e.g. Dundas et al., 2010)**, the latitudinal coverage of HiRISE images is uneven due to the fact that the observations are not acquired at random. Instead, HiRISE images are targeted at locations where a previous dataset has identified a feature of interest **(McEwen et al., 2007a; Auld and Dixon, 2016; Dundas et al., 2017)**. The HiRISE images included in our investigation are located only on the slopes of crater walls. We focus on crater walls mainly because they provide us a unique opportunity to assess the influence of slope orientation on the distribution and development of lobate gully-forms **(Kneissl et al., 2010)**. Another reason to exclusively focus on crater wall slopes is that this is the setting for the majority of gullies as shown by a number of previous studies **(Balme et al., 2006; Heldmann et al., 2007; Kneissl et al., 2010; Harrison et al., 2015)**.

Images that contained overlapping coverage of the same portions of crater wall are rendered within ArcGIS to eradicate redundant observations. For a given crater, it is possible that there can be more than one HiRISE image covering different portions of the crater wall in which gullies could be present. Additionally, portions of crater wall for which there is no HiRISE image or the image is poorly illuminated may contain gullies. For instance, there are many larger diameter (e.g. >50 km) craters where HiRISE images do not cover the crater wall completely. If we find gullies in any of the HiRISE images covering the crater wall, we annotate that crater as 'crater with gullies in HiRISE'. For the craters in which we do not find gullies in

the available HiRISE images, we annotate those craters as ‘crater without gullies in HiRISE’.

For the identification of gullies in HiRISE images, we adopt the definition of a gully as proposed by **Malin and Edgett (2000)**: “gullies are relatively small steep-sloped drainage systems typically consisting of an alcove, a channel and a depositional apron”. Based on this definition, each HiRISE image was inspected for the presence or absence of gullies using the Multi-Temporal Database of Planetary Image Data (MUTED) **(Erkeling et al., 2016; Heyer et al., 2018)**. To identify overlapping lobate deposits, we based our search on morphologies resembling those already identified in the literature (e.g., **Lanza et al., 2010, Reiss et al., 2011, Johnsson et al., 2014, De Haas et al., 2015a and Sinha et al., 2019)** in which evidence for lobate deposits was reported inside 6 craters **(Table 4.1)**. Of these 6 craters, 2 craters located in the northern hemisphere are reported by **Sinha et al. (2019)** and the remaining 4 craters in the southern hemisphere are reported by **Lanza et al., 2010, Reiss et al., 2011, Johnsson et al., 2014,** and **De Haas et al., 2015a**. An overlapping lobate deposit can be identified as a lobe that partly covers another formerly deposited lobe in the downslope direction. This distinct overlapping characteristic of lobes was previously recognized on a few fans **(Lanza et al., 2010; Levy et al., 2010b; Reiss et al., 2011; Johnsson et al., 2014; De Haas et al., 2015a; Sinha et al., 2019)**. In the present study and in the previous reports, overlapping lobes are recognized by the stacking of relatively small-sized individual lobes or laterally elongated lobes at the fan surface or termini. Images were examined at a map scale of 1:1000 using ESRI’s (Environmental Systems Research Institute, Inc. Redlands, CA, USA) ArcMap10.0.

Digital Terrain Models (DTMs) aligned on the Mars Orbiter Laser Altimeter (MOLA) topography were generated at a resolution of ~18 m/pixel from CTX stereo imagery through the stereo-restitution pipeline of the Mars Information System application **(Lozac'h et al., 2015; Quantin-Nataf et al., 2018; Tao et al., 2018)**. Using ESRI's ArcGIS, we overlay the CTX images on the DTM to visually locate the crater wall slope surfaces where gullies and overlapping lobate deposits are found. Gully slopes were measured from alcove head to lobe termini along the main gully channel.

Using a combination of HiRISE and CTX images the orientation of crater wall slopes dominated by gullies accompanying overlapping lobate deposits is measured with respect to the geographic north **(Heldmann et al., 2007)**. We used the mosaics of CTX and HiRISE images to count the number of gullies formed on the crater wall slopes. The absolute elevation of the source alcoves of gullies associated with overlapping lobate deposits was extracted from Mars Orbiter Laser Altimeter (MOLA) data **(Smith et al., 2001)**.

The geological context of the craters containing evidence of lobate deposits is categorized according to the morphology of the crater wall and floor. The interior of the craters is identified as glaciated if it contained morphologic evidence of viscous flow features such as lobate debris apron (LDA) **(Head et al., 2010)** or concentric crater fill (CCF) **(Levy et al., 2010a)**, or small-scale LDAs **(Sinha and Vijayan, 2017)**. Such viscous flow features can be recognised by spatulate depressions **(Head et al., 2008)** and/or arcuate ridges **(Arfstrom & Hartmann, 2005; Hubbard et al., 2011)** at their margins, surficial contrasting ridge structures or lineations at the terminus **(Arfstrom & Hartmann, 2005)**, and divergence over/around

obstacles **(Baker et al., 2010; Sinha and Vijayan, 2017)**. Additional key-attributes include brain-terrain texture **(Noe Dobrea et al., 2007; Levy et al., 2010a)**, polygonal cracks of varying size and type **(Levy et al., 2009a)** and ring-mold craters **(Kress and Head, 2008)**. The identification of glaciated and non-glaciated craters was used for assessing the influence of glacial deposits on gullies associated with lobate deposits **(De Haas et al., 2019a)**. We define the topography of the crater interior as undulated on the basis of hummocky units (e.g., cone and mesa-like features) and crater wall slump terraces on the crater wall and on the floor.

Morphological evidence of the latitude-dependent mantle (LDM; defined as a smooth, meters thick deposit of ice and dust) (e.g. **Head et al., 2003**) within and around the craters is recognized based on the appearance of softened topography on gully alcoves, gully channels, and crater walls and ejecta **(Mustard et al., 2001; Kreslavsky & Head, 2002)**. To confirm LDM deposits such deposits have to display polygonized material and/or slope-contouring fracturing **(Levy et al., 2009a; Dickson et al., 2015; Jawin et al., 2018; De Haas et al., 2019a)**. We also identified texturally disrupted bedrock exposures on the inner and outer walls of craters as evidence of LDM deposits **(Conway et al., 2018)**.

CraterTools is used for measuring the crater size-frequency distribution over the ejecta blanket of craters containing lobate deposits **(Kneissl et al., 2011; Michael et al., 2012)**. For those craters where ejecta is not apparent, appears modified or is superimposed by the ejecta of adjacent craters, we measure the crater size-frequency distribution over the small lobate debris apron (LDA) formed on the floor of the crater **(Sinha and Vijayan, 2017)**. Craterstats 2.0 is used for plotting the counted craters and for determining the best-fit absolute model age.

The crater count statistics are interpreted based on the production function by **Ivanov (2001)**.

We classify the surface texture of the lobate deposits as either clast-rich or clast-poor **(Johnsson et al., 2014)**. The size (longest dimension) of a clast is measured with the help of CraterTools using the method of three-point fitting. Evidence of recent rock fall activity in the form of boulder trails at the foot of crater wall slopes is recognized as reflecting an active weathering environment within the crater **(De Haas et al., 2013; Johnsson et al., 2014; Tesson et al., 2019)**.

4.3. Observations and Results

4.3.1. Geographic Distribution

In total, we have analysed 1726 craters using HiRISE images within the 30˚-75˚ latitude range **(Figure 4.1)**. Of these 1726 craters, 988 craters are in the northern hemisphere and 738 craters are in the southern hemisphere. In the northern hemisphere, we find gullies in 278 craters (28.13% of total) covered by a total of 405 HiRISE images. In the southern hemisphere, gullies are found on the crater walls of 487 craters (65.98% of total), covered by 599 HiRISE images. Within these 278 gullied craters in the northern hemisphere, overlapping lobate deposits are found in 6 craters - referred to as 'craters hosting lobate deposits' from this point onwards **(Table 4.1; Figure 4.1)**. Previously, 2 craters hosting lobate deposits were identified in the northern hemisphere by **Sinha et al. (2019) (Table 4.1; Figure 4.1)**. Of the 487 gullied craters present in the southern hemisphere, we have found 14 craters hosting lobate deposits **(Figure 4.1)**. In the southern hemisphere, 4 craters hosting lobate deposits were identified by **Lanza et al. (2010), Reiss et al. (2011), Johnsson et al. (2014),** and **De Haas et al. (2015a)**

(Table 4.1; Figure 4.1). This results in a total of 26 craters in which lobate deposits occur in gullies.

We find that the craters hosting lobate deposits are not clustered in any particular region within either hemisphere. In the southern hemisphere, the craters hosting lobate deposits span a wide range of longitudes **(Table 4.1)**, while the latitudinal distribution of craters hosting lobate deposits is confined between ~33.0˚-46.0˚ S **(Figure 4.1)**. The craters hosting lobate deposits in the northern hemisphere are found within 134.5˚ W to 26.5˚ E and 40.5˚ N to 53.7˚N **(Table 4.1; Figure 4.1)**. Overall, the craters hosting lobate deposits in the northern hemisphere have a slightly larger latitudinal range than the craters hosting lobate deposits in the southern hemisphere. We find that overlapping lobate deposits occur in craters with diameters ranging from ~2 – 30 km and ~3 – 36 km in the northern and southern hemispheres, respectively **(Table 4.1)**. The alcoves of gullies consistent with lobate deposits are found at elevations ranging from ~-3.9 to ~2.7 km in the northern hemisphere and ~0.3 to ~5 km in the southern hemisphere **(Table 4.1)**.

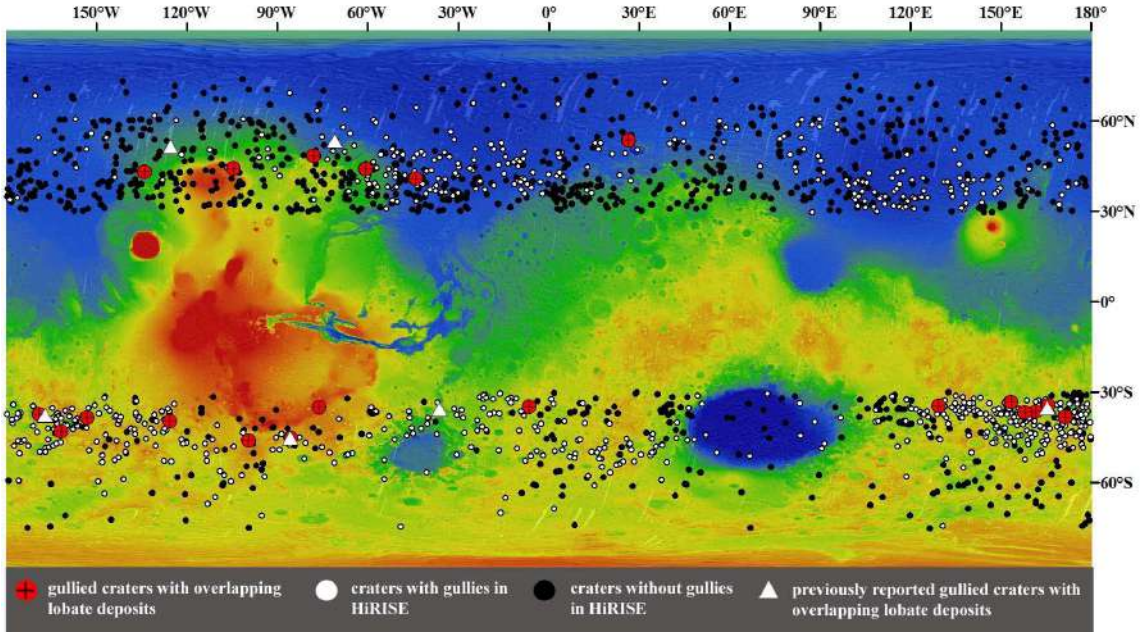

Figure 4.1. Distribution of overlapping lobate deposits in gullied craters between 30˚-75˚ N and S plotted over the Mars Orbiter Laser Altimeter (MOLA; red is high elevation and blue is low elevation) topographic data superposed on the Mars Odyssey THEMIS daytime thermal infrared global mosaic (100 m/pixel). The colors of the symbols indicate: white circles – craters with gullies in HiRISE, black circles–craters without gullies in HiRISE, red circle with plus – gullied craters with overlapping lobate deposits, and white triangles – previously reported gullied craters with overlapping lobate deposits. Basemap image credit: MOLA/GSFC/USGS.

Table 4.1. Summary of detailed characteristics of gullied craters hosting lobate deposits.

Crater name	Lat./Long.	Diameter	Alcove elevation	Slope (at lobate deposits/middle/top)	Gully/lobate deposit orientation	Evidence of LDM/Glaciation	Best-fit age, crater diameter, count area	HiRISE Id	CTX Id	Reference
Craters hosting lobate deposits in the northern hemisphere										
Unnamed (NU-1)	43.24° N, 134.20° W	~6.5 km	~-1.8 km	~25°/~32°/~41°	Poleward/Poleward	Yes/No	~1.6±0.2 Ma, 35-120 m, Ejecta	ESP_046028_2235	B17_016332_2248, D03_028569_2235	This study
Unnamed (NU-2)	44.20° N, 104.61° W	~2.2 km	~2.65 km	~23°/~34°/~36°	Poleward/Poleward	Yes/No	~9.1±2 Ma, 30-70 m, Ejecta	ESP_043073_2245	D13_032405_2244	
Unnamed (NU-3)	48.29° N, 78.16° W	~7.0 km	~-0.55 km	CTX DEM not available	Poleward/Poleward	Yes/No	~15±5 Ma, 100-400 m, Ejecta	ESP_028290_2285	P15_007034_2277, P16_007390_2291	
Unnamed (NU-4)	44.06° N, 60.78° W	~15.5 km	~-1.6 km	CTX DEM not available	Poleward-Equatorward/Poleward	Yes/No	~3.8±0.6 Ma, 70-300 m, Ejecta	ESP_025797_2245	B01_010079_2243, B02_010290_2244, P22_009723_2251	
Gamboa	40.79° N, 44.34° W	~30.0 km	~-3.2 km	~19°/~25°/~25°	Poleward-Equatorward/Poleward	Yes/No	~270±60 Ma, 500-1700 m, Ejecta	ESP_036451_2210	B18_016487_2213, D01_027603_2205, D03_028236_2205, D05_02908_2195, F02_036451_	

									2194, F04_037242_2195, F06_038152_2202, P16_007257_2213
Unnamed (NU-5)	53.61˚ N, 26.30˚ E	~4.5 km	~-3.83 km	CTX DEM not available	Poleward-Equatorward/Equatorward	Yes/No	Only one crater is present on the ejecta	ESP_036501_2340	B17_016181_2337, G23_027231_2335
Craters hosting lobate deposits in the southern hemisphere									
Unnamed (SU-1)	37.17˚ S, 169.16˚ W	~18.0 km	~0.38 km	~10˚/~30˚/~32˚	Poleward/Poleward	Yes/No	~3.0±0.3 Ga, 600-2000 m, Ejecta	ESP_036324_1425	G16_024575_1441, P06_003438_1430, P07_003794_1430, F22_044368_1428
Unnamed (SU-2)	42.84˚ S, 161.92˚ W	~17.70 km	~1.95 km	~16˚/~21˚/~21˚	Poleward-Equatorward/Poleward	Yes/Yes	~33±10 Ma, 100-300 m, small-scale LDA	PSP_007143_1370	P12_005719_1381, B19_016940_1386, P17_007644_1381
Unnamed (SU-3)	38.27˚ S, 153.23˚ W	~13.2 km	~2.67 km	~14˚/~21˚/~29˚	Poleward/Poleward	Yes/Yes	~2.0±0.3 Ga, 350-1100 m, Ejecta	ESP_038473_1415	D08_030482_1414, D09_030904_1394, P17_007525_1425

Taltal	39.50˚ S, 125.78˚ W	~10.0 km	~2.44 km	~17˚/~22˚/~19˚	Poleward/Poleward	Yes/Yes	~490±100 Ma, 300-1000 m, Ejecta	ESP_016042_1400	B17_016108_1403, B1_017031_1405, D02_028002_1402, P14_006667_1398
Unnamed (SU-4)	45.84˚ S, 99.79˚ W	~33.2 km	~2.78 km	~6˚/~15˚/~16˚	Poleward-Equatorward/Poleward	Yes/Yes	Ejecta boundary cannot be delineated	ESP_030045_1340	P18_008090_1344, P15_007088_1328, G12_022766_1328, G11_022344_1328
Unnamed (SU-5)	45.28˚ S, 85.52˚ W	~17.0 km	~2.73 km	~8˚/~9˚/~20˚	Poleward-Equatorward/Poleward	Yes/Yes	~140±40 Ma, 350-700 m, Ejecta	ESP_047464_1345	B11_013944_1346, P15_006837_1331, B19_017135_1353
Los	35.08˚ S, 76.22˚ W	~7.8 km	~4.93 km	~23˚/~30˚/~9˚	Poleward/Poleward	No/No	~7.9±3 Ma, 90-250 m, Ejecta	ESP_020774_1445	P14_006652_1439, B18_016594_1441, B02_010225_1446
Unnamed (SU-6)	34.65˚ S, 6.6˚ W	~3.4 km	~1.93 km	~7˚/~23˚/~35˚	Poleward/Poleward	Yes/No	Ejecta is not evident	PSP_007045_1450	B17_016130_1451
Unnamed (SU-7)	34.45˚ S, 129.16˚ E	~13.2 km	~1.94 km	~16˚/~23˚/~28˚	Poleward/Poleward	Yes/Yes	~28±8 Ma, 45-120 m, small-scale LDA	ESP_013870_1450	J02_045755_1437, G01_018538_1452, B03_010824_1451

Unnamed (SU-8)	33.18˚ S, 153.19˚ E	~12.6 km	~1.5 km	~10˚/~19˚/~25˚	Poleward/Poleward	Yes/No	Ejecta boundary cannot be delineated	ESP_016757_1465	F07_038343_1465, P15_006960_1469, P16_007461_1458	
Unnamed (SU-9)	36.65˚ S, 157.74˚ E	~4.4 km	~1.07 km	CTX DEM not available	Poleward/Poleward	Yes/Yes	~240±60 Ma, 120-600 m, Ejecta	ESP_023640_1430	B18_016625_1434, B19_017192_1443.	
Unnamed (SU-10)	36.34˚ S, 161.45˚ E	~6.3 km	~0.6 km	~12˚/~21˚/~24˚	Poleward/Poleward	Yes/No	~150±40 Ma, 140-400 m, Ejecta	ESP_028308_1435	G14_023864_1442	
Unnamed (SU-11)	34.21˚ S, 165.58˚ E	~3.1 km	~1.7 km	~23˚/~31˚/~20˚	Poleward/Poleward	Yes/Yes	~250±60 Ma, 120-300 m, Ejecta	ESP_047125_1455	F01_036259_1455	
Tarq	38.10˚ S, 171.22˚ E	~35.4 km	~1.79 km	~21˚/~14˚/~24˚	Poleward/Poleward	Yes/Yes	~30±10 Ma, 90-250 m, small-scale LDA	ESP_036839_1420	P11_005298_1418, P16_007434_1416, P18_007935_1401, B19_016941_1416	
Previously reported craters hosting lobate deposits in the northern and southern hemispheres										
Domoni	51.38˚ N, 125.61˚ W	~13.8 km	~-2.1 km	0-10˚/NA/>30˚	Equatorward/Equatorward	Yes/No	~19.2±5.3 Ma, 100-200 m, Ejecta	ESP_016213_2315	NA	Sinha et al., 2019; de Haas et al., 2019b

Maricourt	53.34˚ N, 71.17˚ W	~9.9 km	~-3.52 km	0-14˚/NA/>30˚	Equatorward/Equatorward	No/No	~10±2.8 Ma, >62 m, Ejecta	ESP_026061_2335	NA	Sinha et al., 2019
Galap	37.66˚ S, 167.07˚ W	~6.0 km	~1.03 km	5-10˚/15-20˚/30-40˚	Poleward/Poleward	No/No	~6.5 Ma	PSP_003939_1420	NA	de Haas et al., 2015a
Istok	45.10˚ S, 85.81˚ W	~4.6 km	~2.57 km	8-20˚/20-35˚/35-45˚	Poleward/Poleward	No/No	~.19±.04 Ma, <25 m, Ejecta	PSP_006837_1345	NA	Johnsson et al., 2014
Hale	35.69˚ S, 36.35˚ W	~137.3 km	~1.6 km	Between 20 and 30˚	All directions/east-facing	Yes/No	Minimum age: ~1 Ga	PSP_006822_1440	NA	Reiss et al., 2009, 2011; Jones et al., 2011
Unnamed	35.16˚ S, 165.34˚ E	~6.6 km	~1.11 km	10˚/25˚/NA	Poleward/Poleward	Yes/Yes	Not estimated	PSP_003162_1445	NA	Lanza et al., 2010

NU: North unnamed,
SU: South unnamed

NA: Not available

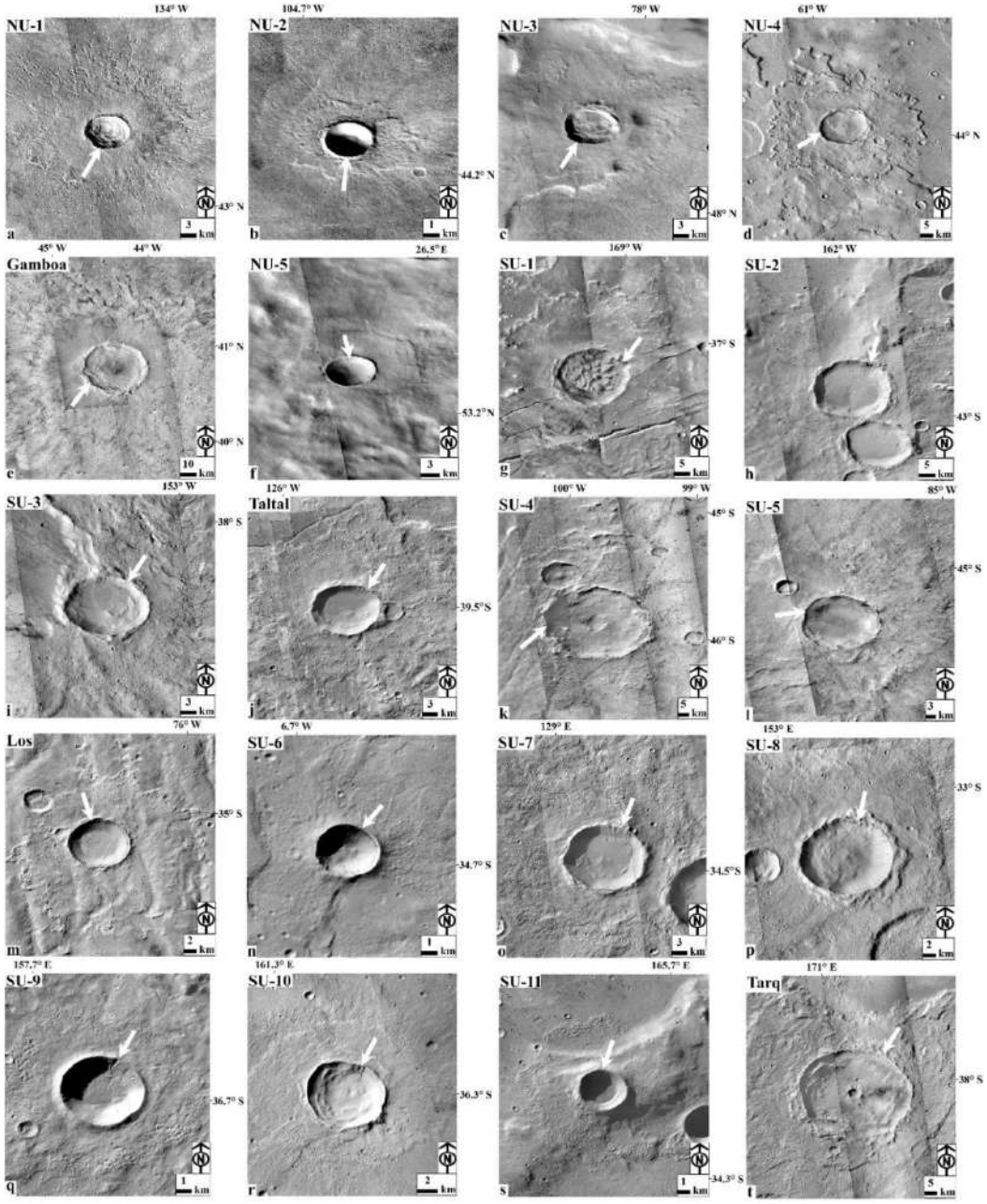

Figure 4.2. CTX mosaics of the 20 craters in which lobate deposits in gullies are newly identified in the northern and southern hemisphere. The arrow for each of these craters shows the location of the gully systems where we have identified overlapping lobate deposits. Detailed panels showing the lobate deposits are shown in Figure 3. The CTX image IDs are given in Table 4.1. Image credit: NASA/JPL-Caltech/MSSS.

4.3.2. Morphology of overlapping lobate deposits

Figure 4.2 shows the 20 previously unidentified craters in which overlapping lobate deposits are found in gullies **(Figure 4.3)**. The lobes typically have a convex-up tongue-shape, and commonly display a straight to slightly sinuous flow pattern in plan view. In some instances, lobes are connected to channels, which are often flanked by lateral levees **(Figure 4.4a).** While channels are not evidently connected to lobes in other instances, this is likely a result of burial by subsequent events **(Figure 4.4b)**. There can be a series of terminal lobes stacked together, often regressively by backstepping **(Figure 4.4c, f)**, or laterally thereby forming broad deposit complexes **(Figure 4.4g, h)**. Both these forms co-exist within most of the gullies hosting lobate deposits. Lobes generally form local areas of high relief **(Figure 4.4i, j)** that steer subsequent flow deposits towards topographically lower areas **(Figure 4.4k-o)**. In a few examples, the fan surfaces adjacent to stacked lobes are rich in boulders **(Figure 4.4p)**.

We often observe patterns of channel plugging, backstepping, and avulsion, typical for the spatio-temporal evolution of fans formed by lobate deposits **(Figure 4.5) (De Haas et al., 2016, 2018, 2019c**). Most notably, in Taltal, Los, SU-5, SU-7, SU-10, and NU-1 craters, channels that emplaced an elongated lobate deposit or that were blocked by a lobate deposit were completely buried as a result of channel backfilling by subsequent lobe emplacement, ultimately resulting in avulsion **(Figure 4.5a-l)**. The channel and deposits are elongated when there was effective levee formation (e.g. in SU-4, NU-1) **(Figure 4.5m, n)**, while the unchannelized flows formed short and wide deposits (e.g. in SU-6) **(Figure 4.5o)**. These differences appear to be related to the grain size distribution in the lobes, where an absence of

sufficient large particles inhibits levee formation and enhances lateral spreading. Such behaviour is common in terrestrial debris flows **(De Haas et al., 2015c; Blair and McPherson, 2009)**. In Figure 4.6 we present a sketch summarizing the observations of the morphological attributes of the lobate deposits in martian gullies that we observed, **(Figure 4.6)**.

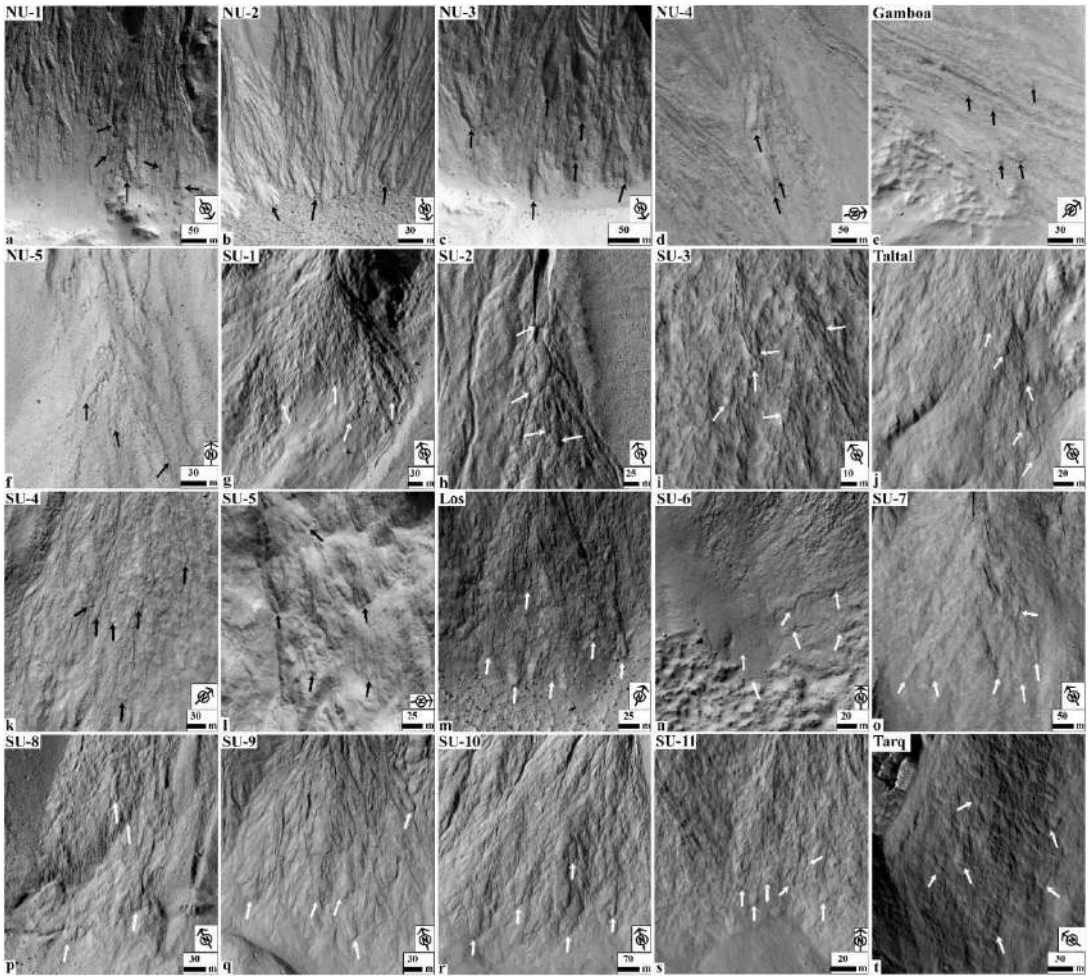

Figure 4.3. Morphology of overlapping lobate deposits (shown by arrows) within gullies in the 20 craters newly identified in the northern and southern hemisphere in this study. The location of these zoomed-in figures is shown by the arrows in Figure 4.2. The HiRISE image IDs of corresponding craters are given in Table 4.1. Image credit: NASA/JPL-Caltech/University of Arizona.

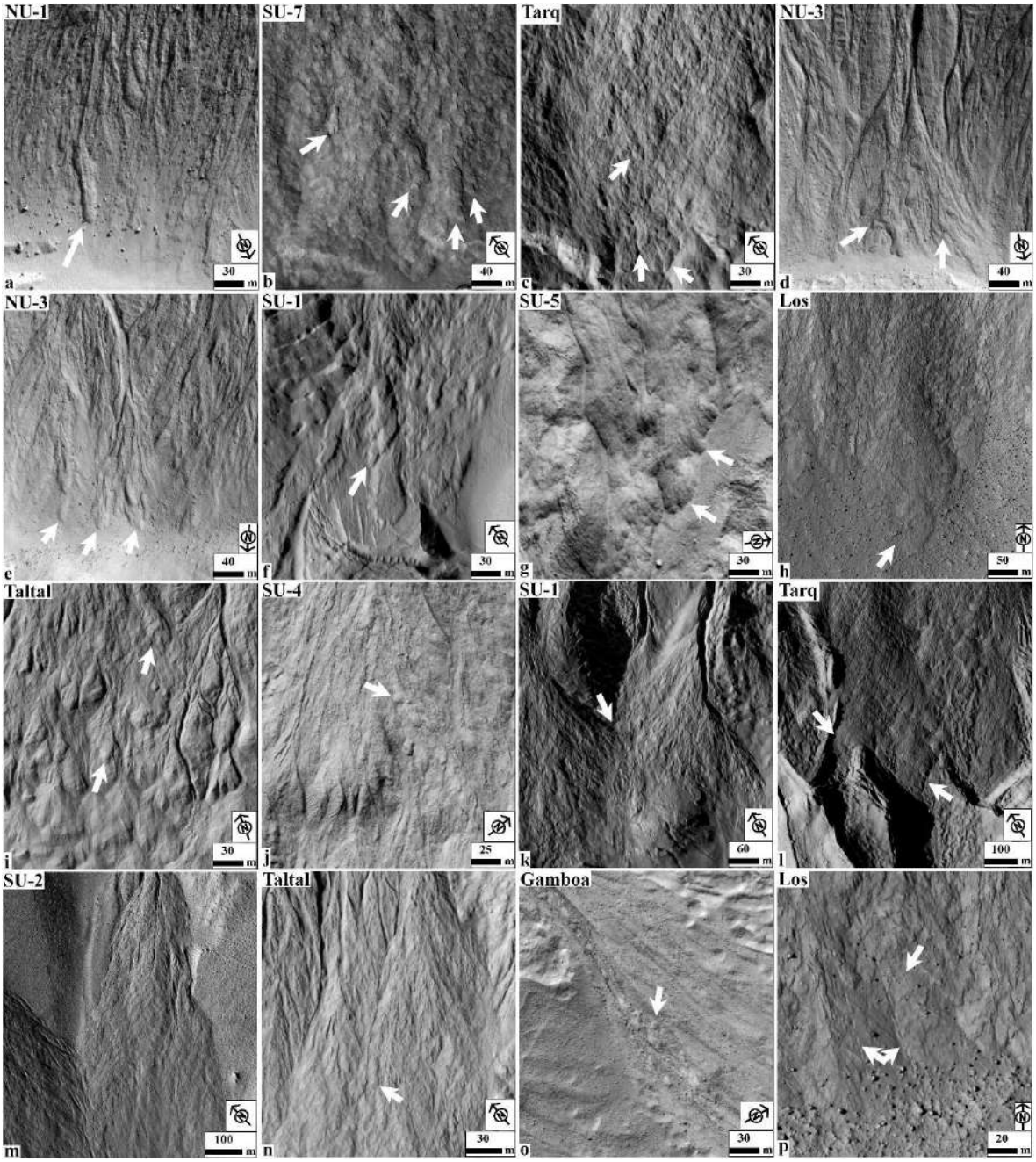

Figure 4.4. Examples of morphologies (shown by arrows) observed within the overlapping lobate deposits. **(a)** Lobate deposit connected to a channel (HIRISE: ESP_046028_2235). **(b)** Lobate deposit without an upslope connected channel (HIRISE: ESP_013870_1450). **(c-d)** Evidence for multiple lobes stacked together on a gully fan surface (HIRISE:

ESP_036839_1420, ESP_028290_2285). **(e-f)** Successive emplacement of lobes (HIRISE: ESP_028290_2285, ESP_036324_1425). **(g-h)** Broad deposits formed from laterally accumulating lobes (HIRISE: ESP_047464_1345, ESP_020774_1445). **(i-j)** Relatively high relief of lobes in comparison to adjacent fan surface (HIRISE: ESP_016042_1400, ESP_030045_1340). **(k)** Orientation and emplacement of lobes constrained by the local relief of older deposits (HIRISE: ESP_036324_1425). **(l)** Emplacement of a lobe constrained by the topography of downslope features (HIRISE: ESP_036839_1420). **(m)** Complex stratigraphy of overlapping lobes and associated channels (HIRISE: PSP_007143_1370). **(n-o)** Channel superposition by lobes (HIRISE: PSP_007143_1370, ESP_036451_2210). **(p)** Boulder trails evident on the fan surface (HIRISE: ESP_020774_1445). Image credit: NASA/JPL-Caltech/University of Arizona.

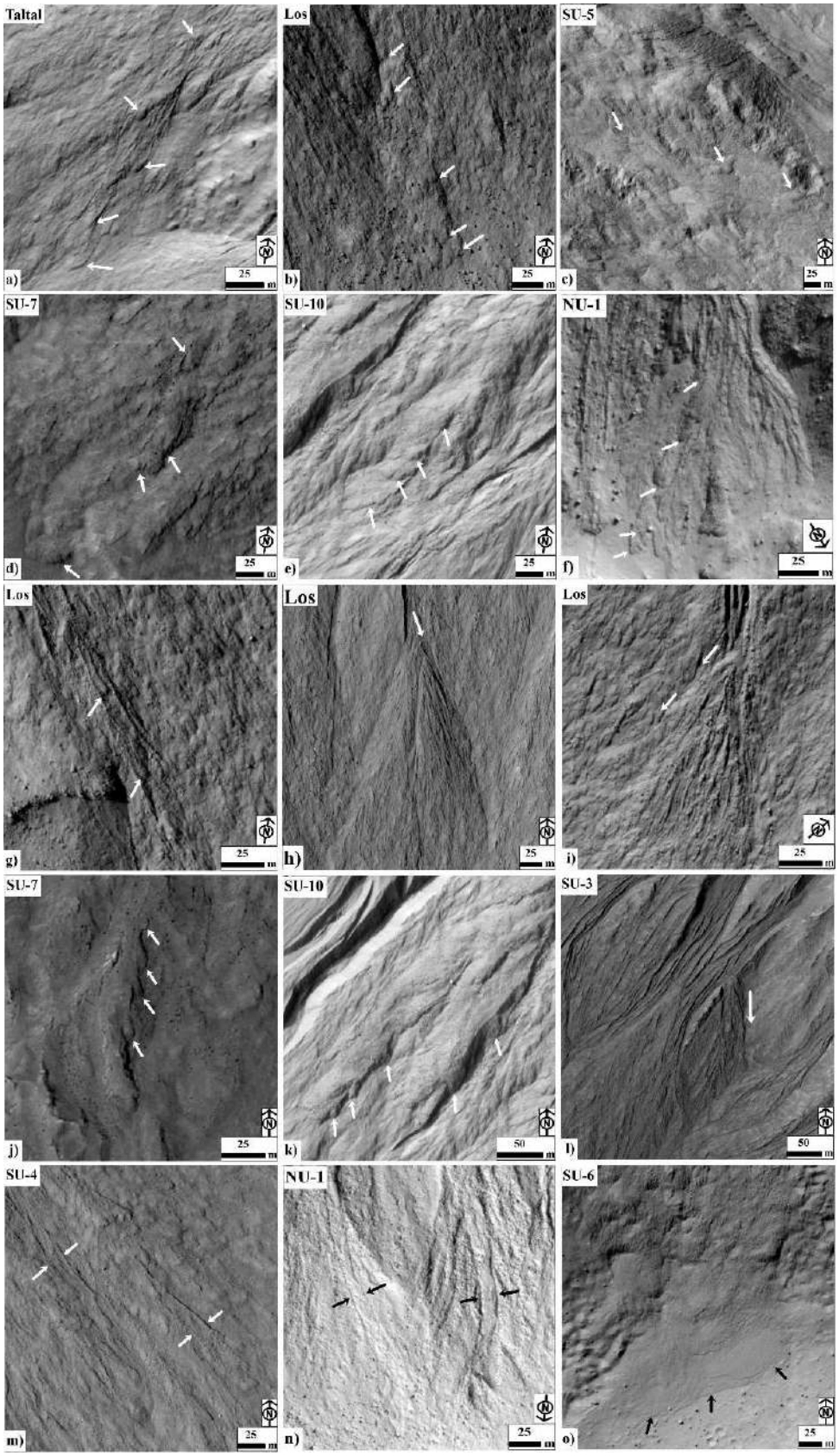
Taltal
a)
25 m
Los
b)
25 m
SU-5
c)
25 m
SU-7
d)
25 m
SU-10
e)
25 m
NU-1
f)
25 m
Los
g)
25 m
Los
h)
25 m
Los
i)
25 m
SU-7
j)
25 m
SU-10
k)
50 m
SU-3
l)
50 m
SU-4
m)
25 m
NU-1
n)
25 m
SU-6
o)
25 m

Figure 4.5. (a-f) Channel backfilling by backstepping of subsequent lobe deposits (HIRISE: ESP_016042_1400, HIRISE: ESP_020774_1445, ESP_047464_1345, ESP_013870_1450, ESP_028308_1435, ESP_046028_2235). **(g)**Channel plugs (HIRISE: ESP_020774_1445). **(h)** Avulsion leading to formation of new channel (HIRISE: ESP_020774_1445). **(i-k)** Examples of unchannelized avulsion (HIRISE: ESP_020774_1445, ESP_013870_1450, ESP_028308_1435). **(l)** Possible breach and overbank flow (HIRISE: ESP_038473_1415). **(m-n)**Levees formed in elongated channelized flows (HIRISE: ESP_030045_1340, ESP_046028_2235). **(o)** Short and wide unchannelized flow (HIRISE: PSP_007045_1450). Image credit: NASA/JPL-Caltech/University of Arizona.

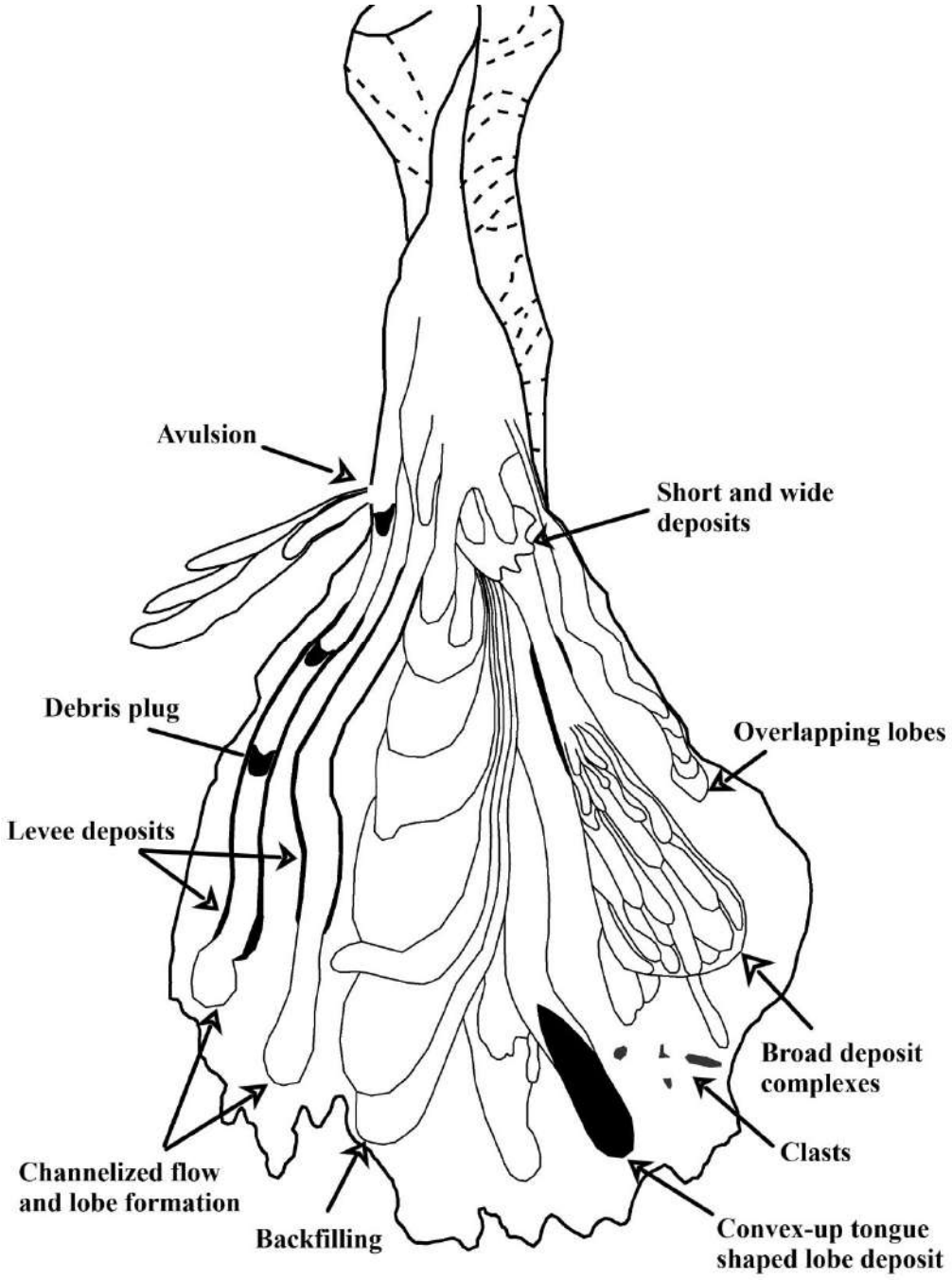

Figure 4.6. A sketch representing the range of morphological attributes of the lobate deposits identified in the gully systems investigated in this study. Note that not all the features are observed at the same time in the gully systems analyzed in this study.

4.3.3. Slope relationships

Slope ranges estimated for the top, middle and bottom of gullies associated with lobate deposits within 16 of the 20 craters are shown in **Figure 4.7**. For the remaining 4 craters (NU-3, NU-4, NU-5 and SU-9), CTX stereo imagery is not available for DTM generation. In the northern hemisphere, the average slopes at the top, middle, and bottom portions of gullies associated with lobate deposits are 33˚ (σ =5˚), 30˚ (σ =8˚), and 22˚ (σ =6˚), respectively. Similarly, in the southern hemisphere, the average slope at the top, middle, and bottom portions of gullies associated with lobate deposits are 23˚ (σ =9˚), 21˚ (σ =8˚), and 15˚ (σ =7˚), respectively. As such, the average slopes on which lobate deposits are deposited are slightly higher in the northern compared to the southern hemisphere. The slopes of gullies with lobate deposits do not show any correlation with the latitude **(Figure 4.7)**. The interquartile range of the slopes at the lobate deposits is smaller than the slopes at the middle and top of the gullies, as the lobate deposits are typically found near the base of the gullies.

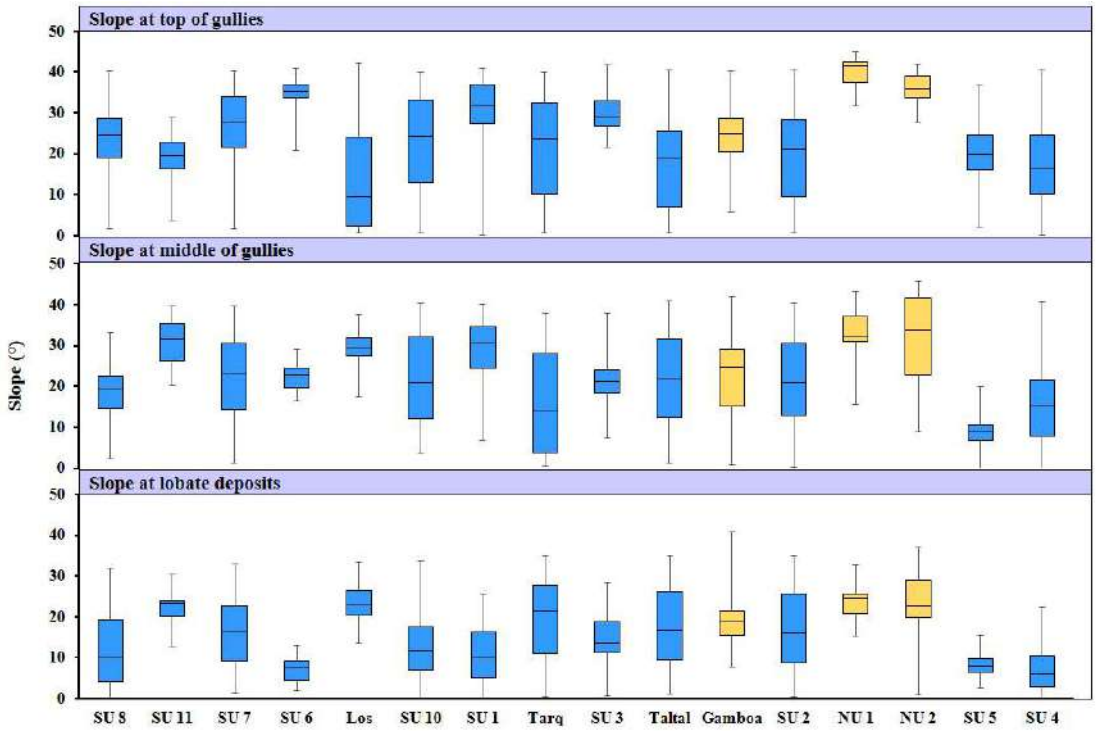

Figure 4.7. Box plots of the slopes extracted from one representative long-profile of a single gully with lobate deposits at each study site. The top panel shows the slope data at the top of the gully, the middle panel is for slope data gathered at the middle of the gully, and the bottom panel is for the slope data gathered at the lobate deposits. Blue boxes indicate the craters in the southern hemisphere and yellow boxes indicate craters in the northern hemisphere. The boxes indicate the interquartile range, whiskers the maximum and minimum values, horizontal black line in the boxes is the median value. Note that the craters investigated in the study are plotted in increasing order of latitude. Each box represents datapoints between 20 and 170.

4.3.4. Orientation

The orientation of gullies inside the craters wherein we have identified overlapping lobate deposits, with respect to latitude is shown in **Figure 4.8**, wherein the orientation of the

gullies with and without lobate deposits in the craters hosting gullies with lobate deposits is depicted. Overall, the vast majority of gullies, both with and without lobate deposits, are found on poleward-facing slopes in both the northern and southern hemispheres, and there are no differences in the orientation preference between gullies with and without lobate deposits.

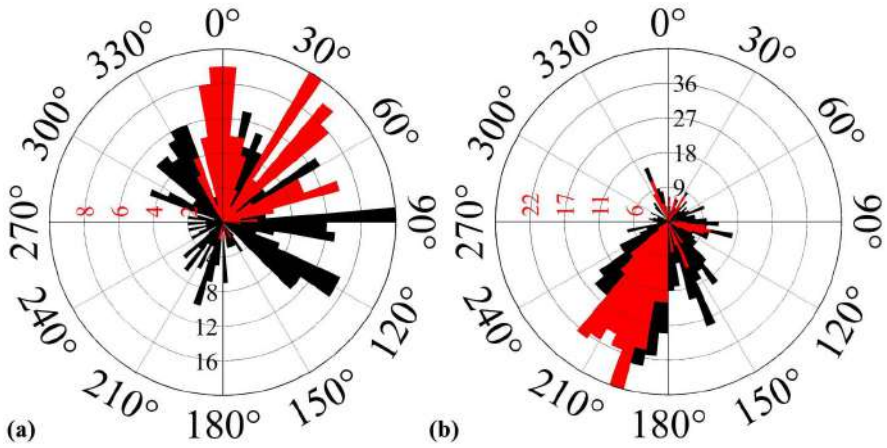

Figure 4.8. Orientation of crater wall slopes having gullies without lobate deposits (black) and gullies with lobate deposits (red). **8a.** Orientation of gullies and gullies with lobate deposits in the northern hemisphere. **8b.** Orientation of gullies and gullies with lobate deposits in the southern hemisphere.

Figure 4.8a reveals that the gullies with and without lobate deposits inside the craters located within the 40-54˚ N latitude range show a dominant poleward-facing trend. Out of the 515 gullies counted using the mosaic of CTX and HiRISE images of 6 craters in the northern hemisphere, there are 305 gullies (59.22%) formed on poleward-facing slopes and 210 gullies (40.78%) formed on equatorward-facing slopes **(Figure 4.9a-b)**. 118 gullies out of the total 515 gullies are associated with lobate deposits and all are found on poleward-facing slopes, except in NU-5 **(Figure 4.9a-b)**. 5 gullies (~4.8%) out of 105 gullies inside NU-5 are associated

with the lobate deposits and all of them have formed on equatorward-facing slopes **(Figure 4.9b)**.

Gullies with and without lobate deposits are both almost exclusively found on the poleward-facing slopes between 30°-46° S **(Figure 4.8b)**. Among the 14 craters in which we find lobate deposits, all within 30-46˚ S latitude range, gullies with and without lobate deposits both show a dominant poleward-facing trend **(Figure 4.8b) (Table 4.1)**. A count of gullies using the mosaic of CTX and HiRISE images of 14 craters revealed that there are 852 gullies inside these craters in total, of which 719 gullies (~84.38%) have formed on poleward-facing slopes and the remaining 133 gullies (~15.62%) have formed on equatorward-facing slopes **(Figure 4.9c-d)**. Furthermore, 282 gullies (~33.09%) are associated with lobate deposits and all have formed on poleward-facing slopes **(Figure 4.9c-d)**.

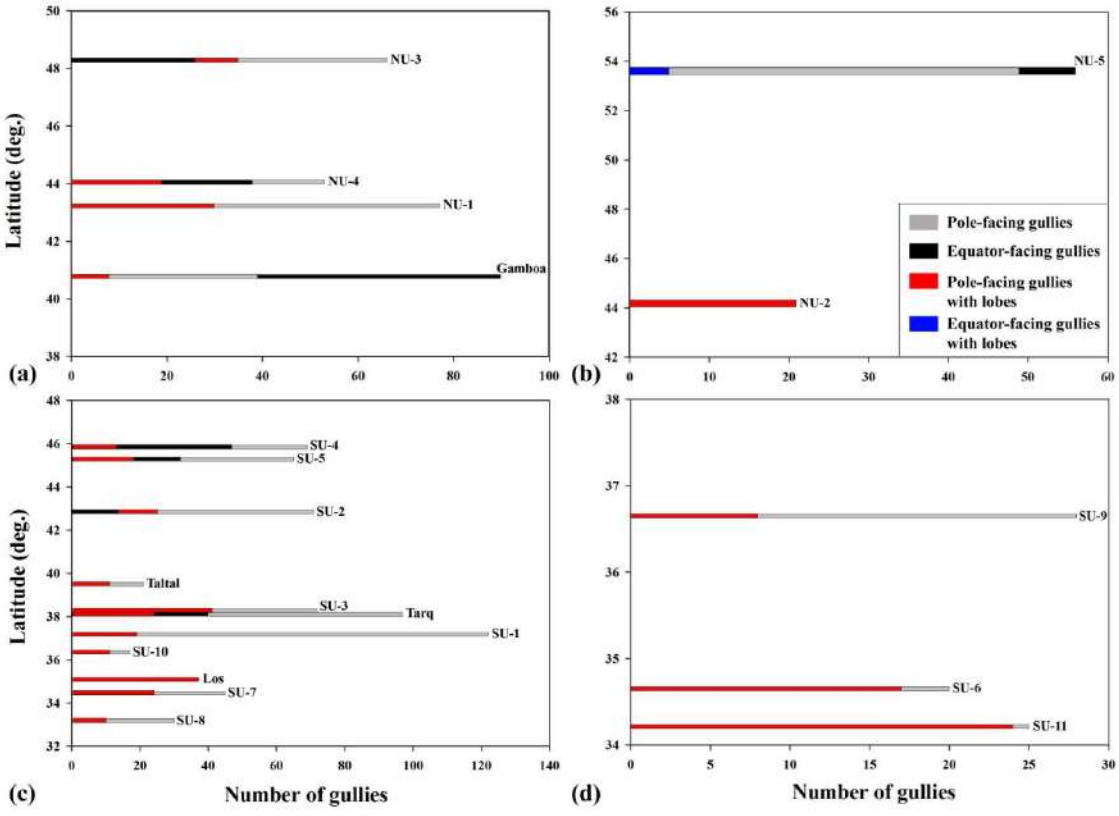

Figure 4.9. Bar graphs representing the orientation and number of gullies with and without lobate deposits with respect to latitude. Note that there are two plots for each hemisphere. **Panels 4.9a and 4.9b** represents gully distribution in the northern hemisphere. **Panel 4.9c and 4.9d** represents gully distribution in the southern hemisphere. **Panels 4.9a and 4.9c** are made using CTX data and **panels 4.9b and 4.9d** are made using HiRISE data.

4.3.5. Association with glacial and LDM deposits

In the northern hemisphere, none of the craters hosting lobate deposits have their interior filled with LDA/CCF **(Table 4.1)**. This suggests that the gullies and lobate deposits formed in these craters are not associated with glacial deposits. This could explain the relatively high slopes of the gullies with lobate deposits in the northern hemisphere. Still, NU-1, NU-3, NU-4 and Gamboa are characterized by undulated crater floor topography possibly resulting from their hummocky interior and slump terraces over the crater wall and on the floor **(Figure 4.2)**. These four craters have circular and elongated pits evident on their floor **(e.g. Figure 4.10 a)**. NU-3 and Gamboa are the only two craters with polygons on gully walls and alcoves. In NU-4, the polygons are distinctly mantled by dust hindering their identification. NU-3 also hosts polygonal cracks on its floor, which seem to have formed within material draped over the pre-existing surface **(Figure 4.10b)**. In NU-3 and NU-5 polygonized material is evident on the outer wall region outside the crater **(e.g. Figure 4.10c)**. All the craters hosting lobate deposits in the northern hemisphere are dominated by numerous clasts/boulders over the gullied walls **(e.g. Figure 4.10d)**. Fresh boulder trails are evident at the foot of the walls of NU-1, NU-4 and Gamboa. NU-4 has preserved dunes, ripples and transverse aeolian ridges (TARs) on its floor.

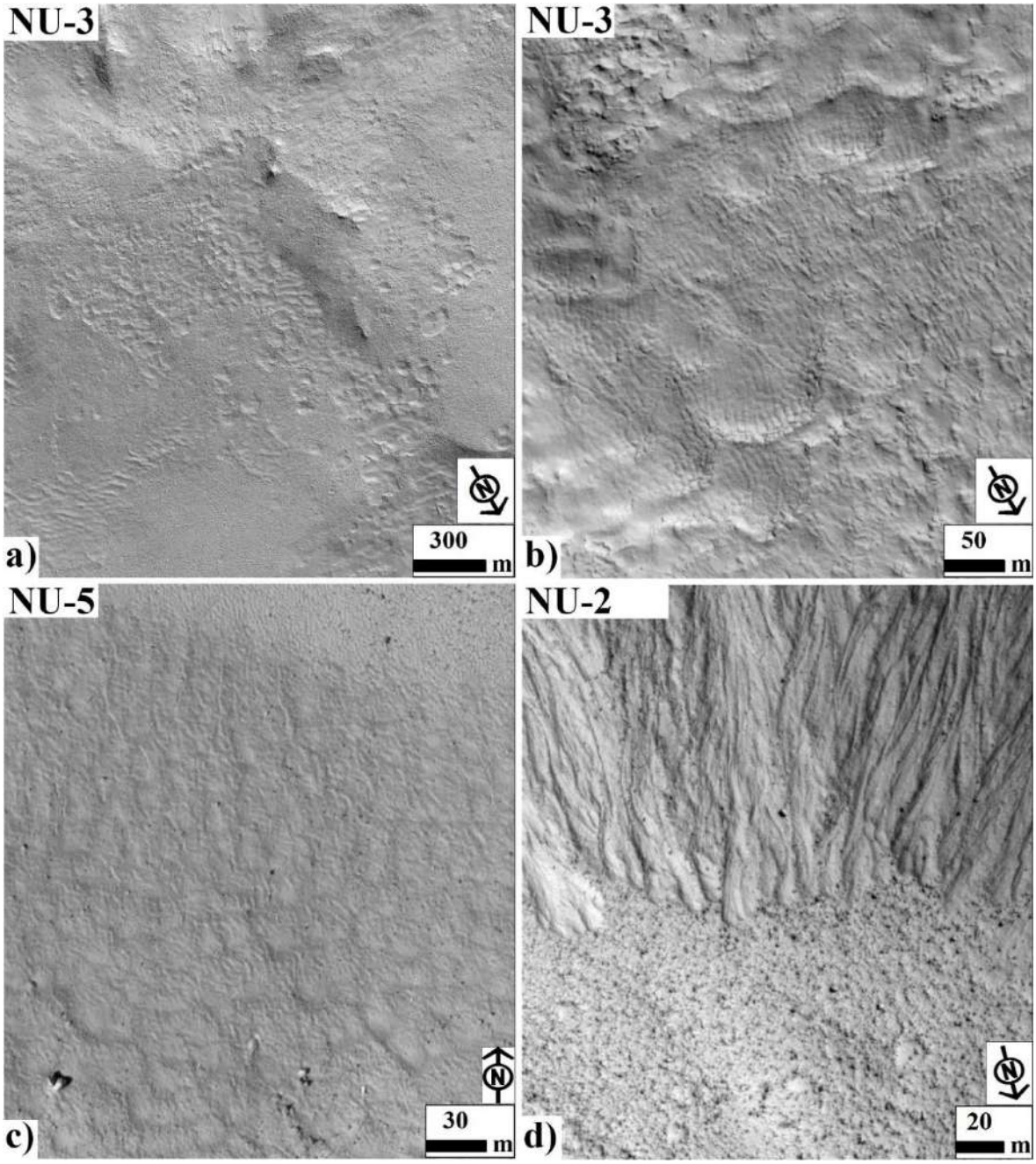

Figure 4.10. (a) Circular and elongated pits on the floor (HIRISE: ESP_028290_2285). **(b)** Polygon cracks on crater floor (HIRISE: ESP_028290_2285). **(c)** Polygonal cracks in the outer wall region of a crater (HIRISE: ESP_036501_2340). **(d)** Boulders accumulated at the foot of the wall of a crater (HIRISE: ESP_043073_2245).Image credit: NASA/JPL-Caltech/University of Arizona.

The softened appearance of the topography of the alcoves and gully-fan deposits in NU-1, NU-2, NU-3, NU-4, and NU-5 suggests that they are covered by LDM deposits **(e.g. Figure 4.11a-c)**. The evidence of draped LDM deposits in the downslope of texturally disrupted bedrock on the inner wall is evident in Gamboa, as implied by the patterned ground in these deposits **(Figure 4.11d)**.

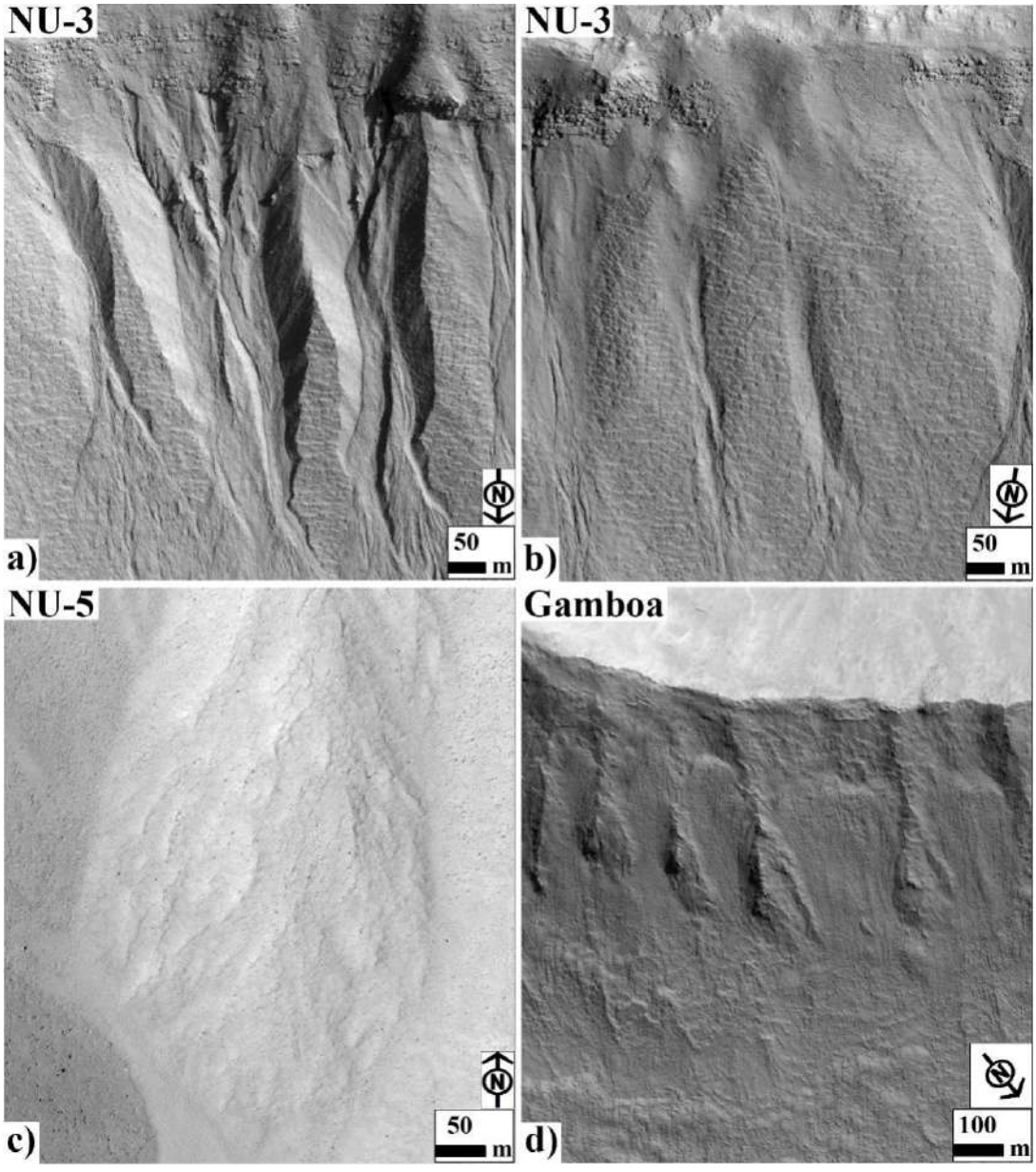

Figure 4.11. (a) Polygonized alcoves and gully walls (HIRISE: ESP_028290_2285). **(b)** Softened topography of the crater wall (HIRISE: ESP_028290_2285). **(c)** Softened topography of the gully fan (HIRISE: ESP_036501_2340). **(d)** Draped LDM deposits on the texturally disrupted wall of a crater (HIRISE: ESP_036451_2210).Image credit: NASA/JPL-Caltech/University of Arizona.

In the southern hemisphere, small-scale LDAs are emplaced from the pole-facing crater wall slopes of SU-2, SU-3, Taltal, SU-4, SU-5, SU-7, SU-9, SU-11, and Tarq **(Figure 4.2)**. The surfaces of these small-scale LDAs are consistent with brain-terrain texture and spatulate depressions at the headward margin of the LDAs **(e.g. Figure 4.12 a-c)**. Arcuate ridges are commonly observed in all the craters with glacial deposits **(e.g. Figure 4.12d)**. In SU-1, Los, SU-6, SU-8 and SU-10 glacial deposits are absent. All walls of the craters with lobate deposits in the southern hemisphere are rich in clasts/boulders, suggesting an active weathering environment. Further, polygonized crater wall surfaces and gully alcoves are evident in SU-2, SU-3, Taltal, SU-4, SU-5, SU-6, SU-7, SU-9, SU-11, and Tarq **(e.g. Figure 4.12e)**. Furthermore, these craters show softened topography resulting from LDM cover **(e.g. Figure 4.12 f)**. In SU-8 and SU-10, there is no evidence of polygonized material although softened crater wall topography and infilled alcoves are evident. Los is the only crater in the southern hemisphere with no evidence of LDM or glacial deposits. There is some evidence of fresh gullies in the mantled crater wall of SU-1 **(Figure 4.12 g)** and beheaded gullies and fans in SU-5, SU-7, and SU-11 **(e.g. Figure 4.12 h)**. Crater wall slopes of SU-1 host gully-fan systems that shows superposing relationships with dunes/TARs in the interior of the crater **(Figure 4.12 i)**.

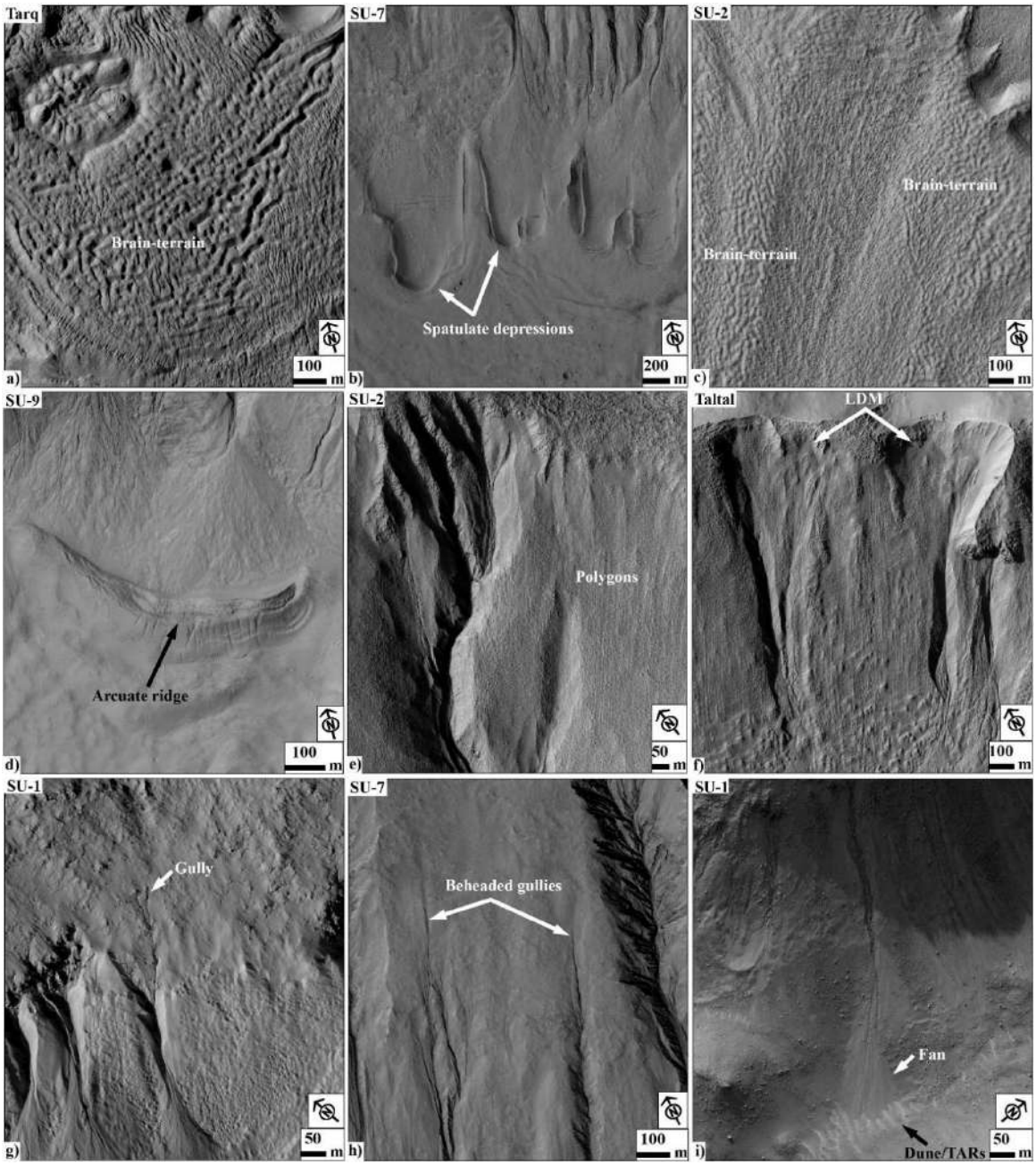

Figure 4.12. (a) LDA surface consistent with brain-terrain texture (HIRISE: ESP_036839_1420). **(b)** LDA flow feature with spatulate depressions (arrow) (HIRISE: ESP_013870_1450). **(c)** CCF consistent with brain-terrain surface texture (HIRISE: PSP_007143_1370). **(d)** Arcuate ridge on the floor of a crater (arrow) (HIRISE: ESP_023640_1430). **(e)** Polygonal cracks on the wall of a crater (HIRISE: PSP_007143_1370).

(f) LDM deposits draped over alcoves and gully walls (HIRISE: ESP_016042_1400). **(g)** Fresh gullies over the wall of a crater (arrow) (HIRISE: ESP_036324_1425). **(h)** Beheaded gullies on the wall of a crater (arrow) (HIRISE: ESP_013870_1450). **(i)** Gully fans superposed over dune/TARs (arrow) (HIRISE: ESP_036324_1425). Image credit: NASA/JPL-Caltech/University of Arizona.

4.3.6. Age relationships

We have estimated the maximum ages of gully formation for 16 craters based on the crater size-frequency distribution (CSFD) **(Table 4.1)**. For SU-2, SU-7 and Tarq, CSFD measurements have been done on the small-scale LDA flow units on the crater floor, while for the remaining 13 craters CSFD measurements have been done on the craters' ejecta. For NU-1, SU-4, SU-6 and SU-8, CSFD could not be performed because the ejecta was heavily mantled, not apparent, or mixed with the ejecta of adjacent craters.

Lobate deposits are found in host craters of all ages **(Figure 4.13)**. The host craters in the northern hemisphere have model ages in the range of ~1.6±0.2 Ma to ~270±60 Ma **(Table 4.1)**. In the southern hemisphere, the host craters range in model age between ~7.9±3 Ma to ~3.0±0.3 Ga **(Table 4.1)**. The glacial deposits emplaced over the floor of SU-2, SU-7 and Tarq yield an average model age of ~30 Ma **(Table 4.1)**. For these craters cross-cutting relations show that the lobate deposits formed in gullies are younger than the model age of the glacial deposits emplaced.

All the craters hosting lobate deposits in the northern hemisphere are found to be affected by LDM deposits and unaffected by LDA/CCF regardless of their age **(Figure 4.13;**

Table 4.1). In the southern hemisphere, Los is the only crater unaffected by LDM or glaciation **(Figure 4.13)**, and it is also the youngest host crater (~7.9±3 Ma). The other craters hosting lobate deposits in the southern hemisphere are affected by LDM deposits and LDA/CCF, except for SU-10 which is affected by LDM only. This shows that lobate deposits can form in any type of crater wall and source material, either previously affected or unaffected by glacial deposits.

SU-4, SU-5, SU-7 and SU-11 contain evidence for multiple generations of gullies and all these craters host glacial deposits, supporting the ideas of **De Haas et al. (2019b)** that gullies go through phases of removal and formation as a result of glacial advance and retreat. For example, in SU-7 **(Figure 4.14)**, there appear to be five morphologically different gully types representing different generations of gully activity: (i) alcoves that are mantled to an extent such that its gullies and fans are completely obscured, (ii) mantled alcove but unmantled gully-fans, (iii) unmantled alcove-gully-fan, (iv) small and younger alcove-gully-fans on the crater walls that are located below the larger alcoves at the crater rim, and (v) multiple beheaded gully-fan systems. Overlapping lobes are evident on the gully types that are still connected to an alcove (ii-v), while absent on the oldest type (i) where gully deposits are largely obscured. On the gully fans of SU-11, colour tones on a false colour image reveal gully fan sectors of different ages. We observe that the overlapping lobate deposits are present in the two youngest sectors, which appear in tones of blue and yellow **(Figure 4.15)**. This shows that only on the most recent parts of the gully fans did lobate deposits form and preserve, while on the older parts of the gully fan they did either not form or did form but were subsequently removed by post-depositional processes.

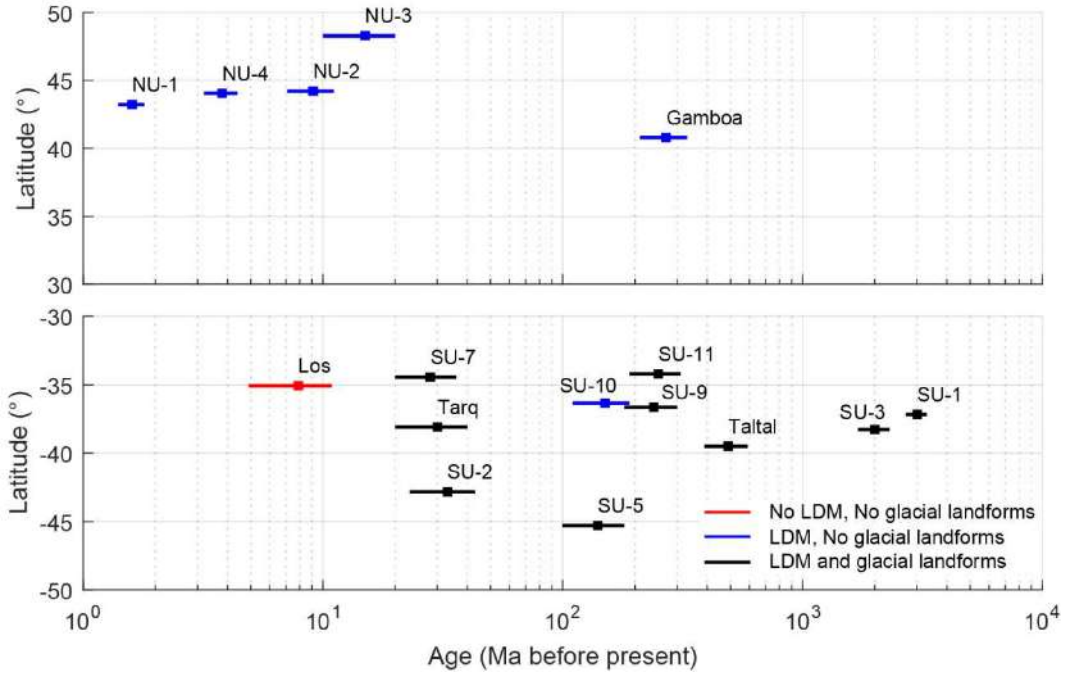

Figure 4.13. Maximum age of the gullies with lobate deposits, inferred from LDA (SU-2, SU-7 and Tarq) or host crater dating. All the craters in the northern hemisphere are having LDM but no glacial landforms. In the southern hemisphere, Los crater is without LDM and glacial landforms and SU-10 is with LDM but no glacial landforms. The other craters in the southern hemisphere are influenced by both LDM and glacial landforms.

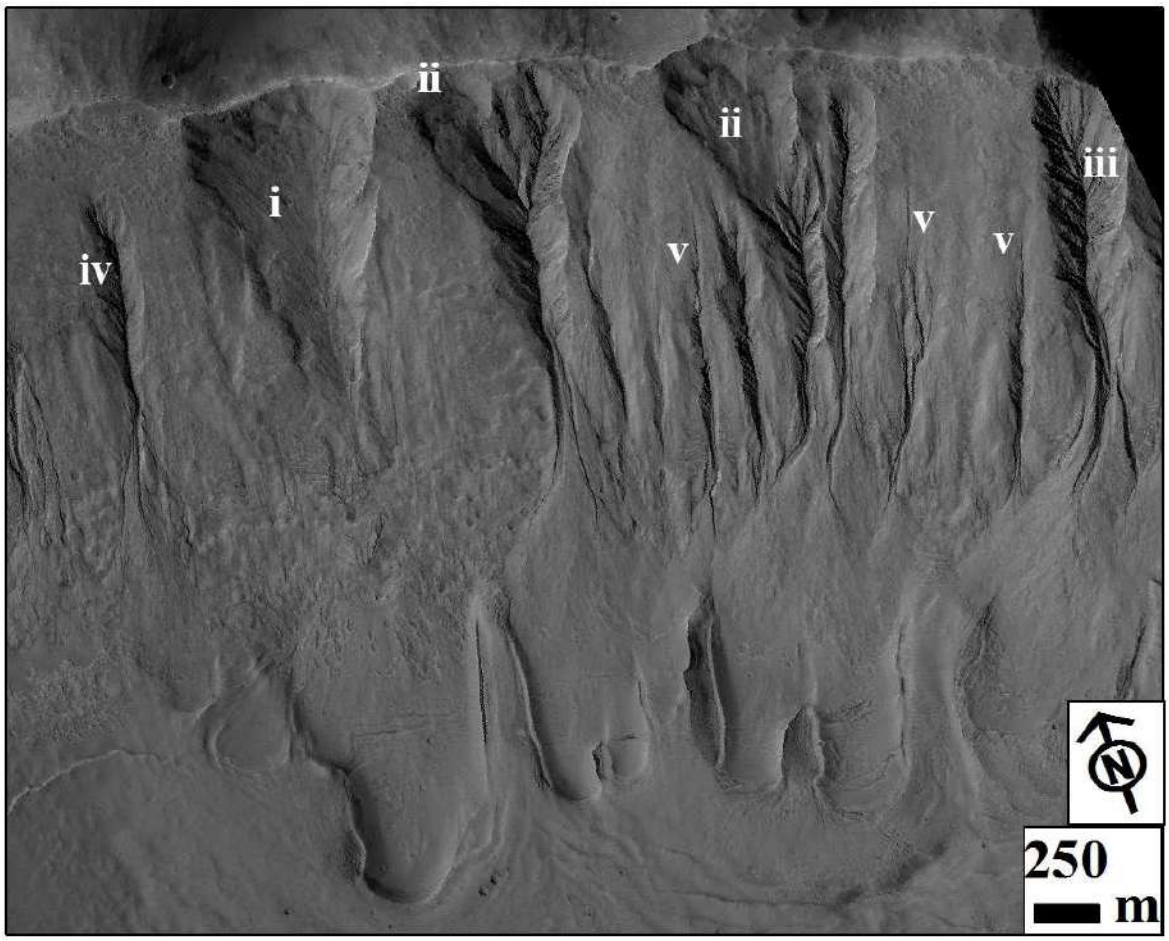

Figure 4.14. Different stages of gully formation and modification within SU-7 (HIRISE: ESP_013870_1450). (i) Extensively mantled alcove-gully-fan. (ii) Mantled alcove; but unmantled gully-fan. (iii) Mantled alcove-gully-fan. (iv) Possibly smaller and younger alcove-gully-fan located well below the larger gully systems that extent to the top of the crater wall. (v) Beheaded gully-fan systems. Image credit: NASA/JPL-Caltech/University of Arizona.

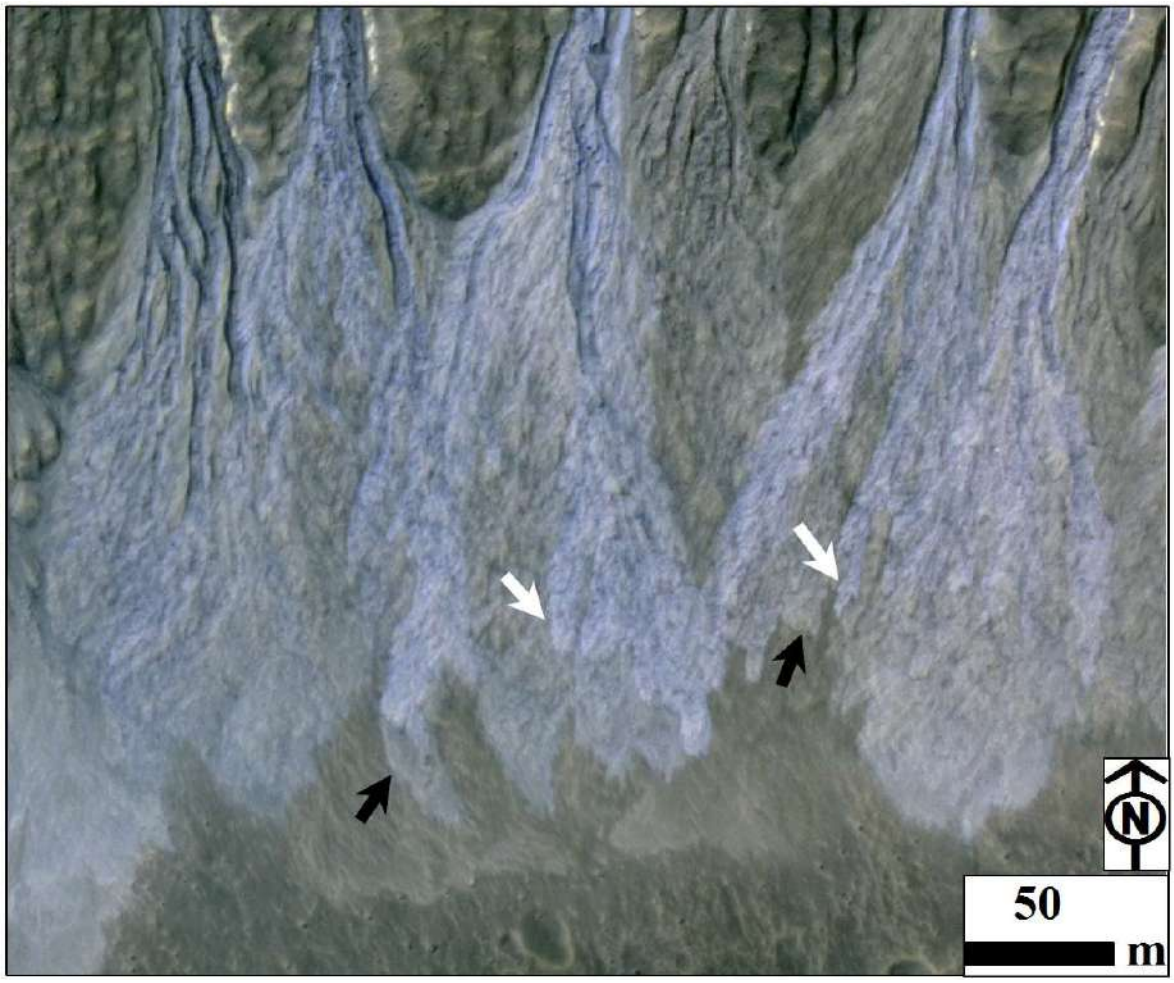

Figure 4.15. HiRISE false color composite image of lobate deposits within SU-11 using the IR, red and BG filters (HIRISE: ESP_047125_1455). The overlapping lobate deposits show distinct tonal appearance mainly in the shades of blue (white arrows) and yellow (black arrows), where color moves from blue to yellow with age. Image credit: NASA/JPL-Caltech/University of Arizona.

4.3.7 Texture of lobate deposits

Large numbers of clasts of varying sizes are present on the walls of craters hosting lobate deposits in the northern and southern hemispheres **(Figure 4.16)**. In general, clasts are abundant in alcoves, along gully banks and over the fan surfaces. Embedded clasts are evident on the top, near the front and along the sides of individual lobes. In our study craters clasts with diameters of~1-4 m are abundant, although smaller sized clasts not resolvable in the HiRISE imagery are likely present as well **(Figure 4.17)**. The size of the clasts is independent of the age of the host crater and presence of LDM or glacial landforms. The peak in the average size range of the observable clasts occurs between 1-2 m. Relatively larger clast, ~4-5 m in diameter, are evident in SU-5 and NU-4 **(Figure 4.17)**.

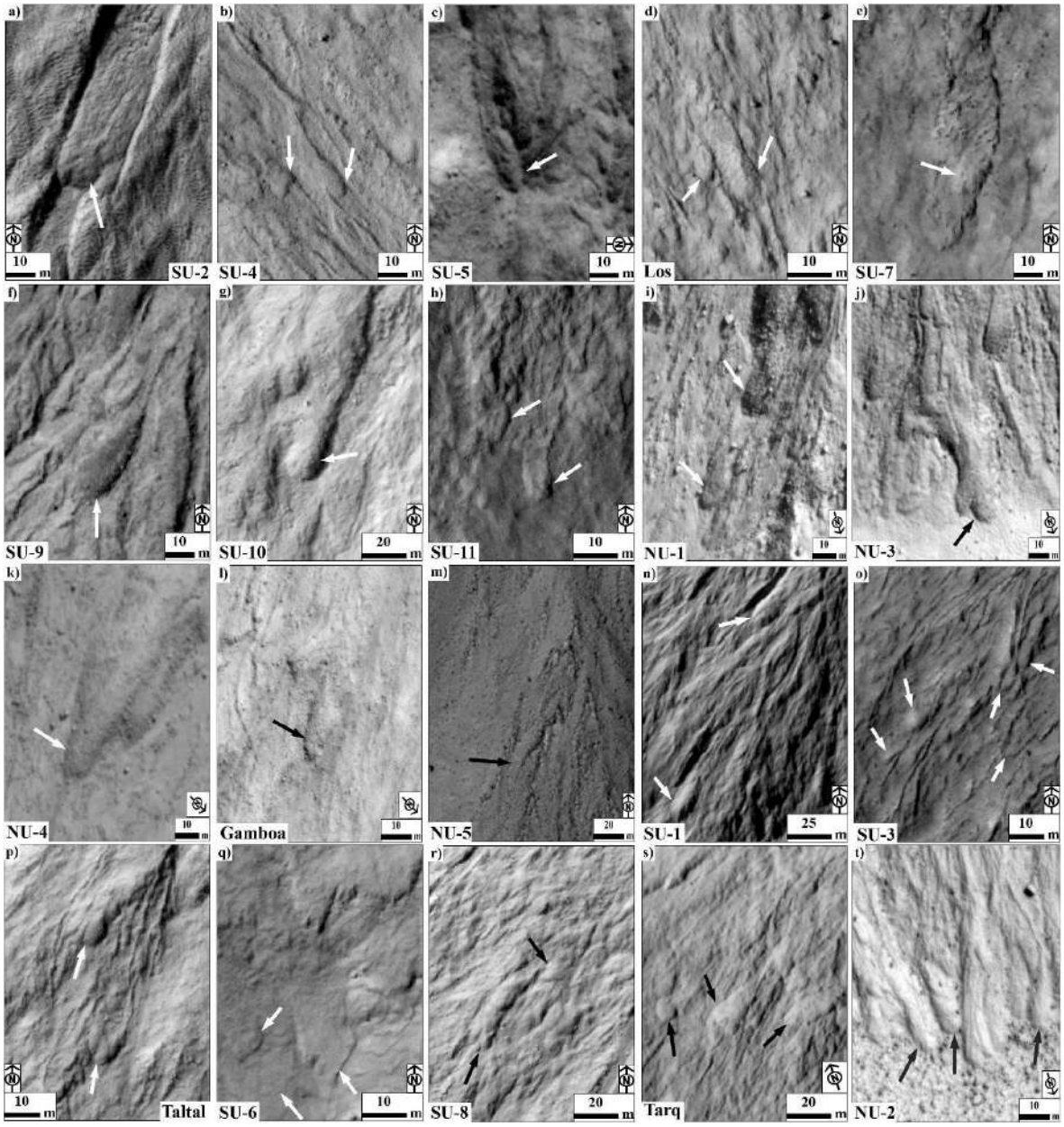

Figure 4.16. Zoomed-in views of lobate deposits. **(a-p)** Examples in which embedded clasts are evident on the top, near the front and along the sides of individual lobes. **(q-t)** Examples of lobes in which clasts could not be resolved. The HiRISE image IDs corresponding to the name of the craters are given in Table 4.1. Image credit: NASA/JPL-Caltech/University of Arizona.

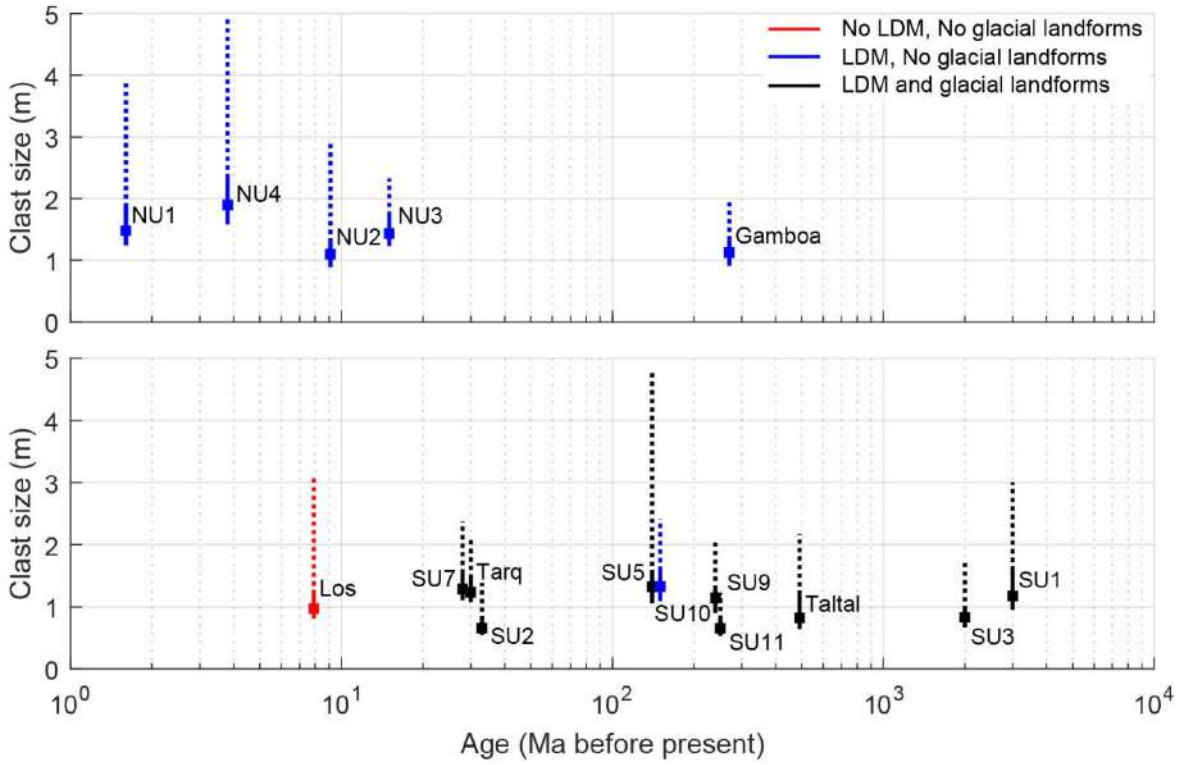

Figure 4.17. Box-plot showing the clast size variation with respect to the age of craters. Top panel shows the clasts within craters in the northern hemisphere and bottom panel is for clasts within craters in the southern hemisphere. The box indicates the median, the solid line the 25th to 75th percentile range, and the top of the dashed line indicates the maximum boulder size. The number of clasts measured in each crater is typically in the range 90-100.

4.3.8. Post-depositional modification of lobate deposits

The older parts of the studied gully fans have a relatively smooth texture and host fewer boulders in comparison to the younger parts of the gully fans **(Figure 4.18a-b)**. On the majority of the gully fans (SU-2, SU-4, SU-5, SU-6, SU-7, SU-8, SU-9, SU-10, and Tarq) **(Figure 4.18c-d)**, there is a marked difference between the number of lobate deposits on the younger, upslope,

parts of the fans versus the older, downslope, fan surfaces, with the younger lobes hosting more and better preserved lobate deposits. If visible on older fan surfaces, lobe margins are generally only faintly evident. The depositional lobes on the younger fan surfaces have a sharper relief and more embedded clasts than the lobes on the older fan surfaces. A few other fans have surfaces that show evidence of post-depositional modification as a result of (1) aeolian activity (Taltal, SU-9, and SU-10) **(Figure 4.18e)** dust mantling (SU-3, Los, SU-8,SU-11, and Gamboa) **(Figure 4.18f-g)** and emplacement of LDM deposits (SU-2, SU-6, SU-8, SU-10,Tarq, NU-1, NU-3, Gamboa, and NU-5) **(Figure 4.18h-i)**. We find that the aeolian activity (wind erosion in particular) has modified the initial fan surface morphology (i.e. lobes and levees) into ridges characterized by sharp, narrow, and subparallel crests that are similar in shape and spatial pattern to aeolian bedforms, such as ripples and small dunes. Wherever LDM is observed, we have noted that the primary morphology is completely masked by the LDM, thereby constraining the identification of lobate deposits even if they were present prior to the emplacement of LDM. In aggregate, our observations show that lobate deposits become progressively obscured over time, by a combination of post-depositional processes. Similar post-depositional fan surface modification has been observed on many gully-fan surfaces reported in a previous study **(De Haas et al., 2015a)**. As lobate deposits are generally only preserved on the youngest parts of gully fans, we infer that they are deposits that formed relatively recently during the latest stages of gully activity.

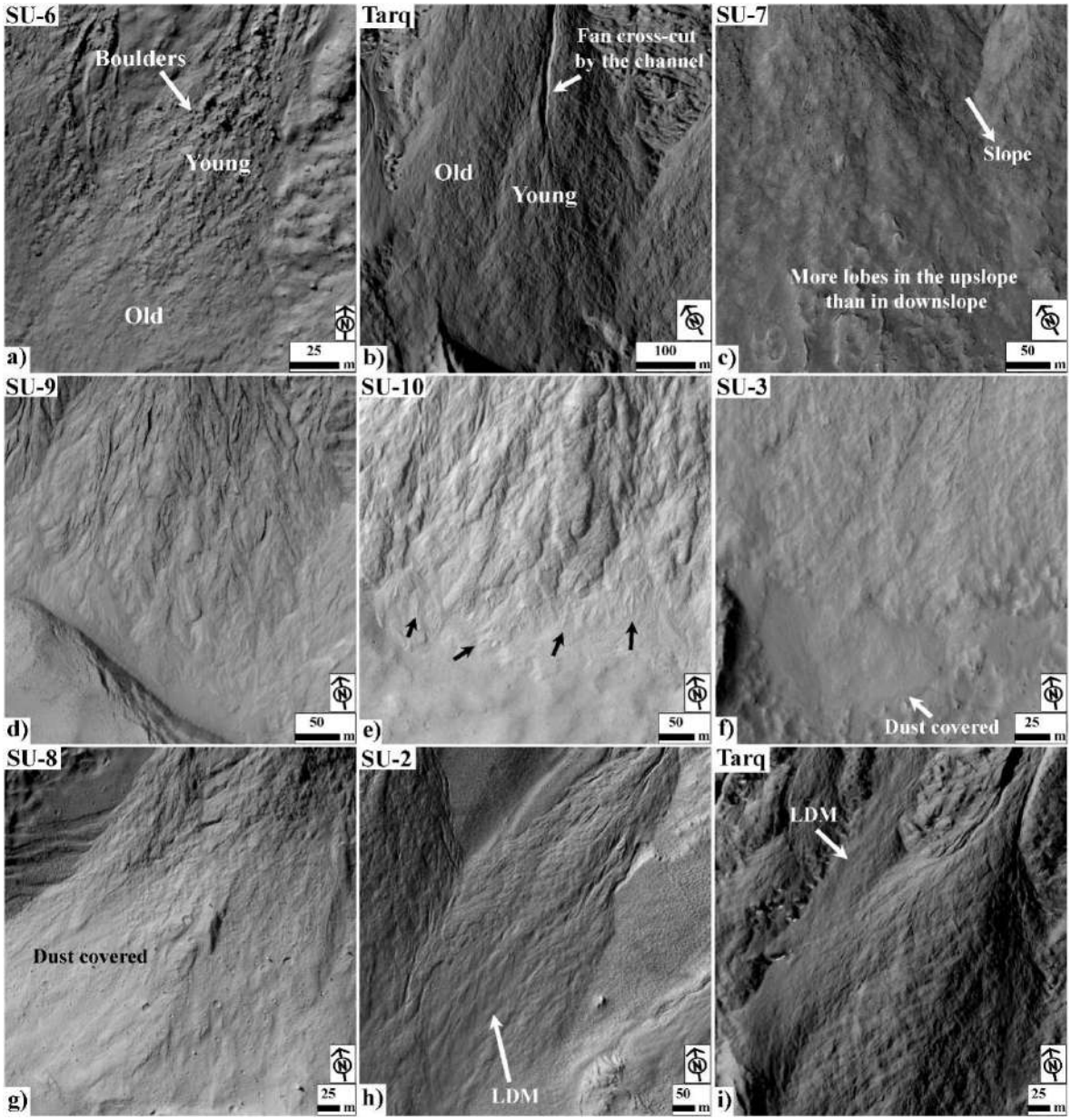

Figure 4.18. Examples of post-depositional modification of lobate deposits on gully-fan surfaces. **(a)**Younger and older parts of the gully-fan surfaces. The younger part hosts more boulders and has more pronounced topography (HIRISE: PSP_007045_1450). **(b)** Older fan surface cross-cut by a channel and superposed by a young channel-fan complex (HIRISE: ESP_036839_1420). **(c-d)**Younger upslope fan surface hosting more lobes than an older more

downslope fan surface (HIRISE: ESP_013870_1450, ESP_023640_1430). **(e)** Fan surface modification by aeolian erosion. Note that the distal part of the fan surface is reworked by aeolian erosion into ventifact or yardang-like features (HIRISE: ESP_028308_1435). **(f-g)** Distal fan surfaces obscured by dust (HIRISE: ESP_038473_1415, ESP_016757_1465). **(h-i)** Fan surfaces masked by LDM cover (HIRISE: PSP_007143_1370, ESP_036839_1420). Image credit: NASA/JPL-Caltech/University of Arizona.

4.3.9. Geomorphic evidence of present-day activity

We examine temporal HiRISE imagery for the craters where we have found lobate deposits, to determine whether the main gully systems have been active in the present day or not. In the southern hemisphere, 8 out of the 14 craters have multi-temporal coverage by HiRISE. For these craters, there is a HiRISE image of Martian winter, and for all these winter season images there is a corresponding HiRISE image of a different season that has a minimum temporal resolution of half a Martian year. Morphological changes only occurred within the gullies formed in SU-1 and SU-2. Here multiple dark flows have formed within the channels in the upper alcove of the main gully system **(Figure 4.19)**. These flows did not appear to have caused any change in the topography of the channels, however. In addition, recurring slope lineae (RSL) have formed nearby on the wall of SU-1 **(Figure 4.19) (Stillman and Grimm, 2018)**. These appear to have originated from the rocky outcrops along the crater rim and their presence is ubiquitous at several locations where there are no gullies. RSLs are also evident in the summer images of Taltal and Tarq **(Stillman and Grimm, 2018)**.

In the northern hemisphere, 4 out of the 6 craters have temporal coverage by HiRISE.

HiRISE images of NU-1 and Gamboa are mainly of summer and spring seasons and despite having a temporal resolution of nearly 3 Martian years we have not observed any significant and/or minor morphological activities in these craters. None of the summer images have evidence of RSL. Nevertheless, in NU-5 we have observed evidence for defrosting in the gully in the form of dark flows **(Figure 4.20)**. Nevertheless, these flows do not seem to have caused any significant change in gully topography. Apart from the aforementioned minor activity, we have not found any evidence for present day formation of lobate deposits nor changes in which the morphology and topography of the gully is distinctly affected.

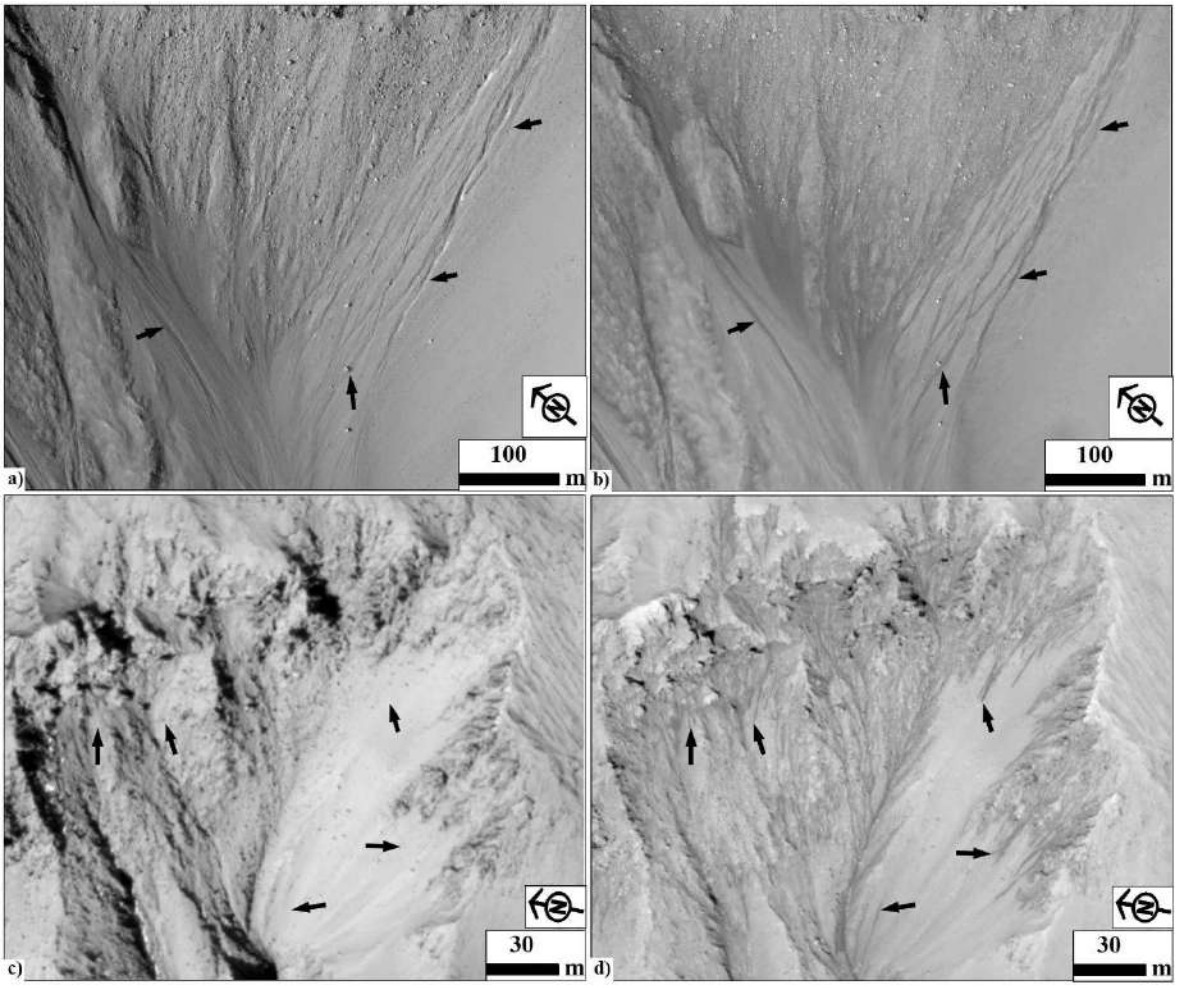

Figure 4.19. (a-b) Morphologic evidence of dark flows inside channels formed in SU-1 (HIRISE: ESP_036324_1425). **(c-d)** Multiple dark flows in the upper alcove of a gully system within SU-2 (HIRISE: PSP_007143_1370). HiRISE image acquisition details: (a) MY 29, L_s: 28.9˚, autumn season. (b) MY 34, L_s: 290.6˚, summer season, (c) MY 32, L_s: 141.5˚, winter season. (d) MY 34, L_s: 288.1˚, summer season. Image credit: NASA/JPL-Caltech/University of Arizona.

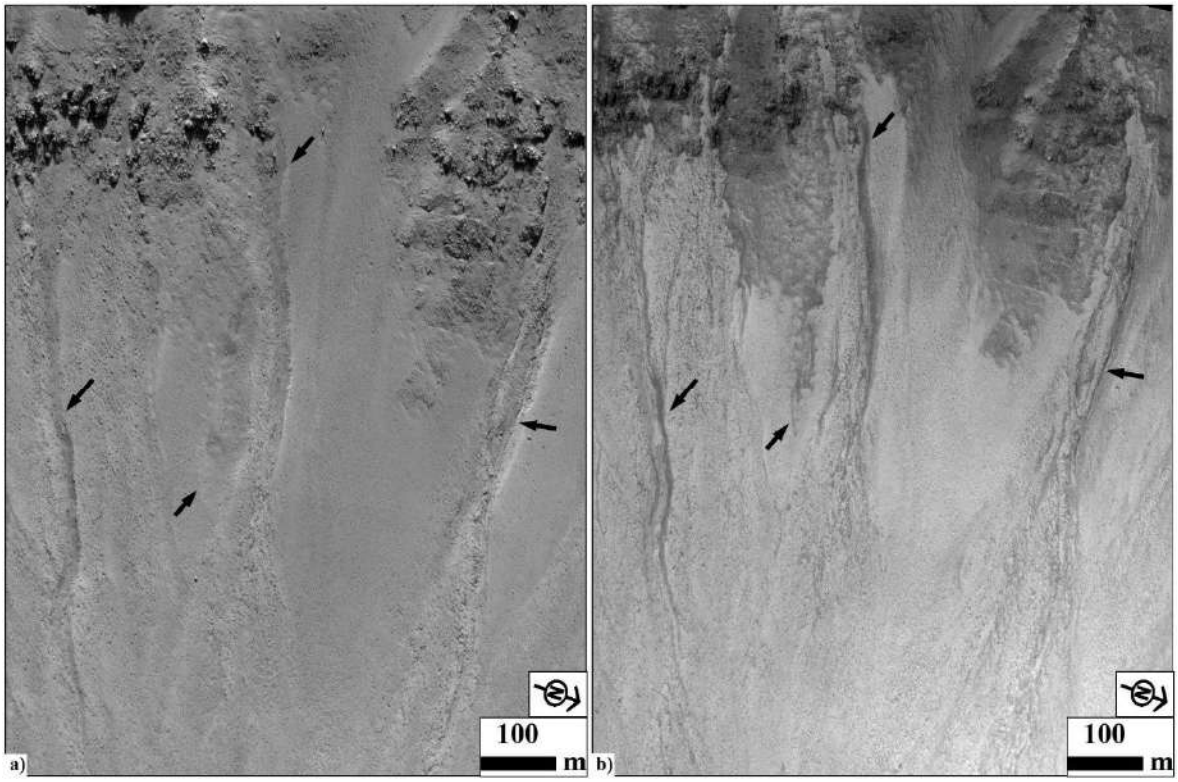

Figure 4.20. (a-b) Example of defrosting flows (arrows) in the gully channels formed within NU-5 (HIRISE: ESP_036501_2340).HiRISE image acquisition details: (a) MY 31, L_s: 112.1˚, summer season. (b) MY 34, L_s: 333.6˚, winter season. Image credit: NASA/JPL-Caltech/University of Arizona.

4.4. Discussions

Our morphological observations of overlapping lobate deposits are in agreement with previous research, which concluded that they closely resemble deposits from debris flows on Earth **(Johnsson et al., 2014; De Haas et al., 2015a; Sinha et al., 2019)**. The key morphological attributes observed are: convex-up, tongue-shaped lobes at channel termini connected to levee deposits along the channel margin, channel backfilling, plug formation and avulsion. Similar spatio-temporal patterns are common on debris-flow fans on Earth **(De Haas et al., 2016; 2018; 2019c)**. The average slope of lobate deposits at the foot of the martian gully fans is 22° in the northern hemisphere and 15° in the southern hemisphere **(Figure 4.7)**. These slope gradients are broadly consistent with the slope values reported at the foot of the gully fans dominated by overlapping lobes in Istok, Galap, Domoni and Maricourt craters **(Johnsson et al., 2014; De Haas et al., 2015a; Sinha et al., 2019)**. These in turn are consistent with deposition slopes of debris flow dominated alluvial fans on Earth in arid and Polar Regions **(De Haas et al., 2015c)** and also deposition slopes for debris flows in talus and hillslope contexts **(Lee et al., 2001; Godin et al., 2019; Conway et al., 2011; Sinha et al., 2019)**.

We found that the interquartile range of slope at the top of gullies for two of the youngest craters (NU-1: ~1.6 Ma and NU-2: ~9.1 Ma) in the northern hemisphere are in the range of 34° to 43°, and in our oldest craters (SU-1: ~3 Ga and SU-3: ~2 Ga) in the southern hemisphere the interquartile range of the slope at the top of the gullies has reduced to 28° to 38° **(Figure 4.7, Table 4.1)**. Among the craters unmodified by glaciation, the interquartile range of slopes at the top and bottom of gullies with lobate deposits in older craters (SU-1, SU-

10, and Gamboa) is lower in comparison to the younger craters (NU-1 and NU-2) **(Figure 4.7, Table 4.1)**. These findings suggest that the age of the craters, LDM, and emplacement of glacial landforms have influenced the slope of the gullied craters with lobate deposits. Los is an exceptionally young (~7.9 Ma) crater in the southern hemisphere which is unmodified by both LDM and glaciation and shows larger variation in the interquartile range of slope values at the top (3° to 24°) and bottom (20° to 27°) of gullies with lobate deposits **(Figure 4.7, Table 4.1)**.

By combining the morphological observations of gullies analysed in this study and those that are reported in the literature **(Lanza et al., 2010; Levy et al., 2010b; Reiss et al., 2011; Johnsson et al., 2014; De Haas et al., 2015a; Sinha et al., 2019)**, we have identified a total of 26 craters within 30-75° latitudes on Mars in which overlapping lobate deposits are evident at the surface of gullies **(Table 4.1)**. This corresponds to 3.39% in total of the 765 craters studied using HiRISE images, which implies that craters hosting lobate deposits are not common, yet they have a wide spatial distribution. We suggest that post-depositional modification of gully-fan surficial features may be crucial in hindering the identification of lobate deposits in gullies. For instance, the surfaces of gully-fan deposits reported here and in the literature have been observed to host polygonized material, covered by LDM and reworked by aeolian activity **(De Haas et al., 2015a; Dickson et al., 2015)**. Evidence for the relative youth of these features is their location at the top of the stratigraphy of gully fans (which may or may not have evidence of underlying lobate deposits) and the presence of abundant surface clasts in the lobes in all the craters in this study bearing morphological resemblance to lobes that are referred to as textured, clast-rich in **Johnsson et al. (2014)** and **Sinha et al. (2019)**. **Figure 4.17** reveals that the clast sizes do not seem to vary with host-crater age and the presence

of LDM and/or glacial landforms, which is in agreement with our observation that lobate deposits are recent deposits formed on the youngest fan sector. We have not observed any significant present-day changes in the morphology and topography of gullies with lobate deposits reported in this study. Only in NU-5, defrosting flows within gully channels present in the winter HiRISE image, but no associated material transport is evident with the available data. **Dundas et al. (2019)** reported the formation of boulder-rich levees and a lobate deposit in Istok crater which occurred during winter coincident with CO_2 frost sublimation. The relative paucity of monitoring data does not allow us to conclude whether overlapping lobate deposits are actively forming in the present day or not, despite our morphological analysis suggesting they are relatively recent.

The gullies hosting lobate deposits reported here do not show any (1) location preference or (2) correlation with regions reported to have high gully density **(Harrison et al., 2015; Conway et al., 2019)**. The presence of lobate deposits inside gullied craters does not appear to be constrained by the crater's diameter. The absolute elevation of gully alcoves associated with lobate deposits shows a wide range in both the northern and southern hemispheres. We find that the dominant orientation preference with respect to latitude for gullies with lobate deposits in the northern and southern hemispheres is poleward-facing and consistent with the previous reports for lobate deposits **(Lanza et al., 2010; Reiss et al., 2011; Johnsson et al., 2014)**. We only find one example of equator-facing gullies with lobate deposits, which could reflect the change to equatorward-facing slopes at latitudes >50°, as in **Sinha et al. (2019)**. The observed latitudinal and orientation distributions of gullies with lobate deposits emphasize the role of insolation and atmospheric conditions in gully formation.

Despite the presence of LDM deposits in all the craters containing lobate deposits in the northern hemisphere, there is no evidence for the presence of glacial landforms. In the southern hemisphere, all but 4 out of 14 craters contain morphological evidence for glaciation and all but one crater (Los crater) contain LDM deposits. Among the previously reported craters hosting lobate deposits, Istok, Galap and Maricourt are the craters in which there is no evidence of glacial landforms and LDM deposits **(Johnsson et al., 2014; De Haas et al., 2015a; Sinha et al., 2019)**. Therefore, lobate deposits are not associated with any particular landscape feature, being found in craters without LDM, with LDM and with both LDM and signs of glaciation, similar to the gully population as a whole **(e.g., De Haas et al., 2019a)**.

The craters containing lobate deposits studied here show a maximum and minimum age of ~3.0 Ga and ~1.6 Ma, respectively. This implies that lobate deposits form on gullies in craters of all ages. Notably, the number of young craters (<10 Ma) is larger in the northern hemisphere (4 craters) in comparison to only 1 crater (Los) in the southern hemisphere. Los is the only young crater that lacks both glacial and LDM deposits. For all other craters, morphological evidence for LDM is present regardless of host crater age. Craters that are unaffected by glaciation do not show a relationship with their age, i.e. craters with model age <10 Ma and >10 Ma both lack evidence of glaciation. There are 4 craters that have preserved evidence for episodic gully formation, regardless of their age. Again, these findings are consistent with the gully population as a whole, where gullies are found on steep slopes regardless of their age of formation.

In summary, the lack of particular spatial, orientation or landscape context for the lobate deposits within the general martian gully population argues that the presence of lobate deposits is not due to a specific process occurring in any given context, but rather a result of a common process, where preservation of the deposits is poor. We argue that the process forming lobate deposits has been active more widely, but its morphological expression is only preserved where lobate deposits formed very recently, or where there are low rates of post-depositional modification **(De Haas et al., 2013, 2015a; Dickson et al., 2015).** This is supported by the fact that lobate deposits are systematically associated with the most recently active fan sector and have abundant surface clasts. Nevertheless, we cannot completely rule out the possibility that lobate deposits are formed by a rare and unique process amongst other processes. In the future, we expect that with the increase in HiRISE coverage of gullies, there will be an increase in the number of lobes identified in gullies although we do not expect large differences in the percentage of gullies hosting lobate deposits. In addition, lobate deposits could also be preserved in gullies formed on massifs, pits, and valleys - which are awaiting morphological investigation.

Further, our results suggest that debris-flow like processes are important for the formation of the lobate deposits and by extension gully-fans on Mars and therefore the transport of sediment through gullies. To produce deposits that resemble those produced by debris flows on Earth implies the involvement of a fluidizing agent, which is most likely to be CO_2 **(De Haas et al., 2019b)** and/or liquid water **(Johnsson et al., 2014)**. The surface environment of Mars under present climate conditions does not allow for sufficient accumulation of liquid water necessary to mobilise a debris flow, but these conditions could have occurred in the last

few million years **(e.g., De Haas et al. 2015b)**. Our data do not allow us to determine if these processes are continuing at the present day, but the observation of new lobate deposits in Istok crater in winter by **Dundas et al. (2019)** suggests these processes could be ongoing. If substantiated by future observations, this would imply that sublimating CO_2 is capable of producing debris-flow like deposits. **Dundas et al. (2019)** outline the mechanism by which sublimating CO_2 mobilises sediment, as follows: a mix of sediment and CO_2 ice fails and its potential energy is converted into kinetic energy and consumed in the phase change of CO_2 ice to gas while falling downslope within a gully channel, and input of additional heat from eroded sediment should maintain the gas generation **(Dundas et al., 2019; De Haas et al., 2019b)**. A recent modelling study has revealed that even small volumetric fractions of CO_2 frost (<1%) within mass flows can generate gas fluxes adequate to fluidize present-day flows in gullies **(De Haas et al., 2019b)**. There are important physical differences between gas-supported granular flows and liquid-supported ones, which should result in morphological differences, but detailed numerical or laboratory investigations would be needed to infer these. Hence, we leave open the possibility that such deposits could be created via water-saturated debris flows under different, yet recent climate conditions.

4.5. Key Findings

We have analysed the geographical distribution of overlapping lobate deposits, their morphological characteristics, slope relationships, orientation preferences, surface texture and clast-size distribution, characteristics of their host craters, evidence of LDM and former ice-related landforms, and age relationships to ultimately speculate on their formation mechanisms.

We have identified 26 craters in which lobate deposits occur in gullies, of which 6 were previously reported. Of these sites, 8 are in the northern hemisphere and 18 are in the southern hemisphere. We find that gullies with overlapping lobate deposits are not differentiable from the general population. They (1) do not show any location preference, (2) are generally poleward-facing in agreement with the gully population as a whole, (3) can be present in craters with and without latitude dependent mantle (LDM) and/or glacier-like-forms, (4) are emplaced at slopes averaging 22° in the northern hemisphere and 15° in the southern hemisphere, and (5) form in craters of all ages.

We infer that the expression of lobate deposits within gullies is based on the preservation of these deposits, wherein, in the older gully fans, the morphological signature of the lobate deposits has been erased by post-depositional processes, as suggested by **De Haas et al. (2015a)**. This inference is supported by evidence for the relatively young age of these deposits compared to other gully-fans, based on our observations of superposition relationships and their association with abundant clasts, and their occurrence on the youngest sectors of gully fans.

Our observations of overlapping convex-up, tongue-shaped terminal lobes, lateral deposits (levees), channel backfilling, plug formation and avulsion, steep deposition slopes, and abundance of clasts (~1-4 m size), also typical in terrestrial debris flows, reinforce the previous interpretation that these deposits are a result of a debris flow-like process. Our data do not allow us to distinguish whether the fluidising agent for this process is sublimating CO_2 ice or liquid water under past climate conditions.

CHAPTER 5

Morphologic and Morphometric Differences in Gullies Formed in Different Substrates on Mars: New Insights into the Gully Formation Processes

Ask the right questions, and nature will open the doors to her secrets.

- Dr. CV Raman

5. Morphologic and Morphometric Differences in Gullies Formed in Different Substrates on Mars: New Insights into the Gully Formation Processes

5.1. Introduction

Gullies are found on steep slopes polewards of about 30° latitude on Mars as a kilometer-scale geologically young feature (formed within the last few million years) comprising an alcove, channel, and depositional fan **(Malin and Edgett, 2000; Dickson et al., 2007; Reiss et al., 2004; Schon et al., 2009)**. Gullies occur in a wide assortment of settings, varying from the walls and central peaks of craters to walls of valleys, and steep faces of dunes, hills, and polar pits **(e.g. Balme et al., 2006; Dickson et al., 2007; Dickson and Head, 2009; Conway et al., 2011, 2015; Harrison et al., 2015)**. On the walls of craters, gullies are found to have incised into the (1) surfaces covered by latitude dependent mantle (LDM; defined as a smooth, meters thick deposit primarily composed of dust and ice), (2) surfaces modified by former episodes of glaciation, and (3) bedrock **(e.g. Mustard et al., 2001; Hubbard et al., 2011; Dickson et al., 2012, 2015; Souness et al., 2012; Souness and Hubbard, 2012; Johnsson et al., 2014; Sinha and Vijayan, 2017; de Haas et al., 2019a; Sinha et al., 2020)**. Detailed investigation of gullies formed over the discriminated substrates is key to understanding the intricacies of past processes by which these gullies have formed on Mars **(Conway et al., 2015; de Haas et al., 2019a)**.

A variety of models have been proposed to explain the formation of gullies, which includes: (1) dry flows triggered by sublimation of CO_2 frost **(e.g. Cedillo-Flores et al., 2011;**

Dundas et al., 2012, 2015; Pilorget and Forget, 2016; de Haas et al., 2019b), (2) debris-flows of both dry and aqueous nature **(e.g. Costard et al., 2002; Levy et al., 2010b; Conway et al., 2011; Johnsson et al., 2014; de Haas et al., 2019a; Sinha et al., 2020)**, and (3) fluvial flows **(e.g. Heldmann and Mellon, 2004; Heldmann et al., 2005; Dickson et al., 2007; Reiss et al., 2011)**. To better understand the gully formation processes, morphometric investigation of gullies formed over discriminated substrates needs to be undertaken at a detail previously not attempted. Previously, only a few studies have analyzed the morphometric characteristics of the gullies by studying long topographic profiles of gullies **(e.g. Hobbs et al., 2014; Conway et al., 2015)**. These studies have suggested that the differences in the properties of substrate into which the gullies incise play a significant role in promoting the flows that led to gully formation. Hence, for a more detailed differentiation of the gully types and interpretation of the dominant flow type that led to gully formation on Mars, quantification of the morphometric characteristics of the entire gully system is crucial.

Global distribution of gullies shows a good spatial correlation with the landforms indicative of glaciation and LDM deposition on Mars **(e.g. Levy et al., 2011; Dickson et al., 2015; Harrison et al., 2015; Conway et al., 2018; de Haas et al., 2019a; Sinha et al., 2020)**. Gullies formed on the formerly glaciated walls of craters are fed from alcoves that do not extend up to the crater rim, and appear elongated to V-shaped, implying gully-channel incision into ice-rich, unlithified sediments **(e.g. Aston et al., 2011; de Haas et al., 2019a)**. The alcoves, channels and fan deposits of gullies formed within craters covered by a smooth drape of LDM, are usually found to have experienced multiple episodes of LDM covering and subsequent reactivation of some of the pre-existing channels or formation of fresh channels within the

draped LDM deposits **(e.g. Dickson et al., 2015; de Haas et al., 2019a)**. Additionally, there are gullies that directly emanate from well-defined bedrock alcoves that cut into the crater rim in absence of LDM and/or glacial deposits **(e.g. Johnsson et al., 2014; de Haas et al., 2019a; Sinha et al., 2020)**. Gullies formed in these craters have pristine alcoves consistent with finely notched edges all around, exposing the underlying bedrock, and hosting many meter-sized boulders throughout in the gully system **(e.g. Johnsson et al., 2014; de Haas et al., 2019a; Sinha et al., 2020)**. Thus, detailed investigation of the morphology and morphometry of the gullies formed over contrasting substrates is important for improving our understanding of the formative mechanisms of gullies.

In this work, we focus on addressing the following research questions:

(1) Do the morphology and morphometry of gully systems formed in different substrates differ (i.e. LDM/glacial deposits and bedrock)?

(2) How do the morphometric characteristics of gullies formed on Mars compare to those formed by a range of processes on Earth, and what does that tell us about the formative processes of Martian gullies?

5.2. Study Sites and Datasets

We characterize the morphology and morphometry of gullies in 29 craters distributed over the southern hemisphere between 30° S and 75° S latitude **(Figure 5.1)**. These 29 craters are selected based on the availability of publicly released High Resolution Imaging Science Experiment (HiRISE) stereo-pair based global digital terrain model (DTM) or the presence of suitable HiRISE stereo-pair images to produce a DTM ourselves. The HiRISE stereo-pair

images are usually ~0.25 - 0.5 m/pixel **(McEwen et al., 2007a)**, so the DTM post spacing is ~1-2 m with vertical precision in the range of tens of centimeters **(Kirk et al., 2008)**. Among the 29 gullied craters, publicly released DTMs are available for 25 craters (https://www.uahirise.org/hiwish/maps/dtms.jsp - last accessed 18th September 2021) **(Table 5.1)**. For the remaining 4 craters, DTMs are produced with the software packages ISIS and SocetSet **(Table 5.1)**. We investigated HiRISE images of these 29 gullied craters for detailed morphological characterization of the substrate in which gullies incised **(Table 5.1)**.

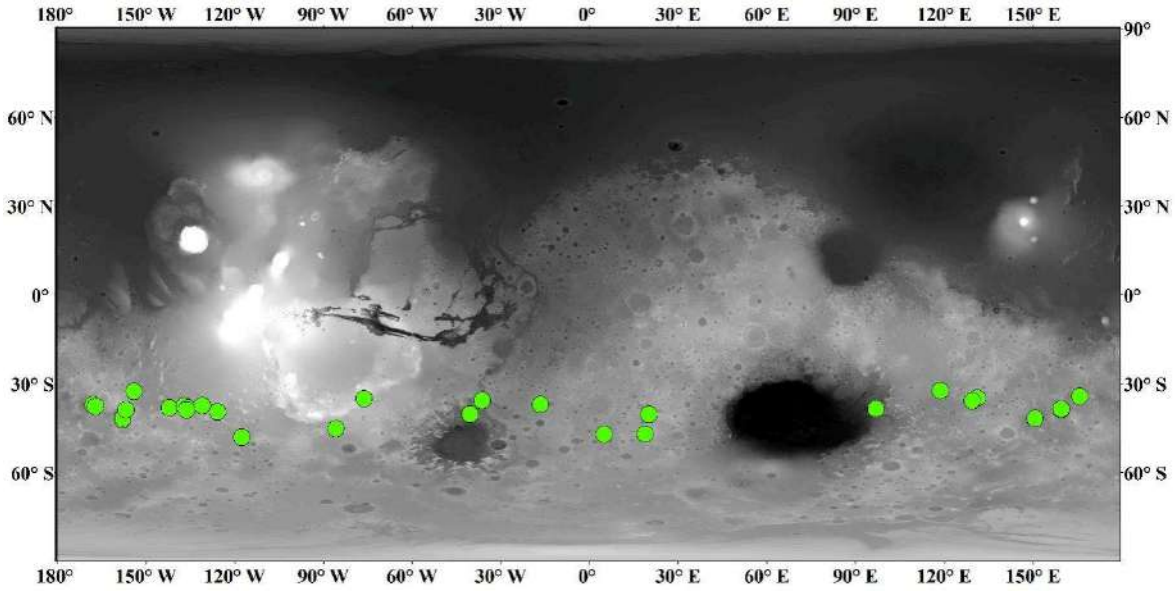

Figure 5.1. Locations of craters analyzed in this study. Background: Mars Orbiter Laser Altimeter gridded data, credit MOLA Science Team/NASA/JPL.

Table 5.1. Summary of the craters included in this study, their locations, diameter, substrate on the crater wall in which gullies have incised, key morphological attributes of the substrate, and IDs of HiRISE imagery and DTM used for morphological and morphometric investigation of gullies in these craters.

Crater	Lati-tude	Long-itude	Dia-meter	Substrate	Key morphological attributes	HiRISE ID	HiRISE DTM ID
Artik	34.8 S	131.02 E	5.4 km	LDM/glacial deposits	Polygons, V-shaped incisions, arcuate ridges, small-scale LDAs on the floor	ESP_020740_1450	DTEEC_012459_1450_012314_1450_A01
Asimov	47.53 S	4.41 E	80.8 km	LDM/glacial deposits	Polygons, V-shaped incisions, mantled alcoves/channels/fans, arcuate ridges, small-scale LDAs inside valleys	ESP_012912_1320	DTEEC_012912_1320_012767_1320_A01
Bunnik	38.07 S	142.07 W	29 km	LDM/glacial deposits	Polygons, V-shaped incisions, mantled alcoves/channels/fans, arcuate ridges	ESP_047044_1420	DTEEC_002659_1420_002514_1420_U01
Corozal	38.78 S	159.48 E	8.3 km	LDM/glacial deposits	Polygons, mantled alcoves/channels/fans, arcuate ridges, small-scale LDAs on the floor	PSP_006261_1410	DTEEC_006261_1410_014093_1410_A01
Dechu	42.23 S	158 W	22 km	LDM/glacial deposits	Polygons, mantled alcoves/channels/fans, arcuate ridges, small-scale LDAs on the floor	PSP_006866_1375	DTEED_023546_1375_023612_1375_A01
Dunkassa	37.46 S	137.06 W	8 km	LDM/glacial deposits	Polygons, V-shaped incisions, mantled alcoves/channels/fans, arcuate ridges, small-scale LDAs on the floor	ESP_032011_1425	DTEEC_039488_1420_039343_1420_A01
Hale	35.7 S	36.4 W	137.3 km	LDM/glacial deposits	Polygons, V-shaped incisions, mantled alcoves/channels/fans, talus slope deposits	PSP_003209_1445	DTEEC_002932_1445_003209_1445_A01
Langtang	38.13 S	135.95 W	9.8 km	LDM/glacial deposits	Polygons, V-shaped incisions, mantled alcoves/channels/fans, arcuate ridges, small-scale LDAs on the floor	ESP_030099_1415	DTEEC_024099_1415_023809_1415_U01
Moni	46.97 S	18.79 E	5.4 km	LDM/glacial deposits	Partly infilled alcoves, mantled fan surfaces, arcuate ridges	ESP_056862_1325	DTEEC_007110_1325_006820_1325_A01

Nybyen	37.03 S	16.66 W	6.2 km	LDM/glacial deposits	Polygons, mantled alcoves/channels/fans, arcuate ridges	ESP_059448_1425	DTEEC_006663_1425_011436_1425_A01
Palikir	41.56 S	157.87 W	15.6 km	LDM/glacial deposits	Polygons, V-shaped incisions, mantled alcoves/channels/fans, arcuate ridges, small-scale LDAs on the floor	ESP_057462_1380	DTEEC_005943_1380_011428_1380_A01
Penticton	38.38 S	96.8 E	8.2 km	LDM/glacial deposits	Polygons, V-shaped incisions, mantled alcoves/channels/fans, arcuate ridges, small-scale LDAs on the floor	ESP_029062_1415	DTEEC_001714_1415_001846_1415_U01
Selevac	37.37 S	131.07 W	7.3 km	LDM/glacial deposits	Polygons, mantled alcoves/channels/fans, small-scale flows on the floor	ESP_045158_1425	DTEEC_003252_1425_003674_1425_A01
Raga	48.1 S	117.57 W	3.4 km	LDM	Polygons, mantled alcoves/channels/fans	ESP_041017_1315	DTEEC_014011_1315_014288_1315_A01
Roseau	41.7 S	150.6 E	6.5 km	LDM	Polygons, mantled alcoves/channels/fans	ESP_024115_1380	ESP_024115_1380_ESP_011509_1380*
Taltal	39.5 S	125.8 W	10 km	LDM/glacial deposits	Polygons, V-shaped incisions, mantled alcoves/channels/fans, arcuate ridges, small-scale LDAs on the floor	ESP_037074_1400	ESP_037074_1400_ESP_031259_1400*
Talu	40.34 S	20.11 E	10 km	LDM/glacial deposits	Polygons, V-shaped incisions, mantled alcoves/channels/fans, arcuate ridges, small-scale LDAs on the floor	ESP_011817_1395	DTEEC_011817_1395_011672_1395_O01
Triolet	37.08 S	168.02 W	12.1 km	LDM/glacial deposits	Polygons, V-shaped incisions, mantled alcoves/channels/fans, arcuate ridges, small-scale LDAs on the floor	ESP_047190_1425	DTEEC_023586_1425_024008_1425_A01
Unnamed crater	32.31 S	118.55 E	4.2 km	LDM/glacial deposits	Polygons, mantled alcoves/channels/fans, arcuate ridges, small-scale LDAs on the floor	PSP_006869_1475	DTEEC_021914_1475_022336_1475_U01
Unnamed crater in the Argyre basin	40.3 S	40.4 W	13.1 km	LDM/glacial deposits	Polygons, mantled alcoves/channels/fans, arcuate ridges, small-scale LDAs on the floor	ESP_032047_1395	DTEEC_012795_1395_013507_1395_A01
Unnamed crater in the Newton basin	38.8 S	156.8 W	35.2 km	LDM	Polygons, V-shaped incisions, mantled alcoves/channels/fans	PSP_002686_1410	DTEEC_002620_1410_002686_1410_A01

Unnamed crater north of Corozal crater	38.53 S	159.44 E	4.6 km	LDM/glacial deposits	Polygons, mantled alcoves/channels/fans, small-scale LDAs on the floor	ESP_020884_1410	DTEEC_020884_1410_020950_1410_A01
Unnamed crater-1 in the Terra Sirenum	32.55 S	154.11 W	2.4 km	LDM	Mantled alcoves/channels/fans	PSP_007380_1470	DTEEC_010597_1470_007380_1470_U01
Unnamed crater-2 in the Terra Sirenum	38.88 S	136.36 W	9.5 km	LDM/glacial deposits	Polygons, V-shaped incisions, mantled alcoves/channels/fans, arcuate ridges, small-scale LDAs on the floor	ESP_020407_1410	DTEEC_022108_1410_022385_1410_A01
Istok	45.1 S	85.82 W	4.8 km	Bedrock	Alcove cut directly into the original crater-wall material, clasts embedded into fresh deposits on fan	ESP_056668_1345	DTEEC_040607_1345_040251_1345_A01
Galap	37.66 S	167.07 W	6 km	Bedrock	Alcove cut directly into the original crater-wall material, clasts embedded into fresh deposits on fan	ESP_059770_1420	DTEEC_048983_1420_048693_1420_U01
Gasa	35.73 S	129.4 E	7 km	Bedrock	Alcove cut directly into the original crater-wall material, clasts embedded into fresh deposits on fan	ESP_057491_1440	DTEEC_021584_1440_022217_1440_A01
Los	35.08 S	76.23 W	8.1 km	Bedrock	Alcove cut directly into the original crater-wall material, clasts embedded into fresh deposits on fan	ESP_020774_1445	ESP_020774_1445_ESP_050127_1445*
Unnamed crater-3 in the Terra Sirenum	34.27 S	165.71 E	3.4 km	Bedrock	Alcove cut directly into the original crater-wall material, clasts embedded into fresh deposits on fan	ESP_049261_1455	ESP_049261_1455_ ESP_049828_1455*

(*) DTMs are produced with the software packages ISIS and SocetSet.

5.3. Approach

5.3.1. Identification of substrate

The substrate into which the gullies have incised is identified based on the following criteria:

1. LDM/glacial deposits: Any gullied crater whose walls appear to be softened by the drape of smooth mantling material consistent with polygonal cracks is inferred to have LDM as the substrate within which gullies have incised **(e.g. Mustard et al., 2001; Kreslavsky and Head, 2002; Levy et al., 2009a; Conway et al., 2018; de Haas et al., 2019a) (Figure 5.2a)**. The alcoves on the walls of these craters maybe partially to completely filled, and in some cases, polygonized LDM materials may be seen covering the alcove walls **(Figure 5.2b) (e.g. Christensen, 2003; Conway et al., 2018; de Haas et al., 2019a)**. Additionally, gullied craters that show evidence in the form of arcuate ridges at the foot of the walls and small-scale lobate debris apron (LDA) like deposits that cover part or the entire crater floor are inferred to have been modified by one or multiple episodes of glaciation **(Figure 5.2c) (e.g. Arfstrom and Hartmann, 2005; Head et al., 2010; Milliken et al., 2003; Hubbard et al., 2011)**. The crater walls on which gullies are present in these craters are often, at least partly, covered by LDM deposits.
2. Bedrock: Crater walls that do not appear softened as a result of the drape of smooth mantling material and lack arcuate ridges along the base of the crater wall or deposits on the crater floor are expected to have exposed fractured bedrock in which gully alcoves have incised **(Figure 5.2d)**.

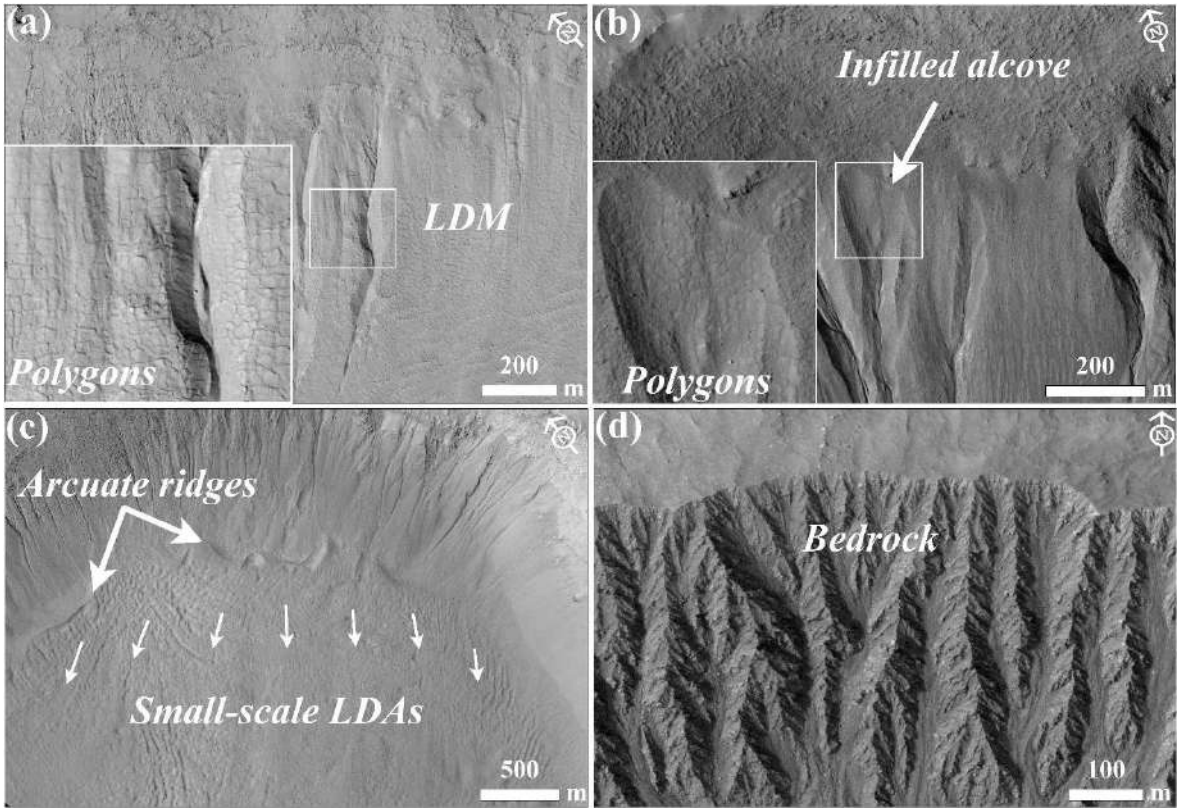

Figure 5.2. Examples of morphological evidence used to identify LDM, glacial deposits, and bedrock. **(a)** Smooth mantling material inferred as LDM draped on the wall of Talu crater on the basis of polygonal cracks formed in the material. The bigger box is an expanded view of the polygons seen over the region outlined by the smaller box. (HiRISE image ESP_011817_1395). **(b)** An infilled alcove on the wall of an unnamed crater-2 in the Terra Sirenum. Evidence of polygons in the infilled material suggests presence of LDM deposits draped on the wall. The region shown in smaller box is expanded in the bigger box to show evidence of polygons. (HiRISE image ESP_020407_1410). **(c)** Glaciation inferred in the Corozal crater on the basis of arcuate ridges formed at the foot of the crater wall and small-scale LDAs on the crater floor. Arrows indicate the downslope flow of LDAs on the floor. (HiRISE image PSP_006261_1410). **(d)** Exposed fractured bedrock identified on the walls of

Istok crater within which alcoves have incised. (HiRISE image ESP_056668_1345). HiRISE image credit: NASA/JPL-Caltech/University of Arizona.

5.3.2. Morphometric variables

The key features of a gully system includes alcove area, alcove perimeter, alcove length, alcove width, alcove gradient, fan area, fan length, fan width, and fan gradient. In total, 18 morphometric variables were used to characterize each gully fan and its alcove. Morphometric variables are classified into geometry, relief, gradient, and dimensionless variables and were evaluated with established mathematical equations shown in **Table 5.2**. For the gradient measurement using DTM, topographic profile from (1) crest of the alcove to the apex of the fan was extracted for alcove, and (2) apex to foot of the fan was extracted for fan.

5.3.3. Gully system selection for morphometric measurements

We have selected only those gully systems for morphometric measurements in which: (i) the depositional fan from an alcove-channel system is not superimposed or mixed with the fans from the neighboring channels, (ii) there is clear association between the primary channel emanating from the alcove that extends downslope to deposit its respective fan, (iii) no evidence of extensive cross-cutting is seen with the neighboring channels on the walls, (iv) no evidence of extensive mantling by dust/aeolian landforms is apparent, and (v) no evidence of channel/fan superposition on any topographic obstacle on the walls or the floor is apparent, which may eventually influence the morphometric measurements. Note that the selection of the gully fans was also constrained by the coverage of HiRISE DTM that was used for morphometric analysis.

Table 5.2. Set of morphometric variables extracted from the studied gully systems and their formulas and/or description of method.

Morphometric variable	Formula and/or description of method	References
Alcove length and width	Measured in km	**Tomczyk, 2021**
Alcove area	Measured in km^2	**Tomczyk, 2021**
Fan length and width	Measured in km	**Tomczyk, 2021**
Fan area	Measured in km^2	**Tomczyk, 2021**
Melton ratio	(Alcove relief)/(Alcove area$^{-0.5}$)	**Melton, 1957**
Relative concavity index	Concavity Index/(maximum relief between the uppermost and lowermost points along the gully fan profile/2). Concavity Index is estimated as $\sum (H_i^* - H_i) / N$, where H_i^* is the elevation along the straight line, H_i is the elevation along the gully fan profile, N is the total number of measurement points.	**Langbein, 1964; Phillips and Lutz, 2008**
Alcove gradient	Measured in (°)	**Tomczyk, 2021**
Fan gradient	Measured in (°)	**Tomczyk, 2021**
Alcove relief	Measured in km	**Tomczyk, 2021**
Fan relief	Measured in km	**Tomczyk, 2021**
Relief ratio (alcove and fan)	Alcove/fan relief divided by the length of the alcove/fan	**Schumm, 1956a, b**
Perimeter	Measured in km	**Schumm, 1956a, b**
Form factor	Alcove area divided by the square of the length of the alcove	**Horton, 1932**
Elongation ratio	Diameter of a circle of the same area as the alcove divided by the maximum alcove length	**Schumm, 1956a, b**
Circularity ratio	Alcove area divided by the area of the circle having the same perimeter as the alcove perimeter	**Miller, 1953**

5.3.4. Statistical analysis of morphometric variables

We have two groups of gullies in our study: (1) gullies incised into LDM/glacial deposits and (2) gullies incised into the bedrock. At first, for both the groups we have calculated descriptive statistics for each of the morphometric variables shown in **Table 5.2**. The significance of the difference in the values of each morphometric variables between the groups was tested using Student's *t*-tests. The *t*-test can be used to determine whether the two sample means are statistically different from each other. To apply t-tests, we have transformed the morphometric variables to remove skewness by taking their natural logarithm. Correlation analysis has been used to investigate the correlation between the selected morphometric attributes of alcoves and fans. We infer strong positive correlations between variables if the correlation coefficient value is more than 0.7 and strong negative correlations if the value is less than -0.7. Very strong positive correlation between variables is inferred if the correlation coefficient is >0.9. Further, we used canonical discriminant analysis (CDA) to determine morphometric variables that produce a best discrimination between the groups of gullies. In CDA, functions are generated according to the number of groups, until a number equal to *n*-1 functions is reached (*n* is the number of groups) **(Conway et al., 2015)**. For the two groups of gullies in our study, there is going to be a function for which there is a standardised canonical discriminant function coefficient associated with the morphometric variable. The higher the magnitude of this coefficient for a particular morphometric variable, the higher would be the role of that variable in separating the groups of gullies.

5.4. Results

5.4.1. Morphology of gully systems

Out of the 29 gullied craters analysed in this work, we have found that there are 24 craters with LDM and glacial deposits as the primary substrate, within which gullies have incised. The remaining 5 craters have gullies incised into the exposed underlying bedrock on the wall of the crater. Below we describe the substrates identified in the studied craters and then compare the morphology of the gullies formed into those substrates.

We found morphological evidence of LDM in the form of polygonized, smooth textured material on the pole-facing walls of 4 craters namely Raga, Roseau, and unnamed craters in Newton basin and Terra Sirenum. Morphological evidence of glacial deposits is not evident in these craters. In these craters, the gully-alcoves and the gully-fan deposits both are covered by a smooth drape of polygonized LDM material. A typical example of this can be found in the unnamed crater formed inside the Newton basin **(Figure 5.3a)**. Roseau crater, in particular, contains a large number of gully systems whose alcoves and fans are extensively mantled **(Figure 5.3b)**. The remaining 20 out of 24 craters contain evidence for both LDM and glacial deposits **(Table 5.1)**. The base of the pole-facing walls and the floor of the craters within which the gully systems have formed host linear-to-sinuous arcuate ridges and small-scale LDAs, respectively. Typical examples of these glacial deposits can be found in Corozal, Talu, unnamed craters in Terra Sirenum and Argyre basin, Langtang, Dechu and Dunkassa craters **(Figure 5.3c)**. Gullies incised into LDM/glacial deposits are found to have a distinctive V-shaped cross section in their mid-section, they do not extend up to the crater rim, and often show multiple

episode of activity, by the presence of fresh channel incision on the gully-fan surfaces **(Figure 5.3d-e)**.

Istok, Galap, Gasa, Los, and an unnamed crater in the Terra Sirenum contain gully systems on the pole-facing walls that are not associated with LDM and glacial deposits **(Table 5.1)**. The alcoves inside these craters have a crenulated shape and appear to have formed by headward erosion into the crater rim **(Figure 5.3f)**. These craters have formed large gully systems on their pole-facing walls, with brecciated alcoves, comprising of multiple sub-alcoves and hosting many clasts/boulders **(Figure 5.3f)**.

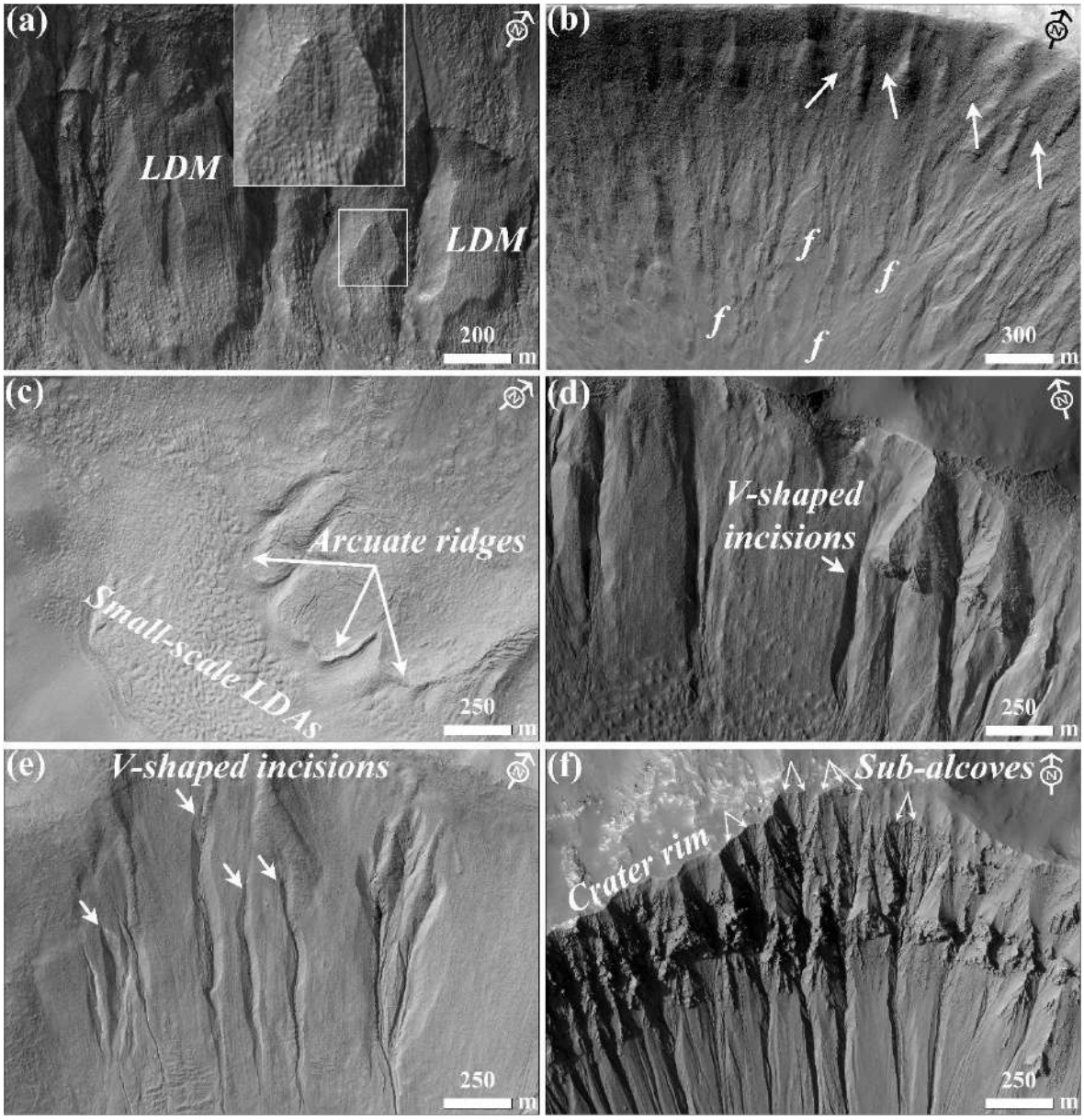

Figure 5.3. (a) LDM draped on the wall of an unnamed crater in the Newton basin. The smaller box is expanded to present the evidence of polygons ion the bigger box. (HiRISE image PSP_002686_1410). **(b)** Infilled alcoves (arrows) and mantled fan surfaces (marked by letter 'f') on the wall of Roseau crater. (HiRISE image ESP_024115_1380). **(c)** Arcuate ridges at the foot of wall and small-scale LDAs on the floor in Langtang crater. (HiRISE image ESP_030099_1415). **(d)** V-shaped incisions on the LDM draped walls of Taltal (HiRISE image

ESP_037074_1400) and Langtang crater (HiRISE image ESP_030099_1415) **(e)**. **(f)** Alcoves formed in Los crater by headward erosion into the crater rim. Individual alcoves formed in bedrock have multiple sub-alcoves. (HiRISE image ESP_020774_1445).

5.4.2. Morphometry of gully systems

Based on the criteria summarized in section 3.3, we have studied 167 gullies across 29 craters for calculation of morphometric variables. 130 gullies are formed within LDM/glacial deposits, and 37 gullies are formed within the bedrock. The results of morphometric calculations are summarized for visual comparison as a boxplot **(Figure 5.4)**.

The results of the Student's t-test indicates that all of the morphometric variables in **Table 5.2**, except fan width, fan area, melton ratio, form factor, elongation ratio, and circularity ratio, differ significantly between LDM/glacial deposits and bedrock **(Figure 5.4)**. Compared to the mean gradient of gully-fans formed in LDM/glacial deposits, bedrock gully-fans are relatively steeper and possess higher relief ratio. The interquartile range of length, relief, and perimeter of alcoves formed in bedrock are also higher than the interquartile range of similar variables in LDM/glacial deposits, but the alcoves in LDM/glacial deposits possess much higher values of length, relief, and perimeter **(Figure 5.4)**.

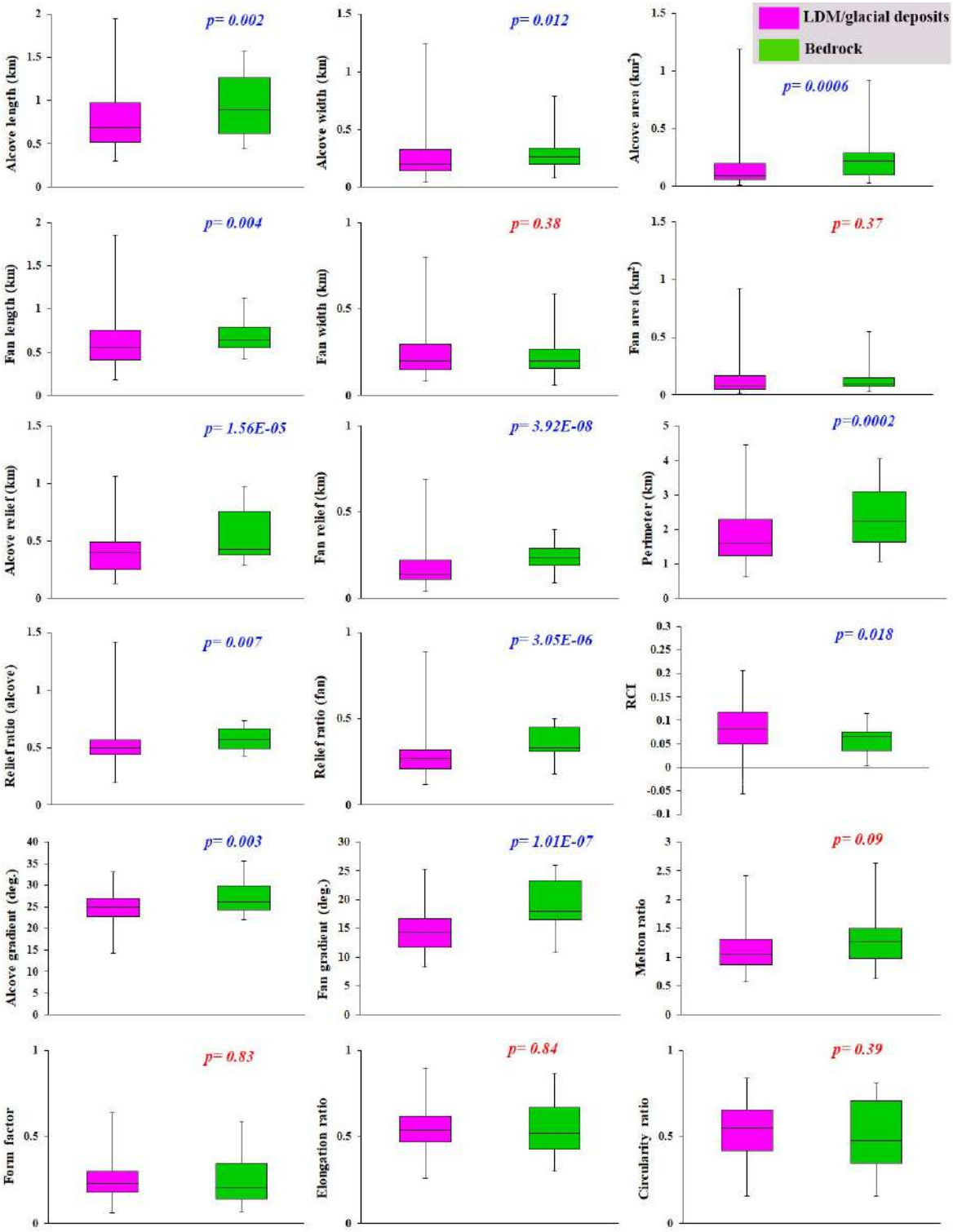
LDM/glacial deposits
Bedrock
Alcove length (km)
p= 0.002
Alcove width (km)
p= 0.012
Alcove area (km²)
p= 0.0006
Fan length (km)
p= 0.004
Fan width (km)
p= 0.38
Fan area (km²)
p= 0.37
Alcove relief (km)
p= 1.56E-05
Fan relief (km)
p= 3.92E-08
Perimeter (km)
p=0.0002
Relief ratio (alcove)
p= 0.007
Relief ratio (fan)
p= 3.05E-06
RCI
p= 0.018
Alcove gradient (deg.)
p= 0.003
Fan gradient (deg.)
p= 1.01E-07
Melton ratio
p= 0.09
Form factor
p= 0.83
Elongation ratio
p= 0.84
Circularity ratio
p= 0.39

Figure 5.4. Boxplots showing the range of values of alcove/fan geometry, relief, gradient, and dimensionless variables of gullies incised into LDM/glacial deposits (pink) and bedrock (green). P-values on the plots represent the results of the student's t-tests for testing the significance of difference in means of the morphometric variables between gully systems formed on LDM/Glacial deposits and bedrock. P-values in blue correspond to significant difference and those in red are non-significant.

Correlations between morphometric attributes of alcoves and fans formed in bedrock and LDM/glacial deposits are summarized in **Figure 5.5.** For bedrock, there are strong positive correlations between 12 pairs of morphometric variables and strong negative correlations between 3 pairs of morphometric variables. For LDM/glacial deposits, there are strong positive correlations between 18 pairs of morphometric variables and strong negative correlations between 3 pairs of morphometric variables. Very strong positive correlations are found between 9 pairs of morphometric variables for bedrock and between 4 pairs of morphometric variables for LDM/glacial deposits.

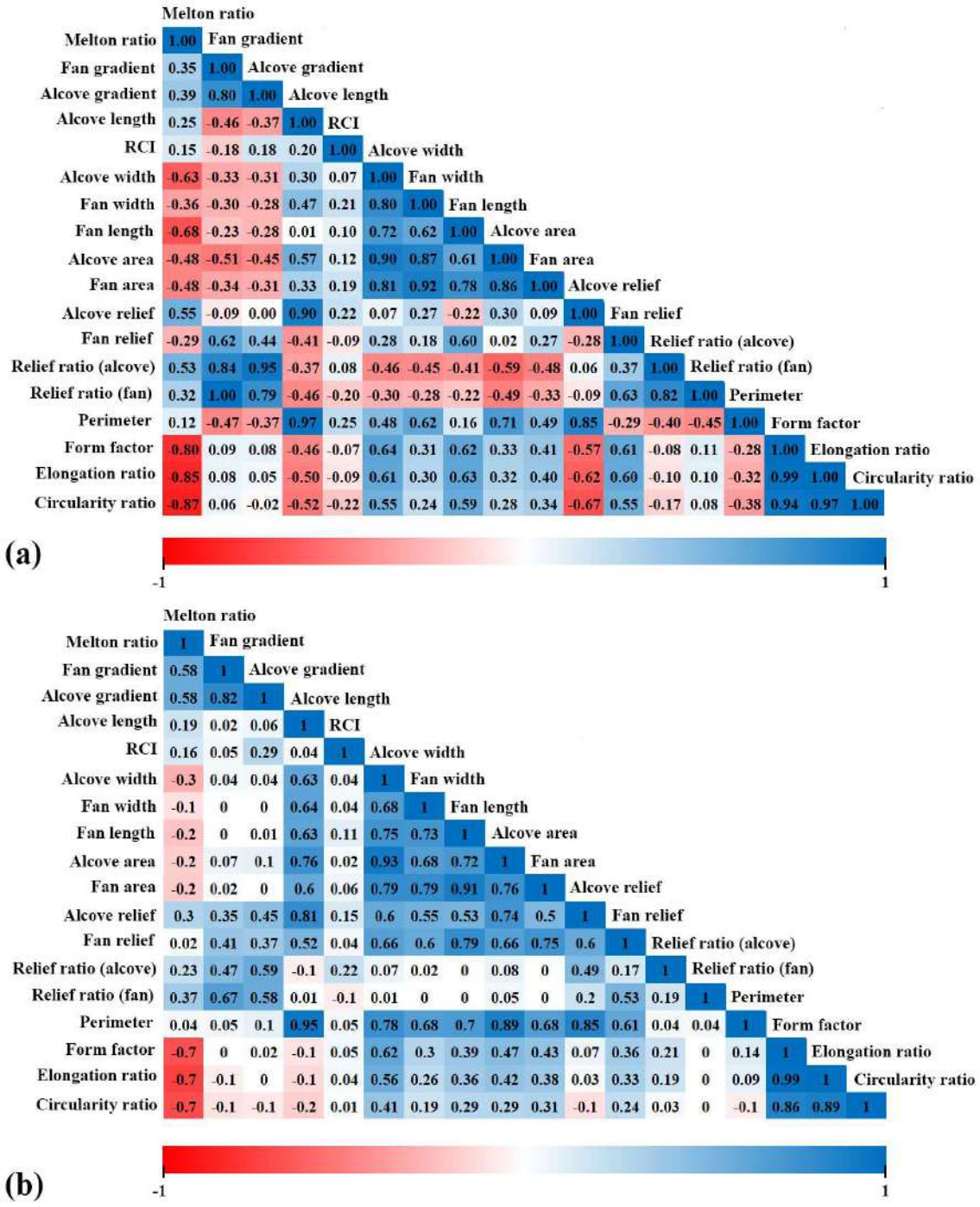

Figure 5.5. Correlations between morphometric attributes of alcoves and fans formed in **(a)** bedrock and **(b)** LDM/glacial deposits. Higher the value of the correlation coefficient, higher is the strength of the correlation.

The discriminatory analysis reveals differences between the gully systems formed in LDM/glacial deposits and bedrock on the following morphometric variables, in descending order of importance: alcove length, fan gradient, form factor, fan length, circularity ratio, elongation ratio, alcove gradient, alcove relief, fan width, melton ratio, fan area, fan relief, alcove width, and perimeter **(Table 5.3)**. The alcove length participates significantly in discriminating among the gully systems formed within LDM/glacial deposits and bedrock, and the next two important variables have greater than half of the weight of the most important variable. The remaining variables, except alcove width and perimeter, have half of the weight of the most important variable or lesser discriminatory power in separating the gullies formed in LDM/glacial deposits and bedrock. The variables with the smallest magnitude, alcove width and perimeter, have 1/5 the weight of the most important variable or lesser in separating the gully systems. We find that the alcove area does not participate at all in separating between the gully systems.

Table 5.3. Standardised canonical discriminant function coefficients that best separate gully systems formed on LDM/Glacial deposits and bedrock.

Variable	F1
Alcove length	1.904
Fan gradient	1.367
Form factor	1.245
Fan length	0.898
Circularity ratio	-0.897
Elongation ratio	0.870
Alcove gradient	-0.782
Alcove relief	-0.687
Fan width	-0.657
Melton ratio	0.602
Fan area	-0.589
Fan relief	-0.557
Alcove width	-0.387
Perimeter	0.051
Alcove area	0.000

5.5. Discussions

5.5.1. Unique morphology and morphometry of gully systems in different substrates

We have found that the gully systems formed in LDM/glacial deposits and bedrock can, using discriminatory analysis, be distinguished from one another in terms of the length of alcoves. Additionally, we have found a statistically significant difference between the length of alcoves formed in LDM/glacial deposits and bedrock. It is likely that these differences in the length of alcoves formed within morphologically distinct substrates could be due to the integral nature of the surface material within which the alcoves have formed. In other words, it is possible that the differences in the physical properties of the sediments (viz. grain size, compactness etc.) within which alcoves have formed played a key role in the erosion of the substrate leading to differences in their morphometric variables. Below we elaborate on the uniqueness of the substrates within which alcoves have formed, and discuss further the relationships between the morphometric variables of the morphologically distinct gully systems.

On Mars, LDAs are glacial landforms interpreted to have formed from the mobilization and flow of ice-cemented debris composed of boulders and fine-grained sediments **(Sharp, 1973; Squyres, 1978, 1979; Squyres and Carr, 1986)**. Their surfaces have been interpreted to be comprised of finer, reworked debris derived from the sublimation of the underlying ice **(Mangold, 2003b; Levy et al., 2009a; Morgan et al., 2009)**. The smooth, meters-thick draping unit on the walls of formerly glaciated craters has been suggested to be derived from the atmosphere as a layer of dust-rich ice primarily constituting fine-grained materials

(Kreslavsky and Head, 2000; Mustard et al., 2001). The fine-grained materials are loosely-packed, unconsolidated materials exhibiting low thermal inertia values **(Mellon et al., 2000; Putzig et al., 2005)**. Typically, gullies formed within this substrate display a smooth surface texture, wherein, evidence of individual clasts or meter-scale boulders is not resolvable in HiRISE images, substantiating the dominant component of fine-grained materials within the LDM **(e.g., Levy et al., 2010b; de Haas et al., 2015a, 2019a)**. Additionally, it has been found that alcoves incised into the LDM always have a distinctive V-shaped cross-section in their mid-section, which when compared with similar-scaled systems on Earth also corresponds to the presence of loose sediments constituting the LDM **(Conway et al., 2018)**. The alcoves that are V-shaped in cross section are often elongated, suggesting incision into ice-rich unlithified sediments **(Aston et al., 2011)**. In the studied craters, we have found that gullies incised into LDM/glacial deposits are having an elongated, V-shaped cross-section in their mid-section. We propose that the presence of fine-grained, loosely packed, unconsolidated materials within LDM/glacial deposits has facilitated formation of elongated alcoves with length relatively longer than the length of alcoves formed in coarse-grained bedrock substrate. This is consistent with the previous studies suggesting that gullies eroding into LDM/glacial deposits have elongated catchments, whereas gullies eroding into the bedrock have more amphitheater-shaped catchments **(Levy et al., 2009c)**. Additionally, the presence of fine-grained sediments in LDM/glacial deposits is the likely cause of the V-shape of the incision of alcoves investigated in this study. On Earth, V-shaped incisions through glacial ice-rich moraines have been observed to have occurred during the paraglacial phase of glacial retreat **(Bennett et al., 2000; Ewertowski and Tomczyk, 2015) (Figure 5.6)**. The paraglacial phase refers to a terrestrial

post-glacial period that represents the response of changing environment to deglaciation **(Jawin and Head, 2021)**.

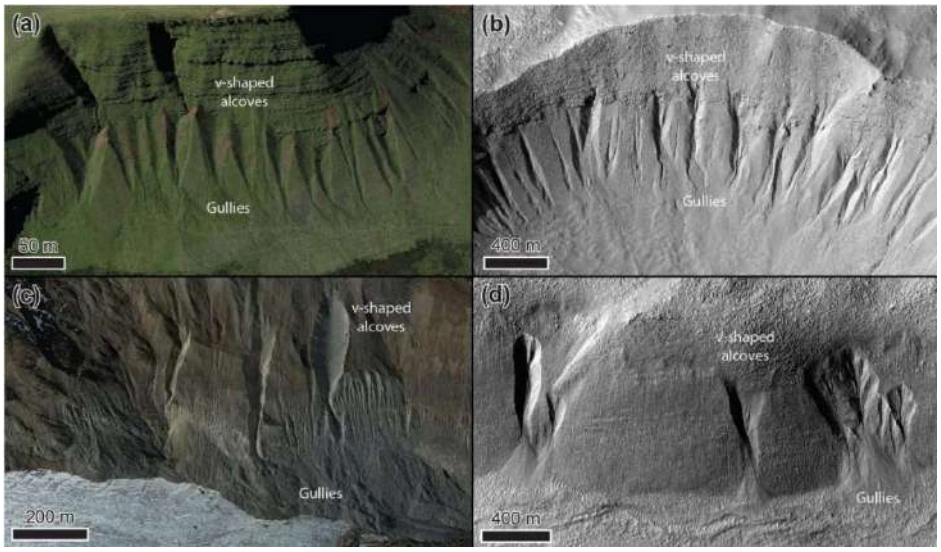

Figure 5.6. Gullies forming in glacial sediments in deglaciated terrain in (a) the Brecon Beacons, Wales, UK (Google Earth coordinates: 51°52'59.11"N, 3°43'33.26"W) and (c) at the Hintereisferner, Austria (Google Earth coordinates: 46°48'54.25"N, 10°47'8.18"E), on Earth, and Talu crater (https://www.uahirise.org/ESP_011817_1395) (b) and Bunnik crater (https://www.uahirise.org/ESP_047044_1420) (d) on Mars. HiRISE image credit: NASA/JPL-Caltech/University of Arizona.

The erosion of crater walls in formerly glaciated craters has resulted in mobilization of significant volume of material from the walls, thereby lowering the crater wall slopes **(e.g., Conway et al., 2018)**. In this context, from the discriminatory analysis we have found that the mean gradient of gully fans formed in LDM/glacial deposits and bedrock are separable from one another. Additionally, there is statistically significant difference between the mean gradient values of fans formed in both the substrates. At the foot of the fans, mean gradient of the interior of the crater wall with LDM/glacial deposits is <15° for 61% of the studied fans. For bedrock,

84% of the studied fans have mean gradient >15° at the foot of the fans. Based on these measurements, we propose that gully-fans formed in bedrock are emplaced at a relatively steeper gradient than the fans formed from gullies in LDM/glacial deposits.

5.5.2. Evaluation of the gully formation process

On Earth, alcove-fan systems can roughly be subdivided into flood-dominated, debris-flow dominated, and colluvial systems. Following the terminology of **De Haas et al., (2015a)** and **Tomczyk (2021)**, we define these systems as follows:

1) Flood-dominated systems: These are systems dominated by fluid-gravity flows, i.e., water floods, hyper concentrated floods, and debris floods. The fans of such systems are commonly referred to as fluvial or alluvial fans **(e.g., Ryder, 1971; Blair and McPherson, 1994; Hartley et al., 2005).**

2) Debris-flow dominated systems: These are systems dominated by sediment-gravity flows, i.e., debris flows and mud flows. Irrespective of their radial extent and depositional gradients, the fans aggraded by these systems can be commonly called debris-flow fans or debris fans **(Blikra and Nemec, 1998; de Scally et al., 2010)**.

3) Colluvial systems: These are systems dominated by rock-gravity and sediment-gravity flows, with their dominant activity relating to rockfalls, grain flows, and snow avalanches (in periglacial and alpine settings). Debris flows typically constitute only a relatively minor component of geomorphic processes in such systems. The fans of these systems are also commonly known as colluvial cones or talus cones **(Siewert et al., 2012; De Haas et al., 2015c)**.

Although these systems may be dominated by one type of geomorphic process, it is important to stress that other processes may also occur. For example, on Earth water floods are not uncommon in many debris-flow dominated systems, while debris-flow deposits are commonly recognized on colluvial cones.

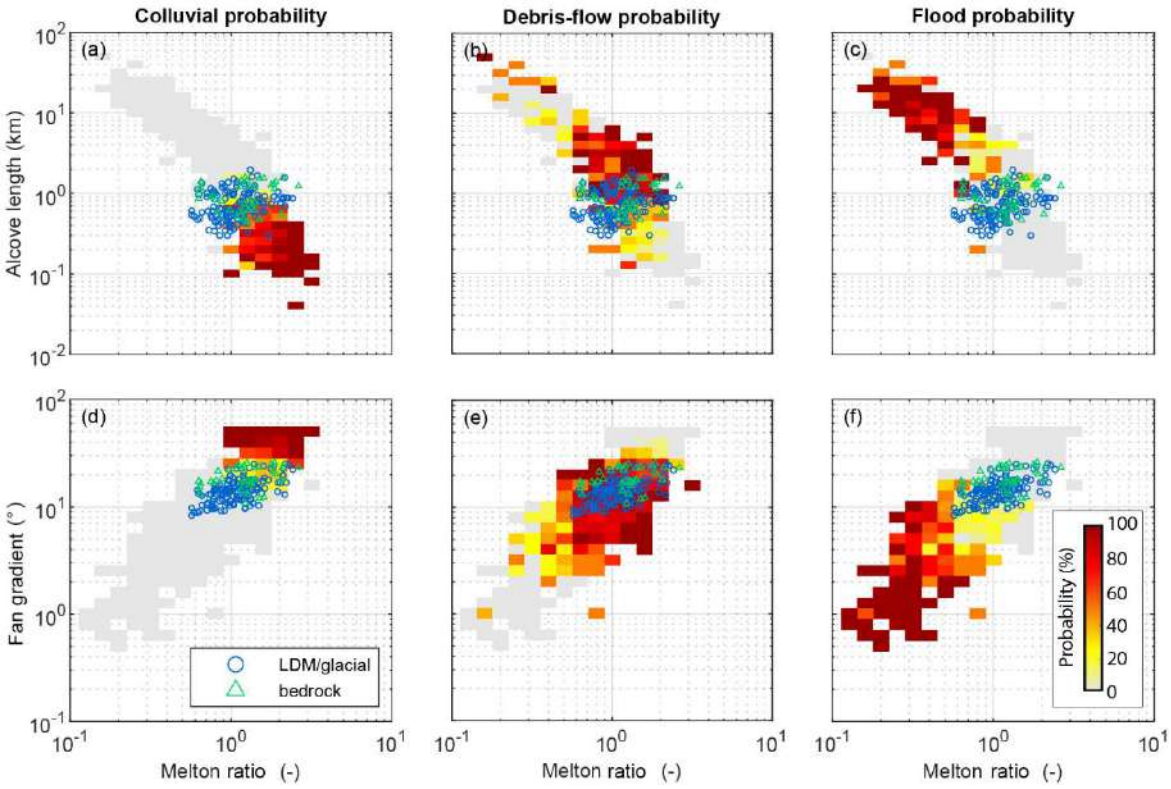

Figure 5.7. Comparison of combinations of Melton ratio with Alcove length and Fan gradient. The Martian gully systems formed in LDM/glacial deposits and bedrock are found to be in the debris-flow regime on Earth.

To compare the morphometric characteristics of the Martian gully systems to terrestrial systems, we have compiled morphometric data of alcoves and fans across several continents,

mountain ranges, climate zones, and process types. This dataset includes published data from the Himalayas, Ladakh, India **(Stolle et al., 2013)**, the tropical Andes, Columbia **(Arango et al., 2021)**, Spitsbergen, Svalbard **(Tomczyk, 2021)**, British Columbia, Canada **(Kostaschuk, 1986; Jackson et al., 1987; and newly presented data)**, the southern Carpathians, Romania **(Ilinca et al., 2021)**, the Southern Alps, New Zealand **(De Scally and Owens, 2004; De Scally et al., 2010)**, the North Cascade Foothills, USA, the European Alps (including Switzerland, Italy, France, and Austria), and the Pyrenees (from multiple authors compiled by **Bertrand et al., 2013**). The dataset comprises information from colluvial, debris-flow, and flood (also including debris flood) dominated systems. In total, it contains 231 colluvial systems, 749 debris-flow dominated systems, and 369 flood-dominated systems. In total, data were compiled for 1349 systems, although not all information was available for all systems, with data availability ranging from 729 sites for alcove length to all 1349 systems for Melton index and process type. Based on this data we have made a heatmap of the probability of flood, debris-flow, or colluvially-dominated conditions for combinations of Melton ratio with alcove length and fan gradient, to which we compare the Martian gullies **(Figure 5.7)**. We have found that the Martian gullies are indeed in the debris-flow regime on Earth. Moreover, they are closer to the transition to the smaller and steeper colluvial cones than to transition to flood-dominated fans.

According to the previous reports of debris-flow like deposits found in Martian gullies **(e.g. Johnsson et al., 2014; Sinha et al., 2019, 2020)**, the morphological attributes of debris-flow like deposits typically include overlapping tongue-shaped lobes with embedded clasts, channels with medial deposits, and channels with clearly defined lateral levees. Although it is

still not clear whether the formation of these deposits in gullies are from sublimation of CO_2 ice or due to meltwater generation. **De Haas et al., 2019b** have shown that CO_2 sublimation may lead to flow fluidization on Mars in a manner similar to fluidization by water in terrestrial debris flows; a concept supported by the recent finding of lobate deposits and boulder-rich levees formation during the present-day in Istok crater (45.1° S, 85.82° W) **(Dundas et al., 2019)**. The formation of these morphologically similar deposits during the present-day is attributed to the sublimating CO_2 frost, which produces the necessary fluidization likely by gas generated from entrained CO_2 frost **(Dundas et al., 2019)**. On the basis of these recent reports **(De Haas et al., 2019b; Dundas et al., 2019)** and based on our own findings in this study, we argue that a debris-flow like process similar to those operated in the terrestrial gully systems has likely dominated the flow types that lead to gully formation on Mars.

5.6. Key Findings

This paper compares morphological and morphometric characteristics of alcoves-fans formed in LDM/glacial deposits and bedrock over walls of 29 craters between 30° S and 75° S latitudes. 5 craters out of 29 have alcoves-fans formed within the bedrock and the remaining 24 craters have alcoves-fans formed within LDM/glacial deposits. From our analysis of 167 gullies, we posit that gully systems formed in LDM/glacial deposits and bedrock differ from one another using the following lines of evidence:

- Alcoves formed in LDM/glacial deposits are relatively elongated than the alcoves formed in bedrock, and possess a distinctive V-shaped cross-section.

- Mean gradient of gully-fans formed in bedrock is relatively steeper than the mean gradient of fans formed from gullies in LDM/glacial deposits.

Based on the combinations of Melton ratio with alcove length and fan gradient, we suggest that the gully systems studied in this work were likely subjected to terrestrial debris-flow like process in the past. This is consistent with the findings reported in previous studies that showed evidence of the formation of deposits morphologically similar to terrestrial debris-flow like deposits, both in the past and during the present-day **(e.g., Johnsson et al., 2014; Dundas et al., 2019)**. The present-day sublimation of CO_2 ice on Mars is envisaged to provide the necessary flow fluidization for the emplacement of deposits similar to debris-flow like deposits on Earth **(De Haas et al., 2019b)**.

CHAPTER 6

Morphological changes currently occurring in dust/sand-filled gully channels on Mars: Implications for the role of substrate inside channels

Success can come to you by courageous devotion to the task lying in front of you.

- Dr. CV Raman

6. Morphological changes currently occurring in dust/sand-filled gully channels on Mars: Implications for the role of substrate inside channels

6.1. Introduction

Gullies on Mars are kilometer-scale, geologically very young landforms on steep surfaces most often found polewards of about 30° latitude that comprise a theater-shaped alcove at the top, a linear-to-sinuous channel in the middle, and a depositional apron in the bottom **(e.g., Malin and Edgett, 2000; Reiss et al., 2004; Schon et al., 2009; Johnsson et al., 2014)**. Since gullies were first reported, they were considered morphological evidence for liquid water flow in the geologically recent past **(Malin and Edgett, 2001)**. Two main candidates have been proposed for the probable source of water: groundwater **(e.g., Malin and Edgett, 2000; Heldmann et al., 2004)** and melting of ground ice/snow **(e.g., Costard et al., 2002; Christensen, 2003; Bridges and Lackner, 2006; Dickson et al., 2007; Dickson and Head, 2009; Lanza et al., 2010; Levy et al., 2010b; Schon et al., 2009; Schon and Head, 2011; Williams et al., 2009)**. However, Mars' surface conditions during the Late Amazonian are not favorable for the existence of water **(e.g., Mellon and Phillips, 2001)**. During the past decade, many studies have reported a handful of morphological evidence for contemporary changes in gullies whose timing correlates with the time of removal of the seasonal CO_2 frost **(e.g., Diniega et al., 2010; Dundas et al., 2010, 2012, 2015, 2019; Raack et al., 2015)**. Frost occurs on pole-facing slopes in the lower mid-latitudes, and on most surfaces at high latitudes; most of this frost is CO_2 although traces of H_2O also occur (**Vincendon, 2015**). Removal of

the seasonal CO_2 frost can be triggered by basal sublimation, which could lead to erosion of the substrate **(e.g., Hoffman, 2002; Dundas et al., 2012, 2015; Pilorget and Forget, 2016)**. Erosion of the substrate could result in channel incision and large-scale mass movements in gullies **(e.g., Dundas et al., 2012)**. Morphological evidence of landforms resulting from these changes include erosion of alcoves, widening and lengthening of channels, extension of aprons, new terraces, migrating sinuous segments, and channel abandonment **(e.g., Diniega et al., 2010; Dundas et al., 2010, 2012, 2015, 2019)**. Dark defrosting spots and flows have been also observed as dust/sand exposure or downslope movement due to localized CO_2 frost sublimation **(e.g., Dundas et al., 2012)**. Together, this evidence has led to the suggestion that the currently active processes are not only modifying gullies but also initiating new gullies **(e.g., Dundas et al., 2012, 2019)**. Hitherto, ongoing changes of these types have been found to occur within gullies formed over all the naturally occurring substrates and steep surfaces. Thus, a detailed investigation of recent changes is crucial to determine the processes currently shaping the Martian gullies.

The substrates within which gullies have formed have been a key factor in controlling the type and timing of changes and the extent of morphological changes in gullies **(e.g., Conway et al., 2015; Harrison et al., 2015; de Haas et al., 2019; Dundas et al., 2019)**. Gullies on sand dunes are consistent with the loose, unconsolidated substrate, which promotes gully changes at a far faster rate than the gullies formed on non-sandy substrates **(e.g., Diniega et al., 2010; Hansen et al., 2011; Dundas et al., 2012, 2015)**. Additionally, frost-driven erosion is quite effective on the loose substrate of a sand dune gully, which results in extensive morphological changes in gullies **(Diniega et al., 2010; Hansen et al., 2011; Dundas et al.,**

2012). Sandy slopes consistent with large ripples form another type of substrate in which new incision and defrosting flows within older channels are the most common recent changes observed in gullies **(e.g., Dundas et al., 2019)**. This sandy slope characterized by ripples is also found on the floor of channels formed within crater-wall gullies **(e.g., Dundas et al., 2019; Khuller et al., 2021)**. There is only one example reported to date in which a cut-off of a sinuous curve by a new incision within dust/sand-fill in a crater-wall gully channel has been observed **(Dundas et al., 2019)**. Here, we aim to constrain the temporal evolution of dust/sand-filled gully channels characterized by ripples. Little previous work has been done with a particular focus on understanding recent changes in dust/sand-filled gully channels. The dust/sand-fill within these channels favors recent change because it is consistent with loose, unconsolidated materials **(e.g., Dundas et al., 2012; Khuller et al., 2021)**, and thus could have recent changes occurring at a rate and scale similar to the dune gullies. In order to record the changes occurring on the floor of dust/sand-filled channels by processes active in the present-day, we aim to investigate all the gullied craters between 30°S and 75°S using the High Resolution Imaging Science Experiment (HiRISE) images. More specifically, in this work, we aim to conduct a detailed temporal investigation to infer the extent, types, and timing sequence of the morphological changes currently occurring in the interior of dust/sand-filled gully channels. We will compare the observations with the previously reported morphological changes in gullies on sand dunes **(e.g., Diniega et al., 2010; Dundas et al., 2012)**, to infer the probable mechanisms for the morphological changes currently occurring in the interior of dust/sand-filled gully channels.

These objectives will help us to test the following hypotheses:

A. Morphological changes currently occur in the interior of the dust/sand-filled gully channels.

B. The newly observed morphological changes in the interior of dust/sand-filled gully channels are not suggestive of new gully formation.

If A is true, we anticipate seeing active morphological changes occurring in the interior of the dust/sand-filled channels because from previous studies we already know that both dune gullies and gullies formed on sandy slopes exhibit active modification in the present-day **(e.g., Dundas et al., 2012, 2019)**. If B is true, we expect to perceive that the morphological changes occurring in the interior of the dust/sand-filled gully channels are consistent with a muted appearance as they are simply the dust/sand covered pre-existing features that are being exposed by the wind. Furthermore, the observable morphological changes would not be connected with the frost and there is no seasonal control on the formation of features. We infer the timing of recent changes (i.e., sequence of events) to infer the role of frost and seasonal control on the formation of features.

6.2. Criteria for recognition of dust/sand-filled gully channels

We focus our observations on looking for gully channels that have ripples on the channel floor **(e.g., Dundas et al., 2012, 2019; Khuller et al., 2021)**. Presence of ripples corresponds to the evidence of sand- or dust-fill inside gully channels and a surficial layer of mobile sediments on the floor of the channels **(e.g., Bridges et al., 2010; Dundas et al., 2012; Geissler, 2014)**. Typically, the ripples should be well-organized, vary in wavelength from 1 - 5 m, relatively dark than the surrounding surface, and appear morphologically similar to the

ripples formed on dune gullies and sand dunes **(Bridges et al., 2012)**. The rippled surfaces within channels in dune gullies often show evidence of ripple migration in temporal images **(e.g., Dundas et al., 2012)**. Additionally, the rippled surfaces can have boulder fall tracks that often disrupt and/or cross-cut the pre-existing ripples, which further substantiate the presence of loose, unconsolidated dust/sand-filled surfaces on the floor of the channels. The loose dust/sand can erode out of the gully wall material or it can be simply trapped by the topography of gully channels.

6.3. Data and methods

We used HiRISE images acquired from MY28, L_s =165.5° (January 12, 2007) through MY35, L_s =341.4° (January 02, 2021) **(Clancy et al., 2000)**. HiRISE images are of high resolution with a pixel scale as small as 0.25 m, and typically cover areas 5-6 km wide and up to tens of km long, with a central swath of 1.0-1.2 km acquired through blue-green (BG) and near-infrared (IR) filters to produce enhanced-color images. An initial survey of HiRISE images of craters between 30-75° was conducted to examine the distribution of gullied craters having temporal coverage of crater- wall gullies. We conducted observations of gullies formed on the crater walls because we can assess the significance of the orientation of crater wall slopes on the gully morphology and the substrate into which the gullies incise. Additionally, we exclusively focused between 30 - 75°S because the gully density map clearly shows relatively higher number of gullied sites in this latitude range than in between 30 - 75°N **(Conway et al., 2019)**. A gully crater was surveyed in detail for the identification of dust/sand-filled gully channels only if the gullies are covered by at least two HiRISE images. We followed the

previous approach of **Dundas et al., 2012** to identify sites with overlapping HiRISE images. The center coordinates of overlapping images are within the range of the extremes of each other. We selected only those HiRISE images with similar lightning and atmospheric conditions for the detection of temporal changes in dust/sand-filled gully channels. The resulting data set includes 98 gullied craters with dust/sand-filled gully channels that are adequately covered by more than two HiRISE images **(Appendix 1)**.

We infer new changes within dust/sand-filled gully channels if we find morphological evidence for (1) new channel incision - formation of a new channel segment, (2) new channels with terminal pits - circular pit formation at the ends of the newly incised channels, (3) mass movements in channels - infilling of a channel by downslope material (dust/sand and/or boulder) transport, and/or (4) dark flows inside channels **(e.g., Dundas et al., 2012, 2015, 2019)**. On the other hand, morphological evidence for the local dust/sand rearranging and erasing of channels is not indicative of a new formation but would simply suggest that the older channels are getting concealed or re-exposed by the wind.

Morphological changes for a recent change are confirmed only when the recent change disrupts the pre-existing ripples or results in changes that can be resolved in terms of surficial morphology as opposed to subtle changes that only change the albedo. For our reference, we adopted the observational inferences outlined by **Dundas et al., 2012, 2015, 2019** to identify and confirm each piece of evidence for recent morphological changes in gullies. In all cases, we manually compared the images with the maximum time separation to identify the sites with morphological changes. Subsequently, we searched for the HiRISE image pair in which the

morphological changes appeared first to delimit the time separation between the changes and determine the timing of the events. Each site was monitored using all the available HiRISE images to obtain detailed constraints on the timing of the gully events. This approach is similar to that of **Dundas et al., 2015a, 2019**.

It is likely that we have missed some small or subtle changes in the morphology, mainly in cases where the change has not resulted in substantial morphological change and/or extensive mass movement or deposition. With respect to data biases, we do not limit ourselves to focus only on those sites for detailed investigation where changes were observed in the previous studies. Some potential biases may be present in our data set as we focus our observations mainly on the crater-wall gullies. Gullies found on other steep surfaces such as central peak of craters, valley walls, graben walls, and plateau escarpments could be more or less active than those on the crater walls.

This survey was carried out in parallel with, and independently of, an updated survey of gully activity in the mid-latitudes (**Dundas, 2020**). The two include many of the same changes but are not expected to agree perfectly due to the different survey methods and foci.

6.4. Observations

6.4.1. Characteristics of gullied craters with recent changes

Our survey of HiRISE images between 30 - 75°S resulted in the identification of 98 gullied craters with dust/sand-filled gully channels. Detailed temporal investigation of dust/sand-filled gully channels in these craters led us to identify 25 gullied craters with morphological evidence for recent flows **(Figure 6.1, Table 6.1)**. Throughout this paper, craters

that do not have formal International Astronomical Union (IAU) names will be referenced by their Table 6.1 sample numbers, i.e., the unnamed crater at –47.73, 160.74E will be called Crater 2. All these craters have the morphological evidence for the presence of ripples on the channel floor **(Figure 6.2)**. The geographic distribution of these craters is between 37°S and 52°S latitude and they span the full range of longitude from ±180°. The diameter of the craters ranges from ~3 to ~33 km. The orientation of the gullied slope is pole-facing for most of the craters (86% of the craters). Remaining craters have both poleward and equatorward facing orientation preference as they are located at higher latitudes (>45°S), consistent with broader surveys **(Harrison et al., 2015)**.

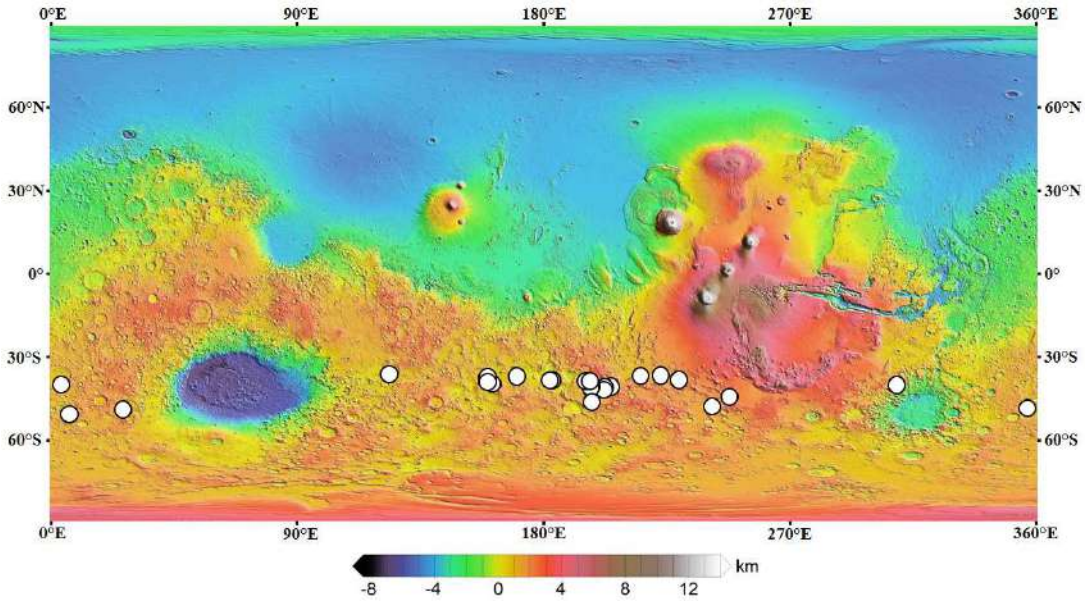

Figure 6.1. Map showing the locations (white circles with black outline) of 25 active gully sites with dust/sand-filled channels in the southern mid-latitudes of Mars. Background is Mars Orbiter Laser Altimeter (MOLA) – High Resolution Stereo Camera (HRSC) blended global digital elevation model v2 (retrieved from http://bit.ly/HRSC_MOLA_Blend_v0; **Fergason et al., 2018**).

Table 6.1. List of 25 craters that showed recent activity in dust/sand filled gully channels. Details of HiRISE image ID Mars year (MY), and sola longitude (Ls) is given to give an idea of the seasons and timing of the observable morphological changes. Craters that have sand filled gully channels found to be active in a time gap of 1 (marked by *) and 2 (marked by **) Mars years are marked.

Serial No.	Crater name	Latitude	Longitude	HiRISE Image ID	MY	Ls
1	Nqutu crater**	37.9°S	169.55°E	ESP_050329_1420	33	353.3
				ESP_064452_1420	35	190.3
2	Unnamed crater	40.73°S	160.74°E	ESP_032844_1390	31	359.1
				ESP_066035_1390	35	266.6
3	Unnamed crater	38.52°S	159.44°E	ESP_023930_1410	30	355.2
				ESP_057635_1410	34	286.9
4	Corozal crater*	38.79°S	159.48°E	ESP_043367_1410	33	60.5
				ESP_045332_1410	33	129.2
				ESP_049103_1410	33	300.3
5	Gebog crater*	37.26°S	124.16°E	ESP_016046_1425	30	30.2
				ESP_042353_1425	33	25.1
				ESP_045386_1425	33	131.2
				ESP_046309_1425	33	168
				ESP_053904_1425	34	120.2
				ESP_062344_1425	35	106.4
				ESP_066775_1425	35	302.1
6	Unnamed crater	39.36°S	5.09°E	PSP_007361_1405	29	34.8
				ESP_059434_1405	35	4.5
7	Unnamed crater**	40.46°S	309.92°E	ESP_012202_1390	29	220.7
				ESP_039564_1390	32	265.6
				ESP_048491_1390	33	271
				ESP_066821_1395	35	233.8

8	Unnamed crater*	39.33°S	229.7°E	ESP_048784_1405	33	285.2
				ESP_058160_1405	34	311.4
				ESP_064885_1405	35	210.4
9	Dunkassa crater*	37.49°S	222.95°E	ESP_013115_1420	29	265.6
				ESP_032011_1425	31	324.7
				ESP_039343_1420	32	254.7
				ESP_048125_1420	33	253
				ESP_064516_1420	35	193.2
10	Unnamed crater**	38.09°S	215.9°E	ESP_029651_1415	31	211.9
				ESP_047110_1415	33	203.7
11	Unnamed crater**	41.08°S	204.09°E	ESP_029124_1385	31	187.5
				ESP_047084_1385	33	202.5
				ESP_065519_1385	35	241.2
				ESP_067379_1385	35	329.1
12	Palikir crater*	41.56°S	202.39°E	ESP_047717_1380	33	232.8
				ESP_057462_1380	34	278.5
				ESP_064741_1380	35	203.6
				ESP_066482_1380	35	288.3
13	Dechu crater	42.27°S	201.86°E	PSP_003675_1375	28	338.1
				ESP_066205_1375	35	275
14	Unnamed crater	40.3°S	196.83°E	PSP_005930_1395	28	340.3
				ESP_049972_1395	33	338.7
15	Unnamed crater	41.13°S	196.63°E	PSP_007499_1385	29	39.7
				ESP_051040_1385	34	20.4
16	Unnamed crater*	38.88°S	195.93°E	PSP_002172_1410	28	165.6
				ESP_049194_1410	33	304.6
				ESP_057792_1410	34	294.3
				ESP_064873_1410	35	209.8
17	Unnamed crater	38.9°S	196.26°E	PSP_003662_1410	28	234.1
				ESP_032724_1410	31	354.4
18	Unnamed crater	38.6°S	183.8°E	ESP_023494_1410	30	337.5

				ESP_049867_1410	33	334.3
19	Unnamed crater	38.63°S	183.33°E	ESP_031841_1410	31	317.2
				ESP_065955_1410	35	262.7
20	Unnamed crater**	46.37°S	197.8°E	ESP_050183_1335	33	347.4
				ESP_064240_1335	35	180.8
21	Raga crater*	48.1°S	242.44°E	ESP_023993_1315	30	357.7
				ESP_027316_1315	31	115.1
				ESP_029149_1315	31	188.6
				ESP_037443_1315	32	165.9
				ESP_039250_1315	32	250.1
22	Unnamed crater*	45.41°S	248.32°E	ESP_021461_1345	30	242.4
				ESP_040041_1340	32	288.8
				ESP_047188_1340	33	207.3
				ESP_058489_1340	34	326
23	Unnamed crater	49.73°S	355.8°E	ESP_032560_1300	31	347.8
				ESP_067545_1300	35	336.2
24	Unnamed crater	51.26°S	6.82°E	ESP_022472_1285	30	291.8
				ESP_065856_1285	35	257.8
25	Unnamed crater*	49.04°S	27.22°E	ESP_046906_1305	33	194.2
				ESP_057785_1305	34	294

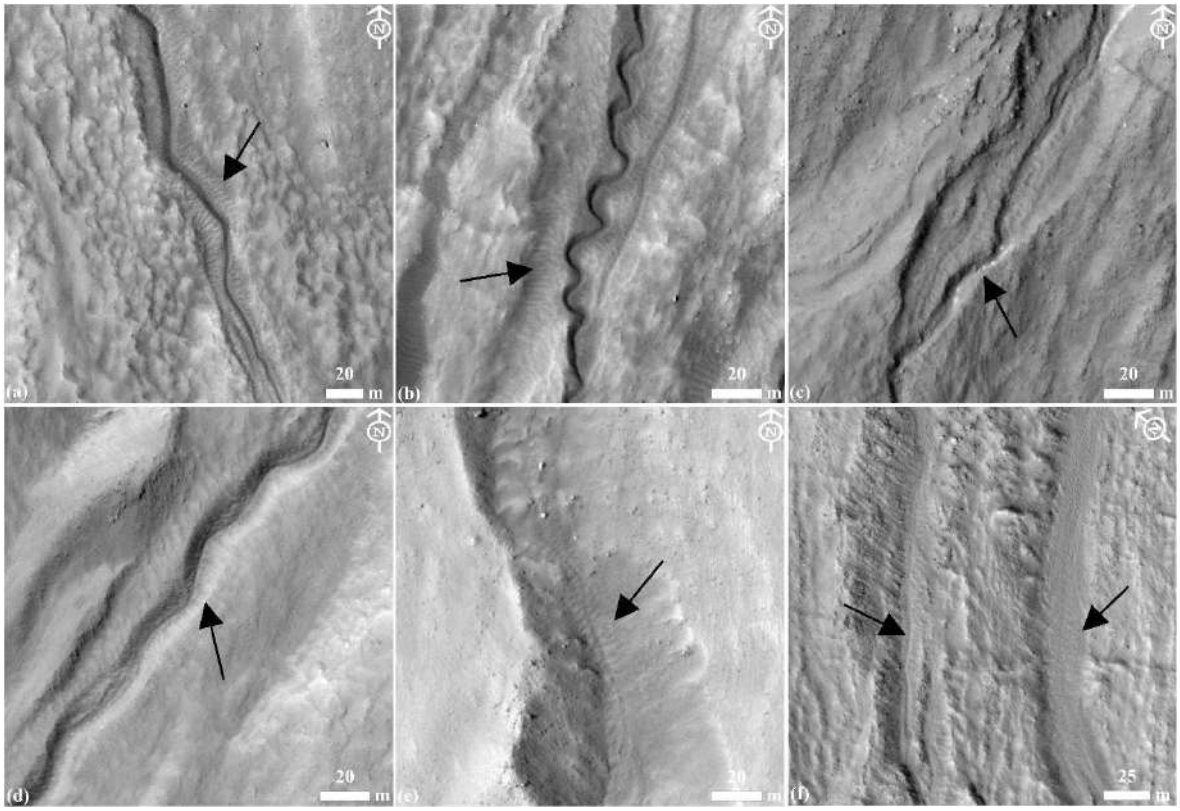

Figure 6.2. (a-f) HiRISE images showing the examples of dust/sand-filled gully channels investigated in this work. The floor of the channels (marked by arrows) is filled with dust/sand consistent with well-organized ripples. (a) ESP_032369_1420, (b) ESP_066775_1425, (c) ESP_064885_1405, (d) PSP_005930_1395, (e) ESP_066045_1340, and (f) ESP_029124_1385. HiRISE image credit: NASA/JPL-Caltech/University of Arizona.

6.4.2. Morphological Evidence Indicative of New Changes in Gullies

6.4.2.1. New Channel Incision

A series of monitoring images acquired over Gebog crater (37.26°S, 124.16°E) in the east of Hellas basin provided the evidence for morphological changes suggestive of new channel incision **(Figure 6.3)**. In this gully system, dust/sand is apparent in the gully alcove,

within the channel, on the walls of the channel, and in the proximal areas outside the channel. Morphological comparison of a sinuous channel in images acquired during MY 30 (areocentric longitude of the sun; Ls=30.2°) and MY 33 (Ls=25.1°) revealed that a major channel has formed that disrupted the ripples on its way **(Figure 6.3b)**. The newly formed channel is suggestive of avulsion and channel incision: the active flow appears to have broken out of a sinuous channel upslope, creating a new flow path outside the sinuous channel. The other image acquired during MY 33 (Ls=168°) reveals that the newly incised channel has further extended in the downslope direction **(Figure 6.3c)**. This observation demonstrates rapid changes occurring within a Mars year in this newly incised channel during the present-day. Subsequently, the image acquired during late MY 35 (Ls=302.1°) revealed that an additional flow has incised fresh channels upslope and extended the newly incised channel **(Figure 6.3d)**. Overall, the newly incised sinuous channel has extended ~50 m between images acquired during MY 30 (Ls=30.2°) and MY 35 (Ls=302.1°). This observation demonstrates a new site where active flows in the upslope lead to avulsion, channel incision, and rapid extension.

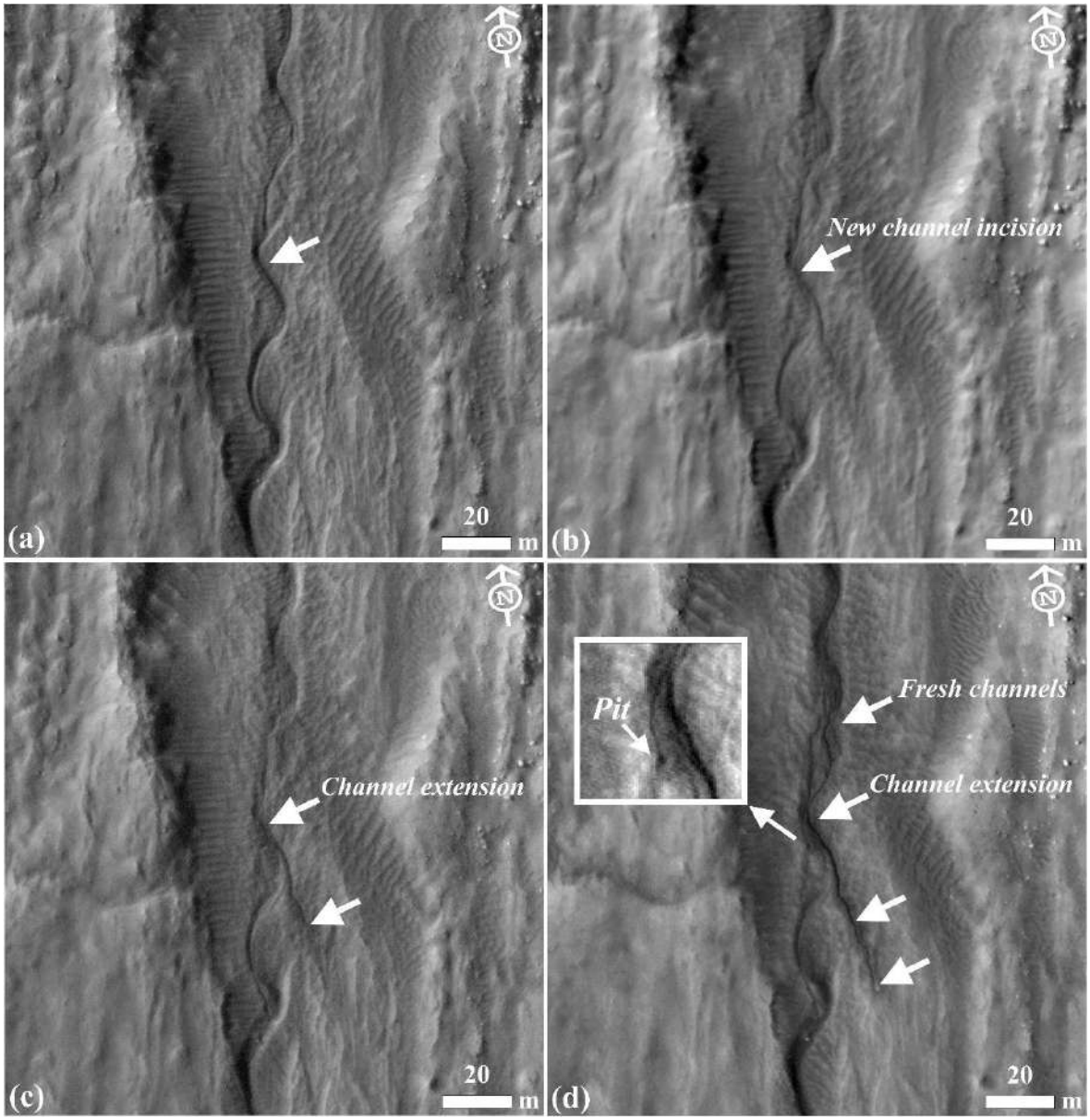

Figure 6.3. (a-d) Active flows in the upslope (upper arrow in all the figures) led to avulsion, new channel incision, and extension of channel in Gebog crater located at 37.26°S, 124.16°E. (a) ESP_016046_1425, MY 30, Ls=30.2°, (b) ESP_042353_1425, MY 33, Ls=25.1°, (c) ESP_046309_1425, MY 33, Ls=168°, and (d) ESP_066775_1425, MY 35, Ls=302.1°. HiRISE image credit: NASA/JPL-Caltech/University of Arizona.

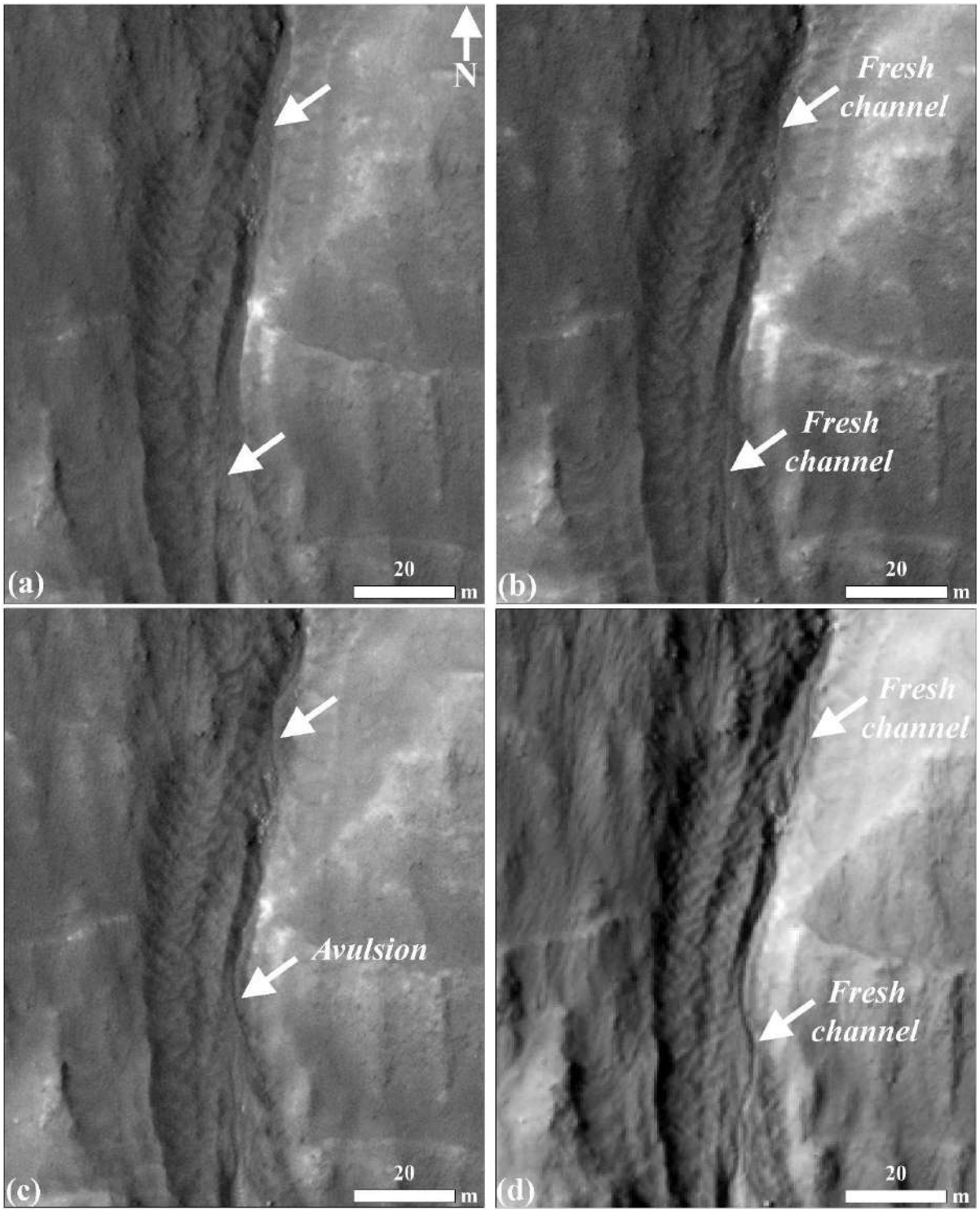
N
(a)
20
m
Fresh
channel
Fresh
channel
(b)
20
m
Avulsion
(c)
20
m
Fresh
channel
Fresh
channel
(d)
20
m

Figure 6.4. Fresh channel incision (arrows) on the floor of a sand-filled gully channel in Dunkassa crater (37.49° S, 137.05° W). Changes were observed in the images acquired during MY 29 (Ls=265.6°), MY 31 (Ls=324.7°), MY 32 (Ls=254.7°), MY 33 (Ls=253°), and MY 35 (Ls=193.2°). In this figure, images acquired during MY 29, MY 31, MY 33, and MY 35 are shown to demonstrate the overall extent of the change. (a) ESP_013115_1420, MY 29, Ls=265.6°, (b) ESP_032011_1425, MY 31, Ls=324.7°, (c) ESP_048125_1420, MY 33, Ls=253°, and (d) ESP_064516_1420, MY 35, Ls=193.2°. HiRISE image credit: NASA/JPL-Caltech/University of Arizona.

Another example of a new channel incision on the floor of dust/sand-filled gully channels was observed in the Dunkassa crater (37.49°S, 222.95°E) **(Figure 6.4)**. Our morphological comparison of images acquired during MY 29 (Ls=265.6°), MY 31 (Ls=324.7°), MY 32 (Ls=254.7°), MY 33 (Ls=253°), and MY 35 (Ls=193.2°) revealed episodic observable changes illustrative of the avulsion, channel incision, widening and extension, channel abandonment, and flow over a new path. Morphological evidence of fresh channel incision is evident in the upslope of the main channel.

Morphological evidence of new channel incision is found at many more locations that includes (1) Nqutu crater (37.9°S,169.55°E) between MY 33 (Ls=353.3°) and MY 35 (Ls=190.3°), (2) an unnamed crater (39.33°S, 229.7°E) between MY 33 (Ls=285.2°) and MY 35 (Ls=210.4°), (3) an unnamed crater (40.3°S, 196.83°E) between MY 28 (Ls=340.3°) and MY 33 (Ls=338.7°), (4) an unnamed crater (38.63° S, 183.33°E) between MY 31 (Ls=317.2°) and MY 35 (Ls=262.7°), (5) an unnamed crater (46.37°S, 197.8°E) between MY 33 (Ls=347.4°) and MY 35

(Ls=180.8°), (6) an unnamed crater (49.73°S, 355.8°E) between MY 31 (Ls=347.8°) and MY 35 (Ls=336.2°), (7) an unnamed crater (51.26°S, 6.82°E) between MY 30 (Ls=291.8°) and MY 35 (Ls=257.8°), (8) an unnamed crater (49.04° S, 27.22°E) between MY 33 (Ls=194.2°) and MY 34 (Ls=294°), (9) Gebog crater (37.26°S, 124.16°E) between MY 30 (Ls=30.2°) and MY 35 (Ls=302.1°), (10) an unnamed crater (39.36°S, 5.09°E) between MY 29 (Ls=34.8°) and MY 35 (Ls=4.5°), (11) an unnamed crater (45.41°S, 248.32°E) between MY 32 (Ls=288.8°) and MY 33 (Ls=207.3°), and (12) an unnamed crater (40.46°S, 309.92°E) between MY 29 (Ls=220.7°) and MY 32 (Ls=265.6°) and between MY 33 (Ls=271°) and MY 35 (Ls=233.8°). The channel in all these examples is infilled with dust/sand and a new channel is being incised into the dust/sand on the channel floor. The dust/sand deposit looks thick enough that the newly incised channels are within them, and the channel segments are very sharply defined.

6.4.2.2. New Channels with Terminal Pits

We discovered channels with terminal pits within dust/sand-filled gully channels on the walls of Corozal crater (38.79°S, 159.48°E) **(Figure 6.5a-b)**. The images acquired during MY 33 (Ls=129.2°) and MY 33 (Ls=300.3°) showed morphological evidence of newly incised multiple channels associated with pits at the terminus of the channels **(Figure 6.5b)**. The pits (~3-4 m average diameter) formed along terminus of the thin channels (~1-2 m average width). The channels extend out from a pre-existing dust/sand-filled gully channel, and they are typically low in albedo as compared to their surroundings. Subsequent to this, our investigation of terminal pits and associated channels revealed that they have not disappeared or shown any evidence of morphological change through MY 35 (Ls=312.3°).

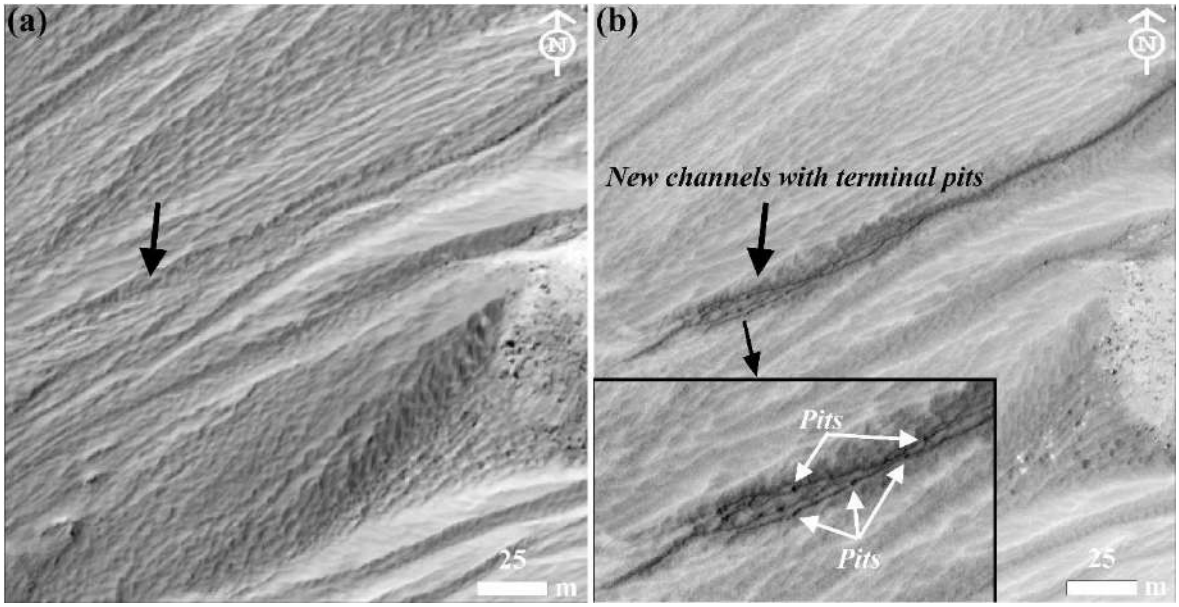

Figure 6.5. (a-b) Formation of new channels with terminal pits (arrow) in less than a Mars year inside Corozal crater at 38.79° S, 159.48° E. (a) ESP_045332_1410, MY 33, Ls=129.2°, and (b) ESP_049103_1410, MY 33, Ls=300.3°. Channels and terminal pits shown in (b) are enlarged for clear presentation. HiRISE image credit: NASA/JPL-Caltech/University of Arizona.

Another example of channels with terminal pits was observed in an unnamed crater (41.08° S, 155.91° W) **(Figure 6.6a-c)**. Our initial observation revealed that a channel appeared on the floor of a dust/sand-filled gully channel between MY 31 (Ls=187.5°) and MY 33 (Ls=202.5°) **(Figure 6.6a-b)**. Subsequent comparison of images acquired during MY 33 (Ls=202.5°) and MY 35 (Ls=241.2°) revealed that two channels with terminal pits have formed at the same place where a channel appeared at Ls=202.5° **(Figure 6.6c)**. The channels are relatively darker in albedo than their surroundings, very thin (~1 m average width), and of different lengths, so the terminal pits (~1-2 m average diameter) are separated by ~27 m from

each other. In this pair of images, a channel with terminal pit was also observed to have formed further down the lower/right channel **(Figure 6.6c)**.

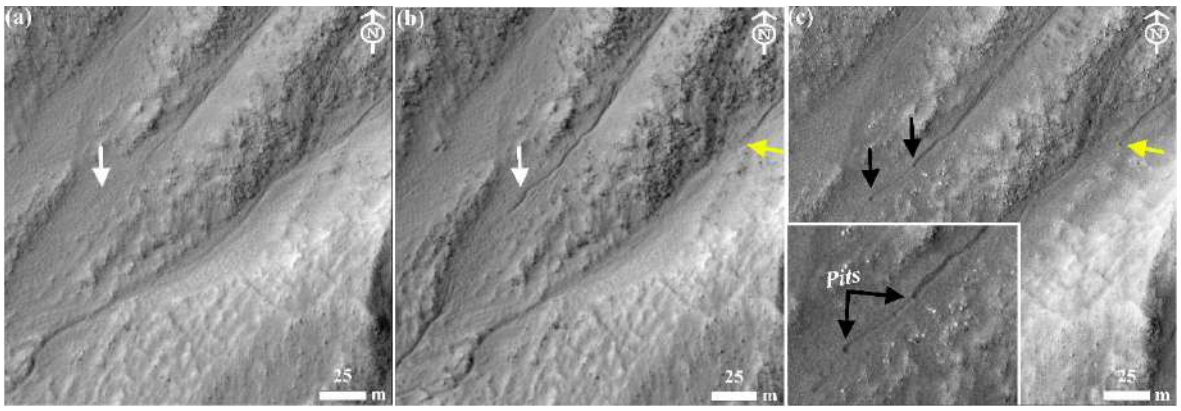

Figure 6.6. (a-b) Appearance of a new channel (marked by a white arrow) in a gully system in an unnamed crater at 41.08° S, 204.09°E. (c) Subsequent formation of two channels with terminal pits (black arrows) at the same place where a channel appeared previously in (b). Enlarged view of pits is shown for clear presentation. Additional changes further down the lower/right channel are marked by yellow arrow in (b-c). (a) ESP_029124_1385, MY 31, Ls=187.5°, (b) ESP_047084_1385, MY 33, Ls=202.5°, and (c) ESP_065519_1385, MY 35, Ls=241.2°. HiRISE image credit: NASA/JPL-Caltech/University of Arizona.

6.4.2.3. Mass Movement inside Channels

Extensive mass movements were discovered in the form of downslope flow and accumulation of mobilized dust/sand inside a channel, downslope transport of materials from the interior of a channel, and downslope movement of boulders inside a channel. In Palikir crater (41.56°S, 202.39°E), morphological comparison of the images acquired during MY 33 (Ls=232.8°) and MY 34 (Ls=278.5º) revealed evidence of dust/sand flow inside a channel up

to an overall length of ~250 m **(Figure 6.7a-b)**. Subsequently, in the image acquired at MY 35 (Ls=203.60°), we found that a new channel has formed over the surface just outside the channel. Dust/sand was deposited over this shallow channel in several segments **(Figure 6.7c)**. Together, our observations demonstrate the extensive flow of mobilized dust/sand inside a channel, localized accumulation of dust/sand following the channel topography, formation of dust/sand-filled channel, and dust/sand deposition over a newly formed channel, all happening currently at the same site and within a time gap of a Mars year between successive events. An additional example of dust/sand movement that formed lumpy deposits inside a channel was found in an unnamed crater (41.13° S, 196.63°E) between MY 29 (Ls=39.7º) and MY 34 (Ls=20.4º).

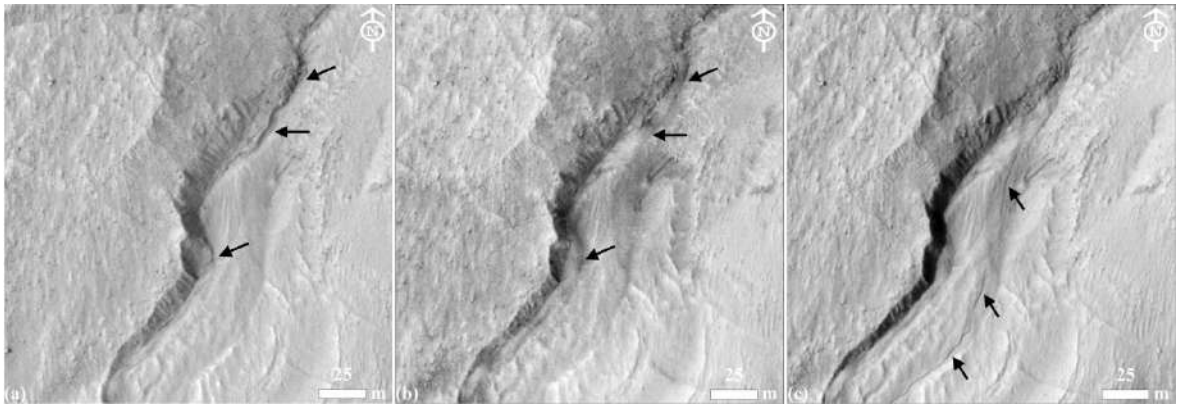

Figure 6.7. (a-b) Extensive mass movement representing downslope flow and accumulation of mobilized dust/sand inside a channel (arrows) up to an overall length of ~250 m in Palikir crater (41.56°S, 202.39°E). (c) Dust/sand deposition over a newly formed channel (arrows) in several segments. (a) ESP_047717_1380, MY 33, Ls=232.8°, (b) ESP_057462_1380, MY 34, Ls=278.5°, and (c) ESP_064741_1380, MY 35, Ls=203.6°. HiRISE image credit: NASA/JPL-Caltech/University of Arizona.

Further, channels formed on the walls of an unnamed crater (41.08°S, 204.09°E) showed morphological evidence of downslope transport of dust/sand in the images acquired during MY 33 (Ls=202.45°) and MY 35 (Ls=329.12°). We found that dust/sand deposited over a ~28 m long segment of the channel. Morphological evidence for downslope transport of materials from the interior of a dust/sand-filled gully channel, formation of a small deposit (~26 m length and ~7 m width) in the downslope area, and further advancement of the active flows in the upslope part of the main channel was found from the comparison of images acquired during MY 28 (Ls=165.62°) and MY 35 (Ls=209.81°) of an unnamed crater (38.88°S, 195.93°E).

Lastly, we have recorded morphological evidence of rapid movement of boulders inside a dust/sand-filled gully channel within an unnamed crater (45.41°S, 248.32°E) **(Figure 6.8a-b)**. We observe two boulders disappearing within a channel and a new boulder appearing at a nearby site (at a linear distance of ~30 m towards the downslope) inside the same channel. All this has happened within a period less than a Mars year, during MY 32 (Ls=288.76°) and MY 33 (Ls=207.33°).

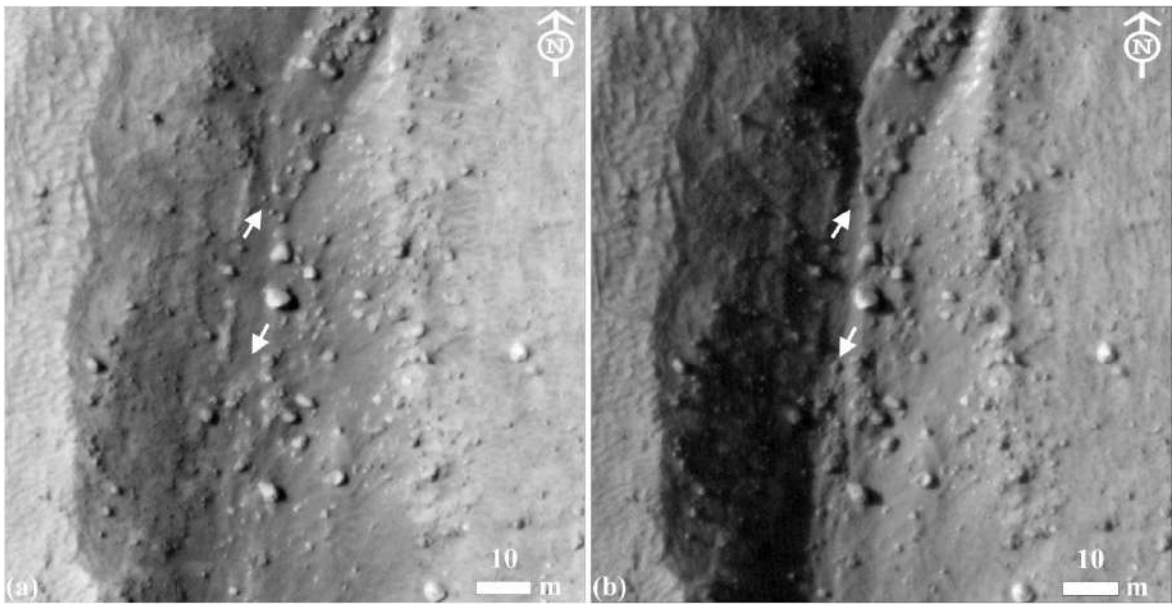

Figure 6.8. (a-b) Rapid (in less than a Mars year) movement of boulders inside a dust/sand-filled gully channel within an unnamed crater (45.41°S, 248.32°E). (a) Two boulders from the upslope (upper arrow) have disappeared in (b). A new boulder (bottom arrow) appeared in (b) which was not evident in (a). (a) ESP_040041_1340, MY 32, Ls=288.76° and (b) ESP_047188_1340, MY 33, Ls=207.33°. HiRISE image credit: NASA/JPL-Caltech/University of Arizona.

6.4.2.4. Dark Flows inside Channels

We discovered morphological evidence for dark flows inside dust/sand-filled channels in two unnamed craters located at: (1) 40.73°S, 160.74°E, and (2) 38.09°S, 215.9°E. At the first location, dark, multiple dark flows appeared inside the pre-existing channels between MY 31 (Ls=359.1°) and MY 35 (Ls=266.6°). As it appears, the dark flows do not disrupt the pre-existing ripples inside the channel **(Figure 6.9a-d)**. However, at the second location, we found from a comparison of images acquired during MY 31 (Ls=211.9°) and MY 33 (Ls=203.7°) that

the dark flows in two pre-existing channels had not simply appeared inside them but had also extended by ~25 m in one of the channels. This means that dark flows are not confined and can extend out of the pre-existing downslope topography of the channels and can gradually result in the formation of channel-like features.

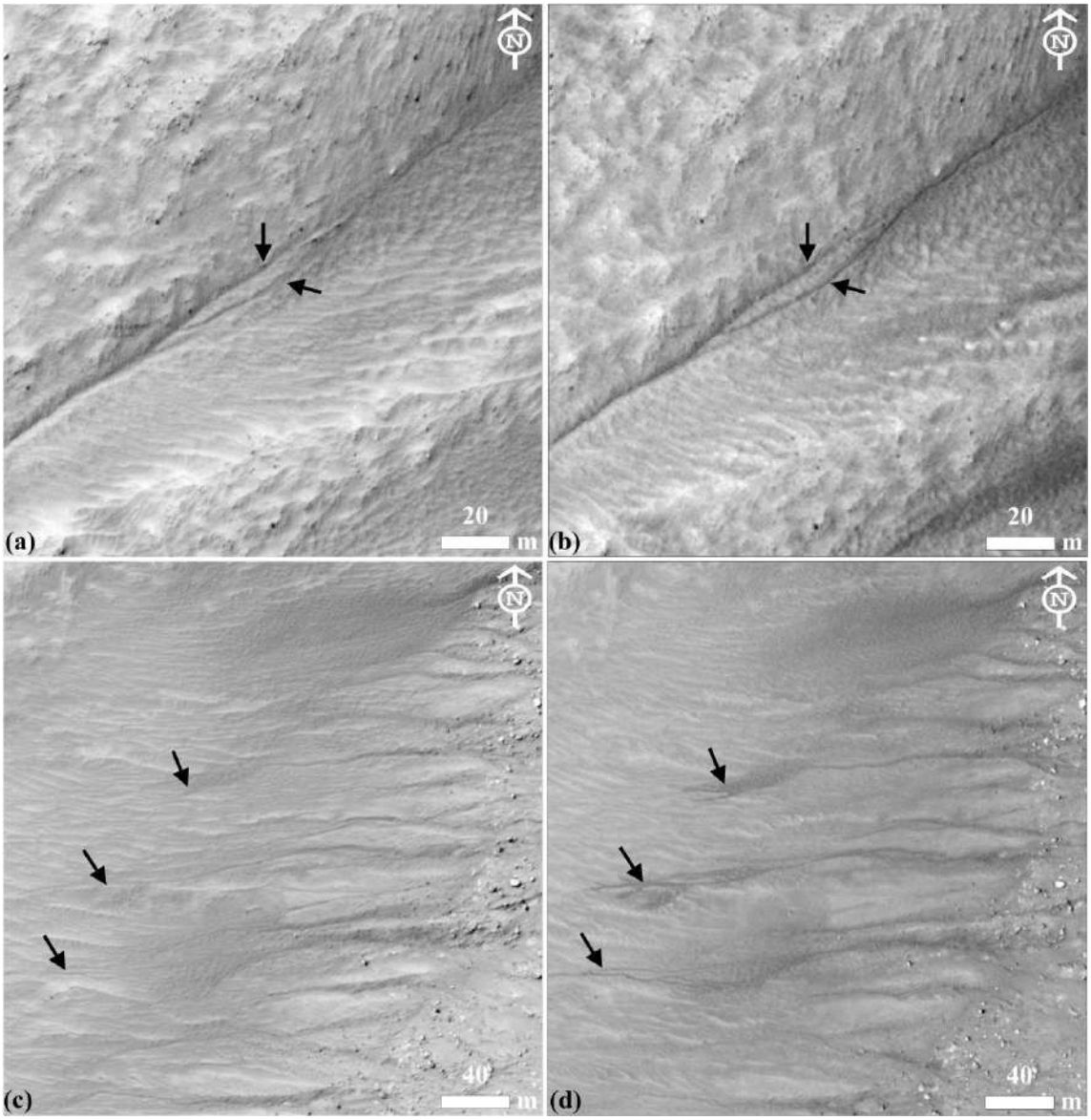

Figure 6.9. (a-d) Dark flows within sand-filled gully channels in an unnamed crater at 40.73°S, 160.74°E. Dark flows appear inside channels in (b) and (d) between MY 31 and 35. (a and c) ESP_032844_1390, MY 31, Ls=359.1° and (b and d) ESP_066035_1390, MY 35, Ls=266.6°. HiRISE image credit: NASA/JPL-Caltech/University of Arizona.

Furthermore, we found morphological evidence of thin dark flows appearing and extending downslope within the dust/sand-filled gully channels inside the Raga crater (48.1°S, 242.44°E) **(Figure 6.10a-c)**. Previously, **Dundas et al., 2019** found evidence for active flows occurring between MY 31, Ls 115-189° and MY 32, Ls 36-166° in this crater. We observed that the dark flows first appeared in one of the channels in the upslope region sometime between MY 30 (Ls=357.7°) and MY 31 (Ls=188.6°) **(Figure 6.10b)**. Subsequently, during MY 32 (Ls=250.1°), the second event of dark flows extended down the main channel, which buried the first flow and continued to flow further for ~100 m along the downslope and was emplaced over the depositional apron **(Figure 6.10c)**. We have monitored this dark flow through MY 35 (Ls=333°); however, apart from a subtle change in the albedo of the dark flows, we have not found any evidence to support any further change in the channels.

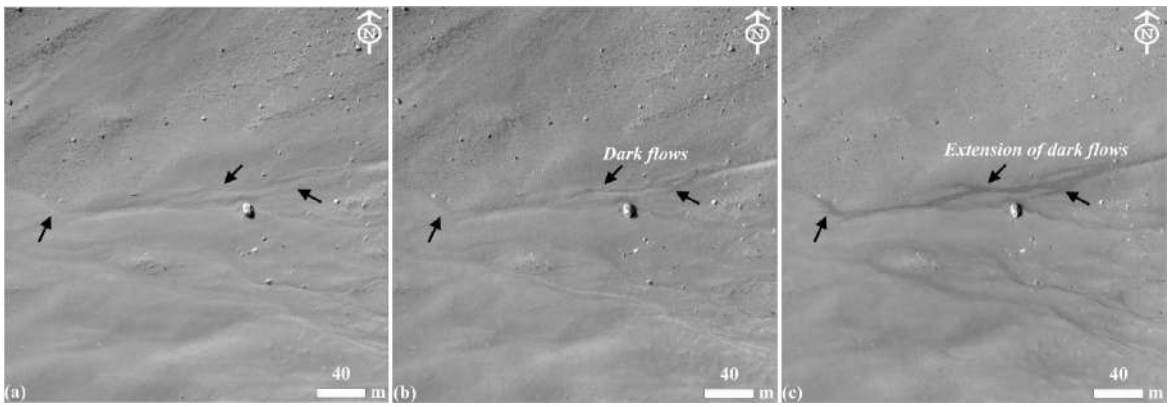

Figure 6.10. Dark flows within dust/sand-filled gully channels in Raga crater (48.1° S, 242.44°E). The dark flows have first appeared inside channels in (b), which gradually extended in the other channels of the gully system in (c). The time gap between images shown in (a-c) is around one Mars year. Note that the slope on which gullies have formed in this crater is sandy, although the dark flows appear and extend mainly on the floor of dust/sand-filled gully channels. (a) ESP_023993_1315, MY 30, Ls=357.7°, (b) ESP_029149_1315, MY 31, Ls=188.6°, and (c) ESP_039250_1315, MY 32, Ls=250.1°. HiRISE image credit: NASA/JPL-Caltech/University of Arizona.

6.4.3. Morphological Observations not Indicative of New Changes in Gullies

Local dust/sand rearranging and erasing of channels refers to partial or complete concealment of a pre-existing dust/sand-filled gully channel on the crater walls. Typically, local dust/sand rearranging can result in infilling of the channel, which in turn can reduce the depth to make it look very shallow, and gradually bury the channel until it disappears. This type of erasing of channel was observed in an unnamed crater (38.9°S, 196.26°E), wherein, a dust/sand-filled gully channel was found to have been erased by local dust/sand rearranging sometime between MY 28 (Ls=234.1°) and MY 31 (Ls=354.4°) **(Figure 6.11)**. Image acquired during MY 31 revealed that the morphology of the erased part of the channel has been softened and the channel was apparently very shallow in comparison to its non-mantled counterpart in image acquired during MY 28.

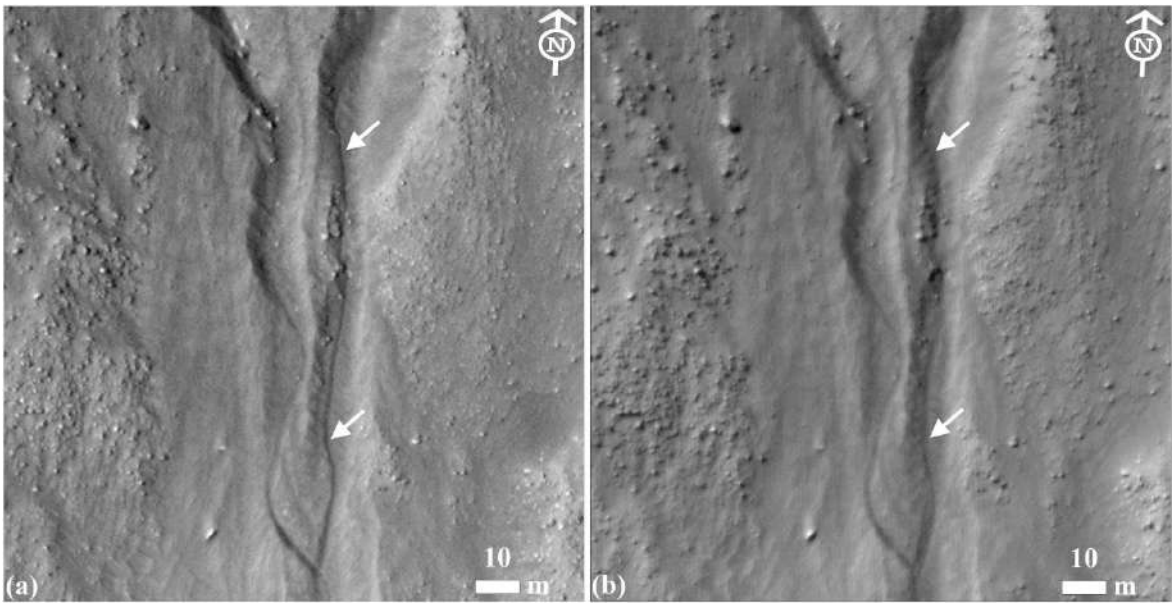

Figure 6.11. (a) A dust/sand-filled gully channel in an unnamed crater (38.9° S, 196.26°E) eventually buried by local dust/sand rearranging as seen in (b, arrows). (a) PSP_003662_1410, MY 28, Ls=234.1° and (b) ESP_032724_1410, MY 31, Ls=354.4°. HiRISE image credit: NASA/JPL-Caltech/University of Arizona.

Additionally, local dust/sand rearranging can also lead to reappearance of the previously concealed channels. We found morphological evidence of dust/sand getting cleaned out from a previously hidden channel in an unnamed crater (38.52°S, 159.44°E) between MY 30 (Ls=355.2°) and MY 34 (Ls=286.9°). The main channel was already present at the site and only some parts of the main channel were hidden under dust/sand, which gradually cleaned out by wind over the course of time.

6.4.4. Timings of Recent Changes

Like previous workers, where extensive image coverage is found, we have inferred the overall sequence and timing of the key events observed in the course of this study. We check

the presence of frost by examining the images acquired prior to the period when a change was observed in gully channels. Among 25 craters investigated in this study, gullies formed in ten craters lack the temporal coverage by an image in between the images that exhibited observable change in the morphology. Further, temporal coverage of gullies in two craters during the frosted period (winter season) is insufficient; all the available images are from spring and summer seasons. Additionally, for two craters frost is not evident on the crater walls in the available images of winter season. Therefore, in this study, the sequence and timing of recent changes in the gully channels could be inferred for 11 craters **(Table 6.1)**. These craters cover the entire range of recent changes reported in this paper.

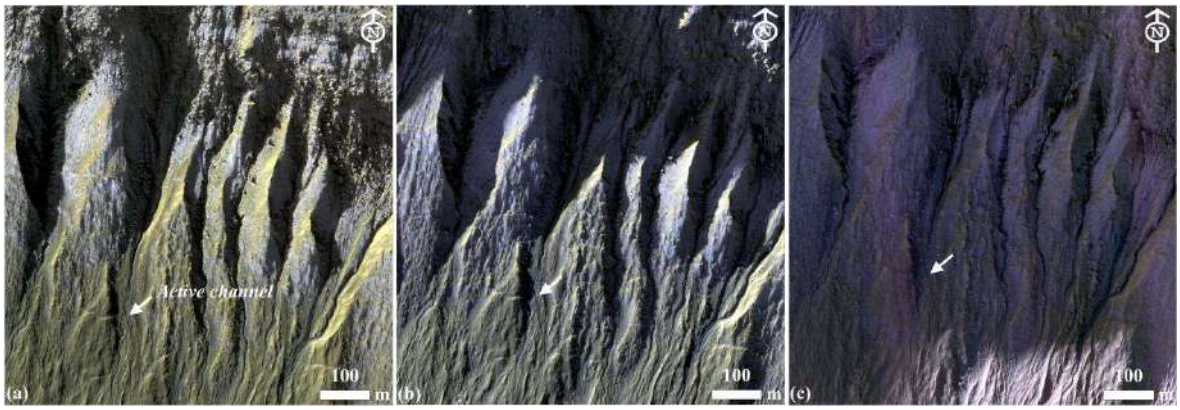

Figure 6.12. Seasonal frost (bright, relatively bluish-white material) in the gully system of the dust/sand-filled active channel (arrow) in which avulsion, new channel incision, channel extension, and gradual formation of a new channel was observed **(Figure 6.3)**. The HiRISE color images have been stretched to show detail in shadow; original image available at www.uahirise.org. (a) ESP_045386_1425, MY 33, Ls=131.2º, (b) ESP_053904_1425, MY 34, Ls=120.2º, and (c) ESP_062344_1425, MY 35, Ls=106.4º. HiRISE image credit: NASA/JPL-Caltech/University of Arizona.

Avulsion in a pre-existing sinuous channel in the Gebog crater at 37.26°S, 124.16°E was observed to have initiated in the image acquired between MY 30, Ls=30.2° and MY 33, Ls=25.1° **(Figure 6.3a-b)**. Coverage of this channel during the successive winter seasons (MY 33, Ls=131.2°; MY 34, Ls=120.2°; MY 35, Ls=106.4°) revealed that frost accumulates repeatedly at this location in large amounts **(Figure 6.12)**. Furthermore, the flow activity in the upslope and the newly incised channel in the downslope have shown evidence of rapid extension between the middle and late winter season (between Ls=131-168°; when the frost is about to completely disappear) of MY 33 **(Figure 6.3c)**, which again extended sometime between Ls=106-302° of MY 35 to gradually form a new channel within a period less than a Mars year **(Figure 6.3d)**. The timings of the changes observed in this crater are consistent with seasonal control; the connection with frost is clear, and the occurrence of events on transitioning from the winter season in successive Mars years is evident. Similarly, the coverage of channels during the successive winter seasons (MY 32, Ls=138.4°; MY 33, Ls=138.1°; MY 34, Ls=119.1°; MY 35, Ls=145.2°) in the Dunkassa crater has revealed evidence of frost present in large amounts in images acquired prior to the image in which morphological changes were observed **(Figure 6.4)**. Morphological evidence of avulsion, formation of the new channels, bypassing of older channels, and channel abandonment has occurred typically around the time when the frost coverage has decreased, implying a possible connection with the frost sublimation.

The rapid change (in less than a Mars year) related to the formation of new channels with terminal pits in the Corozal crater shows a similar relationship with the frost **(Figure 6.5a-b)**. The timing of the image acquired prior to the image in which the change was observed

correlates with the time of the year (MY 33, Ls=129.2°) when frost is present in large amounts in the alcove and inside channel – near the middle of the winter season **(Figure 6.13)**. As winter progressed, frost disappeared and new channels with terminal pits formed between Ls=129.2-300.3° of MY 33, which is consistent with late winter (and given all the other timing evidence there is a strong reason to believe that it was in the winter part of that interval rather than spring/summer).

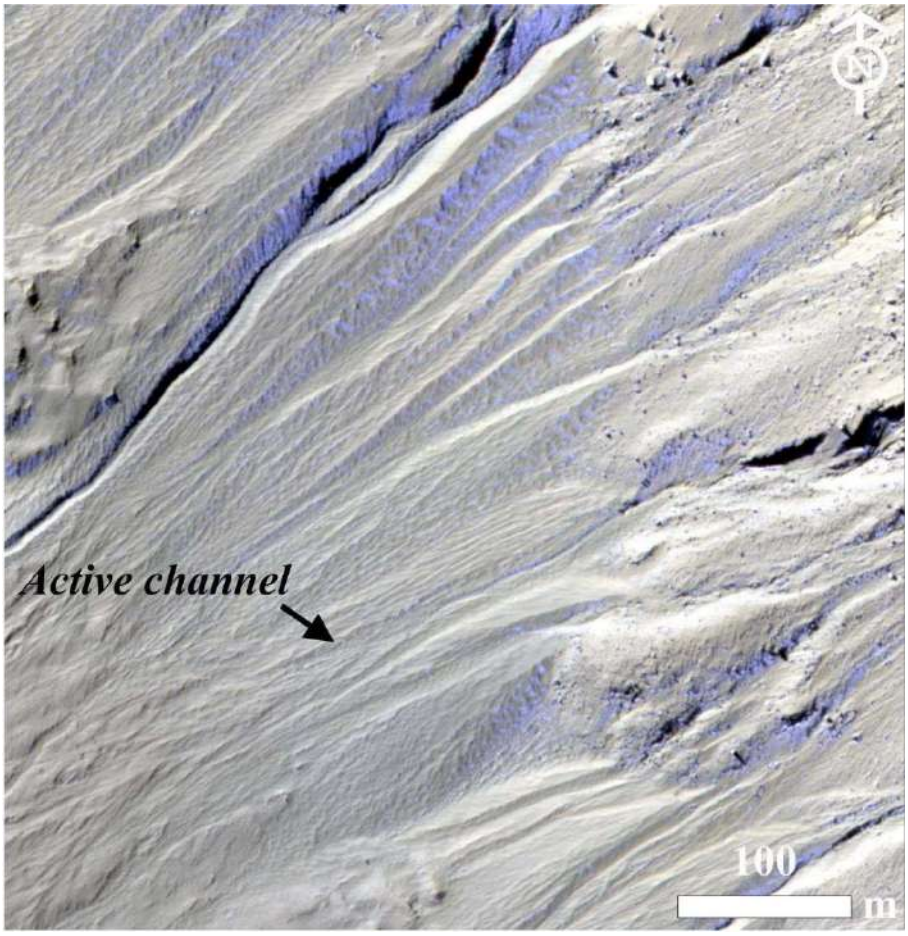

Figure 6.13. Seasonal frost (bright, relatively bluish-white material) in the alcove and inside the dust/sand-filled channel (arrow) in which new linear channels with terminal pits were

observed in the subsequent image. Please refer to **Figure 6.5a-b**. The HiRISE color images have been stretched for contrast. ESP_045332_1410, MY 33, Ls=129.2°. HiRISE image credit: NASA/JPL- Caltech/University of Arizona.

The timing of observation of advancement of active flow and downslope material transport during MY 34 (Ls=294.33°) and MY 35 (Ls=209.81°) inside a channel in the unnamed crater at 38.88° S, 195.93°E further demonstrate correlation of the recent change with the frost in this crater, as observed in the intermediate image acquired at MY 35 (Ls=86°). This intermediate image acquired just around the time when winter season begins has clear presence of frost in the adjoining channels and alcoves. Recent changes occurred in the channel near the end of winter, and likely ceased when most of the frost disappeared.

The presence of frost in the dust/sand-filled gully channels within Raga crater was not observed prior to MY 30, Ls=357.7° mainly because all the images acquired previously were from spring and/or summer season. However, we found evidence of frost in the channels in the image (MY 31, Ls=115.1°) acquired just before the image in which we first found morphological evidence of dark flows inside channels (MY 31, Ls=188.6°) **(Figures 6.10)**. The dark flows were found to have again extended inside the channels in the downslope in the image acquired during MY 32, Ls=250.1°, and here also we found the presence of frost in the previous image (MY 32, Ls=165.9°) acquired in sequence. In both the cases, where the dark flows have formed and extended inside the channels, we have found evidence of frost in the channels just before the change, suggesting a connection.

In both cases, frost was evident inside the dust/sand-filled gully channel in which we

have observed the recent changes. These observations provide evidence that the recent changes were likely connected with the frost present inside the channel at the same site.

6.5. Summary of Observations

Our detailed investigation of 25 craters with dust/sand-filled gully channels revealed key morphological evidence for: (1) avulsion, new channel incision, old channel abandonment, and channel widening and extension occurring rapidly (within 1-2 Mars years) during the present-day at multiple locations **(e.g., Figures 6.3 and 6.4)**, (2) new channel incision with terminal pits (within 1-2 Mars years) **(e.g., Figures 6.5 and 6.6)**, (3) extensive mass movements in the form of downslope flow and accumulation of mobilized dust/sand inside channels at a time interval of 1 Mars year **(e.g., Figures 6.7)**, (4) downslope movement of dust/sand that formed lumpy deposits inside a channel, (5) rapid (in less than 1 Mars year) boulder movement inside a dust/sand-filled channel **(Figure 6.8)**, (6) appearance of thin, dark flows in both longer (4-5 Mars years) and shorter (in less than 1 Mars year) time scales inside channels **(e.g., Figures 6.9 and 6.10)**, and (7) local rearranging of dust/sand inside channels which resulted in partial concealment and/or reappearance of pre-existing channels **(e.g., Figures 6.11)**. Note that these morphological changes have not been observed from dune gullies but from dust/sand-filled gully channels formed over a latitude-dependent mantle (LDM) -covered and formerly glaciated crater wall substrate. Our observations highlight that the interior of dust/sand-filled gully channels undergoes significant modifications in the present-day, therefore, we believe that the dust/sand in the channel interior is probably a significant factor in controlling the overall morphology of gully systems. The extensive and rapid nature of the morphological

changes supports this notion. Most of the intensively monitored sites showed evidence of seasonal frost in the image acquired before the image in which a change has been observed.

6.6. Interpretations and Discussions

6.6.1. Significance of Morphological Changes due to Recent Changes

The morphological changes observed in the dust/sand-filled gully channels were created via current Martian surface processes. Therefore, it is essential to infer what the extent and timing of morphologies point toward as far as understanding the influence of recent changes on dust/sand-filled gully channels is concerned. Furthermore, it is important to understand whether the recent changes driving the morphological changes in dust/sand-filled gully channels could be responsible for the formation of gullies in the present day.

We found morphological evidence for active flows in the upslope of a dust/sand-filled channel in the Gebog crater at 37.26°S, 124.16°E, which triggered an avulsion that gradually formed a small-scale sinuous channel over a new flow path **(Figure 6.3)**. Subsequently, we noted that the active flow has also formed a thin, curved channel segment with a terminal pit, over a new flow path in the downslope region **(Figure 6.3d)**. Additionally, we found many more locations (14 out of 24 craters) where new channel incision has occurred in the present-day **(Figure 6.4)**. Furthermore, morphological evidence of a new channel incision with terminal pits have been observed on the walls of the Corozal crater and an unnamed crater at 41.08°S, 204.09°E **(Figures 6.5 and 6.6)**. Previously, morphological evidence of linear channels with terminal pits has been often found on dune gullies **(Diniega et al., 2013; Pasquon et al., 2016)** and in linear gullies on the sandy slope in Avire crater **(Dundas et al.,**

2012). The formation of linear channels and pits in these gullies have been inferred to have formed from sliding blocks of CO_2 ice that first initiated the channel formation and then formed pits as the frost sublimated at the terminus of the channels. Our observation implies that the currently active surface processes functional on the surfaces of dune gullies, sandy slopes, and dust/sand-filled gully channels are operating in a similar manner to form channels with terminal pits. Hence, we infer that the active flows upslope of the dust/sand-filled gully channel studied here are likely connected to the sublimating frost. Furthermore, owing to the presence of loose, unconsolidated sediments inside the dust/sand-filled gully channels, the morphological changes recorded in the Gebog crater at 37.26°S, 124.16°E (between Ls=25.1-168°, MY 33; **Figure 6.3a-d**) and Corozal crater (between Ls=129.2-300.3°, MY 33; **Figure 6.5a-b**) have taken place in less than a Mars year. This signifies that the erosion due to sliding blocks of CO_2 ice is significant and can quickly transport material downslope in the dust/sand-filled gully channels, which can often cause new channel incisions.

The extensive mass movements occurring in the form of downslope flow and accumulation of mobilized dust/sand in Palikir crater gully channels resulted in complete concealment of a segment of the channel in almost a Mars year **(Figure 6.7)**. Additional morphological evidence of downslope transport of dust/sand inside channels was found inside 2 craters. This implies that the source region of dust/sand undergoes extensive erosion by currently active processes and dust/sand could be quickly transported based on the local steepness inside the channel. This further signifies that the loose, unconsolidated sediments could be very mobile.

Lastly, in Raga crater, we have found morphological evidence of dark flows to appear inside channels in less than a Mars year, which further extended in the downslope in the other parts of the channel in another Mars year **(Figure 6.10)**. Subsequently, the dark flows have not shown any observable change apart from subtle albedo variations for 3 successive Mars years. This signifies that the defrosting inside channels is subject to differences in the nature and extent of flow during different Mars years, with some periods having attained peak flows and some not causing even slight change inside the channels.

Taken together, the morphological changes due to recent changes signify that new channel formation (new channel incision and formation of channels with terminal pits) is extensively occurring due to the currently active surface processes in the mid-latitudes and the dust/sand-filled gully channels have been undergoing rapid (in less than a Mars year) modification as a result of downslope flow and accumulation of mobilized dust/sand in channel segments, active flows in the upslope, dark flows inside channels, and local rearranging of dust/sand inside the channels) during the present-day. This suggests that the newly observed morphological changes in the interior of dust/sand-filled gully channels are suggestive of new gully formation, which means that hypothesis 'B' is not true.

6.6.2. Relationship of Recent Changes with the Substrate

Our observation of the extent, types and timing of the morphological changes have revealed that rapid and extensive changes are currently occurring in the interior of dust/sand-filled gully channels, which is not simply removing dust/sand from the floor of the channels but also leading to avulsion, new channel incision, channel incision with terminal pit formation,

channel widening and extension, and downslope flow and accumulation of mobilized dust/sand. In most of the intensively monitored sites, seasonal frost occurs in the image prior to the observed change. This provides a clear connection with the sublimating frost inside the channels and suggests a seasonal control that subsequently produces extensive changes during defrosting seasons in approximately a Mars year. Previously, quick, varied and extensive morphological changes have been reported to occur on the dune gullies. A few examples of such morphological changes include dust/sand movement and channel incision **(Diniega et al., 2010; Hansen et al., 2011)**, dark material deposition and extension of debris aprons **(Dundas et al., 2015a)**, new channels with terminal pits **(Dundas et al., 2015a)**, and alcove modification and terrace formation **(Dundas et al., 2017)**. The timing of these changes recorded on dune gullies is well within a few weeks, but sometimes spans a Mars year or more. When tightly constrained, the changes are closely correlated with seasonal frost, particularly with the defrosting season. Hence, we compare the morphological changes recorded within the dust/sand-filled gully channels with the morphological changes previously reported on the dune gullies to gain new insights into the role of the substrate in recent changes in gully and its morphological effects.

The observations of new channels with terminal pits are prominent on many dune gullies (e.g., dune field at 70°S, 178°E) and in gullies on the sandy slopes (e.g., Avire crater at 40.83°S, 200.25°E) **(Dundas et al., 2012)**. In these locations, the linear channels are thought to have formed during sliding of blocks of CO_2 ice, which then produced circular pits at the terminus of the channels after their gradual sublimation. In our survey, we have found morphological evidence of new channels definitively associated with terminal pits on the

surfaces of dust/sand-filled gully channels **(Figures 6.5 and 6.6)**. In both the gully systems, circular pits are associated with thin channels. Furthermore, we commonly observed that within one gully system multiple channels with terminal pits initiate from the main channel in the upslope region, which suggests that the modes in which the channels originate and subsequently develop over the sandy surface are also similar. We have noted from our observations that the channels are confined to the floor of the dust/sand-filled gully channels and they are not evident on the rocky substrate adjacent to the main channel, which indicates that the channels are connected to the sandy substrate on the floor of the main channel. This is consistent with the previous observations, where these channels and pits have been always found on the surface of dune gullies and on the sandy slopes on the crater walls. To date, no example of a linear channel with terminal pit has been observed to form on a bedrock and/or LDM-covered substrate on the crater wall.

Incision of a new channel within the dune gullies and sinuosity development has been observed in dune gullies **(Dundas et al., 2015a; Pasquon et al., 2019)**. Repeated energetic flows tend to result in channel breakout and erosion of the outer bank of the curved channel, leading to evolution of the curved channel into a sinuous shape. We have also found morphological evidence for continuously evolving gully system, where curved channels form, widen, and are cut-off **(e.g., Figures 6.3d)**. The channels evolved as a part of the outcomes of repeated flows in the upslope of the main channel, which included avulsion, new channel incision and gradual extension during subsequent flows. Downslope propagation of energetic flows leading to erosion outside the bank of the channel and migration of sinuous curves to become more sinuous has been observed previously in a dust/sand-filled gully channel. It is

evident that the active flows and subsequent channel breakout of flow have the major control in sinuosity development on both the dune gullies and the dust/sand-filled channels. Hence, the key factors that control the morphological developments in both dune gullies and dust/sand-filled gullies appear to be similar and the currently active processes result in similar morphological developments in the channels.

The dark flows formed on dune gullies in winter are dark relative to the seasonal frost. These flows occur at a very modest scale from the mouth of, and/or within the, pre-existing channels and leave no resolvable topographic signature. We have found morphological evidence of dark flows inside dust/sand-filled gully channels which are relatively darker than the surroundings, remained inside the pre-existing channels at some sites **(e.g., Figure 6.9)**, and gradually widened and extended beyond the channels to form an apron-like feature in the downslope region at the other sites **(e.g., Figure 6.10)**. Similar dark flows have been also found in separate gullies in Asimov crater **(Dundas et al., 2015a)**, although they were not formed on the floor of dust/sand-filled channels. The dark flows in Asimov crater gullies are likely to be seasonally controlled. Although we do not have the images to constrain the timing properly, the image that shows them is from the winter (MY 31, Ls=126.5°), similar to the other gully flows that appear during the winter elsewhere. This is consistent with the seasonal changes observed in the dark flows (characterized by different extent and width during the consecutive periods) on the dune gullies, gullies on sandy slopes, and on the floor of dust/sand-filled gully channels.

Extensive mass movements occurring in form of downslope flow and accumulation of mobilized dust/sand in the dust/sand-filled gully channels have been also observed at multiple sites in our survey **(Figures 6.7)**. Local rearranging of dust/sand has resulted in reappearance of pre-existing channels and erasing of a pre-existing channel segment **(e.g., Figure 6.11)**. Such types of changes are more prevalent only when the mobilized material is composed of loose, unconsolidated sediments.

The loose, unconsolidated sediments on the floor of dust/sand-filled gully channels are similar to the loose substrate of a sand dune, and this is likely the main factor, which suggests similar level of recent change in both the gully types. This would mean that hypothesis A is true, i.e., extensively active morphological changes currently occur in the interior of the dust/sand-filled gully channels. As it appears from our comparisons, the type, extent and timing of morphological changes are similar on both dust/sand-filled gully channels and dune gullies, which substantiates that the currently active surface processes have similar effects on the unconsolidated substrate in both the gully types. The similarities in final morphologies indicate that the controlling processes are also similar.

6.6.3. Possible mechanism for Recent Changes in Gullies

The study of intensively monitored gully systems has revealed several fundamental results, which are the backbone of any model for gully formation and evolution. The study indicates:

- Gullies are forming now, although it is possible that formation extended back to the high-obliquity periods as well. It is entirely possible that some gullies always have sand and dust on their floors even while forming. This could occur if erosion happens during

the most energetic flows (or in locally exposed areas), which start all of the mobile infilling material moving, but some of it gets redeposited as the flow stops, and this is exactly what happens in many fluvial/debris flow systems. For gullies in mantle deposits, another possibility is that sublimation of ice in the mantle releases dust/sand that fills in the bottom of the gully and gets to move down the slope by flows.

- The dust/sand-filled channels are likely to be covered by CO_2 ice during winter season. Basal sublimation within the channels leads to the removal of CO_2 ice during defrosting periods, which subsequently propagates erosion, removal and downslope movement of the dust/sand deposits.
- Extensive mass movements occur in the form of downslope flow and accumulation of mobilized dust/sand in the dust/sand-filled channels and local rearranging of dust can lead to partial concealment and reappearance of the pre-existing channels.
- Sliding blocks of CO_2 ice often lead to the development of new channels with pits at the terminus.
- Defrosting activity likely results in dark flows inside the pre-existing channels. Active flows triggered by sublimation of CO_2 ice might block the flow path of channels upslope or break out of existing channels, which can lead to channel avulsion and gradual incision of a channel over a new flow path. The loose, unconsolidated sediments are likely prone to being more easily mobilized as observed in gullies on sand dunes.

Therefore, the controlling factors that maintain gully activity on sand dunes can also keep dust/sand-filled gully channels active. The observations reported here suggest that the

dust/sand-filled gully channels are frequently active and the morphological changes are extensive in nature.

6.7. Key Findings

Extensive morphological changes are currently occurring inside dust/sand-filled gully channels in the southern mid-latitudes. We have found morphological evidence that demonstrates that new channel incision, extension and widening of channels, formation of newly incised channels associated with pits at the terminus, extensive downslope movement of mobilized dust/sand inside channels, boulder movement inside channels, and dark flows inside channels are all happening currently inside the dust/sand-filled gully channels in around a Mars year time, but are confined to the winter season. We hypothesize that the presence of loose, unconsolidated sediments inside the dust/sand-filled gully channels is a significant factor in controlling the frequency of present-day changes and overall morphological evolution of gully systems studied in this work. Furthermore, we postulate that because the extensive morphological changes demonstrated in this work continue to occur frequently in Martian gully systems, it is likely that dust/sand-filled gully channels formed over varied substrates (e.g., bedrock, LDM-covered, glacially modified crater wall) might continue to form today on Mars. The morphological evidence demonstrated for avulsion, new channel incision, and formation of new channels with terminal pits support this notion. The intensively monitored sites have revealed the presence of seasonal CO_2 frost inside the currently active channels, which further demonstrates the connection between the recent changes and frost.

CHAPTER 7

Summary, Synthesis and Future Scope

I also believe that a person who does not have respect for time, and does not have a sense of timing, can achieve little.

- Dr. Vikram A. Sarabhai

7. Summary, Synthesis and Future Scope

7.1. Summary

The thesis has demonstrated that locations far away from the dichotomy boundary in the northern mid-latitudes of Mars witnessed extensive debris-covered glaciation during the Late Amazonian. Study of glacial landforms formed within the Erebus Montes region reveals that there is a lack of multi-stage glaciation facilitated by the alcove microclimatic conditions in this region.

Erebus Montes region shows a record of very recent emplacement and removal of LDM that eventually degraded the glacial landforms in the region during the last ~30 Ma. LDA deposits examined in Erebus Montes are more consistent with the cold-based glacial behavior - morphological observations supports existence of the sublimation process in the region.

Global investigation of Martian gullies has revealed that terrestrial debris-flow like process is not a rare process in gully formation on Mars. This is implied by evidence of morphological attributes of debris-flow deposits on gully fans and relationships between melton ratio, fan gradient and alcove length.

Detailed morphometric investigation of gully systems formed in different substrates (LDM/glacial deposits and bedrock) reveal that they differ from one another.

Despite the fact that gullies are currently active due to the sublimation of CO_2 ice, the work presented in this thesis shows that the possibility of terrestrial debris-flow like gully formation processes on Mars can't be completely ruled out.

7.2. Synthesis

7.2.1. Are there any differences in glacial processes at locations far away from the dichotomy boundary of Mars?

The work presented in this thesis has revealed that integrated systems of LDA deposits, piedmont-like lobe deposits, bulged LDA deposits, and infilling of craters, all these have formed from extensive ice accumulation and flow at locations far away from the dichotomy boundary during the Late Amazonian. It was found that the LDAs in Erebus Montes were previously more extensive and the emplacement of mantling deposits has caused significant modification/degradation of LDAs. The evidence for LDA modification/degradation was perceived in the form of linear-curvilinear ridges on LDA deposits. When compared with glacial processes that occurred along the dichotomy boundary, we find that our findings support the results from previous studies carried out elsewhere along the dichotomy boundary that suggested LDA deposits as evidence for the past presence of extensive debris-covered glacial landsystems. Although, it was found that in Erebus Montes there is a lack of evidence for the formation of alcove-fed small-sized lobes superposed on the main LDAs. Superposed lobate flows formed over LDAs along the dichotomy boundary represent a less extensive period of ice accumulation and flow, which also corresponds to episodic glacial activity. This probably means that Erebus Montes region lacks evidence for relatively less extensive glacial phases than what formed LDA deposits. Nevertheless, since LDM was found ubiquitously in the study region, it is worth mentioning that emplacement and removal of mantling deposits might result in degradation of flow lineations emerging from alcoves, if any. Furthermore, despite the

presence of extensive LDA deposits in Erebus Montes, SHARAD-based subsurface investigations do not provide substantial evidence for the presence of buried extant ice in the region. This is found inconsistent with the majority of previous studies that reported evidence of subsurface ice beneath LDA deposits along the dichotomy boundary. Although, it has to be kept in mind that radar based subsurface investigation and detection of buried ice deposits is quite challenging. This is because radar signals scatter when there are closely spaced mesas and LDA deposits, the top and bottom layer of subsurface ice might be closer to the surface that they are not detected without ambiguity, and mantling deposits might hinder deep penetration of radar signals to detect the interfaces if any. Therefore, it is suggested that this aspect can be looked upon in detail in a future study. Finally, the LDA deposits in Erebus Montes are found to be one of the youngest LDA deposits on Mars. However, owing to the fact that best-fit ages are entirely based upon the preservation of craters post-resurfacing period; therefore, it is suggested that the best-fit ages should be interpreted with more caution and the glaciation that led to the formation of LDA deposits in Erebus Montes should be better represented by a broad age range of ~10-100 Ma.

7.2.2. Is terrestrial debris-flow like processes a dominant mechanism of gully formation on Mars?

In terrestrial gully systems, debris-flow typically deposits features that appear in the form of convex-up tongue-shaped lobate deposits over the alluvial fans. In majority of cases, the source channel associated with the lobate deposits is found to be flanked by lateral levees. Additionally, stacked lobate deposits are also evident, which represents backstepping in the flow system. Prior to the work reported in this thesis, there has been a common consensus

among the Mars community that lobate deposits and levees are rare in Martian gullies; therefore, possibility of a terrestrial debris-flow like process as the dominant gully formation mechanism on Mars is not at all achievable. The global survey of the mid-latitudes of Mars in both the hemispheres using HiRISE images resulted in the identification of 20 craters that are having gully systems dominated by morphological attributes of debris-flow like deposits. In these craters, gully fans were found to be dominated by overlapping lobate deposits, leveed channels, and the surfaces of lobes contained abundant clasts embedded into them. The ages of the host craters span a wide range from ~1 Ma to 3 Ga, which suggested that debris-flow deposits were quite young. This is also due to the fact that in the hostile environment of Mars where wind-related modifications are currently ongoing and LDM emplacement lasted till the very recent past, small-scale lobate deposits and levees cannot be preserved on the surface for a longer timescale. Furthermore, the morphometric investigations presented in the thesis have shown that the combinations of alcove length and fan gradient with melton ratio shows a strong similarity with the terrestrial gully systems, which further indicates that the Martian gully systems belong to the debris-flow regime on Earth. Finally, a recent study has shown that CO2 sublimation may lead to flow fluidization on Mars in a manner similar to fluidization by water in terrestrial debris flows **(De Haas et al., 2019b)**. This is a concept supported by the recent finding of lobate deposits and boulder-rich levees formation during the present-day in Istok crater (45.1° S, 85.82° W) **(Dundas et al., 2019)**. Based on these aforementioned findings, in this thesis, it has been argued that a debris-flow like process similar to those operated in the terrestrial gully systems has likely dominated the flow types that lead to gully formation on Mars.

7.2.3. What keeps gullies active today?

In the past decade or so, Martian gullies have been reported to be active during the present-day. Gully channels formed over both consolidated (LDM/glacial deposits/bedrock) and unconsolidated (dunes and dust/sand-covered slopes) substrates are found active currently. The gully activity primarily shows new channel incision, extension of pre-existing channels, dark flows inside channels, mass movements inside channels, boulder movement, and dust rearranging to erase pre-existing channels. The proposal explaining these activities includes basal sublimation of the seasonal CO_2 frost, which results in erosion of the substrate. The timing of the gully activity is found to be correlated with the time of removal of the seasonal CO_2 frost. In order to further examine and understand this present-day activity in Martian gullies, temporal investigation of all the gully systems formed between 30° to 60° in the mid-latitudes of the southern hemisphere has been attempted (Chapter 6 of the thesis). 25 new locations (gullied craters) were discovered that showed present-day activity in gullies. The gullies found in these craters have evidence of ripples formed inside channels, which is an indication of the possible presence of dust/sand (unconsolidated material) inside the channels. It is highly likely that if a slab of CO_2 ice is left to flow downstream inside these dust/sand-filled channels, then it can easily move towards the downslope, carving new channels on its way, displacing boulders, inducing a massive flow of dust/sand inside channels, and also modifying the pre-existing channels it will encounter on its way. All these were found to be happening currently in the dust/sand filled channels in the 25 craters investigated in this thesis work. Furthermore, the investigation of the sequence of events in these channels revealed CO_2 frost inside the dust/sand-filled gully channels in the image acquired during winter and prior to

the image in which recent changes have been observed. This suggests a connection with the sublimating frost inside the channels and indicates a seasonal control that subsequently produces extensive changes during defrosting seasons in approximately a Mars year. These observations were compared with the activities currently occurring on the surfaces of dune gullies. The comparison substantiates that the currently active processes have similar effects on the loose, unconsolidated substrate in both the gully types, i.e. dust/sand-filled channels and dune gullies. Together, the results signify that the dust/sand-filled gully channels represent a significant component of present-day gully evolution on Mars.

7.2.4. Evolutionary history of the Late Amazonian geological processes in the mid-latitudes of Mars?

The study of Erebus Montes region well represented that the Late Amazonian period on Mars was dominated by extensive accumulation and flow of ice in the mid-latitudes. Therefore, if the mid-latitude of Mars prevailed a period of net ice accumulation in the past, then the entire terrain would have been completely covered by ice. As the environment changed into an ablating environment, ice sheet would have collapsed to expose the mesa/plateau flanks, which further evolved by erosion and downwasting of debris from the flanks, finally forming debris-covered LDA deposits. During an increase in average orbital obliquity (last ~5 Ma), redistribution of ice from polar caps to the mid-latitudes has taken place. Ice has mantled the LDA deposits - evidence of that is apparent in the form of surface textures corresponding to brain-terrain, polygonal cracks, and ring-mold craters. Then, gully formation has taken place over the same crater wall slope over which LDM has been emplaced during the last ~5 Ma and

previously (~100 Ma) glacial landforms have been deposited to fill the floor of craters. In a more recent period (~1 Ma), when changes in average obliquity have not lead to accumulation of ice deposits over the crater wall slopes, fresh debris-flow like deposits have formed on the gully fans due to a terrestrial debris-flow like process. In the present-day, the gully systems continue to be active due to the fluidization from sublimation of seasonal CO_2 frost. The presence of dust-sand filled channels is found to represent as a strong member of Martian gullies that show rapid activity in the present-day.

7.3. Future Scope

An extension of the detailed analysis of glacial landforms found in Erebus Montes to other glaciated regions in the mid-latitudes of Mars would confirm that this is a holistic approach to decipher the morphology, topography, subsurface and chronological details of the LDA deposits, which would in turn help understand the evolutionary history of glaciated landscapes during the Late Amazonian. As alcove-fed lobate flows superposed on the main LDA are lacking in Erebus Montes, this can be checked and verified from other locations with the similar geologic settings on Mars to infer the influence of alcove microclimatic conditions in facilitating multi-stage glaciation on Mars. The mesa-LDA deposits in the Erebus Montes region are at a lower elevation range (−2600 to −4300 m) in comparison to the LDAs formed along the dichotomy boundary. The influence of low elevation on LDM emplacement and removal from the LDA deposits in the Erebus Montes region can be further examined. An even more robust analysis of radargrams and supportive morphological attributes of near subsurface ice could be taken up in the future to identify potential areas with subsurface ice deposits.

The analysis carried out on Martian gully fans in this thesis has enormous scope for extending the morphometric analysis to other fan-shaped deposits on Mars. For example, estimation of the concavity index of fan-shaped deposits in impact craters can help distinguish the mechanisms that have led to the formation of the fans. If debris-flow like processes has any bearing on the formation and evolution of fan-shaped deposits then it would be evident in the combination of relationships between the fan gradient and Melton ratio of the catchment forming the deposits. Such an analysis in the future would also verify the conclusions presented in this thesis that catchments with fan gradient >7.5°, catchment length <2.7 km and Melton ratio >0.57 represent systems dominated by terrestrial debris-flow like processes. Furthermore, the comparison between dust/sand-filled gully channels and dune gullies can be further extended to decipher the potential role of the dry debris flow mechanism in these types of gullies that currently undergo modification by completely dry seasonal frost-related sublimation processes. In the future, field observations can be planned to terrestrial analogous sites, such as Ladakh Himalaya, which has preserved debris-flow deposits on gully fans that are morphologically similar to debris-flow deposits identified and discussed in this thesis. This will open up many interesting and useful avenues for establishing the potential role of debris-flow like processes in gully formation on Mars.

Appendix A

List of investigated craters with dust/sand-filled gully channels.

Serial No.	Latitude (S)	Longitude (E)
1	36.2	190.43
2	37.14	190.64
3	36.48	193.82
4	36.09	214.31
5	36.48	322.72
6	35.87	330.9
7	34.88	119.53
8	35.53	121.72
9	35.75	129.42
10	35.08	130.57
11	34.8	133.57
12	30.97	149.58
13	36	174.69
14	37.3	178.12
15	39.66	175.94
16	39.64	173.8
17	37.91	169.55
18	41.2	168.5
19	42.71	158.57
20	40.8	160.74
21	38.98	160.23
22	38.8	159.48
23	39.45	158.16
24	38.35	155.36
25	37.39	130.66
26	37.73	126.03
27	37.26	124.11
28	37.25	123.64
29	39.64	123.07
30	39.37	5.03
31	43.24	343.17
32	37.11	340.25
33	38.61	319.94
34	40.42	309.92
35	40.83	349.83

36	43.29	229.18
37	39.39	229.68
38	38.92	225.51
39	43.86	222.56
40	38.12	224.02
41	37.49	222.95
42	38.95	223.63
43	38.91	221.8
44	40.28	217.05
45	37.74	143.82
46	38.12	215.88
47	42.59	214.79
48	39.42	210.76
49	40.73	211.78
50	41.48	210.57
51	40.1	204.77
52	41.04	204.07
53	39.37	202.64
54	41.58	202.24
55	42.24	201.99
56	42.03	195.47
57	40.32	196.88
58	41.07	196.64
59	38.9	195.92
60	38.91	196.23
61	38.35	195.33
62	37.72	195.84
63	38.81	193.98
64	38.31	193.3
65	37.67	192.96
66	37.1	191.96
67	37.12	190.98
68	41.06	189.02
69	38.22	185.53
70	38.2	183.93
71	38.6	183.79
72	38.54	183.31
73	38.77	182.08
74	38.71	181.72
75	37.95	180.47

76	37.07	183.79
77	46.37	197.79
78	46.51	200.69
79	45.4	238.27
80	48.11	242.45
81	46.76	245.84
82	45.44	248.34
83	45.72	259.9
84	48.89	268.23
85	49.08	270.38
86	45.09	274.19
87	46.68	279.34
88	48.56	280.11
89	49.74	355.82
90	51.28	6.74
91	50.41	8.76
92	46.18	18.8
93	46.99	18.78
94	45.43	25.63
95	46.96	26.7
96	49.05	27.21
97	45.86	158.84
98	47.17	176.77

References

Bridges, N.T. and Lackner, C.N., 2006. Northern hemisphere Martian gullies and mantled terrain: Implications for near-surface water migration in Mars' recent past. Journal of Geophysical Research: Planets, 111(E9).

Arango, M. I., Aristizábal, E., & Gómez, F. (2021). Morphometrical analysis of torrential flows-prone catchments in tropical and mountainous terrain of the Colombian Andes by machine learning techniques. Natural Hazards, 105(1), 983-1012.

Arfstrom, J. & Hartmann, W.K. 2005. Martian flow features, moraine-like ridges, and gullies: terrestrial analogs and interrelationships. Icarus, 174, 321–335.

Aston, A., Conway, S. & Balme, M. 2011. Identifying Martian Gully Evolution. In: Balme, M.R., Bargery, A.S., Gallagher, C.J. & Gupta, S. (eds) Martian Geomorphology. Geological Society, London, Special Publications, 356, 151–169, https://doi.org/10.1144/SP356.9.

Baker, D.M. and Head, J.W., 2015. Extensive Middle Amazonian mantling of debris aprons and plains in DeuteronilusMensae, Mars: Implications for the record of mid-latitude glaciation. Icarus, 260, pp.269-288.

Baker, D.M., Head, J.W. and Marchant, D.R., 2010. Flow patterns of lobate debris aprons and lineated valley fill north of Ismeniae Fossae, Mars: Evidence for extensive mid-latitude glaciation in the Late Amazonian. Icarus, 207(1), pp.186-209.

Balme, M., Mangold, N. Et Al. 2006. Orientation and distribution of recent gullies in the southern hemisphere of Mars: observations from High Resolution Stereo Camera/Mars Express (HRSC/MEX) and Mars Orbiter Camera/Mars Global Surveyor (MOC/MGS) data. Journal of Geophysical Research: Planets, 111, E05001.

Barlow, N.G., 2006. Impact craters in the northern hemisphere of Mars: Layered ejecta and central pit characteristics. Meteoritics& Planetary Science, 41(10), pp.1425-1436.

Bart, G.D., 2007. Comparison of small lunar landslides and Martian gullies. Icarus, 187(2), pp.417-421.

Berman, D.C., Chuang, F.C., Smith, I.B. and Crown, D.A., 2021. Ice-rich landforms of the southern mid-latitudes of Mars: A case study in Nereidum Montes. Icarus, 355, p.114170.

Berman, D.C., Crown, D.A. and Joseph, E.C., 2015. Formation and mantling ages of lobate debris aprons on Mars: Insights from categorized crater counts. Planetary and Space Science, 111, pp.83-99.

Bertrand, M., Liébault, F., & Piégay, H. (2013). Debris-flow susceptibility of upland catchments. Natural Hazards, 67(2), 497-511.

Blair, T. C., & McPherson, J. G., 2009. Processes and forms of alluvial fans. In Geomorphology of desert environments (pp. 413-467). Springer, Dordrecht.

Blair, T.C., 1999. Sedimentology of the debris-flow-dominated Warm Spring Canyon alluvial fan, Death Valley, California. Sedimentology 46 (5), 941–965.

Blikra, L.H., Nemec, W. (2000). Post-glacial colluvium in western Norway: depositional processes, facies and palaeocolimatic record. Reply. Sedimentology, 47, 1058-1068.

Bramson, A.M., Byrne, S., Putzig, N.E., Sutton, S., Plaut, J.J., Brothers, T.C. and Holt, J.W., 2015. Widespread excess ice in Arcadia Planitia, Mars. Geophysical Research Letters, 42(16), pp.6566-6574.

Bramson, E.I., Bain, Z.M., Putzig, N.E., Morgan, G.A., Mastrogiuseppe, M., Perry, M.R. and Smith, I.B., 2019, March. MARS SUBSURFACE WATER ICE MAPPING (SWIM): RADAR SUBSURFACE REFLECTORS. AM. In Lunar and Planetary Science Conference (No. 2132, p. 2069).

Bridges, N. T., Banks, M. E., Beyer, R. A., Chuang, F. C., Dobrea, E. N., Herkenhoff, K. E., ... & Wray, J. J. (2010). Aeolian bedforms, yardangs, and indurated surfaces in the Tharsis Montes as seen by the HiRISE Camera: Evidence for dust aggregates. Icarus, 205(1), 165-182.

Bridges, N.T., Bourke, M.C., Geissler, P.E., Banks, M.E., Colon, C., Diniega, S., Golombek, M.P., Hansen, C.J., Mattson, S., McEwen, A.S. and Mellon, M.T., 2012. Planet-wide sand motion on Mars. Geology, 40(1), pp.31-34.

Butcher, F.E., Balme, M.R., Conway, S.J., Gallagher, C., Arnold, N.S., Storrar, R.D., Lewis, S.R., Hagermann, A. and Davis, J.M., 2020. Sinuous ridges in Chukhung crater, Tempe Terra, Mars: Implications for fluvial, glacial, and glaciofluvial activity. Icarus, p.114131.

Carr, M.H. and Head III, J.W., 2009. Geologic history of Mars. Earth and Planetary Science Letters, 294(3-4), pp.185-203.

Cedillo-Flores, Y., Treiman, A.H., Lasue, J. & Clifford, S.M. 2011. CO2 gas fluidization in the initiation and formation of Martian polar gullies. Geophysical Research Letters, 38, L21202.

Choudhary, P., Holt, J.W. and Kempf, S.D., 2016. Surface clutter and echo location analysis for the interpretation of SHARAD data from Mars. IEEE Geoscience and Remote Sensing Letters, 13(9), pp.1285-1289.

Christensen, P.R. 2003. Formation of recent Martian gullies through melting of extensive

water-rich snow deposits. Nature, 422, 45–48.

Chuang, F.C. and Crown, D.A., 2005. Surface characteristics and degradational history of debris aprons in the Tempe Terra/Mareotis fossae region of Mars. Icarus, 179(1), pp.24-42.

Chuang, F.C., Crown, D.A. and Berman, D.C., 2014, March. Glacial modification of Eastern Nereidum Montes, Mars: Observations from Southern Hemisphere mapping of lobate debris aprons and ice-rich flow features. In Proceedings of the 45rd Lunar and Planetary Science Conference.

Clancy, R. T., Sandor, B. J., Wolff, M. J., Christensen, P. R., Smith, M. D., Pearl, J. C., ... & Wilson, R. J. (2000). An intercomparison of ground-based millimeter, MGS TES, and Viking atmospheric temperature measurements: Seasonal and interannual variability of temperatures and dust loading in the global Mars atmosphere. Journal of Geophysical Research: Planets, 105(E4), 9553-9571.

Conway, S. J., Butcher, F. E., de Haas, T., Deijns, A. A., Grindrod, P. M., & Davis, J. M. (2018). Glacial and gully erosion on Mars: A terrestrial perspective. Geomorphology, 318, 26-57.

Conway, S., 2010. Debris flows on Earth and Mars (Doctoral dissertation, Open University).http://oro.open.ac.uk/44593/

Conway, S.J. & Balme, M.R. 2014. Decameter thick remnant glacial ice deposits on Mars. Geophysical Research Letters, 41, 5402–5409.

Conway, S.J., Balme, M.R., Kreslavsky, M.A., Murray, J.B. & Towner, M.C. 2015. The comparison of topographic long profiles of gullies on Earth to gullies on Mars: a signal of water on Mars. Icarus, 253, 189–204.

Conway, S.J., Balme, M.R., Murray, J.B., Towner, M.C., Okubo, C.H. & Grindrod, P.M. 2011. The indication of Martian gully formation processes by slope–area analysis. In: Balme, M.R., Bargery, A.S., Gallagher, C.J. & Gupta, S. (eds) Martian Geomorphology. Geological Society, London, Special Publications, 356, 171–201, https://doi.org/10.1144/SP356.10

Conway, S.J., Harrison, T.N., Soare, R.J., Britton, A.W. & Steele, L.J. 2017. New slope-normalized global gully density and orientation maps for Mars. In: Conway, S.J., Carrivick, J.L., Carling, P.A., De Haas, T. & Harrison, T.N. (eds) Martian Gullies and their Earth Analogues. Geological Society, London, Special Publications, 467. First published online November 27, 2017, https://doi.org/10.1144/SP467.3

Costard, F., Forget, F., Mangold, N. & Peulvast, J.P. 2002. Formation of recent Martian debris flows by melting of near-surface ground ice at high obliquity. Science, 295, 110–113.

Crosta, G.B., Frattini, P., 2004. Controls on modern alluvial fan processes in the central Alps,

northern Italy. Earth Surf. Proc. Land. 29 (3), 267–293. https://doi.org/10.1002/esp.1009.

de Haas, T., Conway, S.J., Butcher, F.E.G., Levy, J.S., Grindrod, P.M., Balme, M.R., Goudge, T.A., 2019a. Time will tell: temporal evolution of Martian gullies and paleoclimatic implications. Geol. Soc. Lond. Spec. Publ. 467 in press. https://doi.org/10.1144/SP467.1.

De Haas, T., Densmore, A.L., Stoffel, M., Suwa, H., Imaizumi, F., Ballesteros-Cánovas, J.A. and Wasklewicz, T., 2018. Avulsions and the spatio-temporal evolution of debris-flow fans. Earth-Science Reviews, 177, pp.53-75.

De Haas, T., Hauber, E. & Kleinhans, M.G. 2013. Local late Amazonian boulder breakdown and denudation rate on Mars. Geophysical Research Letters, 40, 3527–3531.

De Haas, T., Hauber, E., Conway, S.J., Van Steijn, H., Johnsson, A. and Kleinhans, M.G., 2015b. Earth-like aqueous debris-flow activity on Mars at high orbital obliquity in the last million years. Nature communications, 6, p.7543.

De Haas, T., Kleinhans, M. G., Carbonneau, P. E., Rubensdotter, L., & Hauber, E. (2015c). Surface morphology of fans in the high-Arctic periglacial environment of Svalbard: Controls and processes. Earth-Science Reviews, 146, 163-182.

de Haas, T., McArdell, B. W., Conway, S. J., McElwaine, J. N., Kleinhans, M. G., Salese, F., & Grindrod, P. M. (2019b). Initiation and flow conditions of contemporary flows in Martian gullies. Journal of Geophysical Research: Planets, 124(8), 2246-2271.

De Haas, T., van den Berg, W., Braat, L. and Kleinhans, M.G., 2016. Autogenic avulsion, channelization and backfilling dynamics of debris-flow fans. Sedimentology, 63(6), pp.1596-1619.

De Haas, T., Ventra, D., Hauber, E., Conway, S.J. & Kleinhans, M.G. 2015a. Sedimentological analyses of Martian gullies: the subsurface as the key to the surface. Icarus, 258, 92–108.

de Scally, F. A., & Owens, I. F. (2004). Morphometric controls and geomorphic responses on fans in the Southern Alps, New Zealand. Earth Surface Processes and Landforms: The Journal of the British Geomorphological Research Group, 29(3), 311-322.

De Scally, F.A., Owens, I.F., Louis, J., 2010. Controls on fan depositional processes in the schist ranges of the Southern Alps, New Zealand, and implications for debris-flow hazard assessment. Geomorphology 122 (1–2), 99–116. https://doi.org/10.1016/j.geomorph.2010.06.002.

Dickson, J.L. & Head, J.W. 2009. The formation and evolution of youthful gullies on Mars: gullies as the latestage phase of Mars most recent ice age. Icarus, 204, 63–86.

Dickson, J.L. et al., 2015. Recent climate cycles on Mars: Stratigraphic relationships between multiple generations of gullies and the latitude dependent mantle. Icarus 252, 83–94. http://dx.doi.org/10.1016/j.icarus.2014.12.035.

Dickson, J.L., Head, J.W. and Kreslavsky, M., 2007. Martian gullies in the southern mid-latitudes of Mars: Evidence for climate-controlled formation of young fluvial features based upon local and global topography. Icarus, 188(2), pp.315-323.

Dickson, J.L., Head, J.W. and Marchant, D.R., 2008. Late Amazonian glaciation at the dichotomy boundary on Mars: Evidence for glacial thickness maxima and multiple glacial phases. Geology, 36(5), pp.411-414.

Dickson, J.L., Head, J.W. and Marchant, D.R., 2010. Kilometer-thick ice accumulation and glaciation in the northern mid-latitudes of Mars: Evidence for crater-filling events in the Late Amazonian at the Phlegra Montes. Earth and Planetary Science Letters, 294(3-4), pp.332-342.

Dickson, J.L., Head, J.W., Fassett, C.I., 2012. Patterns of accumulation and flow of ice in the mid-latitudes of Mars during the Amazonian. Icarus 219, 723–732. http://dx.doi.org/10.1016/j.icarus.2012.03.010.

Dickson, J.L., Head, J.W., Goudge, T.A. and Barbieri, L., 2015. Recent climate cycles on Mars: Stratigraphic relationships between multiple generations of gullies and the latitude dependent mantle. Icarus, 252, pp.83-94.

Dickson, J.L., Head, J.W., Kreslavsky, M., 2007. Martian gullies in the southern midlatitudes of Mars: Evidence for climate-controlled formation of young fluvial features based upon local and global topography. Icarus 188, 315–323.

Diniega, S., Byrne, S., Bridges, N.T., Dundas, C.M. and McEwen, A.S., 2010. Seasonality of present-day Martian dune-gully activity. Geology, 38(11), pp.1047-1050.

Diniega, S., Hansen, C. J., McElwaine, J. N., Hugenholtz, C. H., Dundas, C. M., McEwen, A. S., & Bourke, M. C. (2013). A new dry hypothesis for the formation of Martian linear gullies. Icarus, 225(1), 526-537.

Dobrea, E.Z.N., Asphaug, E., Grant, J.A., Kessler, M.A., Mellon, M. T., 2007. Patterned ground as an alternative explanation for the formation of brain coral textures in the mid latitudes of Mars: HiRISE observations of lineated valley fill textures. In: Proc. 7th International Conference on Mars. Abstract #3358.

Dundas, C. M., 2020. Frequency and morphological consequences of Martian gully activity. 7th International Conference on Mars Polar Science and Exploration, abstract #6028.

Dundas, C. M., McEwen, A. S., Diniega, S., Hansen, C. J., Byrne, S., & McElwaine, J. N.

(2019). The formation of gullies on Mars today. Geological Society, London, Special Publications, 467(1), 67-94.

Dundas, C.M., Diniega, S. and McEwen, A.S., 2015a. Long-term monitoring of martian gully formation and evolution with MRO/HiRISE. Icarus, 251, pp.244-263.

Dundas, C.M., Byrne, S. and McEwen, A.S., 2015b. Modeling the development of martian sublimation thermokarst landforms. Icarus, 262, pp.154-169.

Dundas, C.M., Diniega, S., Hansen, C.J., Byrne, S. and McEwen, A.S., 2012. Seasonal activity and morphological changes in Martian gullies. Icarus, 220(1), pp.124-143.

Dundas, C.M., McEwen, A.S., Diniega, S., Byrne, S. and Martinez-Alonso, S., 2010. New and recent gully activity on Mars as seen by HiRISE. Geophysical Research Letters, 37(7).

Erkeling, G., Luesebrink, D., Hiesinger, H., Reiss, D., Heyer, T. and Jaumann, R., 2016. The Multi Temporal Database of Planetary Image Data (MUTED): A database to support the identification of surface changes and short-lived surface processes. Planetary and Space Science, 125, pp.43-61.

Fastook, J.L., Head, J.W. and Marchant, D.R., 2014. Formation of lobate debris aprons on Mars: Assessment of regional ice sheet collapse and debris-cover armoring. Icarus, 228, pp.54-63.

Fergason, R. L, Hare, T. M., & Laura, J. (2018). HRSC and MOLA Blended Digital Elevation Model at 200m v2. Astrogeology PDS Annex, U.S. Geological Survey. http://bit.ly/HRSC_MOLA_Blend_v0

Gallagher, C. and Balme, M., 2015. Eskers in a complete, wet-based glacial system in the Phlegra Montes region, Mars. Earth and Planetary Science Letters, 431, pp.96-109.

Gallagher, C., Butcher, F.E., Balme, M., Smith, I. and Arnold, N., 2020. Landforms indicative of regional warm based glaciation, Phlegra Montes, Mars. Icarus, p.114173.

Geissler, P. E. (2014). The birth and death of transverse aeolian ridges on Mars. Journal of Geophysical Research: Planets, 119(12), 2583-2599.

Glasser, N.F., Jennings, S.J.A., Hambrey, M.J. and Hubbard, B., 2015. Origin and dynamic significance of longitudinal structures (“flow stripes") in the Antarctic Ice Sheet. Earth Surface Dynamics, 3(2), pp.239-249.

Godin, E.; Osinski, G. R.; Harrison, T. N.; Pontefract, A. & Zanetti, M.Geomorphology of Gullies at Thomas Lee Inlet, Devon Island, Canadian High Arctic Permafrost and Periglacial Processes, 2019 , 30 , 19-34.

Haberle, R.M., McKay, C.P., Schaeffer, J., Cabrol, N.A., Grin, E.A., Zent, A.P. and Quinn, R., 2001. On the possibility of liquid water on present-day Mars. Journal of Geophysical Research: Planets, 106(E10), pp.23317-23326.

Hansen, C.J., Bourke, M., Bridges, N.T., Byrne, S., Colon, C., Diniega, S., Dundas, C., Herkenhoff, K., McEwen, A., Mellon, M. and Portyankina, G., 2011. Seasonal erosion and restoration of Mars' northern polar dunes. Science, 331(6017), pp.575-578.

Harrison, T.N., Osinski, G.R., Tornabene, L.L. and Jones, E., 2015. Global documentation of gullies with the Mars Reconnaissance Orbiter Context Camera and implications for their formation. Icarus, 252, pp.236-254.

Hartley, A.J., Mather, A.E., Jolley, E., Turner, P. (2005). Climatic controls on alluvial-fan activity, Coastal Cordillera, northern Chile. In: Harvey, A.M., Mather, A.E., Stokes, M. (Eds.), Alluvial Fans: Geomorphology, Sedimentology, Dynamics. Geological Society of London, Special Publication 251, 95-115.

Hartmann, W.K., 2005. Martian cratering 8: Isochron refinement and the chronology of Mars. Icarus, 174(2), pp.294-320.

Hartmann, W.K., Thorsteinsson, T. and Sigurdsson, F., 2003. Martian hillside gullies and Icelandic analogs. Icarus, 162(2), pp.259-277.

Head, J.W., Marchant, D.R. and Kreslavsky, M.A., 2008. Formation of gullies on Mars: Link to recent climate history and insolation microenvironments implicate surface water flow origin. Proceedings of the National academy of Sciences, 105(36), pp.13258-13263.

Head, J.W., Marchant, D.R., Agnew, M.C., Fassett, C.I. and Kreslavsky, M.A., 2006a. Extensive valley glacier deposits in the northern mid-latitudes of Mars: Evidence for Late Amazonian obliquity-driven climate change. Earth and Planetary Science Letters, 241(3-4), pp.663-671.

Head, J.W., Marchant, D.R., Dickson, J.L., Kress, A.M., Baker, D.M., 2010. Northern midlatitude glaciation in the Late Amazonian period of Mars: criteria for the recognition of debris-covered glacier and valley glacier landsystem deposits. Earth Planet. Sci. Lett. 294:306–320. https://doi.org/10.1016/j.epsl.2009.06.041.

Head, J.W., Marchant, D.R., Forget, F., Laskar, J., Madeleine, J.B. and Fastook, J.L., 2009. Deciphering the Late Amazonian climate history of Mars: Assessing obliquity predictions with geological observations and atmospheric general circulation models. LPI, p.1349.

Head, J.W., Mustard, J.F., Kreslavsky, M.A., Milliken, R.E. and Marchant, D.R., 2003. Recent ice ages on Mars. Nature, 426(6968), p.797.

Head, J.W., Nahm, A.L., Marchant, D.R. and Neukum, G., 2006b. Modification of the dichotomy boundary on Mars by Amazonian mid-latitude regional glaciation. Geophysical Research Letters, 33(8).

Head, J.W., Neukum, G., Jaumann, R., Hiesinger, H., Hauber, E., Carr, M., Masson, P., Foing, B., Hoffmann, H., Kreslavsky, M., Werner, S., Milkovich, S., van Gasselt, S., The HRSC Co-Investigator Team, 2005. Tropical to mid-latitude snow and ice accumulation, flow and glaciation on Mars. Nature 434, 346–351.

Hecht, M.H., 2002. Metastability of liquid water on Mars. Icarus, 156(2), pp.373-386.

Heldmann, J.L. and Mellon, M.T., 2004. Observations of Martian gullies and constraints on potential formation mechanisms. Icarus, 168(2), pp.285-304.

Heldmann, J.L. et al., 2005. Formation of martian gullies by the action of liquid water flowing under current martian environmental conditions. J. Geophys. Res. Planets 110. http://dx.doi.org/10.1029/2004JE002261.

Heldmann, J.L., Carlsson, E., Johansson, H., Mellon, M.T. and Toon, O.B., 2007. Observations of Martian gullies and constraints on potential formation mechanisms: II. The northern hemisphere. Icarus, 188(2), pp.324-344.

Hepburn, A.J., Ng, F.S.L., Livingstone, S.J., Holt, T.O. and Hubbard, B., 2020. Polyphase mid-latitude glaciation on Mars: Chronology of the formation of superposed glacier-like forms from crater-count dating. Journal of Geophysical Research: Planets, 125(2), p.e2019JE006102.

Herrick R.R., 2014. Elliptical Crater (Oblique Impact). In: Encyclopedia of Planetary Landforms. Springer, New York, NY.

Heyer, T., Hiesinger, H., Reiss, D., Erkeling, G., Bernhardt, H., Luesebrink, D. and Jaumann, R., 2018. The Multi-Temporal Database of Planetary Image Data (MUTED): A web-based tool for studying dynamic Mars. Planetary and Space Science, 159, pp.56-65.

Hibbard, S.M., Williams, N.R., Golombek, M.P., Osinski, G.R. and Godin, E., 2021. Evidence for widespread glaciation in Arcadia Planitia, Mars. Icarus, 359, p.114298.

Hobbs, S.W., Paull, D.J., Clark, J.D.A., 2014. A comparison of semiarid and subhumid terrestrial gullies with gullies on Mars: Implications for martian gully erosion. Geomorphology 204, 344–365. http://dx.doi.org/10.1016/j.geomorph.2013.08.018.

Hoffman, N., 2002. Active polar gullies on Mars and the role of carbon dioxide. Astrobiology, 2(3), pp.313-323.

Hubbard, B., Milliken, R.E., Kargel, J.S., Limaye, A. & Souness, C. 2011. Geomorphological

characterisation and interpretation of a mid-latitude glacier-like form: Hellas Planitia, Mars. Icarus, 211, 330–346.

Ilinca, V. (2021). Using morphometrics to distinguish between debris flow, debris flood and flood (Southern Carpathians, Romania). Catena, 197, 104982.

Ingersoll, A.P., 1970. Mars: Occurrence of liquid water. Science, 168(3934), pp.972-973.

Ishii, T. and Sasaki, S., 2004, March. Formation of recent Martian gullies by avalanches of CO2 frost. In Lunar and Planetary Science Conference (Vol. 35).

Ivanov, B.A., 2001. Mars/Moon cratering rate ratio estimates. Space Science Reviews, 96(1-4), pp.87-104.

Jackson LE, Kostaschuk RA, MacDonald GM (1987) Identification of debris flow hazard on alluvial fans in the Canadian Rocky Mountains. In: Costa JE, Wieczorek GF (eds) Debris flows/avalanches: process, recognition, and mitigation. Rev Eng Geol vol. VII. Geol. Soc. Am.

Jawin, E. R., Head, J. W., & Marchant, D. R. (2018). Transient post-glacial processes on Mars: geomorphologic evidence for a paraglacial period. Icarus, 309, 187-206.

Johnsson, A. et al., 2014. Evidence for very recent melt-water and debris flow activity in gullies in a young mid-latitude crater on Mars. Icarus 235, 37–54. http://dx.doi.org/10.1016/j.icarus.2014.03.005.

Khuller, A.R., Christensen, P.R., Harrison, T.N. and Diniega, S., 2021. The Distribution of Frosts on Mars: Links to Present-Day Gully Activity. Journal of Geophysical Research: Planets, 126(3), p.e2020JE006577.

Kirk, R.L., Howington-Kraus, E., Rosiek, M.R., Anderson, J.A., Archinal, B.A., Becker, K.J., Cook, D.A., Galuszka, D.M., Geissler, P.E., Hare, T.M., Holmberg, I.M., Keszthelyi, L.P., Redding, B.L., Delamere, W.A., Gallagher, D., Chapel, J.D., Eliason, E.M., King, R., McEwen, A.S., 2008. Ultrahigh resolution topographic mapping of Mars with MRO HiRISE stereo images: meter-scale slopes of candidate Phoenix landing sites. J. Geophys. Res. Planets 113. https://doi.org/10.1029/2007JE003000.

Kneissl, T., van Gasselt, S. and Neukum, G., 2011. Map-projection-independent crater size-frequency determination in GIS environments—New software tool for ArcGIS. Planetary and Space Science, 59(11-12), pp.1243-1254.

Kostaschuk, R.A., Macdonald, G.M., Putnam, P.E., 1986. Depositional process and alluvial fan-drainage basin morphometric relationships near banff, Alberta, Canada. Earth Surf. Proc. Land. 11 (5), 471–484.

Kreslavsky, M.A. and Head III, J.W., 2002. Mars: Nature and evolution of young latitude dependent water ice rich mantle. Geophysical Research Letters, 29(15), pp.14-1.

Kreslavsky, M.A., 2008. Slope steepness of channels and aprons: Implications for origin of martian gullies. Workshop Martian Gullies, Workshop on Martian Gullies 2008. Abs.#1301.

Kress, A. and Head, J.W., 2009. Ring-Mold Craters on Lineated Valley Fill, Lobate Debris Aprons, and Concentric Crater Fill on Mars: Implications for Near-Surface Structure, Composition, and Age. LPI, p.1379.

Kress, A.M. and Head, J.W., 2008. Ring-mold craters in lineated valley fill and lobate debris aprons on Mars: Evidence for subsurface glacial ice. Geophysical Research Letters, 35(23).

Langbein, W. B. (1964), Profiles of rivers of uniform discharge, U.S. Geol. Surv. Prof. Pap., 501-B, 119– 122.

Lanza, N. L., Meyer, G. A., Okubo, C. H., Newsom, H. E., & Wiens, R. C. (2010). Evidence for debris flow gully formation initiated by shallow subsurface water on Mars. Icarus, 205(1), 103-112.

Laskar, J., Correia, A.C.M., Gastineau, M., Joutel, F., Levrard, B., Robutel, P., 2004. Long term evolution and chaotic diffusion of the insolation quantities of Mars. Icarus 170, 343–364.

Lee, P., Cockell, C.S., Marinova, M.M., McKay, C.P. and Rice Jr, J.W., 2001. Snow and ice melt flow features on Devon Island, Nunavut, Arctic Canada as possible analogs for recent slope flow features on Mars. In Lunar and Planetary Science Conference (Vol. 32).

Levy, J.S., Fassett, C.I., Head, J.W., Schwartz, C. and Watters, J.L., 2014. Sequestered glacial ice contribution to the global Martian water budget: Geometric constraints on the volume of remnant, midlatitude debris-covered glaciers. Journal of Geophysical Research: Planets, 119(10), pp.2188-2196.

Levy, J.S., Head, J.W. and Marchant, D.R., 2007. Lineated valley fill and lobate debris apron stratigraphy in NilosyrtisMensae, Mars: Evidence for phases of glacial modification of the dichotomy boundary. Journal of Geophysical Research: Planets, 112(E8).

Levy, J., Head, J. and Marchant, D., 2009a. Thermal contraction crack polygons on Mars: Classification, distribution, and climate implications from HiRISE observations. Journal of Geophysical Research: Planets, 114(E1).

Levy, J.S., Head, J.W. and Marchant, D.R., 2009b. Concentric crater fill in Utopia Planitia: History and interaction between glacial “brain terrain” and periglacial mantle processes. Icarus, 202(2), pp.462-476.

Levy, J. S., Head, J. W., Marchant, D. R., Dickson, J. L., & Morgan, G. A. (2009c). Geologically recent gully–polygon relationships on Mars: Insights from the Antarctic Dry Valleys on the roles of permafrost, microclimates, and water sources for surface flow. Icarus, 201(1), 113-126.

Levy, J., Head, J.W. and Marchant, D.R., 2010a. Concentric crater fill in the northern mid-latitudes of Mars: Formation processes and relationships to similar landforms of glacial origin. Icarus, 209(2), pp.390-404.

Levy, J.S. et al., 2010b. Identification of gully debris flow deposits in Protonilus Mensae, Mars: Characterization of a water-bearing, energetic gully-forming process. In: Earth Planet. Sci. Lett. Mars Express after 6 Years in Orbit: Mars Geology from Three-Dimensional Mapping by the High Resolution Stereo Camera (HRSC) Experiment 294, 368–377.

Levy, J.S., Head, J.W., Marchant, D.R., 2011. Gullies, polygons and mantles in Martian permafrost environments: cold desert landforms and sedimentary processes during recent Martian geological history. Geol. Soc. Lond. Spec. Publ. 354:167–182. https://doi.org/10.1144/SP354.10.

Li, H., Robinson, M.S. and Jurdy, D.M., 2005. Origin of martian northern hemisphere mid-latitude lobate debris aprons. Icarus, 176(2), pp.382-394.

Lozac'h, L., Quantin-Nataf, C., Loizeau, D., Clenet, H., Bultel, B., Allemand, P., Thollot, P., Fernando, J., Ody, A. and Harrison, S., 2015, October. MarsSI: Martian surface Data processing Application. In European Planetary Science Congress (Vol. 10).

Lucchitta, B.K., 1981. Mars and Earth: Comparison of cold-climate features. Icarus, 45(2), pp.264-303.

Madeleine, J.-B., Forget, F., Head, J.W., Levrard, B., Montmessin, F., Millour, E., 2009. Amazonian northern mid-latitude glaciation on Mars: a proposed climate scenario. Icarus 203, 390–405.

Malin, M.C. and Edgett, K.S., 2000. Evidence for recent groundwater seepage and surface runoff on Mars. Science, 288(5475), pp.2330-2335.

Mangold, N., 2003a. Geomorphic analysis of lobate debris aprons on Mars at Mars Orbiter Camera scale: Evidence for ice sublimation initiated by fractures. Journal of Geophysical Research: Planets, 108(E4).

Mangold, N., Costard, F. and Forget, F., 2003b. Debris flows over sand dunes on Mars: Evidence for liquid water. Journal of Geophysical Research: Planets, 108(E4).

Mars Information System application (MarsSI), an online application accessible at emars.univ-

lyon1.fr).

McConnell, B.S., Newsom, H.E., Lanza, N., 2007. Recent climate change and presence of near-surface ice deposits: evidence from inverted impact craters located on lineated valley fill, ismenius lacus region. In: Seventh International Conference on Mars, Abstract 3261.

McEwen, A.S., 2018, March. The Future of MRO/HiRISE. In Lunar and Planetary Science Conference (Vol. 49).

Mcewen, A.S., Eliason, E.M. et al. 2007a. Mars reconnaissance orbiter's High Resolution Imaging Science Experiment (HiRISE). Journal of Geophysical Research: Planets, 112, E05S02.

McEwen, A.S., Hansen, C.J., Delamere, W.A., Eliason, E.M., Herkenhoff, K.E., Keszthelyi, L., Gulick, V.C., Kirk, R.L., Mellon, M.T., Grant, J.A. and Thomas, N., 2007b. A closer look at water-related geologic activity on Mars. Science, 317(5845), pp.1706-1709.

Mellon, M.T. and Phillips, R.J., 2001. Recent gullies on Mars and the source of liquid water. Journal of Geophysical Research: Planets, 106(E10), pp.23165-23179.

Melton MA (1957) An analysis of the relation among elements of climate, surface properties and geomorphology. Office of Nav. Res. Dept. Geol. Columbia Univ, NY. Tech. Rep. 11.

Michael, G.G. and Neukum, G., 2010. Planetary surface dating from crater size–frequency distribution measurements: Partial resurfacing events and statistical age uncertainty. Earth and Planetary Science Letters, 294(3-4), pp.223-229.

Michael, G.G., 2013. Planetary surface dating from crater size–frequency distribution measurements: multiple resurfacing episodes and differential isochron fitting. Icarus 226, 885–890.

Michael, G.G., Platz, T., Kneissl, T. and Schmedemann, N., 2012. Planetary surface dating from crater size–frequency distribution measurements: Spatial randomness and clustering. Icarus, 218(1), pp.169-177.

Milliken, R.E., Mustard, J.F., Goldsby, D.L., 2003. Viscous flow features on the surface of Mars: observations from high-resolution Mars Orbiter Camera (MOC) images. J. Geophys. Res. 108. https://doi.org/10.1029/2002JE002005.

Morgan, G.A., Head III, J.W. and Marchant, D.R., 2009. Lineated valley fill (LVF) and lobate debris aprons (LDA) in the DeuteronilusMensae northern dichotomy boundary region, Mars: Constraints on the extent, age and episodicity of Amazonian glacial events. Icarus, 202(1), pp.22-38.

Morgan, G.A., Head, J.W., Forget, F., Madeleine, J.B. and Spiga, A., 2010. Gully formation on Mars: Two recent phases of formation suggested by links between morphology, slope orientation and insolation history. Icarus, 208(2), pp.658-666.

Multi-temporal Database of Planetary Image Data, an online tool accessible at http://muted.wwu.de/.

Mustard, J.F., Cooper, C.D. and Rifkin, M.K., 2001. Evidence for recent climate change on Mars from the identification of youthful near-surface ground ice. Nature, 412(6845), p.411.

Noe Dobrea, E.Z., Asphaug, E., Grant, J.A., Kessler, M.A. and Mellon, M.T., 2007, July. Patterned ground as an alternative explanation for the formation of brain coral textures in the mid latitudes of Mars: HiRISE observations of lineated valley fill textures. In Seventh International Conference on Mars (Vol. 1353, p. 3358).

Orgel, C., Hauber, E., van Gasselt, S., Reiss, D., Johnsson, A., Ramsdale, J.D., Smith, I., Swirad, Z.M., Séjourné, A., Wilson, J.T. and Balme, M.R., 2019. Grid mapping the northern plains of Mars: A new overview of recent water-and ice-related landforms in Acidalia Planitia. Journal of Geophysical Research: Planets, 124(2), pp.454-482.

Pasquon, K., Gargani, J., Massé, M., & Conway, S. J. (2016). Present-day formation and seasonal evolution of linear dune gullies on Mars. Icarus, 274, 195-210.

Pasquon, K., Gargani, J., Massé, M., Vincendon, M., Conway, S.J., Séjourné, A., Jomelli, V., Balme, M.R., Lopez, S. and Guimpier, A., 2019a. Present-day development of gully-channel sinuosity by carbon dioxide gas supported flows on Mars. Icarus, 329, pp.296-313.

Pasquon, K., Gargani, J., Nachon, M., Conway, S.J., Massé, M., Jouannic, G., Balme, M.R., Costard, F. and Vincendon, M., 2019b. Are different Martian gully morphologies due to different processes on the Kaiser dune field?. Geological Society, London, Special Publications, 467(1), pp.145-164.

Pelletier, J.D., Kolb, K.J., McEwen, A.S. and Kirk, R.L., 2008. Recent bright gully deposits on Mars: Wet or dry flow?. Geology, 36(3), pp.211-214.

Phillips, J.D., Lutz, J.D., 2008. Profile convexities in bedrock and alluvial streams. Geomorphology 102, 554–566.

Pierce, T.L. and Crown, D.A., 2003. Morphologic and topographic analyses of debris aprons in the eastern Hellas region, Mars. Icarus, 163(1), pp.46-65.

Pilorget, C. & Forget, F. 2016. Formation of gullies on mars by debris flows triggered by CO2 sublimation. Nature Geoscience, 9, 65–69.

Plaut, J.J., Safaeinili, A., Holt, J.W., Phillips, R.J., Head, J.W., Seu, R., Putzig, N.E. and Frigeri, A., 2009. Radar evidence for ice in lobate debris aprons in the mid-northern latitudes of Mars. Geophysical research letters, 36(2).

Putzig, N.E., Phillips, R.J., Campbell, B.A., Plaut, J.J., Holt, J.W., Bernardini, F., Egan, A.F. and Smith, I.B., 2016. Custom SHARAD processing via the CO-SHARPS Processing Boutique. LPI, (1903), p.3010.

Quantin-Nataf, C., Lozac'h, L., Thollot, P., Loizeau, D., Bultel, B., Fernando, J., Allemand, P., Dubuffet, F., Poulet, F., Ody, A. and Clenet, H., 2018. MarsSI: Martian surface data processing information system. Planetary and Space Science, 150, pp.157-170.

Raack, J., Reiss, D., Appéré, T., Vincendon, M., Ruesch, O. and Hiesinger, H., 2015. Present-day seasonal gully activity in a south polar pit (Sisyphi Cavi) on Mars. Icarus, 251, pp.226-243.

Ramsdale, J.D., Balme, M.R., Gallagher, C., Conway, S.J., Smith, I.B., Hauber, E., Orgel, C., Séjourné, A., Costard, F., Eke, V.R. and van Gasselt, S.A., 2019. Grid Mapping the Northern Plains of Mars: Geomorphological, Radar, and Water Equivalent Hydrogen Results From Arcadia Plantia. Journal of Geophysical Research: Planets, 124(2), pp.504-527.

Reiss, D. and Jaumann, R., 2003. Recent debris flows on Mars: Seasonal observations of the Russell Crater dune field. Geophysical Research Letters, 30(6).

Reiss, D. et al., 2004. Absolute dune ages and implications for the time of formation of gullies in Nirgal Vallis, Mars. J. Geophys. Res.-Planets 109. http://dx.doi.org/10.1029/2004JE002251.

Reiss, D., Hauber, E. Et Al. 2011. Terrestrial gullies and debris-flow tracks on Svalbard as planetary analogs for Mars. In: GARRY, W.B. & BLEACHER, J.E. (eds) Analogs for Planetary Exploration. Geological Society of America Special Papers, 483, 165–175.

Reiss, D., Hiesinger, H., Hauber, E. and Gwinner, K., 2009. Regional differences in gully occurrence on Mars: A comparison between the Hale and Bond craters. Planetary and Space Science, 57(8-9), pp.958-974.

Richardson, M.I. and Mischna, M.A., 2005. Long term evolution of transient liquid water on Mars. Journal of Geophysical Research: Planets, 110(E3).

Rodine, J.D., Johnson, A.M., 1976. The ability of debris, heavily freighted with coarse clastic materials, to flow on gentle slopes. Sedimentology 23, 213–234.

Ryder, J. (1971). Some aspects of the morphometry of paraglacial alluvial fans in South-central British Columbia. Canadian Journal of Earth Sciences 8: 1252-1264.

Safaeinili, A., Holt, J., Plaut, J.J., Posiolova, L., Phillips, R., Head, J.W. and Seu, R., 2009.

New radar evidence for glaciers in Mars Phlegra Montes region. LPI, p.1988.

Schon, S.C. and Head, J.W., 2011. Keys to gully formation processes on Mars: relation to climate cycles and sources of meltwater. Icarus, 213(1), pp.428-432.

Schon, S.C., Head, J.W. and Fassett, C.I., 2009. Unique chronostratigraphic marker in depositional fan stratigraphy on Mars: Evidence for ca. 1.25 Ma gully activity and surficial meltwater origin. Geology, 37(3), pp.207-210.

Sears, D.W. and Moore, S.R., 2005. On laboratory simulation and the evaporation rate of water on Mars. Geophysical research letters, 32(16).

Seu, R., Phillips, R.J., Biccari, D., Orosei, R., Masdea, A., Picardi, G., Safaeinili, A., Campbell, B.A., Plaut, J.J., Marinangeli, L. and Smrekar, S.E., 2007. SHARAD sounding radar on the Mars Reconnaissance Orbiter. Journal of Geophysical Research: Planets, 112(E5).

Siewert, M. B., Krautblatter, M., Christiansen, H. H., & Eckerstorfer, M. (2012). Arctic rockwall retreat rates estimated using laboratory-calibrated ERT measurements of talus cones in Longyeardalen, Svalbard. Earth Surface Processes and Landforms, 37(14), 1542-1555.

Sinha, R. K., Ray, D., De Haas, T., & Conway, S. J. (2020). Global documentation of overlapping lobate deposits in Martian gullies. Icarus, 352, 113979.

Sinha, R. K., Vijayan, S., Shukla, A. D., Das, P., & Bhattacharya, F. (2019). Gullies and debris-flows in Ladakh Himalaya, India: a potential Martian analogue. Geological Society, London, Special Publications, 467(1), 315-342.

Sinha, R.K. and Murty, S.V., 2013a. Geomorphic signatures of glacial activity in the Alba Patera volcanic province: Implications for recent frost accumulation on Mars. Journal of Geophysical Research: Planets, 118(8), pp.1609-1631.

Sinha, R.K. and Murty, S.V.S., 2013b. Evidence of extensive glaciation in Deuteronilus Mensae, Mars: Inferences towards multiple glacial events in the past epochs. Planetary and Space Science, 86, pp.10-32.

Sinha, R.K. and Murty, S.V.S., 2015. Amazonian modification of Moreux crater: Record of recent and episodic glaciation in the ProtonilusMensae region of Mars. Icarus, 245, pp.122-144.

Sinha, R.K. and Vijayan, S., 2017. Geomorphic investigation of craters in Alba Mons, Mars: Implications for Late Amazonian glacial activity in the region. Planetary and Space Science, 144, pp.32-48.

Sinha, R.K., Vijayan, S. and Bharti, R.R., 2017. Study of ice-related flow features around

Tanaica Montes, Mars: Implications for late amazonian debris-covered glaciation. Icarus, 297, pp.217-239.

Smith, D.E., Zuber, M.T., Frey, H.V., Garvin, J.B., Head, J.W., Muhleman, D.O., Pettengill, G.H., Phillips, R.J., Solomon, S.C., Zwally, H.J. and Banerdt, W.B., 2001. Mars Orbiter Laser Altimeter: Experiment summary after the first year of global mapping of Mars. Journal of Geophysical Research: Planets, 106(E10), pp.23689-23722.

Souness, C., & Hubbard, B. (2012). Mid-latitude glaciation on Mars. Progress in Physical Geography, 36(2), 238-261.

Souness, C., Hubbard, B., Milliken, R. E., & Quincey, D. (2012). An inventory and population-scale analysis of martian glacier-like forms. Icarus, 217(1), 243-255.

Squyres, S.W. and Carr, M.H., 1986. Geomorphic evidence for the distribution of ground ice on Mars. Science, 231(4735), pp.249-252.

Squyres, S.W., 1978. Martian fretted terrain: Flow of erosional debris. Icarus, 34(3), pp.600-613.

Squyres, S.W., 1979. The distribution of lobate debris aprons and similar flows on Mars. Journal of Geophysical Research: Solid Earth, 84(B14), pp.8087-8096.

Stillman, D.E. and Grimm, R.E., 2018. Two pulses of seasonal activity in martian southern mid-latitude recurring slope lineae (RSL). Icarus, 302, pp.126-133.

Stock, J.D., Dietrich, W.E., 2006. Erosion of steepland valleys by debris flow. Geol. Soc. Am. Bull. 118 (9/10), 1125–1148. doi:10.1130/B25902.1.

Stolle, A., Langer, M., Blöthe, J. H., & Korup, O. (2015). On predicting debris flows in arid mountain belts. Global and Planetary Change, 126, 1-13.

Tanaka, K.L., Robbins, S.J., Fortezzo, C.M., Skinner Jr, J.A. and Hare, T.M., 2014. The digital global geologic map of Mars: Chronostratigraphic ages, topographic and crater morphologic characteristics, and updated resurfacing history. Planetary and Space Science, 95, pp.11-24.

Tao, Y., Muller, J.P., Sidiropoulos, P., Xiong, S.T., Putri, A.R.D., Walter, S.H.G., Veitch-Michaelis, J. and Yershov, V., 2018. Massive stereo-based DTM production for Mars on cloud computers. Planetary and Space Science, 154, pp.30-58.

Tesson, P.A., Conway, S.J., Mangold, N., Ciazela, J., Lewis, S.R. and Mège, D., 2019. Evidence for thermal-stress-induced rockfalls on Mars impact crater slopes. Icarus, p.113503.

Treiman, A.H., 2003. Geologic settings of Martian gullies: Implications for their origins.

Journal of Geophysical Research: Planets, 108(E4).

Van Gasselt, S., Hauber, E. and Neukum, G., 2010. Lineated valley fill at the Martian dichotomy boundary: Nature and history of degradation. Journal of Geophysical Research: Planets, 115(E8).

Vincendon, M., 2015. Identification of Mars gully activity types associated with ice composition. J. Geophys. Res. Planets, 120, https://doi.org/10.1002/2015JE004909.

Viola, D., McEwen, A.S., Dundas, C.M. and Byrne, S., 2015. Expanded secondary craters in the Arcadia Planitia region, Mars: Evidence for tens of Myr-old shallow subsurface ice. Icarus, 248, pp.190-204.

Welsh, A., Davies, T., 2011. Identification of alluvial fans susceptible to debris-flow hazards. Landslides 8 (2), 183–194.

Wilford, D. J., Sakals, M. E., Innes, J. L., Sidle, R. C., & Bergerud, W. A. (2004). Recognition of debris flow, debris flood and flood hazard through watershed morphometrics. Landslides, 1(1), 61-66.

Williams, K.E., Toon, O.B., Heldmann, J.L. and Mellon, M.T., 2009. Ancient melting of mid-latitude snowpacks on Mars as a water source for gullies. Icarus, 200(2), pp.418-425.